

Lecture Notes in Mechanical Engineering

Magd Abdel Wahab *Editor*


Proceedings of the 9th International Conference on Fracture, Fatigue and Wear

FFW 2021, August 2–3, Ghent
University, Belgium

 Springer


Lecture Notes in Mechanical Engineering

Series Editors

Francisco Cavas-Martínez , Departamento de Estructuras, Construcción y Expresión Gráfica Universidad Politécnica de Cartagena, Cartagena, Murcia, Spain

Fakher Chaari, National School of Engineers, University of Sfax, Sfax, Tunisia

Francesca di Mare, Institute of Energy Technology, Ruhr-Universität Bochum, Bochum, Nordrhein-Westfalen, Germany

Francesco Gherardini , Dipartimento di Ingegneria “Enzo Ferrari”, Università di Modena e Reggio Emilia, Modena, Italy

Mohamed Haddar, National School of Engineers of Sfax (ENIS), Sfax, Tunisia

Vitalii Ivanov, Department of Manufacturing Engineering, Machines and Tools, Sumy State University, Sumy, Ukraine

Young W. Kwon, Department of Manufacturing Engineering and Aerospace Engineering, Graduate School of Engineering and Applied Science, Monterey, CA, USA

Justyna Trojanowska, Poznan University of Technology, Poznan, Poland

Lecture Notes in Mechanical Engineering (LNME) publishes the latest developments in Mechanical Engineering—quickly, informally and with high quality. Original research reported in proceedings and post-proceedings represents the core of LNME. Volumes published in LNME embrace all aspects, subfields and new challenges of mechanical engineering. Topics in the series include:

- Engineering Design
- Machinery and Machine Elements
- Mechanical Structures and Stress Analysis
- Automotive Engineering
- Engine Technology
- Aerospace Technology and Astronautics
- Nanotechnology and Microengineering
- Control, Robotics, Mechatronics
- MEMS
- Theoretical and Applied Mechanics
- Dynamical Systems, Control
- Fluid Mechanics
- Engineering Thermodynamics, Heat and Mass Transfer
- Manufacturing
- Precision Engineering, Instrumentation, Measurement
- Materials Engineering
- Tribology and Surface Technology

To submit a proposal or request further information, please contact the Springer Editor of your location:

China: Ms. Ella Zhang at ella.zhang@springer.com

India: Priya Vyas at priya.vyas@springer.com

Rest of Asia, Australia, New Zealand: Swati Meherishi
at swati.meherishi@springer.com

All other countries: Dr. Leontina Di Cecco at Leontina.dicecco@springer.com

To submit a proposal for a monograph, please check our Springer Tracts in Mechanical Engineering at <https://link.springer.com/bookseries/11693> or contact Leontina.dicecco@springer.com

Indexed by SCOPUS. All books published in the series are submitted for consideration in Web of Science.

More information about this series at <https://link.springer.com/bookseries/11236>

Magd Abdel Wahab
Editor

Proceedings of the 9th International Conference on Fracture, Fatigue and Wear

FFW 2021, August 2–3, Ghent University,
Belgium

 Springer

Editor

Magd Abdel Wahab
Faculty of Engineering and Architecture
Ghent University, Laboratory Soete
Zwijnaarde, Belgium

ISSN 2195-4356

ISSN 2195-4364 (electronic)

Lecture Notes in Mechanical Engineering

ISBN 978-981-16-8809-6

ISBN 978-981-16-8810-2 (eBook)

<https://doi.org/10.1007/978-981-16-8810-2>

© The Editor(s) (if applicable) and The Author(s), under exclusive license to Springer Nature Singapore Pte Ltd. 2022

This work is subject to copyright. All rights are solely and exclusively licensed by the Publisher, whether the whole or part of the material is concerned, specifically the rights of translation, reprinting, reuse of illustrations, recitation, broadcasting, reproduction on microfilms or in any other physical way, and transmission or information storage and retrieval, electronic adaptation, computer software, or by similar or dissimilar methodology now known or hereafter developed.

The use of general descriptive names, registered names, trademarks, service marks, etc. in this publication does not imply, even in the absence of a specific statement, that such names are exempt from the relevant protective laws and regulations and therefore free for general use.

The publisher, the authors and the editors are safe to assume that the advice and information in this book are believed to be true and accurate at the date of publication. Neither the publisher nor the authors or the editors give a warranty, expressed or implied, with respect to the material contained herein or for any errors or omissions that may have been made. The publisher remains neutral with regard to jurisdictional claims in published maps and institutional affiliations.

This Springer imprint is published by the registered company Springer Nature Singapore Pte Ltd.

The registered company address is: 152 Beach Road, #21-01/04 Gateway East, Singapore 189721, Singapore

Organising Committee

Chairman

Prof. Magd Abdel Wahab, Ghent University, Belgium

International Scientific Committee

Prof. S. Abdullah, Universiti Kebangsaan Malaysia, Malaysia
Dr. J. Abenojar, Universidad Carlos III de Madrid, Spain
Dr. R. Das, University of Auckland, New Zealand
Dr. A. H. Ertas, Bursa Technical University, Turkey
Dr. S. Fouvry, Ecole Centrale de Lyon, France
Prof. T. Hattori, Shizuoka Institute of Science and Technology, Japan
Dr. M. Kchaou, University of Sfax, Tunisia
Dr. S. Khatir, Ghent University, Belgium
Dr. C. Le Thanh, Open University Ho Chi Minh City, Vietnam
Dr. K. Masuda, University of Toyama, Japan
Prof. T. Miyazaki, University of Ryukyuu, Japan
Prof. H. Nguyen, HUTECH, Vietnam
Prof. K. Oda, Oita University, Japan
Prof. R. V. Prakash, Indian Institute of Technology, India
Prof. T. Qin, China Agricultural University, China
Prof. F. Rezai-Aria, Ecole des Mines d'Albi, France
Prof. T. Rabczuk, Bauhaus University Weimar, Germany
Dr. A. Rudawska, Lublin University of Technology, Poland
Dr. M. S. Prabhudev, Government Polytechnic, Kalgi, India
Dr. Y. Sano, Kyushu Institute of Technology, Japan
Prof. J. Song, Ostwestfalen-Lippe University, Germany
Prof. J. Toribio, University of Salamanca, Spain

Prof. C. Xu, China Agricultural University, China

Dr. T. Yue, Ghent University, Belgium

Prof. C. Zhou, Nanjing University of Aeronautics and Astronautics, China

Dr. X. Zhuang, Leibniz Universität Hannover, Germany

Preface

This volume contains the proceedings of the 9th International Conference on Fracture, Fatigue and Wear (FFW 2021). Fracture, Fatigue and Wear 2021 is the 9th FFW conference and is held online during 2–3 August 2021. Previous conferences were celebrated in Jinan (China, 2010), Kitakyushu (Japan, 2013), Kitakyushu (Japan, 2014), Ghent (Belgium, 2015), Kitakyushu (Japan, 2016), Porto (Portugal, 2017) and Ghent (Belgium, 2020).

The overall objective of the conference is to bring together international scientists and engineers in academia and industry in fields related to Fracture Mechanics, Fatigue of Materials, Tribology and Wear of Materials. The conference covers industrial engineering applications of the above topics including theoretical and analytical methods, numerical simulations and experimental techniques. One of the aims of the conference is to promote cooperation between international scientists and engineers from a large number of disciplines, who are involved in research related to Fracture, Fatigue and Wear. The presentations of FFW 2021 are divided into 3 main sessions, namely (1) Fracture, (2) Fatigue and (3) Wear.

The organising committee is grateful to keynote speaker, Prof. Luca Susmel, the University of Sheffield, UK, for his interesting keynote speech entitled ‘Critical plane and critical distance approaches to assess damage under variable amplitude fretting fatigue loading’.

Special thanks go to members of the Scientific Committee of FFW 2021 for reviewing the articles published in this volume and for judging their scientific merits. Based on the comments of reviewers and the scientific merits of the submitted manuscripts, the articles were accepted for publication in the conference proceedings and for presentation at the conference venue. The accepted papers are of a very high scientific quality and contribute to the advancement of knowledge in all research topics relevant to the FFW conference.

Finally, the organising committee would like to thank all the authors, who have contributed to this volume and to those who have presented their research work at the conference venue in Ghent.

Zwijnaarde, Belgium

Magd Abdel Wahab
Chairman of FFW 2021

Contents

Fracture

| | |
|--|----|
| Software Development to Calculate the Linear Elastic Fracture Mechanics Stress Intensity Factor with Python | 3 |
| Cádmo Dias, Pedro Cunha, Claysson Vimieiro, János Landre, and Pedro Américo | |
| Shear Failure Analysis with Modelling Multiple Discontinuities in a Concrete Beam Using XFEM | 13 |
| A. Faron and G. A. Rombach | |
| Mode I Crack in Elastically Identical Bimaterial Joined by Under-Matched Weld Interlayer: A New Theoretical Model | 23 |
| Sunil Bhat, H. Adarsha, and J. Deepak | |
| Durability of Cement Mortars with a High Proportion of Mineral Admixture After Bacterial Environment Exposure | 35 |
| Adriana Estokova, Michaela Smolakova, and Alena Luptakova | |
| Unloading of Low Velocity Impact Between Elastic and Elastic-Plastic Bodies | 47 |
| Chuanqing Chen, Magd Abdel Wahab, Qiao Wang, and Xiaochun Yin | |
| Fracture Micro Mechanism of Cryogenically Treated Ledeburitic Tool Steel | 67 |
| Peter Jurči, Jana Ptačinová, and Ivo Dlouhý | |
| Strength of Solder and Adhesive Joints of Copper Sheets | 85 |
| Anna Rudawska, Jakub Szabelski, Izabela Miturska, and Elżbieta Doluk | |
| Design of an Experiment to Analyze Modal Parameters in a Crack and Without Crack Conditions in the Presence of Thermal and Mechanical Vibration | 97 |
| Khangamlung Kamei and Muhammad A. Khan | |

Impact of Mechanical Treatment on Strength of Steel Adhesive Joints 109
 Anna Rudawska, Magd Abdel Wahab, Izabela Miturska, Jakub Szabelski, Elżbieta Doluk, and Dana Stančėková

Modeling of Adhesive Contact of Elastic Bodies with Regular Microgeometry 123
 Yulia Makhovskaya

Tuning the Mechanical Properties of the Viscoelastic Materials, for the Improvement of Their Adhesive Performance 139
 Elena Pierro, Luciano Afferrante, and Giuseppe Carbone

Numerical and Experimental Analysis of Profile Complexity in Aluminum Extrusion 149
 Josiah Cherian Chekotu, Sayyad Zahid Qamar, and Sayyad Basim Qamar

Fatigue

Critical Plane and Critical Distance Approaches to Assess Damage Under Variable Amplitude Fretting Fatigue Loading 161
 C. V. Teuchou Kouanga, D. Nowell, R. S. Dwyer Joyce, and L. Susmel

Change in Surface Topography of Structural Steel Under Cyclic Plastic Deformation 175
 Aleena Saleem, Hiroshi Tamura, and Hiroshi Katsuchi

Comparative Study of Crack Initiation Criteria for Flat–Flat Contacts Subjected to Fretting Fatigue of Drive-Train Components 195
 Denny Knabner, Sebastian Vetter, Lukáš Suchý, and Alexander Hasse

Assessment of a Thermal Fatigue Test Using Open Source CAE and Elastic FEA-Based Simplified Method 217
 Shosuke Miyahira and Terutaka Fujioka

Simple Fatigue Crack Propagation Evaluation by Enhanced Reference Stress Method Using Open-Source CAE 239
 Bohua Li and Terutaka Fujioka

Fatigue Life Prediction Under Interspersed Overload in Constant Amplitude Loading Spectrum via Crack Closure and Plastic Zone Interaction Models—A Comparative Study 253
 Chandra Kant and G. A. Harmain

Wear

Numerical Fretting© Wear Simulation of Deep Groove Ball Bearing Under Radial Variable Load 263
David Cubillas, Mireia Olave, Iñigo Llavori, Ibai Ulacia, Jon Larrañaga, Aitor Zurutuza, and Arkaitz Lopez

Contribution Self-lubrication Mechanism of New Antifriction Copper-Based Composites in the Vehicles’ Heavy-Loaded Friction Units 273
Krzysztof Jamrozak and Tetiana Roik

Wear Behavior of Bovine and Porcine Bone Versus Biocompatible Synthetic Materials, Case of Knee Prosthesis 285
M. Castillo Sánchez, D. Zarate Lara, M. Velázquez Vázquez, G. Rodríguez Castro, and L. H. Hernández Gómez

Prediction of Surface Finish Model in Cutting AISI 4140 Steel with Different Approaches 303
Yusuf Şahin, Acar Can Kocabiçak, and Senai Yalçinkaya

Fracture

Software Development to Calculate the Linear Elastic Fracture Mechanics Stress Intensity Factor with Python



Cádmio Dias, Pedro Cunha, Claysson Vimieiro, János Landre, and Pedro Américo

Abstract In order to develop a software to calculate the linear elastic fracture mechanics stress intensity factor, the present work uses Python programming language and a framework to create graphical user interface called Tkinter. The calculation of the stress intensity factor is an important key to the engineering design once it describes the fatigue growth behavior, one of the main challenges of the structural integrity area in the past years. Besides the increasing use of the finite element method to do so, the use of the linear fracture mechanics approach to give approximate solutions are still very important to analyze failure of structures and machinery components and consequently to support in the estimation of their life. Aiming to validate the results obtained with the aid of the software, examples were made analytically and the results of these two approaches were the same, corroborating with the reliability of the software developed by the present work.

Keywords Linear elastic fracture mechanics · Stress intensity factor · Fatigue crack growth

1 Introduction

Almost all structures have stress concentration because of flaws and holes and such stress induces failures due cracks during the operation of the component, especially when the system passes through alternating loads because of the cyclic plastic deformation [1, 2]. Because of that, some approaches have been used to investigate thoroughly these cases [3–5], as the linear elastic fracture mechanics (LEFM) [6, 7].

The LEFM has received considerable attention in the past years and now it can be employed in engineering design to prevent against the brittle fractures in structures and machinery components [8]. Meanwhile, the use of computational methods in engineering is increasing once most of its problems can be characterized by mathematics solutions as ordinary or partial differential equations [9]. In tandem with this,

C. Dias (✉) · P. Cunha · C. Vimieiro · J. Landre · P. Américo
Pontifícia Universidade Católica de Minas Gerais, Belo Horizonte, MG 30535901, Brazil

problems that would have taken years to work out with the computational methods from 50 years ago in these days can be solved in a few seconds [10], resulting in greater use of simulation models to solve problems and to aid in decision-making [11, 12].

Basically, there are two types of model equations that describe the physical phenomena: Axiomatic ones that are related to balance laws as energy and mass, for example, and equations extracted from collected, natural or synthetic data [13]. The second one describes the fatigue crack growth, which its behavior is a big challenge in the past few decades [14, 15] and after laboratory tests scientists reached a few common crack behaviors [8], as will be approached latter. In this scenario, with the physical models established and the aim to develop a software to simulate these models, the programming language used to develop the algorithm was Python.

Python is renowned programming language that is being used by well-known corporations through past years due its simple, easy and intuitive syntax [16, 17], besides the countless open-source libraries available by its community. Because of these characteristics and being a high-level programming language, Python is also gaining popularity in academia to teach not only computer science and engineering novices, but many other knowledge areas too [18], equipping students with relevant skills that will be primordial in the next years [19]. In this scenario, Python was the chose one programming language to the development the aim of the present work: A software to calculate the LEFM stress intensity factor in structures and machinery components.

2 The Stress Intensity Factor by the Linear Elastic Fracture Mechanics Approach

The LEFM is a widely used method for damage tolerance analysis and this approach will be used in the present work. Basically, this approach is based on the fact that a crack with an initial size will grow till the final size which will lead the component to failure [20]. Besides the widespread use of the finite element method (FEM) recently, approximate solutions are still very important to analyze failure of structures [21].

According to the LEFM, the stress intensity factor (K) controls the crack growth and relates the crack size, structural geometry and remote load, as can be seen below where σ is the applied stress, a is the crack length, and β is a factor that depends on the specimen geometry and the crack length [8].

$$K = \beta * \sigma * \sqrt{\pi * a} \quad (1)$$

Once β is dimensionless, K is given by unit of stress times length^{1/2}. Due the fact that β depends on the specimen geometry, it has to be described in specific ways for each case. Classic literatures of structural integrity present the most common cases [8], showed in Fig. 1.

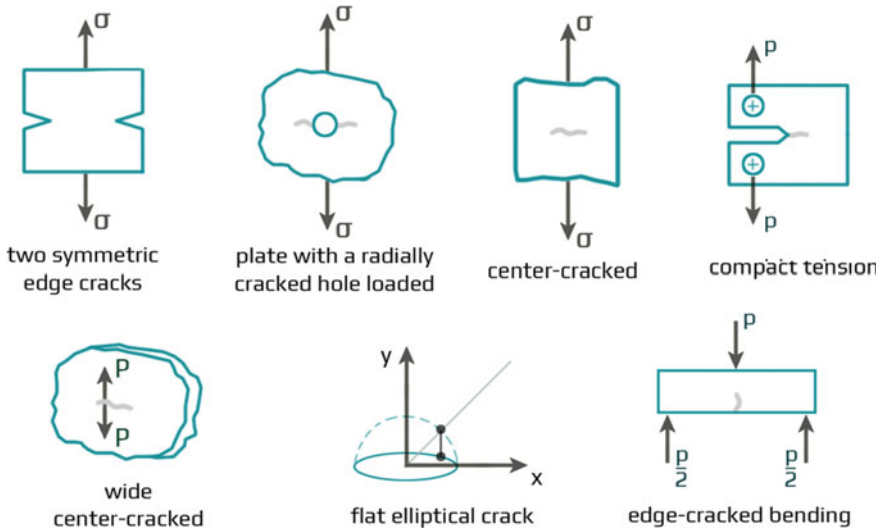


Fig. 1 Common crack types

As will be seeing in the next topic of the present work, the approached examples are the center-cracked and the wide center-cracked. Due to this, only the equations that describe these cases will be shown below.

The center-cracked specimen test is one of the most common cases to be seen. Let the crack longitudinal size be represented by a , as the width of the specimen be represented by W . Equation (2) describes the stress intensity factor for this case.

$$K = \sigma * \sqrt{\pi \cdot a} * \sec\left(\frac{\pi * a}{W}\right)^{1/2} \tag{2}$$

According to Fig. 1, σ of the equation above is the stress value. Other important detail about this factor is that it is reliable only when the following condition presented by Eq. (3) is true.

$$\left(\frac{2 * a}{W}\right) \leq 0.8 \tag{3}$$

Despite the fact that it is a condition for the presented case, not all of the crack types have this characteristic, for example the wide center-cracked which its K is expressed by the Eq. (4).

$$K = \frac{P}{B * \sqrt{\pi \cdot a}} * \left(\frac{a + b}{a - b}\right)^{1/2} \tag{4}$$

In the equation above, P is the load applied in the crack with b longitudinal distance from the crack center, while B is the thickness of the component.

3 Developing a Software to Fatigue Crack Growth Calculation

Aiming the objective of the present work, Anaconda Python was used to develop the script. This software is an open-source distribution of Python which ship most of available tools and libraries of the language [22, 23], justifying why this software was the chose one. From these libraries, the most used was Tkinter, a free graphical user interface (GUI) framework that is also licensed under a free software license [24] and is part of the Python standard libraries [25].

With almost three-hundred code lines, the software here presented has three levels basically: The first one where the user can start the process or define some configurations like the units system to be used, the second one where the user choose the type of crack and finally the third one, where the user input the component data and obtain the results. Figure 2 shows the first level, represented by the main page of the software, now on referred as Fatigue Crack Growth Calculator (FCGC).

As can be seen in the figure above, besides the “start” and “options” options previously described that is a “about” option too, which basically display information about the software development.

Once the user select the “start” option, the software shows the eight most commons fatigue crack types: Center-cracked, edge-cracked, wide center-cracked, plate with



Fig. 2 Main window of fatigue crack growth calculator

a radially cracked hole loaded, two symmetric edge cracks, compact tension, edge-cracked bending and flat elliptical crack, all earlier described in more detail in the second topic of the present work. Figure 3 shows one of the three pages available for the user choose the desired crack type. With the aid of the arrow icons in the bottom right corner, the user can swipe and see the others crack types.

Immediately after the user has chosen the crack type, the third and final level of the software allows to input properties such as geometry and loads, for instance. Once which crack type has its specific characteristics, this final level is variant according to the situation required by the user. For the purposes of illustration, Fig. 4 presents the wide center-cracked window.

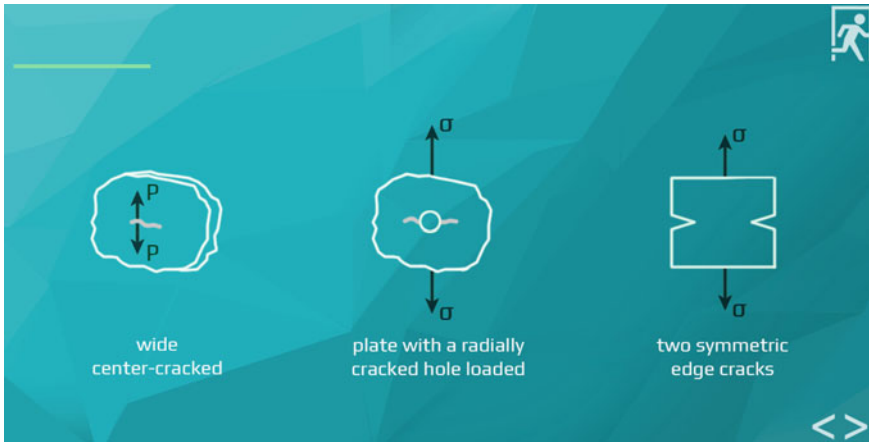


Fig. 3 Choosing the desired crack type

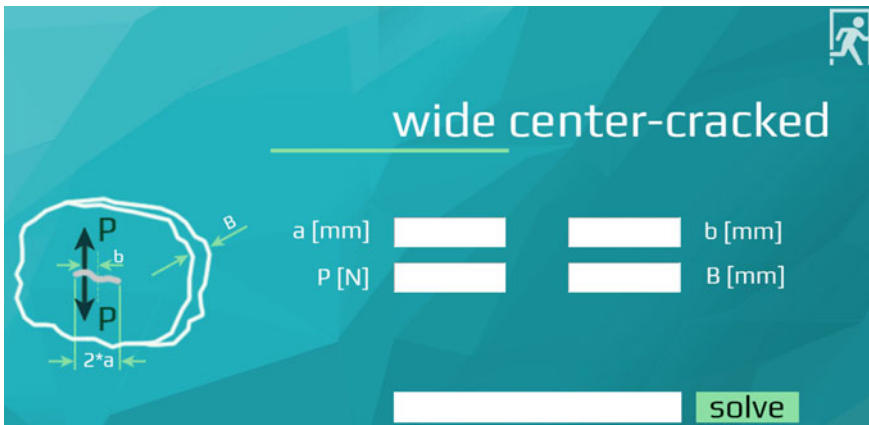


Fig. 4 Wide center-cracked window

Regarding the figure above, it is possible to see that white blank spaces are available for the user inputs data. Once one of the focus of the software here developed is to make a friendly and intuitively interface, a more detailed figure with all the parameters to be inputted is showed in every crack type too. After all required data is inserted, the K value is calculated and shown when the user selects “solve”.

As could be seen in the present topic, the software developed in this work aimed to thrive an easy and intuitively solution to find K, an important value for fatigue crack growth calculation. In the next topic, an experimental example will be made to correlate and validate the software.

4 Validating the Software by Comparing Its Results with Analytical Methods

In order to validate the software, a result comparison was made between Fatigue Crack Growth Calculator and the analytically assessment with the aid of MATLAB, a widely used software in many areas, especially in Engineering.

Be considered a 10 mm width center-cracked test specimen with 6 mm crack length and under 500 MPa stress. By Eq. (2), the stress intensity factor expect is 2002.10 MPa.m^{1/2}, as can be seen below.

$$K = \sigma * \sqrt{\pi \cdot a} * \sec\left(\frac{\pi * a}{W}\right)^{1/2}$$

$$K = 500 * \sqrt{\pi \cdot 3} * \sec\left(\frac{\pi * 3}{10}\right)^{1/2}$$

$$K = 2002.10 \text{ MPA} * \text{m}^{1/2}$$

Using Fatigue Crack Growth Calculator with the input data provided, the result found follow what was expected and it is the same founded analytically, as follows in Fig. 5.

The figure above allows to see that the software developed by the present work not only shows the value of K, but also if the equation used for this case is reliable or not because of the relation between the fatigue crack length and the test specimen width.

To corroborate with the result found for the center-cracked test specimen, other loop was made in the software and analytically, but this time with a wide center-cracked type. In this case, the test specimen considered has 50 mm thickness, 10 mm crack length and 30 kN load applied with 2 mm offset from the crack center. While the analytical calculation using Eq. (4) can be seen below, the software result is show in Fig. 6. One more time, the expect result was obtained from both methods once the values are equals.

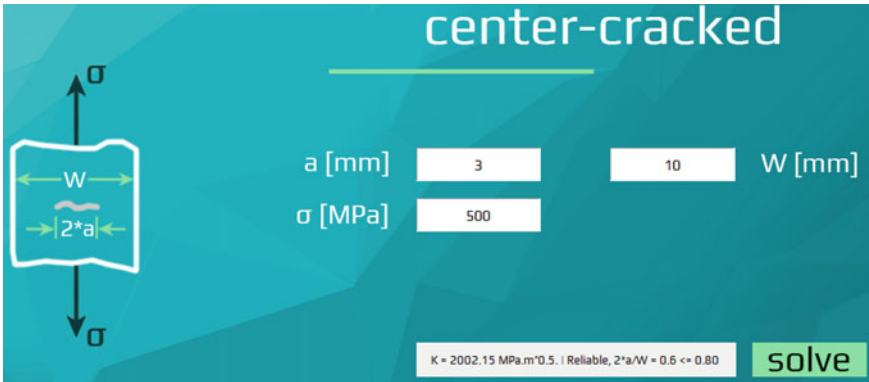


Fig. 5 Center-cracked calculation in the software



Fig. 6 Wide center-cracked calculation with the aid of the software

$$K = \frac{P}{B * \sqrt{\pi * a}} * \left(\frac{a + b}{a - b} \right)^{1/2}$$

$$K = \frac{30E3}{50 * \sqrt{\pi * 5}} * \left(\frac{5 + 2}{5 - 2} \right)^{1/2}$$

$$K = 231.25 M P A * m^{1/2}$$

Once the two loops tested in the software and analytically gave the same results respectively, it is possible to confirm that the software results are validated.

5 Results and Discussion

The Finite Element Methods is being widely used in many Engineering applications in the past years, including structures and machinery damage calculation. Yet, approximate solutions and estimative are still important to understand the system and its behavior, making very important to know parameters like the stress intensity factor which is highly influenceable the fatigue crack growth in specimens.

Year over year Computational Science has been having more and more vital role in the Engineering applications. In the present work and regarding this scenario, through Python computer programming language and with the aid of Anaconda, an open-source distribution of Python, a software to calculate the Linear Elastic Fracture Mechanics stress intensity factor was developed. With the objective of create a user-friendly graphical interface, the software here developed and named Fatigue Crack Growth Calculator also used Tkinter, a framework to create graphical user interfaces.

Aiming to validate the results obtained with the FCGC, two examples were made with the aid of the software developed and analytically. Inasmuch the results of these two methodologies were equals, it is possible to confirm that the software developed in the present work produces valid results.

It is very probably that the future of Engineering does not take a separate path from the Computational Science once every day this knowledge area provides even more resources to solve modern Engineering problems. The use and the development of tools through the aids of computer programming tend to be a primordial skill to the engineers who wants to optimize and have better results in the area.

Acknowledgements The authors thank Pontifícia Universidade Católica de Minas Gerais (PUC Minas) for the support. This study was financed in part by the Coordenação de Aperfeiçoamento de Pessoal de Nível Superior—Brasil (CAPES)—Finance Code 001.

References

1. Hu J, Xie L, Zhang R, Yin W (2019) Failure analysis of a crack on a train bolster. *Eng Fail Anal* 97(1):32–42
2. Savaidis G, Savaidis A, Zerres P, Vormwald M (2010) Mode I fatigue crack growth at notches considering crack closure. *Int J Fatigue* 32(10):1543–1558
3. Sankararaman S, Ling Y, Mahadevan S (2011) Uncertainty quantification and model validation of fatigue crack growth prediction. *Eng Fract Mech* 78(7):1487–1504
4. Rabczuk T, Bordas S, Goangseup Z (2010) On three-dimensional modelling of crack growth using partition of unity method. *Comput Struct* 88(23–24):1391–1411
5. Qing C, Chengwen Z, Xiaohu J (2018) Comparative research on calculation methods of stress intensity factors and crack propagation criterion. In: *Proceedings of the 7th International conference on fracture fatigue and wear*. Springer, Singapore, pp 202–209
6. Correia J, Blasón S, De Jesus A, Canteli A, Moreira P, Tavares P (2016) Fatigue life prediction based on an equivalent initial flaw size approach and a new normalized fatigue crack growth model. *Eng Fail Anal* 69(1):15–28

7. Leuders S, Thöne M, Riemer A et al (2013) On the mechanical behaviour of titanium alloy TiAl6V4 manufactured by selective laser melting: fatigue resistance and crack growth performance. *Int J Fatigue* 48(1):300–307
8. Grandt A (2004) *Fundamentals of structural integrity*, 1st edn. John Wiley & Sons Inc., Canada
9. Dong L, Alotaibi A, Mohiuddine S et al (2014) Computational methods in engineering: a variety of primal & mixed methods, with global & local interpolations, for well-posed or ill-posed BCs. *Comput Model Eng Sci* 99(1):1–85
10. Pletcher R, Tannehill J, Anderson D (2013) *Computational fluid mechanics and heat transfer*, 3rd edn. CRC Press, USA
11. Sargent R (2018) Verification and validation of simulation models. In: *Proceedings of the 2010 winter simulation conference*. IEEE, Baltimore, pp 166–183
12. Sarin H, Kokkolaras M, Hulbert G et al (2010) Comparing time histories for validation of simulation models: error measures and metrics. *J Dyn Syst Measur Control* 132(6):1–10
13. Ibañez R, Abisset-Chavanne E, Aguado J et al (2018) A Manifold learning approach to data-driven computational elasticity and inelasticity. *Arch Comput Meth Eng* 25(1):47–57
14. Nosikov A (2018) Modelling of short crack arrest and fatigue propagation using non-local fracture criteria. In: *Proceedings of the 7th international conference on fracture fatigue and wear*. Springer, Singapore, pp 491–499
15. Pereira K, Wahab M (2018) Effect of short crack behavior on the propagation life prediction for a fretting cylindrical pad configuration. In: *Proceedings of the 7th international conference on fracture fatigue and wear*. Springer, Singapore, pp 539–546
16. Šimović V, Varga M, Soleša D, Vladislavljević R (2019) Architectural element of rose flower decoration shown with python. *J Agron Technol Eng Manage* 2(1):35–42
17. Hussain Z, Khan M (2018) Introducing python programming for engineering scholars. *Int J Comput Sci Netw Secur* 18(12):26–33
18. Marowka A (2018) On parallel software engineering education using python. *Educ Inf Technol Secur* 23(1):357–372
19. Tan S, Naraharisetti P, Chin S et al (2020) Simple visual-aided automated titration using the python programming language. *J Chem Educ* 97(3):850–854
20. Lu Y, Liu Y (2010) Crack growth-based fatigue life prediction using an equivalent initial flaw model. Part I: Uniaxial loading. *Int J Fatigue* 32(2):341–349
21. Weißgraeber P, Felger J, Geipel D et al (2016) Cracks at elliptical holes: stress intensity factor and finite fracture mechanics solution. *Eur J Mech A Solids* 55(1):192–198
22. Duchesnay E, Löfstedt T (2015) *Statistics and machine learning in python*, 2nd edn. France
23. Snyman J, Wilke D (2018) Practical computational optimization using python. *Pract Math Optim* 133(1):311–340
24. David L (2018) *Tkinter GUI programming by example*, 1st edn. Packt Publishing Ltd., UK
25. Moore A (2018) *Python GUI programming with Tkinter: develop responsive and powerful GUI applications with Tkinter*, 1st edn. Packt Publishing Ltd., UK

Shear Failure Analysis with Modelling Multiple Discontinuities in a Concrete Beam Using XFEM



A. Faron and G. A. Rombach

Abstract Despite intensive research in the last decades, the shear force transfer and crack propagation in structural concrete members is still disputed. In order to investigate the load bearing behaviour, an understanding of crack growth and flow of internal forces is essential. In this context, various techniques have been developed in the recent years to analyze the crack pattern and to detect fracture failure in advance. This paper presents the investigation of discrete crack propagation and the shear bearing behaviour of a concrete beam without transverse reinforcement using the extended finite element method (XFEM). By applying the cohesive zone model (CZM) under different traction separation laws and describing the damage evolution, crack growth is modelled with several discontinuities. In this framework, the load bearing behavior and the development of the crack with its dimensions are discussed. Linear, bilinear and nonlinear softening curves of the fracture process zone for the investigation of one to several cracks are presented. The numerical analysis are validated by experimental results. The findings are compared and evaluated with the isotropic material model ‘concrete damage plasticity’ (CDP). The smeared and discrete crack pattern are contrasted. It is concluded that the numerical analyses make useful predictions of the fracture behavior of reinforced concrete members and provide further possibilities for research purposes.

Keywords Crack propagation · Damage mechanics · Extended finite element method · Cohesive zone model · Concrete damage plasticity

A. Faron · G. A. Rombach (✉)
Institute of Structural Concrete, Hamburg University of Technology (TUHH), Denickestrasse 17,
21073 Hamburg, Germany
e-mail: rombach@tuhh.de

A. Faron
e-mail: a.faron@tuhh.de

1 Introduction

Concrete is a quasi-brittle material with heterogeneous properties whose damage evolution is characterized by the fracture process zone at the crack tip and the associated softening laws. Due to the non-linearity, the load-bearing behavior has been intensively investigated for decades. An important effect on the structural system in this context is the formation and growth of cracks. Numerically the crack growth can be modelled in two different ways, discrete or smeared. This paper presents the results of both approaches for a three-point reinforced concrete beam with shear failure.

For the discrete description, the “extended finite element method (XFEM)” is used. Although there are several numerical models for the discrete description of crack growth, the XFEM offers a quick and practical method for structural analysis. To describe the complex non-linear phenomena in the fracture process zone the cohesive zone model (CZM) is used. The stress-crack displacements are compared in this paper with different softening curves (linear, bilinear and non-linear or exponential). For the smeared description of crack propagation, the non-linear material model „concrete damage plasticity (CDP)“ by Lee and Fenves [1] is used, which is based on the combination of the plasticity and damage theory. When the load is relieved, part of the deformation is retained and the damage is taken into account by a reduced stiffness. The software package Abaqus [2] is used for the numerical simulations. The results show a good agreement among each other and with experiments.

2 Damage Evolution

2.1 Cohesive Zone Model (CZM)

One of the widely known methods for describing crack propagation in fracture mechanics is the cohesive zone model (CZM), whereby non-linear fracture processes at the crack tip are described by cohesive effects. The analysis consists of several steps. A general elastic material behavior is present if the occurring material stresses do not cause a separation of elements in the component. If, however, a fracture criterion is exceeded, e.g. the tensile strength of concrete is reached, crack initiation occurs. Just before this happens, micro cracks gradually appear which, after the stress in the component has reached the tensile strength, continue to grow and connect with further micro cracks. In this context, an area is finally reached that is characterized by the failure evolution of non-linear cohesive laws. The surface stresses at the crack surfaces result from the crack branching and intersection as well as from the weakened interface between the aggregates and the cement paste. The region is characterized by the softening curve, which represents the relationship between the tensile stress σ_{ct} and the crack opening width w . In the last step a

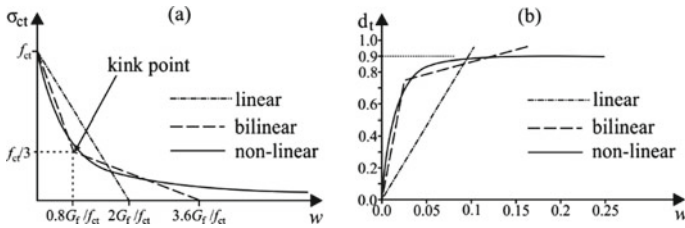


Fig. 1 a Softening curves and b damage variable d_t versus crack width w curves

complete separation of the finite element occurs. A macroscopic crack is thus formed from the micro cracks, which can no longer transfer any tractive force.

In order to analyze the characteristics at the crack tip for the shear failure of a beam under bending using XFEM, different softening curves—linear, bilinear and non-linear—are considered in detail, see Fig. 1a.

The linear function refers to the relations of Hillerborg et al. [3]. Later Petersson [4] published a bilinear softening curve, whose kink point is at $\sigma_{ct} = f_{ct}/3$ and crack width $w = 0.8G_f/f_{ct}$, as shown in Fig. 1a. Concerning the non-linear effects, the approaches according to fib-Model Code 90 [5] and Mark [6] are used in the XFEM and CDP. One of the important boundary conditions in Abaqus for the description of damage evolution is the specification of the softening curve. If no linear form is used, the damage variable d_t is an important input parameter. The description of the post-cracking behavior of concrete is based on damage. The evolution of the scalar variable d_t is described by a function that relates the state of damage. After exceeding a damage threshold, the fracture evolution begins. If the parameter d_t is equal to zero, then the concrete material is undamaged and if $d_t = 1$ it is completely fractured. For reasons of convergence, the damage value d_t in the non-linear curve is restricted to 0.9 for the discrete and smeared analysis according to Latte [7, 8]. Figure 1b shows d_t versus w -curves used after following the approaches mentioned above.

2.2 Concrete Damage Plasticity (CDP)

Abaqus offers various possibilities to model the non-linear material behavior of concrete. In this paper the concrete damage plasticity model (CDP) is used, which assumes an isotropic damage based on a combination of plasticity and damage theory [1]. It can model the concrete behavior in compression and tension. For the description of the plastic behavior, a flow condition, a flow rule and the formulation of the stress—and strain hardening are needed. Therefore, the uniaxial stress-strain function for compression and tension and the description of the damage are necessary as material functions. For this the material models from fib ModelCode 1990 [5] and Mark [6] are used. As input parameter, the default settings of the finite element software are applied. The simulation for the beam is started with a dilatant angle of $\psi = 30^\circ$,

an eccentricity $\varepsilon = 0.1$, a compression plastic strain ratio $\sigma_{b0}/\sigma_{c0} = 1.16$ and an invariant stress ratio $K_c = 0.667$.

3 Numerical Simulation

3.1 Experimental Beam Test

For the crack analysis, the bending beam no. 1L-2 from Nghiep's [9, 10] test series is chosen for validation. All main parameters of the beam are listed in Table 1. Figure 2 shows the dimensions, the reinforcement layout of the beam and the position of the different crack initiations that were applied in the XFEM simulation to force the crack propagation at certain points and reduce the calculation time. Crack no. 1–3 indicate bending cracks. Crack no. 4 is located close to the starting point of the critical shear crack as shown in Fig. 3.

Furthermore the fracture energy G_F is essential for the crack propagation. This is determined according to fib Model Code 2010 [11] as follows:

$$\begin{aligned} G_F &= 0.073 \cdot f_{cm}^{0.18} = 0.073 \cdot (f_{ck} + 8)^{0.8} \\ &= 0.073 \cdot (49.2 + 8)^{0.18} \cdot 10^3 = 151.2 \text{ N/m} \end{aligned} \quad (1)$$

3.2 Numerical Model

Figure 4 shows a sketch of the numerical model. Due to symmetry of the beam, the model can be restricted to one-half of the beam. 4-noded brick elements (size $2 \times 2 \times 2$ cm) were used for concrete material. The rebar was modelled by truss elements with perfect bond. In the XFEM-analysis the force transfer via the crack, e.g. shear friction, was neglected and the concrete was assumed to behave elastic except in the crack region.

3.3 Numerical Crack Propagation

Faron and Rombach [12, 13] have demonstrated that haunched an unhaunched concrete beams can be analyzed using XFEM and CDP. The following Fig. 5a–d show the discrete crack path with the XFEM simulation and the approach to let the crack initiations act individually and together as multiple discontinuities. Figure 5e on the other hand shows the smeared crack propagation using the CDP. Significant differences can be seen regarding the path of the critical shear crack.

Table 1 Main parameters of the concrete beam

| Beam no. | d (mm) | b (mm) | a/d | ρ_l (%) | f_{ek} (Mpa) | $f_{ct,sp}$ (Mpa) | E_c (Gpa) | f_y (Mpa) | F_u (kN) | Failure |
|----------|----------|----------|-------|--------------|----------------|-------------------|-------------|-------------|------------|---------|
| 1L-2 | 302 | 200 | 5 | 1.56 | 49.2 | 3.6 | 31.29 | 550 | 158.4 | Shear |

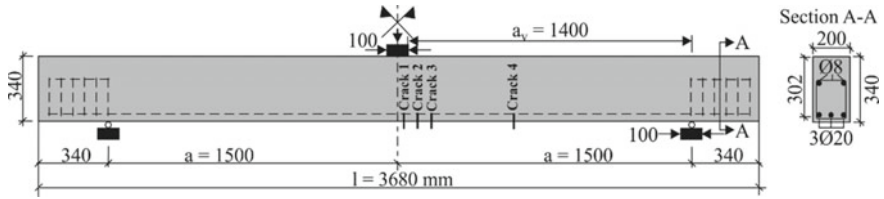


Fig. 2 Test beam with dimensions

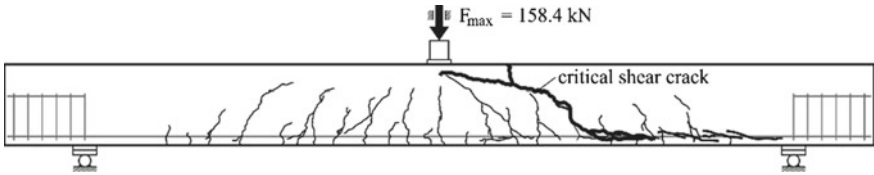


Fig. 3 Real crack pattern of test beam at ultimate load

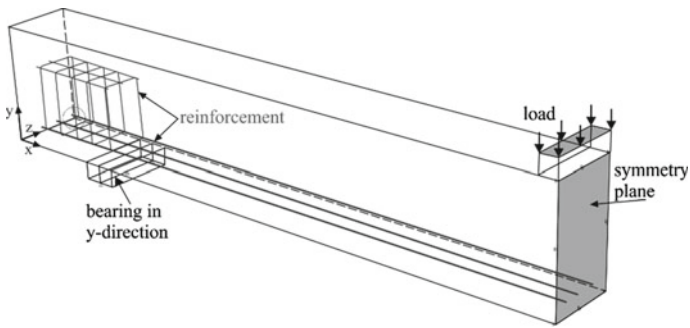


Fig. 4 Numerical model

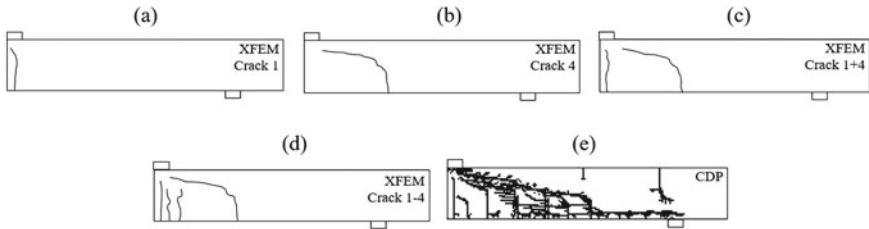


Fig. 5 Crack pattern of test beam using XFEM (a–d) and CDP (e)

3.4 Load-Bearing Behaviour

In order to check the applicability of the numerical simulation processes to real members, the load-bearing behavior is analyzed for the test beam no. 1L-2. The different softening curves are compared and the behavior on the location of crack initiation (see Fig. 2, Crack 1–4) is evaluated. Figure 6a shows the load-displacement behavior with multiple discontinuities. The results of the real test beam are compared with the XFEM simulation and the CDP model. In XFEM the softening curves—linear, bilinear and non-linear—are used. In general, all curves show a relatively equal load-bearing behavior with similar ultimate deformation w_m until failure. Whereby the CDP results show a slightly larger deformation, which however does not have a significant extent. To measure the deformation w_m , a displacement transducer was placed in the middle of the beam during the test.

Figure 6b–d show the load-displacement curves of the different crack initiations depending on the softening function. It can be seen that regardless of the choice, the curves are relatively similar to the real concrete beam. However, the quality of the analysis is improved; graphs are still closest to the real load-bearing behavior when using several discontinuities. The linear softening curve in Fig. 6c shows a negligible smaller final displacement compared to the bilinear and non-linear approach due to the simplified function.

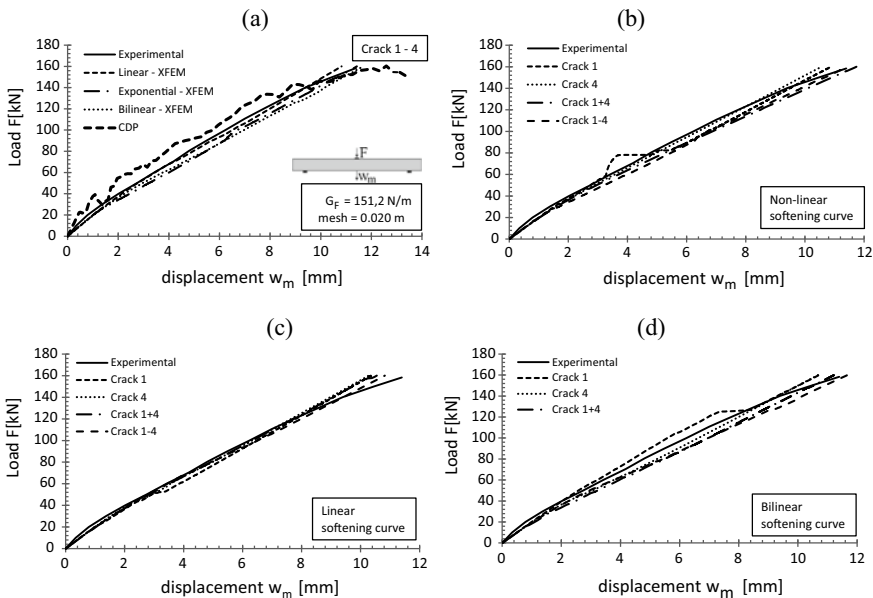


Fig. 6 Load versus displacement curves of test beam

3.5 Load-Crack Width Behaviour

By implementing certain output variables, it is possible to read the relative crack width in the discontinuity jump at any point in the XFEM analysis. Although the computing time increases considerably, it offers the possibility to analyze the beam in more detail. In the test series of Nghiep [9, 10], a displacement transducer was installed at the reinforcement layer to measure the crack width as a function of the load. This was applied after the first bending crack appeared in the middle of the beam.

Figure 7a compares the load F versus crack width w behavior with multiple crack initiations (crack 1–4) depending on the softening curves with that of the test beam. Despite the initial discrepancy due to the non-linearity, the curves approach a common course and show a good agreement. The stiffness of the beam after cracking is reproduced well. Figure 7b–d show the F - w graphs of the different crack initiations depending on the softening curves. Regardless of the choice, all approaches show good agreement towards the end.

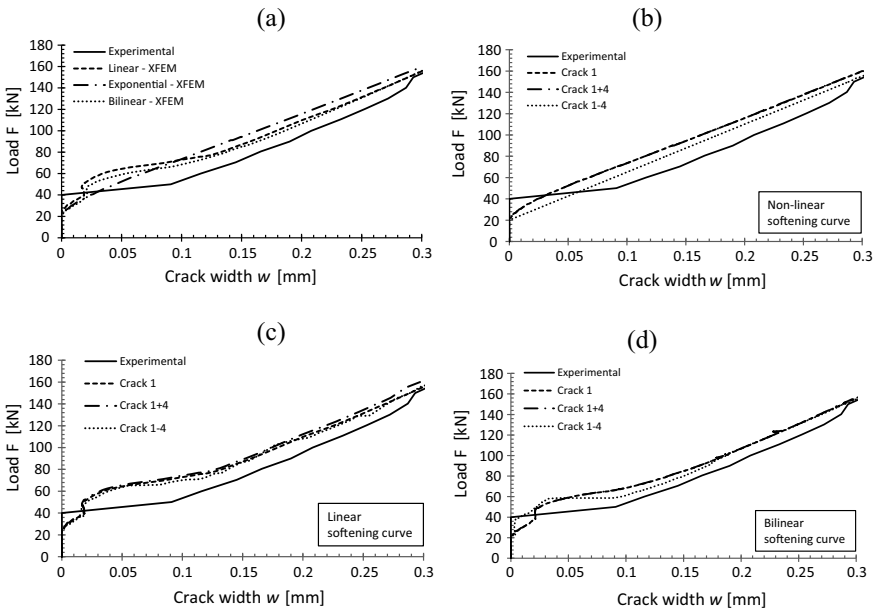


Fig. 7 Load-crack width graphs of test beam

4 Conclusion

This paper provides an overview of non-linear crack propagation analysis in a reinforced concrete beam using discrete and smeared approaches with Abaqus applying XFEM and CDP. The embedding of single and multiple discontinuities in the form of crack initiations and different approaches of softening curves were compared. The findings show good results with those obtained from the real test, regardless of the number of crack initiations and the definition of the softening curve. More precisely, the approach with several discontinuities and the bilinear or non-linear softening curve provides the best results with XFEM. However, these differ only slightly compared to individual cracks and the linear post-cracking behavior and are more complex to determine as boundary conditions for the simulation, which makes it necessary to consider how accurate the numerical simulation should be and whether the effort is necessary. The crack patterns, the load-deformation behavior and the load-crack width comparison with XFEM and CDP provide a sufficient approximation to the test results, which makes the application methods well suited for further analysis and research purposes. Further research will focus on the interaction between the crack edges, e.g. shear friction.

References

1. Lee J, Fenves GL (1998) A plastic-damage concrete model for earthquake analysis of dams. *Earthq Eng Struct Dyn* 27:937–956
2. Dassault-Systemes (2012) Abaqus analysis user's guide 6.12, USA
3. Hillerborg A, Modeer M, Petersson PE (1976) Analysis of crack growth in concrete by means of fracture mechanics and finite elements. *Cem Concr Res* 6(6):773–782
4. Petersson PE (1981) Crack growth and development of fracture zone in plain concrete and similar materials. Report no. TVBM-1006. Division of Building Materials. Lund Institute of Technology, Lund, Sweden
5. Comité Euro-International du Béton (CEB)—Fédération Internationale de la Précontrainte (FIP) Model Code 1990: Design of concrete structures (1993) Thomas Telford, London
6. Mark P (2006) Zweiachsig durch Biegung und Querkräfte beanspruchte Stahlbetonträger. Schriftenreihe des Instituts für Konstruktiven Ingenieurbau an der Ruhr-Universität Bochum (Habilitationsschrift), Heft 2006–3, Shaker Verlag, Aachen
7. Latte S (2010) Zur Tragfähigkeit von Stahlbeton-Fahrbahnplatten ohne Querkraftbewehrung. PhD Thesis, TU Hamburg-Harburg. <https://doi.org/10.15480/882.1052>
8. Rombach G, Latte S (2008) Shear resistance of bridge decks without shear reinforcement. In: Walraven J, Stoelhorst D (eds) *Proceeding of the FIB-Symposium "Tailor Made Concrete Structures"*, Amsterdam 19–21. May, 2008
9. Nghiep VH (2011) Shear design of straight and haunched concrete beams without stirrups. PhD Thesis, Publication Series of the Institute of Structural Concrete of the TUHH. <https://doi.org/10.15480/882.1050>
10. Rombach GA, Kohl M, Nghiep VH (2011) Shear design of concrete members without shear reinforcement—a solved problem? In: *12th East Asia-Pacific Conference on Structural Engineering and Construction (EASEC-12)*, Hong Kong, 26–28 January 2011
11. Fédération internationale du béton: fib Model Code for Concrete Structures 1. Ernst Sohn Berlin (2013)

12. Faron A, Rombach GA (2020) Simulation of crack growth in reinforced concrete beams using extended finite element method. *Eng Fail Anal* 116
13. Rombach GA, Faron A (2019) Numerical analysis of shear crack propagation in a concrete beam without transverse reinforcement. *Proc Struct Integr* 17:766–773

Mode I Crack in Elastically Identical Bimaterial Joined by Under-Matched Weld Interlayer: A New Theoretical Model



Sunil Bhat, H. Adarsha, and J. Deepak

Abstract A novel theoretical model for calculating the intensity of energy release rate at mode I crack tip in the bi-material has been developed. The study discusses the state at crack tip in the bi-material of identical steels connected by a thick but weaker weld inter layer of steel. In such a body, there are two interfaces: one between the stronger parent steel and the weaker weld, and another between the weaker weld and the stronger back up steel. As the fracture develops across the weld interlayer, i.e. strong-weak-strong transition, in the K dominating or SSY regime, the effect of energy transfer owing to the existence of elastically similar but strength mismatched surfaces is measured. The model accounts for non-linearity in plastic characteristics of steel. When the crack tip in parent steel faces the approaching interface of weaker weld during strong-weak transition, the rate of energy release at the crack tip is seen to be greater than the far field value. But when the tip in the weaker weld faces the interface of stronger back up steel during weak-strong transition, the tip energy release rate is reduced. When the crack tip is at the interfaces, the impact of shielding as well as amplification increases.

Keywords Energy transfer · Interface · Strength mismatch · Under-matched · Weld

1 Introduction

In industrial sectors, we frequently see examples of identical steel components being welded together or a damaged steel part being repaired using a lower-strength steel filler wire. Such bi-materials have two interfaces with strength mismatch across them. Strong-weak crack transition occurs between the strong parent steel and the weak weld, while weak-strong crack transition occurs between the weak weld and the strong back up steel. Mode I type of crack in this sort of bi-material encounters the effects of the mentioned interfaces as it grows across the weld interlayer, i.e.

S. Bhat (✉) · H. Adarsha · J. Deepak

Department of Mechanical Engineering, FET, Jain University, Bangalore 562112, India

a strong-weak-strong transition. Energy transfer takes place across the interfaces causing the energy release rate at the tip of the crack, J_{tip} , to be different from the far field value, $J_{applied}$. In the bi-material under K dominating or SSY regime, a novel strain-based theoretical model is constructed for estimating J_{tip} at various crack tip positions. The model takes into account non-linearity in plastic characteristics of the steels. Throughout the bi-material, the modulus of elasticity remains constant. The weld yield strength is assumed to be the same at all the positions within the weld. The effects of heat affected zones and residual stresses are ignored because of the identical coefficients of thermal expansion of base steels and weld materials. An edge crack of various lengths is examined at discrete places across the intermediate weld layer in near infinite domain under monotonic and far field tension with plane stress conditions to investigate the behavior of the model.

2 Literature Review

For Mode I fracture in bi-materials with thick weld inter layers, there are just a few experimental and theoretical results available. Kim et al. [1] used finite element analysis to tackle the problem of a crack in front of a structurally graded interfacial layer among parent and interfacial components with different yield strengths. The influence of strength difference on tip of the crack driving force shielding and amplification was explored. The intermediate layer with homogeneous yield response (i.e., where the yield strength value of the interlayer is the aggregate of component metals) has a higher shielding effect than the interlayer with graded yield behavior, which changes linearly from one end to the other. Predan et al. [2] investigated fracture in the parent base metal that was developing regularly towards over-matched or under-matched thick welds using computational and experimental methods. In terms of theoretical findings, single and thin surfaces with abrupt strength gradients have mostly been addressed. Wappling et al. [3], Reimelmoser and Pippan [4], and Shang et al. [5], provided theoretical models for examining mode I fracture before a thin strength unequal interface but between elastic-perfectly plastic materials in the SSY regime. Bhat et al. established a strain-based theoretical model for strong-weak [6] and weak-strong [7] crack transitions in the SSY regime, emphasizing the influence of non-linearity in the plastic characteristics of the elastic-plastic components. Bhat et al. [8] further extended the work to deal with the case involving thick and strong or overmatched weld interlayer between two steels and came out with the results of mode I crack crossing the interlayer in the form of weak-strong-weak case. Literature survey reveals that the theoretical model for behavior of crack in bi-material with thick but weak or under matched weld interlayer is not available and that is attempted in the present work in order to handle strong-weak-strong crack transition case by employing the fundamental principles stated at [6–8].

3 Theoretical Model

For examination of bi-material yielding that varies from that of the homogeneous body, the static monotonic load, or peak value of the fatigue cycle, is used. The bi-material's yield characteristics, which alter with crack length, are responsible for energy transfer in the bi-material. The transfer of energy is studied in relation to the cracked homogenous body, which is composed of the component of the bi-material containing the crack tip and in which transfer of energy does not occur, resulting in J_{tip} to be equal to $J_{applied}$. Dugdale's crack tip yield zone with sizes r_p^A and r_p^W in hypothetical homogenous bodies constructed with parent as well as back up steels, A, and the intermediate weld steel, W, equals $\frac{\pi}{8} \left(\frac{K_{applied}}{Y^A} \right)^2$ and $\frac{\pi}{8} \left(\frac{K_{applied}}{Y^W} \right)^2$ respectively under plane stress condition in SSY regime where the distant or far field stress intensity parameter, $K_{applied} \approx 1.12 p_{\infty} \sqrt{\pi c}$, holds good for an edge crack of length, c , under monotonic far field tensile stress, p_{∞} , in infinite domain. Remote energy release rate, $J_{applied}$, equals $\frac{K_{applied}^2}{E}$. To include for strain hardening in elastic-plastic materials, non-linearity of each material is defined by Ramberg-Osgood equation. For instance at any location beyond yield point in material A, $\frac{\varepsilon^A}{\varepsilon_Y^A} = \frac{\sigma^A}{Y^A} + \alpha \left[\frac{\sigma^A}{Y^A} \right]^{m^A}$, where σ and ε are total stress and strain at chosen location, ε_Y is maximum elastic strain and α and m are Ramberg-Osgood constants. The equation takes a manipulative form, $\sigma^A \approx Y^A \left[\frac{\varepsilon^A}{n^A} \right]^{\frac{1}{m^A}}$, upon ignoring $\frac{\sigma^A}{E}$ due to large value of E and by using the constant, $n^A = \alpha \varepsilon_Y^A$.

Yield zone size at crack tip in homogeneous material, r_p^A , is utilized to determine plastic strain and map it to the bi-material for stress measurement at the necessary spot in the interface component. This allows calculation of the extent of elastically and plastically impacted zones in the interface material in order to estimate the quantity of transfer of energy across the bi-material interface. Since the analysis handles the plasticity of the crack tip, Eq. (1) is written for plastic strain, ε_{r_p} , along crack axis in the direction of applied stress, in mode I cracked homogenous body, A, at the tip of yield zone that is located at distance, r_p^A , from the crack tip under SSY regime [6, p. 1200]

$$\varepsilon_{r_p} = \frac{K_{applied}}{\sqrt{2\pi r_p^A} E} M (1 - \nu^A) = \varepsilon_Y^A = \frac{Y^A}{E} \quad (1)$$

where ν^A and ε_Y^A are poisson's ratio and maximum elastic strain in homogenous body respectively. The equal and bi-axial tensile stress states, along the crack axis is represented by ν^A , whereas constant M is the correction factor introduced to approximate crack tip plasticity by elasticity factor, $K_{applied}$. With the introduction of M , the plastic strain in the yield zone is confirmed to be greater than ε_Y^A , maximum at $r = 0$ (Crack tip) and minimum i.e. ε_Y^A at $r = r_p^A$ (Tip of yield zone). The elastic

strains beyond $r = r_p^A$ can be found as well with Eq. (1). Substituting the formula for r_p^A in Eq. (1) depicts that the constant M is equal to $\frac{\pi}{2(1-\nu^A)}$ which remains same at all crack lengths. Therefore strain, ε_r , in the direction of load, on crack axis at any distance, r , from the crack tip in SSY regime is expressed as $\varepsilon_r = \frac{\pi K_{applied}}{2\sqrt{2\pi r} E}$. Consequently, the strains at interfaces 1 and 2 in elastically homogeneous bi-material are written as $\varepsilon_{int}^1 = \frac{\pi K_{applied}}{2\sqrt{2\pi a_{int}^1} E}$ and $\varepsilon_{int}^2 = \frac{\pi K_{applied}}{2\sqrt{2\pi a_{int}^2} E}$ respectively where a_{int}^1 and a_{int}^2 are the distances of interfaces 1 and 2 from the crack tip respectively.

Refer Fig. 1. To start with, when the crack tip in strong parent steel, A, faces the interface 1 of weaker weld, W (Strong-weak transition), the crack tip does not experience the effect of approaching weld as long as $\varepsilon_{int}^1 \leq \varepsilon_Y^W$, Fig. 1a), resulting in $J_{tip} = J_{applied}$. On substituting the expressions, $\varepsilon_{int}^1 = \frac{Y^W}{E}$ and $K_{applied} = Y^W \sqrt{\frac{8r_p^W}{\pi}}$, in the stated equation for strain at interface in previous paragraph, one obtains $r_p^W \leq a_{int}^1$. Therefore condition $\varepsilon_{int}^1 \leq \varepsilon_Y^W$ is similar to $r_p^W \leq a_{int}^1$. Stage I of interface 1 (Stage I¹) commences when $\varepsilon_{int}^1 > \varepsilon_Y^W$ or $r_p^W > a_{int}^1$, Fig. 1b), due to which ε_r in the vicinity of the interface in the weld exceeds ε_Y^W but is less than ε_Y^A that causes yielding of weld, resulting in energy density transfer, E_T^I , towards the parent steel (Fig. 2a, Case I). Stage II of interface 1 (Stage II¹) begins as soon as $\varepsilon_{int}^1 > \varepsilon_Y^A$ or $r_p^A > a_{int}^1$. Refer Fig. 1c). The weld in the vicinity of the interface now yields due to ε_r exceeding ε_Y^A that effectuates energy transfer, E_T^{II} , towards the parent steel (Fig. 2b, Case II). This is in addition to E_T^I due to already existing yield zone in the weld where $\varepsilon_Y^A > \varepsilon_r > \varepsilon_Y^W$. Total energy density transfer, E_T , in Stage II¹ equals ($E_T^{II} + E_T^I$). As the crack end enters interface 1 and reaches the weaker overall weld, A (Weak-Strong transition), it does not experience the influence of the back up steel until it reaches interface 2 of the tougher back up steel, $\varepsilon_{int}^2 \leq \varepsilon_Y^W$ or $r_p^W \leq a_{int}^2$, that results in $J_{tip} = J_{applied}$. Stage I² begins when $\varepsilon_{int}^2 > \varepsilon_Y^W$ or $r_p^W > a_{int}^2$, Fig. 1d), As a result of this, ε_r back up steel in the region of the contact exceeds ε_Y^W but is less than ε_Y^A elastically deforms, producing energy density transfer, towards the back up steel. Stage II² begins when or $\varepsilon_{int}^2 > \varepsilon_Y^A$ or $r_p^A > a_{int}^2$, Fig. 1e), that causes ε_r in back up steel in the region of the interface to exceed ε_Y^A and thereby resulting in yielding of back up steel and energy density transfer, E_T^{II} , towards the back up steel. This is in addition to E_T^I that exists due to the already present elastic zone in back up steel where $\varepsilon_Y^A > \varepsilon_r > \varepsilon_Y^W$. Total energy density transfer, E_T , in Stage II² equals ($E_T^{II} + E_T^I$). Finally, whenever the tip of the crack passes interface 2 and reaches back-up steel, the impact of the interfaces remaining over starts to fade due to the growth of compressive stresses at the interfaces and J_{tip} again equals $J_{applied}$.

Energy transfer, $J_{interface}$, in both stages I and II is obtained from $2 \times \int E_T dr$ where factor 2 is introduced to include energy transfer in both load line and transverse directions. Integration is bound by the limits of sizes of affected zones in the interface material. The limits are $(r_p^W - a_{int}^1)$ for case I energy transfer in Stage I¹ and $(r_p^W - r_p^A)$ and $(r_p^A - a_{int}^1)$ for case I and case II energy transfers respectively in Stage II¹. Likewise the limits change to $(r_p^W - a_{int}^2)$ for case I energy transfer in Stage I² and $(r_p^W - r_p^A)$ and $(r_p^A - a_{int}^2)$ for case I and case

Strong-weak-strong transition

Yield zone at crack tip
 Yield zone in weld
 Elastically affected zone in back up material

Material, A – Strong
 Material, W – Weak
 $Y^A > Y^W$; $E^W = E^A$

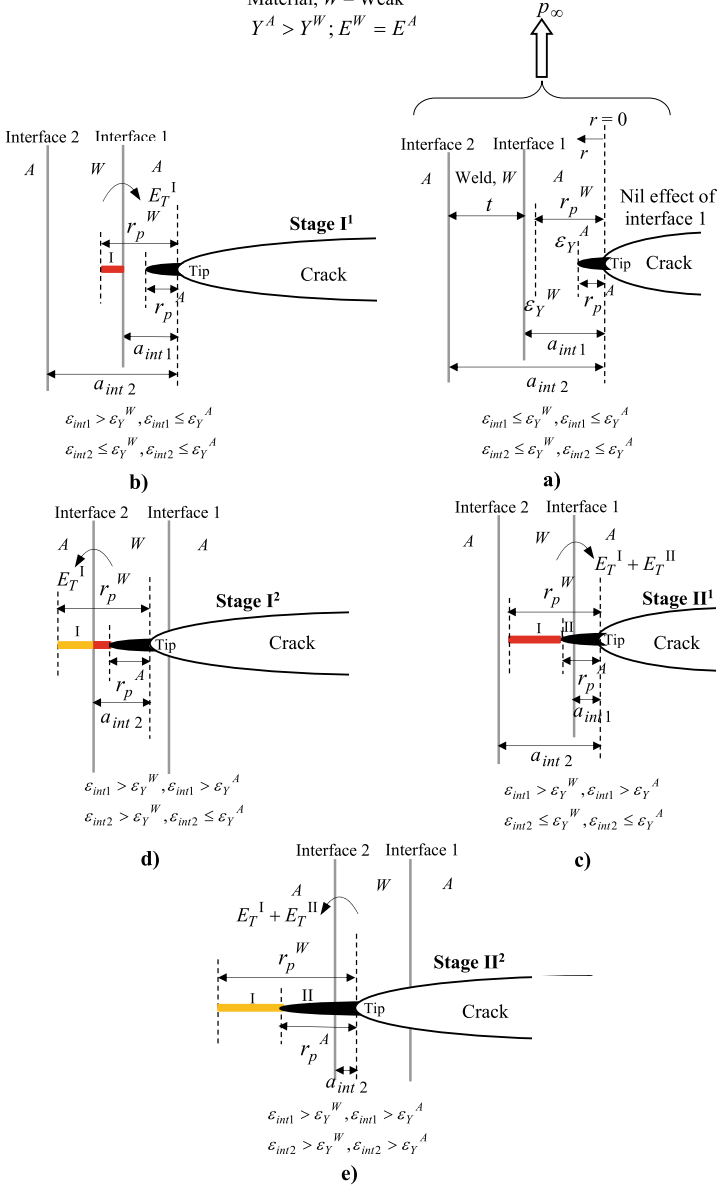


Fig. 1 Various stages of energy transfer during crack growth

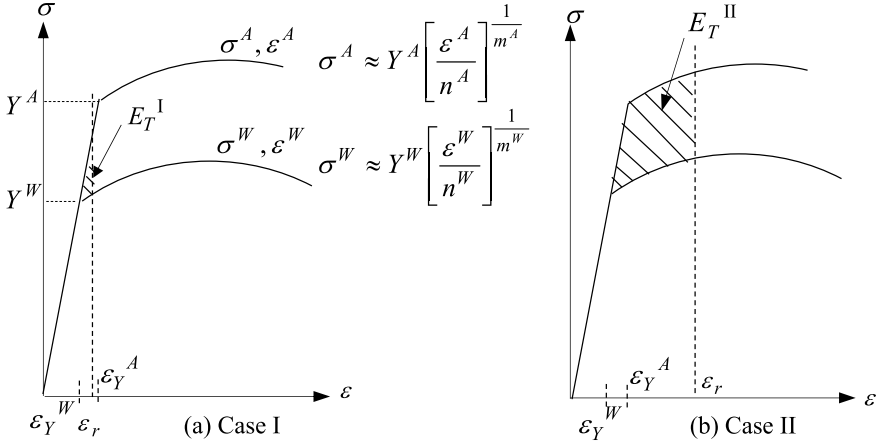


Fig. 2 Magnitudes of Case I and Case II energy transfers

II energy transfers respectively in Stage II². Conservation of energy release rate principle enables to write, $J_{tip} = J_{applied} \pm J_{interface}$, that results in the magnitude of J_{tip} . $J_{tip} = J_{applied} + J_{interface}$ during strong-weak crack transition and $J_{tip} = J_{applied} - J_{interface}$ during weak-strong transition. Stress intensity parameter at crack tip for plane stress condition is finally obtained from, $K_{tip} = \sqrt{E J_{tip}}$.

3.1 Formulations for E_T

As discussed earlier, elastic-plastic, stress-strain ($\sigma - \varepsilon$) properties of steels, A, and weld, W (as depicted in Fig. 2) are governed by Ramberg-Osgood relations, $\sigma^A \approx Y^A \left[\frac{\varepsilon^A}{n^A} \right]^{\frac{1}{m^A}}$ and $\sigma^W \approx Y^W \left[\frac{\varepsilon^W}{n^W} \right]^{\frac{1}{m^W}}$ respectively. The following equations [6, p.1201] represent E_T^I (Case I) and E_T^{II} (Case II) due to a point in the affected interface material:-

$$E_T^I = \frac{1}{2} (\varepsilon_r^2 E - \varepsilon_Y^W Y^W) - Y^W \int_{\varepsilon_Y^W}^{\varepsilon_r} \left[\frac{\varepsilon^W}{n^W} \right]^{\frac{1}{m^W}} d\varepsilon^W \quad (2)$$

$$E_T^{II} = Y^A \int_{\varepsilon_Y^A}^{\varepsilon_r} \left[\frac{\varepsilon^A}{n^A} \right]^{\frac{1}{m^A}} d\varepsilon^A - Y^W \int_{\varepsilon_Y^A}^{\varepsilon_r} \left[\frac{\varepsilon^W}{n^W} \right]^{\frac{1}{m^W}} d\varepsilon^W \\ + \left(\frac{1}{2} Y^A \varepsilon_Y^A - \frac{1}{2} Y^W \varepsilon_Y^W \right) - Y^W \int_{\varepsilon_Y^W}^{\varepsilon_Y^A} \left[\frac{\varepsilon^W}{n^W} \right]^{\frac{1}{m^W}} d\varepsilon^W \quad (3)$$

3.2 Formulations for $J_{interface}$

On substituting ε_r as $\frac{Z}{\sqrt{r}}$ where $Z = \frac{\pi K_{applied}}{2\sqrt{2\pi E}}$ and employing various constants as functions of material plasticity: $-C_1 = \frac{1}{2}Y^W \varepsilon_Y^W$; $C_2 = \frac{1}{2}Y^A \varepsilon_Y^A$; $C_3 = Y^W \left(\frac{1}{n^W}\right)^{\frac{1}{m^W}}$; $C_4 = Y^A \left(\frac{1}{n^A}\right)^{\frac{1}{m^A}}$; $C_5 = \frac{1}{m^W} + 1$; $C_6 = \frac{1}{m^A} + 1$; $C_7 = \frac{1}{2} - \frac{1}{2m^W}$; $C_8 = \frac{1}{2} - \frac{1}{2m^A}$, $J_{interface}$ is obtained by integrating elemental energy transfers as follows..

3.2.1 Crack Tip in Parent Steel, a, Facing Interface 1; Strong-Weak Transition (A-W) [6, pp. 228–229]

Stage I¹

$$J_{interface} = \int_{a_{int}^1}^{r_p^W} E_T^I dr = \frac{1}{2} \left[Z^2 E \ln \frac{r_p^W}{a_{int}^1} - 2C_1 (r_p^W - a_{int}^1) \right] - \frac{C_3}{C_5} \left\{ \frac{Z^{C_5}}{C_7} \left[(r_p^W)^{C_7} - (a_{int}^1)^{C_7} \right] - (\varepsilon_Y^W)^{C_5} (r_p^W - a_{int}^1) \right\} \quad (4)$$

Stage II¹

$$J_{interface} = \int_{a_{int}^1}^{r_p^A} E_T^{II} dr + \int_{r_p^A}^{r_p^W} E_T^I dr = \frac{C_4}{C_6} \left\{ \frac{Z^{C_6}}{C_8} \left[(r_p^A)^{C_8} - (a_{int}^1)^{C_8} \right] - (\varepsilon_Y^A)^{C_6} (r_p^A - a_{int}^1) \right\} - \frac{C_3}{C_5} \left\{ \frac{Z^{C_5}}{C_7} \left[(r_p^A)^{C_7} - (a_{int}^1)^{C_7} \right] - (\varepsilon_Y^A)^{C_5} (r_p^A - a_{int}^1) \right\} + \left\{ (C_2 - C_1) - \frac{C_3}{C_5} \left[(\varepsilon_Y^A)^{C_5} - (\varepsilon_Y^W)^{C_5} \right] \right\} (r_p^A - a_{int}^1) + \text{RHS of Eq. (4) in which } a_{int}^1 \text{ is replaced by } r_p^A \quad (5)$$

3.2.2 Crack Tip in Weld, W, Facing Interface 2; Weak-Strong Transition (W-A) [7, p. 1202]

Stage I²

$$J_{interface} = \int_{a_{int}^2}^{r_p^W} E_T^1 dr = \frac{1}{2} \left[Z^2 E \ln \frac{r_p^W}{a_{int}^2} - 2C_1 (r_p^W - a_{int}^2) \right] - \frac{C_3}{C_5} \left\{ \frac{Z^{C_5}}{C_7} \left[(r_p^W)^{C_7} - (a_{int}^2)^{C_7} \right] - (\varepsilon_Y^W)^{C_5} (r_p^W - a_{int}^2) \right\} \quad (6)$$

Stage II²

$$J_{interface} = \int_{a_{int}^2}^{r_p^A} E_T^{II} dr + \int_{r_p^A}^{r_p^W} E_T^1 dr = \frac{C_4}{C_6} \left\{ \frac{Z^{C_6}}{C_8} \left[(r_p^A)^{C_8} - (a_{int}^2)^{C_8} \right] - (\varepsilon_Y^A)^{C_6} (r_p^A - a_{int}^2) \right\} - \frac{C_3}{C_5} \left\{ \frac{Z^{C_5}}{C_7} \left[(r_p^A)^{C_7} - (a_{int}^2)^{C_7} \right] - (\varepsilon_Y^A)^{C_5} (r_p^A - a_{int}^2) \right\} + \left\{ (C_2 - C_1) - \frac{C_3}{C_5} \left[(\varepsilon_Y^A)^{C_5} - (\varepsilon_Y^W)^{C_5} \right] \right\} (r_p^A - a_{int}^2) + \text{RHS of Eq. (6) in which } a_{int}^2 \text{ is replaced by } r_p^A \quad (7)$$

As explained earlier, $J_{interface}$ found in Sects. 3.2.1 and 3.2.2 correspond to energy transfer in one direction only and is multiplied by the factor of 2 for meeting the requirement of having similar bi-axial stress state on crack axis in affected interface material.

4 Results and Discussion

The material properties of weld and steels used for computational purpose are: $Y^W = 570$ MPa, $n^W = 0.0037$, $m^W = 10.4$, $Y^A = 900$ MPa, $n^A = 0.0047$, $m^A = 10.1$, $E^W = E^A = 2 \times 10^5$ MPa, $\nu^A = \nu^W = 0.3$. The values of ε_Y^W and ε_Y^A are 0.00285 and 0.0045 respectively. The initial or starting length, c_i , of crack in parent steel, A, is considered to be as 45 mm. The distance of crack tip from the interface 1, $a_{i,int}^1$, is assumed as 10 mm. Weld thickness, t , is chosen as 10 mm. p_∞ is taken as 150 MPa to realize SSY conditions. Indicated by Figs. 3 and 4, the crack tip

Fig. 3 Fracture parameters versus crack length ($t = 10$ mm)

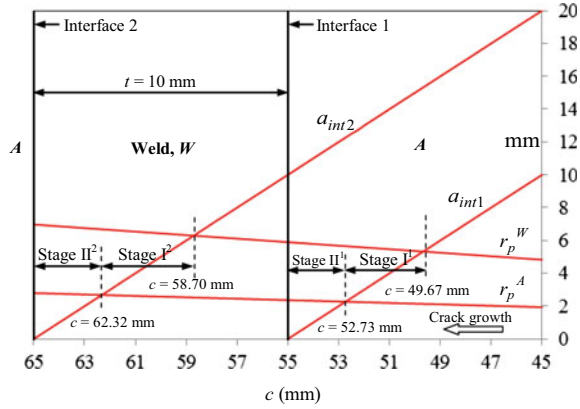
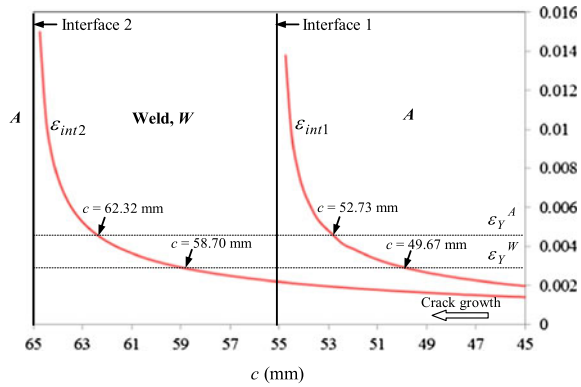
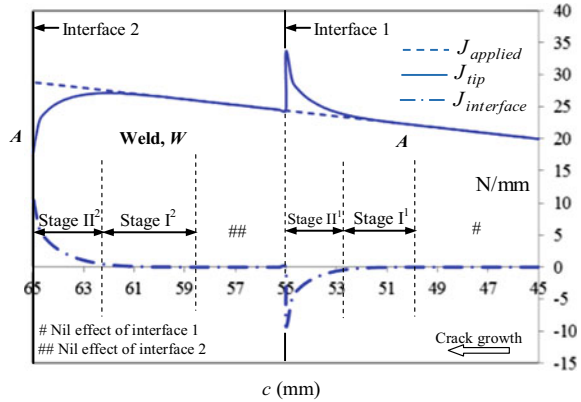


Fig. 4 Strains as interfaces versus crack length ($t = 10$ mm)



remains unaffected by approaching weld during crack growth from length, c , of 45–49.67 mm since $\varepsilon_{int}^1 \leq \varepsilon_Y^W$ or $r_p^W \leq a_{int}^1$ during this period. Stage I¹ begins at c of 49.67 mm that is obtained from, $c = \frac{c_i + a_{i,int}^1}{1 + \frac{\pi^2}{8} \frac{1.12^2 \rho_{\infty}^2}{Y_W^2}}$, on using the condition, $a_{int}^1 = r_p^W$ or $c_i + a_{i,int}^1 - c = r_p^W \cdot \varepsilon_{int}^1 = \varepsilon_Y^W$ is fulfilled at c of 49.67 mm. Stage I¹ continues up to c of 52.73 mm after which Stage II¹ starts that is found from, $c = \frac{c_i + a_{i,int}^1}{1 + \frac{\pi^2}{8} \frac{1.12^2 \rho_{\infty}^2}{Y_A^2}}$, on using the condition, $a_{int}^1 = r_p^A$ or $c_i + a_{i,int}^1 - c = r_p^A \cdot \varepsilon_{int}^1 = \varepsilon_Y^A$ is satisfied at c of 52.73 mm. Stage II¹ progresses till the crack tip touches interface 1 i.e. up to c of 55 mm. On entering into the weld, the crack tip is unaffected by back up steel during crack growth from 55 to 58.70 mm length, since $\varepsilon_{int}^2 \leq \varepsilon_Y^W$ or $r_p^W \leq a_{int}^2$ during this period. Stage I² commences at c of 58.70 mm that is found from, $c = \frac{c_i + a_{i,int}^1 + t}{1 + \frac{\pi^2}{8} \frac{1.12^2 \rho_{\infty}^2}{Y_W^2}}$, on using the condition, $a_{int}^2 = r_p^W$ or $c_i + a_{i,int}^1 + t - c = r_p^W \cdot \varepsilon_{int}^2 = \varepsilon_Y^W$ is fulfilled at c of 58.70 mm. Stage I² progresses till c of 62.32 mm when Stage II² starts that is found

Fig. 5 Energy release rate versus crack length ($t = 10$ mm)



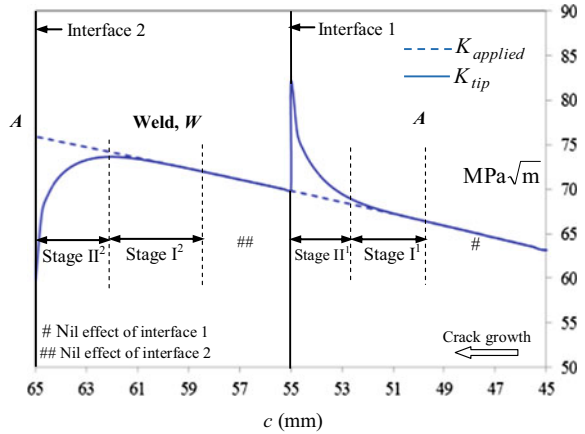
from, $c = \frac{c_i + a_{i,int}^1 + t}{\left[1 + \frac{\pi^2}{8} \frac{1.12^2 p_{\infty}^2}{Y_A^2}\right]}$, on using the condition, $a_{int}^2 = r_p^A$ or $c_i + a_{i,int}^1 + t - c = r_p^A$. $\varepsilon_{int}^2 = \varepsilon_Y^A$ is fulfilled at c of 62.32 mm. Stage II² then progresses till the crack tip touches the interface 2 i.e. up to c of 65 mm.

Refer Fig. 5. As expected, $J_{applied}$ increases linearly with crack length, minimum at c of 45 mm and maximum at c of 65 mm. $J_{tip} = J_{applied}$ till c of 49.67 mm. J_{tip} deviates from $J_{applied}$ with onset of Stage I¹. The deviation increases in Stage II¹. In both the stages, $J_{tip} > J_{applied}$, the difference between the two i.e. $J_{interface}$ being less in Stage I¹ due to Case I energy transfer and higher in Stage II¹ due to Case II energy transfer. Case II energy transfer is substantially higher than Case I energy transfer that is clear from Fig. 2. Again, $J_{tip} = J_{applied}$ during crack growth from 55 to 58.70 mm length. J_{tip} then deviates from $J_{applied}$ with onset of Stage I². The deviation increases in Stage II². In both the stages, $J_{tip} < J_{applied}$, $J_{interface}$ being less in Stage I² due to Case I energy transfer and higher in Stage II² due to Case II energy transfer. Magnitude of $J_{interface}$ in cases of both the interfaces keeps on increasing as the crack tip reaches nearer to each interface and achieves the maximum value when the crack tip touches the interface. Refer Fig. 6. Similar trends are noticed in plots of K_{tip} and $K_{applied}$ vs c with $K_{tip} > K_{applied}$ and $K_{tip} < K_{applied}$ in case of crack growth towards interface 1 and 2 respectively.

5 Conclusions

A novel theoretical model for determining the energy release rate at the tip of a mode I crack that proceeds in the bi-material of similar or comparable steels connected by a weaker or under-matched steel weld interlayer, i.e. strong-weak-strong transition, is described in the work. Under monotonic load, the influence of strength mismatched interfaces among weld and steel is assessed over the tip in SSY regime. The approach

Fig. 6 Strains intensity parameters versus crack length ($t = 10 \text{ mm}$)



takes into account the non-linear plastic properties of the steels. During the strong-weak transition as the tip of the crack in strong parent steel faces the approaching interface of the weaker weld, the energy release rate at the tip of the crack is greater than the far field value, and it is less than the far field variable during the weak-strong transition, i.e. when the tip of the crack in weld faces the interface of back up steel. When the tip is at the interfaces, the effects of shielding and amplification are highest.

The proposed model was previously validated using finite element modeling of crack in front of each type of thin interface [6]. However, future study will include numerical analysis to explore the sequential effect of two interfaces, particularly at fracture length where the crack tip is not exposed to the influence of the interface between weld and back up steel, a phenomena that is dependent on weld thickness.

References

1. Kim AS, Suresh S, Shih CF (1997) Plasticity effects on fracture normal to interfaces with homogeneous and graded compositions. *Int J Solids Struct* 34:3415–3432
2. Predan J, Gubeljak N, Kolednik O (2007) On the local variation of the crack driving force in a double mismatched weld. *Eng Fract Mech* 74:1739–1757
3. Wappling D, Gunnars J, Stahle P (1998) Crack growth across a strength mismatched bimaterial interface. *Int J Fract* 89:223–243
4. Reimelmoser FO, Pippan R (2000) The J-integral at Dugdale cracks perpendicular to interfaces of materials with dissimilar yield stresses. *Int J Fract* 103:397–418
5. Bo SY, Ji SH, Xi WZ, Dong ZG (2006) A crack tip driving force model for mode I crack propagation along linear strength gradient: comparison with the sharp strength gradient case. *Acta Mech* 227:2683–2702
6. Bhat S, Suresh N, Kambar MM, Ukadgaonker VG (2017) Strain based investigation of mode I crack near strong-weak interface in SSY regime. *Int J Mech Sci* 123:224–237

7. Bhat S, Ukadgaonker VG (2015) A refined theoretical model for mode I crack near the interface of strength and plasticity mismatched materials in K dominant regime. *Int J Damage Mech* 24:1194–1213
8. Bhat S, Adarsha H, Ravinarayan V, Kaushik VP (2019) Analytical model for estimation of energy release rate at mode I crack tip in bi-material of identical steels joined by an over-matched weld interlayer. *Proc Struct Integr* 17:21–28

Durability of Cement Mortars with a High Proportion of Mineral Admixture After Bacterial Environment Exposure



Adriana Estokova , Michaela Smolakova, and Alena Luptakova

Abstract Cement-based materials should resist the damage caused by different complex physical, chemical and biological processes such as sulphate and chloride attack, biodegradation, corrosion induced by various agents, freeze-thaw cycles, alkali-silica reaction etc. One of the ways how to increase durability of the cement-based composites, is to incorporate various admixtures with the pozzolanic activity which reduce the amount of portlandite, by mutual reaction forming a more stable calcium silicate-hydrates. This paper presents the study of evaluating the resistance of cement mortars with a high proportion of mineral admixture based on finely ground granular blast furnace slag (from 65 to 95 wt.%) in the environment of sulphur oxidizing bacteria *Acitithiobacillus thiooxidans*. The aim of the paper was to compare, by using thermal analysis, the resistance of composites without and with mineral admixture due to the action of aggressive bacterial environment during 3, 6, 9 and 12 months long experiments. The evaluated parameters such as the degree of hydration and the content of portlandite in mortars showed that despite the bacterial attack, hydration processes prevailed over degradation processes in the studied samples. The results showed a positive effect of the addition of the mineral admixture to increase in durability of mortars. Method of thermal analysis was proved to be an effective analytical tool to monitor and evaluate the microbial corrosion processes of cement composites.

Keywords Blast furnace slag · Microbial corrosion · Cement composite · Concrete · Thermogravimetric analysis TGA

A. Estokova (✉) · M. Smolakova
Technical University of Kosice, Vysokoskolska 4, 042 00 Kosice, Slovakia
e-mail: adriana.estokova@tuke.sk

A. Luptakova
Institute of Geotechnics, Slovak Academy of Sciences, Watsonova 47, 040 01 Kosice, Slovakia

© The Author(s), under exclusive license to Springer Nature Singapore Pte Ltd. 2022
M. Abdel Wahab (ed.), *Proceedings of the 9th International Conference on Fracture, Fatigue and Wear*, Lecture Notes in Mechanical Engineering,
https://doi.org/10.1007/978-981-16-8810-2_4

1 Introduction

Due to climate changes, the pressure to introduce innovative materials and technologies in the construction industry is increasing worldwide. These changes automatically bring new challenges to construction and environmental engineers, architects as well as other professionals in the field of civil engineering. Previously standardized solutions are usually not optimized enough to be considered sustainable and cannot cope with the great diversity of existing building materials and the new demands placed on them [1]. One of the requirements to ensure sustainability in the construction industry is to extend the life of structures, which is associated with the need to develop materials more resistant to different types of mechanical loads as well as to the effects of various degradation mechanisms [1, 2]. Cement-based materials should resist the damage caused by different complex physical, chemical and biological processes such as sulphate and chloride attack, biodegradation, corrosion induced by various agents, freeze-thaw cycles, alkali-silica reaction etc. These mechanisms are largely influenced by the resistance of the material against moisture penetration, whether in liquid or gaseous form, or by aggressive ions through diffusion, capillary absorption or sorption. These mechanisms may occur either in combination or alone [3, 4].

Biological attack on the cement composites, represented e.g. by sulphur oxidizing bacteria *Acidithiobacillus thiooxidans* which activity results in sulfuric acid formation, is manifested by deterioration of the cement matrix due to both acidic and sulphate corrosive mechanisms. Hardened cement paste and concrete are porous materials, which are composed of solid hydration products and space, formed by various large pores existing in the matrix. The most important hydration products include calcium hydroxide or portlandite (CH), calcium silicates hydrates (C-S-H phase) and calcium aluminates hydrates (C-A-H phase), ettringite (AFm) and monosulfate (AFt). In contact with the liquid bacterial medium, dissolution and subsequent leaching of the present phases may occur, which may result in complete disintegration of the cement matrix and loss of functionality of cement composite [3, 4]. The least stable phase is portlandite, which leaches out first, followed by monosulfate, ettringite and finally last leached out phases are the significantly decalcified calcium silicates hydrates [3, 5]. Sulphate corrosion is probably the most common type of chemical corrosion of concrete, the physical consequence of which is corrosion in the form of volume expansion and the formation of cracks, which can lead to disintegration of concrete. Sulphate corrosion is a complex process, the mechanism of which remains controversial, but it is established that the rate of deterioration increases with the calcium aluminate (C_3A) content in the cement. Two basic mechanisms of sulphate corrosion can be described: (a) calcium sulphate formation [6] and (b) ettringite formation [7]. Macroscopic crystals of needle-shaped ettringite form near aggregate grains, while their growth is limited by space, which is the reason for the formation of cracks in the transition zone.

Studies by various authors [8–10] confirmed that blast furnace slag used as a replacement for cement improves the quality of cement-based materials, especially

against sulphate attack [11–13]. The positive effects of pozzolanic materials have been known for a long time, but there is no generally recommended optimum amount of these admixtures to increase the resistance of cementitious composites, and thus most authors have been studying cement replacement in the range of 25–40 wt.% [14, 15]. Several analytical methods such as X-ray diffraction analysis (XRD), X-ray fluorescence analysis (XRF), scanning electron microscopy (SEM) or infrared spectrometry (FTIR) are used to study the resistance of building materials such as mortar and concrete. Very useful methods include also thermal analysis (TA), which allows the evaluation of the amount of calcium hydroxide and calcium silicates hydrates in the cementitious materials by measuring the weight loss during the controlled heating process. Several studies have confirmed the importance of this method, with the authors focusing on the degradation of building materials in the tap or deionized water as well as in the aggressive solution with the Na_2SO_4 . However, studies focusing on the use of thermal analysis to study sulphate biological corrosion, where the aggressive environment is produced by bacteria, are very rare.

This paper presents the possibilities of use of thermal analysis in the study of resistance of cementitious materials with a high proportion of mineral admixture based on finely ground granular blast furnace slag (from 65 to 95 wt.%) in the environment of sulphur oxidizing bacteria *Acitithiobacillus thiooxidans*. The aim of the paper was to compare the resistance of composites without and with mineral admixture to the action of aggressive bacterial environment during 3, 6, 9 and 12 months long experiments.

2 Material and Methods

2.1 Cement Mortars Analyzed

Five types of cement mortar mixtures with different proportions of granulated blast furnace slag were prepared for the biocorrosion experiment. The reference sample (CMS-0) contained sand (1350 ± 5 g), cement (450 ± 2 g) and water (225 ± 1 g) with water to cement ratio (w/c) = 0.5. In remaining samples, the cement was partially replaced by a mineral admixture based on finely ground granulated blast furnace slag in the range of 65 wt.% (CMS-65), 75 wt.% (CMS-75), 85 wt.% (CMS-85) and 95 wt.% (CMS-95). The chemical composition of cement CEM I 52.5 R (Považská cementáreň, Ladce, Slovakia) and mineral admixture (Považská cementáreň, Ladce, Slovakia), used for the preparation of mortar mixtures is shown in Table 1. The mineralogical composition of cement corresponded to 64.10% of alite (C_3S), 11.34% of belite (C_2S), 8.18% of tricalcium aluminate (C_3A), 6.12% of tetracalcium aluminoferrite (C_4AF), up to 5% of gypsum and 5.26% of the other components. The test specimens were approximately $40 \times 40 \times 160$ mm in size and were made according to EU standard EN 196-1 [16].

Table 1 Content of main components in cement and granulated blast furnace slag (wt.%)

| Component | Portland cement | Granulated blast furnace slag |
|--------------------------------|-----------------|-------------------------------|
| CaO | 57.15 | 39.55 |
| SiO ₂ | 19.01 | 38.95 |
| Al ₂ O ₃ | 4.02 | 8.33 |
| Fe ₂ O ₃ | 2.69 | 0.54 |
| SO ₃ | 1.49 | 0.57 |
| MgO | 1.37 | 10.11 |
| K ₂ O | 1.12 | 0.48 |
| P ₂ O ₅ | 0.33 | 0.04 |
| TiO ₂ | 0.18 | 0.37 |
| Cl | 0.06 | 0.02 |
| Other | 12.58 | 1.04 |

2.2 Corrosive Bacterial Environment

The corrosive bacterial environment was simulated with sulphur oxidizing bacteria *Acidithiobacillus thiooxidans*, based on their ability to produce biogenic sulphuric acid. The nutrient medium by Waksman and Joffe [17] was used for preparation and inoculation of the active bacterial culture of *A. thiooxidans*. The nutrient medium used was composed of 0.25 g/L CaCl₂ 0.6H₂O, 0.2 g/L of (NH₄)₂SO₄, 3.0 g/L of K₂HPO₄, 0.5 g/L of MgSO₄ 7H₂O, trace amount FeSO₄·7H₂O, 10.0 g/L of elemental sulfur and 1000 mL of distilled water. *Acidithiobacillus thiooxidans* were isolated from the acid mine drainage from the Pech shaft located near Smolník in the eastern Slovakia [18]. The exposure of cementitious composites took place in glass beakers under aerobic laboratory conditions for 3, 6, 9 and 12 months. During the experiment, an optimal temperature for growth of bacterial culture (28–30 °C) and a pH range from 2.0 to 3.5 was ensured.

2.3 Thermogravimetric Analysis

Thermal analysis (TGA) was used to study content of portlandite in the samples and to estimate the chemically bounded water and hydration degrees of mortars. Cement mortar samples before and after the experiment were dried, crushed, ground and in the form of powder analyzed on a STA Jupiter 4 Thermal analyzer (Netsch, Germany) under nitrogen atmosphere at a heating rate of 30 K/min in a temperature range of 26–900 °C in simultaneous differential scanning calorimetry (DSC) and thermal gravimetry (TG) modes. Approximately 40 mg of sample was heated in corundum pot.

2.4 Scanning Electron Microscopy

Scanning electron microscopy (SEM) was applied to analyze the cracks and new formed voluminous compounds on the surface of the mortars samples exposed to the bacterial attack. Structural surface changes were observed by electron scanning microscopy (SEM) with equipment Jeol JSM-35CF (Japan). The elemental EDX analysis were carried out on the micro-analytical system LINK AN 10 000 operating in secondary mode at a potential 25 kV and at extension 90–5500.

3 Results and Discussion

3.1 Contents of Portlandite and Hydration Degree

Portlandite content in the mortar samples before the experiment was chosen as an indicator to estimate the pozzolanic activity of granulated slag. The peak on the DSC curve representing the decomposition of free portlandite was identified in the range 400–500 °C in accordance with [19]. When comparing the DSC curves of the reference sample (CMS-0) and the samples with added mineral admixture (CMS-65 to CMS-95), there was a decrease in the peak area corresponding to the portlandite, which confirmed the pozzolanic activity of the added mineral admixture (Fig. 1).

The authors in [20] observed similar trend in decrease in the amount of free $\text{Ca}(\text{OH})_2$ for samples with 35 wt.% of blast furnace slag and noted that with increasing amounts of pozzolanic admixture, the amount of free portlandite was reduced. In addition, the slag-based samples had higher formation of the C-S-H phase [21].

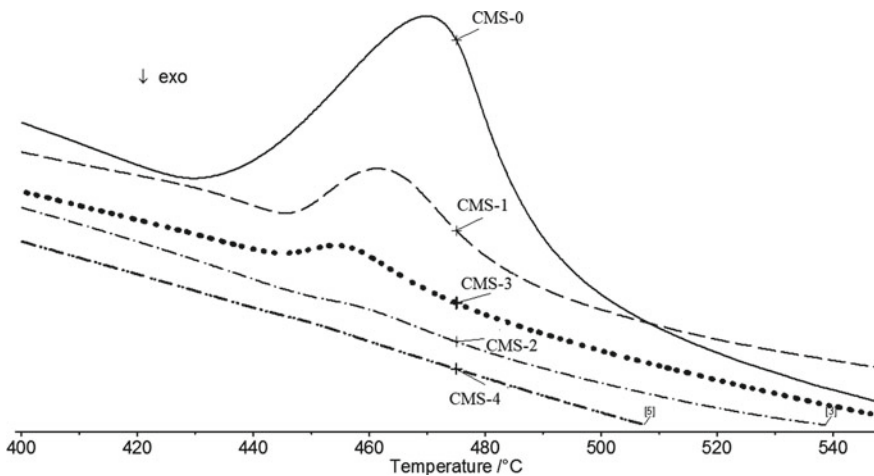


Fig. 1 The comparison of DSC peaks of portlandite in samples without and with blast furnace slag

Table 2 Content of total portlandite in cement mortars before the experiment (wt.%)

| | CMS-0 | CMS-65 | CMS-75 | CMS-85 | CMS-95 |
|-------------------------|-------|--------|--------|--------|--------|
| Ca(OH) ₂ (%) | 21.3 | 7.1 | 5.1 | 6.3 | 3.6 |

Blast-furnace slag composites showed a fourfold higher amount of C-S-H phase compared to the amount of portlandite prior to the experiment. For the reference sample without the addition of slag, the difference between the C-S-H phase and Ca(OH)₂ was the lowest of all the studied samples (approximately 1.5-times).

The decrease in portlandite content of slag samples was also confirmed by calculating a total Ca(OH)₂ (Table 2) by using Eq. (1) according to [22, 23] from TG curves based on the particular weight losses. The amounts of portlandite formed during the hydration of tricalcium and dicalcium silicates in the cements were estimated from both the dehydroxylation and decarbonation losses by using the following expression (1):

$$\text{Ca(OH)}_2(\%) = 4.11 \times \text{ML}_{(P)} + 1.68 \times \text{ML}_{(C)} \quad (1)$$

where ML_(P) is the mass loss related to the portlandite decomposition (400–500 °C) and ML_(C) is the mass loss related to the carbonates decomposition (500–900 °C). The coefficients in the expression are based on the molecular weights of the products in the decomposition reactions. Since the cement and water content represented only 50% of the whole mortars composition, and the silica sand did not contribute in the hydration reactions, however being measured in TGA analysis, the calculated amount of calcium hydroxide were corrected by multiplying the calculated values by 2.

Vejmelkova et al. [24] also confirmed lower amounts of portlandite in samples where the cement was substituted by blast furnace slag by X-ray diffraction (XRD).

The weight losses for the dehydroxylation and decarbonation regions C-S-H, P and C after the particular experimental periods of the bio-corrosion experiment are shown in Table 3.

To study the degradation of cement mortars due to bacterial exposure, the degree of hydration and content of portlandite were evaluated after the experimental periods based on weight losses in the decomposition regions. To assess the degree of hydration of cementitious mortars, that has been exposed to bacteria, the equation according to [14] was used. The degree of hydration α expressed in percentage was calculated according to Eq. (2).

$$\alpha = \frac{W_{CBW}}{0.24 \times k} \times 100 \quad (2)$$

where W_{CBW} represents the amount of chemically bound water and value 0.24 the maximum amount of chemically bound water required for complete hydration of cement particle. This value may vary between 0.23 and 0.25 and represents the

Table 3 Mass losses of the mortars samples after the bio-corrosion experiment per individual regions (wt.%)

| Sample | Duration of the experiment (months) | Mass losses (%) | | |
|--------|--|--------------------------|------------------------|------------------------|
| | | CSH region 106–400 °C | P region 400–500 °C | C region 500–900 °C |
| CMS-0 | 3 | 6.19 | 1.64 | 7.25 |
| | 6 | 7.90 | 1.63 | 8.65 |
| | 9 | 6.76 | 1.66 | 6.76 |
| | 12 | 7.26 | 1.72 | 7.23 |
| CMS-65 | 3 | 5.69 | 0.91 | 4.93 |
| | 6 | 4.94 | 0.72 | 4.59 |
| | 9 | 5.92 | 0.89 | 5.01 |
| | 12 | 7.83 | 1.10 | 5.13 |
| CMS-75 | 3 | 4.60 | 0.96 | 4.34 |
| | 6 | 4.58 | 0.94 | 4.56 |
| | 9 | 5.07 | 0.98 | 5.19 |
| | 12 | 5.84 | 1.23 | 5.71 |
| CMS-85 | 3 | 4.29 | 0.82 | 4.49 |
| | 6 | 4.07 | 0.76 | 3.90 |
| | 9 | 5.02 | 0.95 | 4.88 |
| | 12 | 5.18 | 1.02 | 4.95 |
| CMS-95 | 3 | 4.02 | 0.82 | 4.78 |
| | 6 | 4.32 | 0.83 | 5.25 |
| | 9 | 5.25 | 0.85 | 4.04 |
| | 12 | 5.31 | 0.89 | 5.44 |

maximum amount of chemically bound water required for hydration regardless of used material.

Coefficient k was derived from the composition of the mortar samples to be equal 0.5, and represented the share of the silica sand in mortars. Based on this method, the hydration degree is directly related to the content of chemically bound water W_{CBW} (%), which was calculated according to Eq. (3), based on the study by Bhatti et al. [23].

$$W_{CBW} = ML_{(CSH)} + ML_{(P)} + 0.41 \times ML_{(C)} \quad (3)$$

where $ML_{(CSH)}$, $ML_{(P)}$, $ML_{(C)}$ represent the weight losses in the individual regions related to dehydroxylation and decarbonation reactions. The value 0.41 is the conversion factor derived from the carbonation of portlandite.

The calculated amounts of chemically bound water (W_{CBW}) and the degrees of hydration (α) of the cement mortar samples are compared in Fig. 2.



Fig. 2 Development of chemically bounded water and hydration degrees of the mortar samples **a** CMS-0; **b** CMS-65; **c** CMS-75; **d** CMS-85; and **e** CMS-95 during the 3, 6, 9, and 12-month bio-corrosion experiment

As seen in Fig. 2, the continuous increase in hydration degrees was observed for all slag-based samples except for the CSM-65 sample. The calculated values correlate with the values in Monteagudo et al. [25] taking into account that he analyzed cement pastes. The increase in the degree of hydration can be explained by the fact that during the experiment in the liquid bacterial environment, competitive processes took place at the same time: degradative corrosion process, such as dissolution and leaching and secondary compounds crystallization, but also additional hydration of cement components. On the contrary, as for the reference sample, after the 6-month

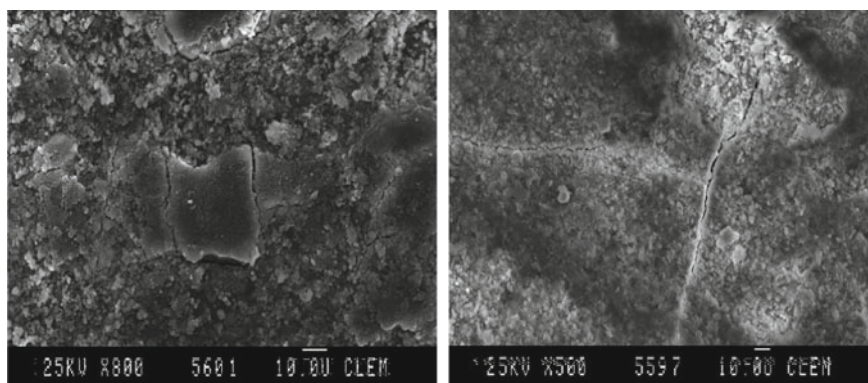


Fig. 3 SEM micrograph of the samples after 12-month exposition to bacteria

bacterial attack a rapid decrease in hydration processes was observed. This pointed to the prevalence of strong deterioration of the cement matrix of the CMS-0 sample. The hydration ratio α_{360}/α_0 comparing the hydration before and after the 12 months of the experiment were used to evaluate the resistance of individual samples. Based on that, all samples with blast furnace slag substitution proved a higher degree of dominance of hydration processes over degradation compared to the sample without mineral admixture.

3.2 Cracks Development and Sulphate Product Formation

Deterioration processes of mortars have been also manifested by observed surface cracks (Fig. 3). Cracks were likely associated with the formation of secondary voluminous compounds like gypsum $\text{CaSO}_4 \times 2\text{H}_2\text{O}$, which is a typical result of the mechanism of sulphate corrosion at low pH values, and which could cause stress inside the material structure and subsequent cracking [26]. White crystals of newly formed sulfate compounds were observed on the surface of the samples as seen in Fig. 4. Based on the semi quantitative EDS elemental analysis, the presence of gypsum was confirmed since the Ca/S and S/O concentration ratios corresponded well to the theoretical ratios.

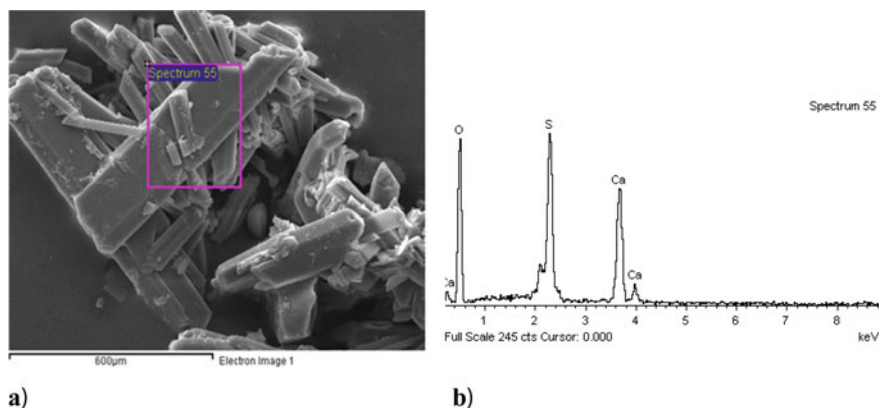


Fig. 4 a) SEM micrograph of the surface product, b) EDS spectrum of identified elements

4 Conclusion

The presented article presented the possibility of using thermal analysis to monitor deterioration changes of cement composites with mineral admixture exposed to aggressive bacterial environment. Evaluated parameters such as degree of hydration and portlandite content showed that the addition of slag as a mineral admixture, had positive effect on resistance of mortars against the action of a bacteria. The suitability of the thermal analysis method to monitor and evaluate a degradation mechanism such as process of biological corrosion was proven.

Acknowledgements The research was supported by the Slovak Grant Agency for Science (VEGA grant No. 2/0142/19).

References

- Schmidt W, Alexander M, John V (2018) *Cem Concr Res* 114:103–114
- Qu F, Li W, Dong W, Tam VWY, Yu T (2021) *J Build Eng* 35:102074
- Al-Kheetan MJ, Rahman MM, Chamberlain DA (2019) *Constr Build Mater* 207:122–135
- Homan L, Ababneh AN, Xi Y (2016) *Constr Build Mater* 125:1189–1195
- Adenot F, Buil M (1992) *Cem Concr Res* 22:489–496
- Zou D, Qin S, Liu T, Jivkov A (2021) *Cem Concr Res* 139:106284
- Chen Y, Liu P, Yu Z (2020) *Constr Build Mater* 260:119951
- Pacheco-Torgal F, Labrincha JA (2013) *Constr Build Mater* 40:1136–1141
- Tang YJ, Zuo XB, He SL, Ayinde O, Yin GJ (2016) *Constr Build Mater* 129:61–69
- Roziere E, Loukili A, El Hachem R, Grondin F (2009) *Cem Concr Res* 39:451–456
- O’Connell M, McNally C, Richardson MG (2010) *Cem Concr Compos* 32:479–485
- Irico S, De Meyst L, Qvaeschning D, Alonso MC, Villar K, De Belie N (2020) *Materials* 13:1431
- Whittaker M, Zajac M, Haha MB, Black L (2016) *Constr Build Mater* 119:356–361

14. Monteagudo SM, Moragues A, Galvez JC, Casati MJ, Reyes E (2014) *Thermochim Acta* 592:37–51
15. Stroh J, Meng B, Emmerling F (2016) *Solid State Sci* 56:29–44
16. EN 196-1 (2016) *Methods of testing cement—Part 1: Determination of strength*
17. Waksman SA, Joffe JS (1922) *J Bacteriol* 7:239–256
18. Kovalcikova M, Estokova A, Luptakova A, Strigac J (2016) *Solid State Phenom* 244:88–93
19. Shi Z, Geiker MR, Lothenbach B, De Weerd K, Garzón SF, Enemark-Rasmussen K, Skibsted J (2017) *Cem Concr Compos* 78:73–83
20. Nasrazadani S, Eghtesad R, Sudoi E, Vupputuri S, Ramsey JD, Ley MT (2016) *Mater Struct* 49:2025–2034
21. Tanwar V, Bisht K, Kabeer SA, Ramana PV (2021) *J Build Eng* 41:102372
22. Rivera Lozano J (2004) *Doctoral thesis. Autonomous University of Madrid, Madrid*
23. Bhatt J (1986) *Thermochim Acta* 106:95–105
24. Vejmelkova E, Pavlikova E, Kersner Z, Rovnanikova P, Ondracek M, Sedlmajer M, Cerny R (2009) *Constr Build Mater* 23:2237–2245
25. Gruyaert E, Robeyt N, De Belie N (2010) *J Therm Anal Calorim* 102:941–951
26. Bankir MB, Sevim UK (2020) *J Build Eng* 32:101443

Unloading of Low Velocity Impact Between Elastic and Elastic-Plastic Bodies



Chuanqing Chen, Magd Abdel Wahab, Qiao Wang, and Xiaochun Yin

Abstract The unloading process of an elastic sphere impacting an elastic-perfectly plastic half-space under low velocity and frictionless conditions is deeply studied in the light of finite element (FE) analysis. The unloading in the FE simulations ranges from elastic-plastic to fully plastic deformation regimes by designed impact velocities and material properties. The cavity profiles after unloading are measured from the FE simulations based on the spherical residual cavity validation. An analytical expression of the radius of spherical residual cavity is derived from the fitting method. The residual radius of curvature is determined by combining its physical definition with the analytical expression. A new revised Hertz unloading model is suggested, which is validated numerically and experimentally.

Keywords Low-velocity impact · Contact mechanics · Unloading · Finite element analysis

1 Introduction

Particle impact is applied in numerous engineering applications, such as mechanical seals [1–3], joints components [4, 5], biological films [6], gear meshing [7–10], rolling element bearings [11, 12] and electronics reliability [13, 14]. Impact is very complex due to its dynamic and nonlinear behaviors [15–17]. The plastic deformation [15, 16] is formed easily during impact loading, which can cause an irreversible

C. Chen · X. Yin (✉)

Department of Mechanics and Engineering Science, School of Science, Nanjing University of Science and Technology, Nanjing, China
e-mail: yinxiaochun@njust.edu.cn

C. Chen · M. Abdel Wahab

Soete Laboratory, Ghent University, Technologiepark Zwijnaarde 903, B-9052 Zwijnaarde, Belgium

Q. Wang

Institute of Equipment Research, Inner Mongolia North Heavy Industries Group Co. Ltd, 3 Binggong Road, Baotou 014030, Inner Mongolia, China

cavity on the indented object. In addition, the generated plastic deformation results in the unloading path are not the same as in the loading path. For a complete impact cycle, both of the loading and unloading phases are important. However, the existing researches mainly pay their attentions to the loading phases [15, 18–28]. To accurately investigate the impact response, the unloading phase should be devoted to as in the case of loading phase [29–31].

Impact is usually related to the static contact problem [15, 21, 32]. It has been shown that both loading and unloading responses could be considered to be quasi-static [23, 33, 34]. Hertz contact model [32] has been widely applied to solve the elastic impact problem. There are many static elastic-plastic contact models [15, 17–23, 35–40] that have been developed for the elastic-plastic impact problem. These developed models are usually limited to the contacts with a rigid sphere or a rigid flat.

During unloading process, there are some complicated deformation phenomena, such as the shallowing [41], piling-up deformation [24, 42–45], re-yielding around the edge of contact area [24, 42] and high residual stress [24]. These phenomena make the study of unloading phase rather complicated. Some simplified assumptions have always been considered. Generally, the unloading is considered as an elastic progress and the unloading laws can be divided into Hertzian-type and non-Hertzian-type. For non-Hertzian-type unloading laws, Etsion et al. [46], Ovcharenko et al. [47], Brake [20], Li and Gu [48], Yan and Li [49], Yigit [35], Majeed et al. [50], Christoforou et al. [51] and Ibrahim and Yigit [52] have presented or validated some empirical relations of contact force to indentation by the finite element simulations and experiments. In our previous study [53], the unloading curve has been numerically verified to follow Hertzian-type unloading law, hence, the following discussions focus on the Hertzian-type unloading laws.

The Hertzian-type unloading laws are characterized by some key parameters: the maximum contact force F_m , maximum contact indentation δ_m , permanent indentation δ_r and residual radius of curvature R^{*e} . To obtain the unloading law, δ_m and F_m are obtained at the end of loading. The remained δ_r and R^{*e} are determined by the aid of different assumptions to account for the plastic deformation generated during loading phase. δ_r represents the plastic deformation level during loading phase. R^{*e} indicates the similarity in geometry between contact surfaces of the impact bodies. For Hertzian-type unloading laws, one of δ_r and R^{*e} should be determined in advance and then the other one can be calculated according to continuity condition between loading phase and unloading phase.

For some Hertzian-type unloading laws, Jackson et al. [54] developed an expression of δ_r by fitting the FE results provided by Jackson et al. [24]. The expression was found to be deviated from the experimental results [55]. Based on the limited experimental and FE data, Ghaednia et al. [55] provided another empirical expression using fitting-curve approach, which can predict δ_r more accurate than the theoretical predictions by Thornton and Ning [56] and another fitted expression by Kogut and Komvopoulos [39]. Kogut and Komvopoulos [39] illustrated that δ_r was dependent on the yield strain of half-space, and fitted a theoretical equation from the FE data.

The unloading model by Ma and Liu [25] could not exactly predict δ_r for the existing experiments.

For other Hertzian-type unloading laws, R^{*e} is usually solved by some theoretical assumptions instead of directly measured by experiment and calculated from FE method. In fact, plastic deformation leads both contact surfaces to a flatter tendency [57] and increases R^{*e} [58], making R^{*e} different from the effective elastic contact radius R^* . The increasing in R^{*e} can be physically explained as that the plastic deformation that makes both contact surfaces flatter and makes the impact bodies becoming geometrically similar. If $R^{*e} = R^*$ is enforced such as that has been done by Du and Wang [59], the shallowing effect [41] resulted by contact plastic deformation should be neglected. Thornton [18] assumed a defined contact area to be continuous to solve R^{*e} , resulting much too soft unloading stiffness [22]. Li et al. [36] calculated R^{*e} by assuming the contact area and indentation to have a parabolic relation. Their unloading model was not in a closed form [60] and required to be solved numerically [61]. Brake [20] suggested different assumptions for R^{*e} of loading phases covering elastic-plastic and fully plastic deformation regimes, however, it can only be suitable for limited contact conditions [25]. By defining a relation of R^{*e} and the contact force, Vu-Quoc et al. [22] determined R^{*e} based on the finite element simulations conducted by Brake [20]. Moreover, Ma and Liu [25] solved R^{*e} based on the assumption of Thornton [18] during elastoplastic loading phase, assuming constant R^{*e} during fully plastic loading phase. Stronge [21] calculated R^{*e} by assuming the residual contact curvature being geometrically similar to the initial contact curvature and this assumption was also applied by Majeed et al. [50] for composite materials. Chen et al. [53], Dong et al. [17], Jin et al. [38] and Zhang et al. [37] found that the continuity of contact force by Stronge's unloading model between the loading and unloading process was not satisfied and they refined this imperfection. In our previous study [53], R^{*e} was solved by the revision of Strong's geometrically similar assumption. The coefficient factor was found to be dependent on the yield strain of half-space, but independent upon other parameters.

As mentioned above, the unloading behavior of post-yield impact is very complicated. The unloading models mentioned were suggested based on the curve-fitting approach by limited FE models and experimental data. Especially, in these unloading models, R^{*e} was almost calculated by the empirical assumptions. A more accurate solution using physical definition of R^{*e} by comprehensive FE analysis is still missing.

In this paper, in the basis of the studies of the residual cavity by a comprehensive FE simulation, a new revised Hertz unloading model is presented to predict the unloading behavior. The accurate solution of R^{*e} is determined by combining its physical definition with the best fitting of the radius of the residual cavity profile. The unloading model is compared with other unloading models from literature and validated numerically and experimentally. This illustrates that the new unloading model has an accurate prediction of the low-velocity unloading behavior.

2 The Unloading Impact Model

Figure 1a and b respectively show the schematics of impact under initial velocity v_0 between an elastic-perfectly plastic half-space and an elastic sphere with radius R_1 during loading phase and after fully unloading. F is the contact force and δ is the contact indentation depth, corresponding to F_m and δ_m at the end of loading phase. a and a' are the real contact radius and the truncated contact radius, respectively. The ratio δ_m/R_1 is very small and the small strain assumption is applied in this paper.

When the indentation reaches the maximum indentation δ_m , the loading phase ends and the unloading phase begins together with the backward movement of the sphere. After the separation of sphere and half-space, a residual cavity due to the plastic deformation during loading phase remains on the half-space surface. The residual cavity profile can be characterized as a residual indentation δ_r , a truncated residual contact radius a_r , and an actual residual contact radius a_c . a_r and a_c respectively correspond to a and a' during loading. The cavity profile after fully unloading was verified to be spherical having a radius R_{res} [53].

In our previous study [53], the unloading curve of $F - \delta$ is numerically verified to obey the elastic Hertz unloading law, but with a new effective contact radius R^{*e}

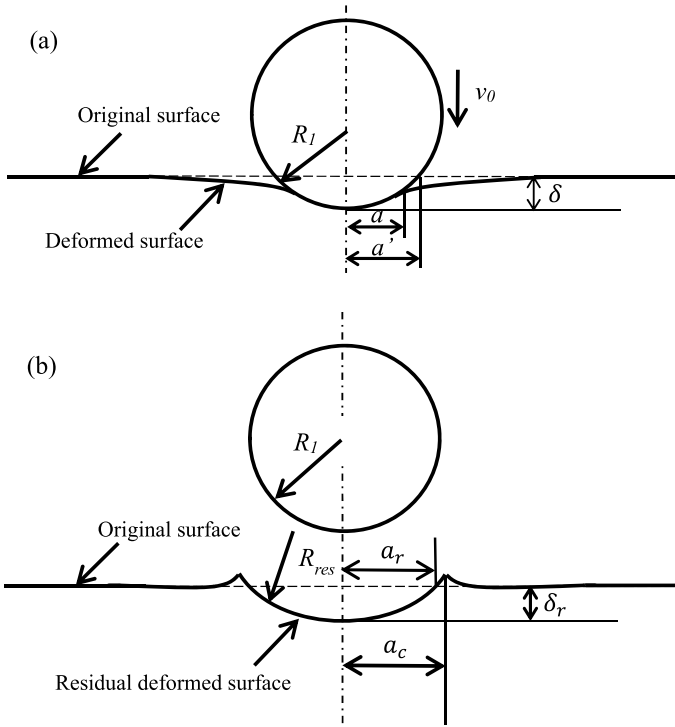


Fig. 1 Impact problem schematics: **a** loading and **b** after unloading

considering the effect of plastic deformation. Equation (1) is the expression of the Hertzian-type unloading law.

$$F = 4E^* \sqrt{R^{*e}} (\delta - \delta_r)^{1.5} / 3 \quad (1)$$

with $1/E^* = 1/E_1^* + 1/E_2^*$ and

$$E_1^* = E_1 / (1 - \nu_1^2), \quad E_2^* = E_2 / (1 - \nu_2^2)$$

where E^* is the effective elastic modulus, E_i is elastic modulus and ν_i is Poisson's ratio ($i=1$ represents sphere and $i = 2$ represents half-space). At initial yield, the contact force F_Y , contact indentation δ_Y and contact radius a_Y are usually used to normalize F , δ and a , and can be expressed as:

$$F_Y = 4E^* R^{*0.5} \delta_Y^{1.5} / 3 \quad (2)$$

where

$$\delta_Y = (3\pi/4)^2 (\vartheta_Y \sigma_Y / E^*)^2 R^*$$

$$a_Y = (\delta_Y R^*)^{0.5}$$

$$1/R^* = 1/R_1 + 1/R_2$$

where $R_2 = \infty$ for half-space, ϑ_Y is a constant defined by Johnson [15], and the yield strength σ_Y [20, 62, 63] is given by:

$$\sigma_Y = \min[\sigma_{Y1}, \sigma_{Y2}] \quad (3)$$

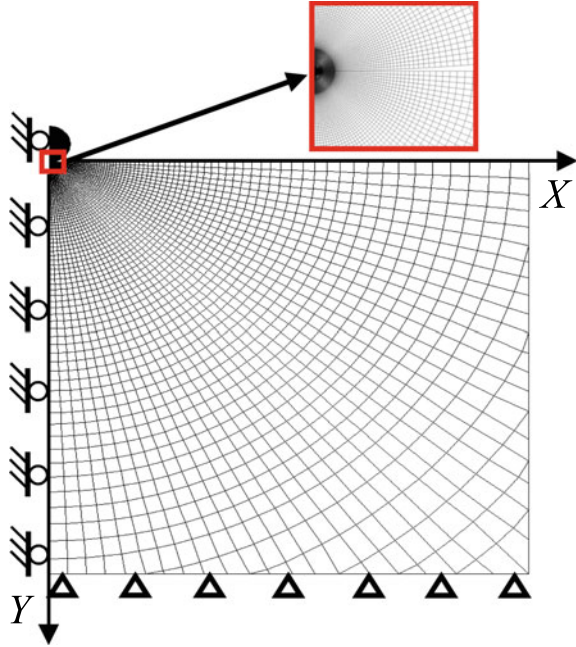
For post-yield impact, a cavity profile with a uniform radius R_{res} [17, 20, 21, 25] remains on half-space after unloading. R^{*e} is physically defined as:

$$1/R^{*e} = 1/R_1 - 1/R_{res} \quad (4)$$

3 The Finite Element Model

We employed FE method to analyze the unloading behavior of an elastic-perfectly plastic half-space impacted by an elastic sphere. In our previous study [53], a fine axisymmetric 2-D impact FE model was established as shown in Fig. 2 using the

Fig. 2 Finite element model (The enlargement shows the details of the transition of the mesh of outside the contact area)



commercial FE software LS-DYNA, which is also used in this paper. The elastic sphere is modeled by a circular with a radius $R_1 = 35$ mm. The half-space is modeled by a square with a length $L = 800$ mm. The solid 182 element type is selected for simulations. Regular and dense elements are dispersed within the contact, where the size of the element is less than $1/80$ of the contact radius. In the region away from the contact area, the mesh size regularly increases to avoid errors due to the abrupt change in mesh size. Contact pair and constrains are built based on penalty method and axisymmetric condition. Further details about the construction of the FE model can be found elsewhere [53] and in the work, the convergence and accuracy of the model have also been verified by comparing the numerical result with the analytical solution [32].

In our previous study [53], 301 FE simulations covering extensive material property, impact velocity and contact deformation regimes were performed. The results are also used in this paper. Here, for the convenience of subsequent expression, we make a brief description for the material combinations of impact cases. The unchanged material properties include the density of half-space, $\rho_2 = 7.8$ g/mm³, yield strength of sphere, $\sigma_{Y1} = 2500$ MPa and Poisson's ratio of both half-space and sphere $\nu_1 = \nu_2 = 0.3$. The other material properties are all listed in Table 1. E_2^*/σ_Y , E_1^*/E_2^* and ρ_1/ρ_2 are chosen as the normalized material parameters. The impact velocity v_0 ranges from 0.03 to 10 m/s, E_2^*/σ_Y varies from 135.36 to 1831.5, E_1^*/E_2^* varies from 0.022 to 50 and ρ_1/ρ_2 varies from 0.01 to 100. The material properties of all the FE simulations have been listed in Table 1, which can be divided

Table 1 Material properties for all FE simulations

| ID | Variable | $\frac{E_2^*}{\sigma_Y}$ | σ_Y (MPa) | $\frac{E_1^*}{E_2^*}$ | $\frac{\rho_1}{\rho_2}$ | v_0 (m/s) |
|----|-----------------|--------------------------|---------------------|-----------------------|-------------------------|----------------|
| 1 | E_1^*/E_2^* | 1831.5 | 120 | | 1.0 | 0.50 |
| | | 0.022 | 0.025 | 0.03 | 0.035 | 0.037 |
| | | 0.039 | 0.041 | 0.043 | 0.046 | 0.048 |
| | | 0.05 | 0.053 | 0.057 | 0.061 | 0.065 |
| | | 0.08 | 0.10 | 0.11 | 0.125 | 0.135 |
| | | 0.15 | 0.175 | 0.20 | 0.252 | 0.29 |
| | | 0.33 | 0.38 | 0.43 | 0.504 | 0.58 |
| | | 0.66 | 0.76 | 0.87 | | |
| 2 | E_1^*/E_2^* | 999 | 220 | | 1.0 | 0.50 |
| | | 0.065 | 0.07 | 0.075 | 0.08 | 0.087 |
| | | 0.094 | 0.10 | 0.106 | 0.112 | 0.115 |
| | | 0.12 | 0.125 | 0.135 | 0.15 | 0.175 |
| | | 0.20 | 0.252 | 0.29 | 0.33 | 0.38 |
| | | 0.43 | 0.50 | 0.58 | 0.66 | 0.76 |
| | | 0.87 | 0.94 | 1.00 | 1.20 | 1.40 |
| | | 1.80 | 2.30 | 2.80 | 3.60 | |
| 3 | ρ_1/ρ_2 | 999 | 220 | 0.08 | | 0.50 |
| | | 0.80 | 2.00 | | | |
| 4 | ρ_1/ρ_2 | 999 | 220 | 0.10 | | 0.50 |
| | | 0.01 | 0.10 | 0.50 | 5.0 | 10.0 |
| 5 | v_0 | 999 | 220 | 0.08 | 1.0 | |
| | | 0.30 | 1.00 | | | |
| 6 | v_0 | 999 | 220 | 1.0 | 1.0 | |
| | | 0.05 | 0.10 | 1.0 | 3.0 | |
| 7 | E_1^*/E_2^* | 999 | 55 | | 1.0 | 0.50 |
| | | 0.05 | 0.07 | 0.10 | 0.30 | 0.50 |
| | | 1.0 | 1.50 | 2.00 | 2.50 | |
| 8 | E_1^*/E_2^* | 637.04 | 345 | | 1.0 | 0.50 |
| | | 0.10 | 0.105 | 0.11 | 0.125 | 0.135 |
| | | 0.15 | 0.163 | 0.175 | 0.183 | 0.20 |
| | | 0.23 | 0.252 | 0.29 | 0.33 | 0.38 |
| | | 0.43 | 0.504 | 0.58 | 0.66 | 0.76 |
| | | 0.87 | 1.00 | 1.20 | 1.40 | 1.60 |
| | | 2.019 | 2.40 | 2.80 | 4.038 | |
| 9 | E_1^*/E_2^* | 637.04 | 43.125 | | 1.0 | 0.5 |

(continued)

Table 1 (continued)

| ID | Variable | $\frac{E_2^*}{\sigma_Y}$ | σ_Y (MPa) | $\frac{E_1^*}{E_2^*}$ | $\frac{\rho_1}{\rho_2}$ | v_0 (m/s) |
|----|-------------------------|--------------------------|---------------------|-----------------------|-------------------------|----------------|
| | | 1.0 | 1.30 | 1.50 | 1.70 | 2.0 |
| | | 3.0 | 5.0 | 10 | 20 | |
| 10 | | 637.04 | 34.5 | 20.0 | 1.0 | 0.50 |
| 11 | E_1^*/E_2^* | 399.60 | 550 | | 1.0 | 0.50 |
| | | 0.175 | 0.20 | 0.252 | 0.29 | 0.33 |
| | | 0.38 | 0.43 | 0.504 | 0.58 | 0.66 |
| | | 0.76 | 0.87 | 1.00 | 1.20 | 1.40 |
| | | 1.60 | 1.80 | 2.019 | 2.40 | 2.80 |
| | | 3.60 | | | | |
| 12 | $\frac{\rho_1}{\rho_2}$ | 399.60 | 550 | 0.504 | | 0.50 |
| | | 0.30 | 0.50 | | | |
| 13 | E_1^*/E_2^* | 399.60 | 55.0 | | 1.0 | 0.50 |
| | | 0.50 | 1.0 | 1.50 | 2.0 | 3.0 |
| | | 5.0 | 20.0 | | | |
| 14 | | 399.60 | 550 | 1.00 | 20 | 0.50 |
| 15 | $\frac{\rho_1}{\rho_2}$ | 399.60 | 550 | 5.20 | | 0.50 |
| | | 20.0 | 30.0 | 50.0 | | |
| 16 | E_1^*/E_2^* | 399.60 | 5.50 | | 1.0 | 0.50 |
| | | 1.0 | 2.0 | 3.0 | 5.0 | 10.0 |
| | | 20.0 | | | | |
| 17 | v_0 | 399.60 | 550 | 0.504 | 1.0 | |
| | | 0.30 | 1.0 | | | |
| 18 | v_0 | 399.60 | 550 | 5.20 | 1.0 | |
| | | 1.0 | 3.0 | | | |
| 19 | E_1^*/E_2^* | 293.04 | 750 | | 1.0 | 0.50 |
| | | 0.252 | 0.29 | 0.33 | 0.38 | 0.43 |
| | | 0.504 | 0.58 | 0.66 | 0.76 | 0.87 |
| | | 1.00 | 1.20 | 1.40 | 1.60 | 1.80 |
| | | 2.019 | 2.40 | 2.80 | 3.20 | 3.60 |
| | | 4.038 | | | | |
| 20 | E_1^*/E_2^* | 293.04 | 75.0 | | 1.0 | 0.50 |
| | | 1.0 | 1.5 | 3.0 | 5.0 | |
| 21 | E_1^*/E_2^* | 293.04 | 7.5 | | 1.0 | 0.50 |
| | | 1.0 | 2.0 | 5.0 | 15 | 20 |
| 22 | σ_Y | 293.04 | | 20.0 | 1.0 | 0.50 |

(continued)

Table 1 (continued)

| | | | | | | |
|----|-----------------|--------|-------|-------|------|-------|
| 18 | v_0 | 399.60 | 550 | 5.20 | 1.0 | |
| | | 1.0 | 3.0 | | | |
| | | 1.875 | 3.75 | | | |
| 23 | E_1^*/E_2^* | 231.35 | 950 | | 1.0 | 0.50 |
| | | 0.43 | 0.504 | 0.58 | 0.66 | 0.76 |
| | | 0.87 | 1.00 | 1.20 | 1.40 | 1.60 |
| | | 1.80 | 2.019 | 2.40 | 2.80 | 3.20 |
| | | 3.60 | | | | |
| 24 | E_1^*/E_2^* | 231.35 | 95.0 | | 1.0 | 0.50 |
| | | 1.0 | 1.50 | 2.0 | 3.0 | 5.0 |
| 25 | E_1^*/E_2^* | 231.35 | 9.5 | | 1.0 | 0.50 |
| | | 1.0 | 2.0 | 5.0 | 10 | 20 |
| 26 | ρ_1/ρ_2 | 231.35 | 9.5 | 20 | | 0.5 |
| | | 2.0 | 3.0 | 5.0 | 10 | 15 |
| 27 | E_1^*/E_2^* | 175.82 | 1250 | | 1.0 | 0.50 |
| | | 0.76 | 0.87 | 1.00 | 1.20 | 1.40 |
| | | 1.60 | 1.80 | 2.019 | 2.40 | 2.80 |
| | | 3.20 | 3.60 | 4.038 | | |
| 28 | E_1^*/E_2^* | 175.82 | 125 | | 1.0 | 0.50 |
| | | 1.0 | 1.50 | 2.0 | 3.0 | 5.0 |
| 29 | E_1^*/E_2^* | 175.82 | 12.5 | | 1.0 | 0.50 |
| | | 1.0 | 1.20 | 2.0 | 5.0 | 10.0 |
| | | 20.0 | | | | |
| 30 | σ_Y | 175.82 | | 50 | 1.0 | 0.50 |
| | | 3.15 | 6.25 | | | |
| 31 | σ_Y | 175.82 | | 200 | 1.0 | 0.50 |
| | | 0.3125 | 0.625 | 1.25 | | |
| 32 | E_1^*/E_2^* | 135.36 | 1600 | | 1.0 | 0.50 |
| | | 1.20 | 1.40 | 1.60 | 1.80 | 2.019 |
| | | 2.40 | 2.80 | 3.20 | 3.60 | 4.038 |
| | | 5.20 | | | | |
| 33 | ρ_1/ρ_2 | 135.36 | 1600 | 4.038 | | 0.50 |
| | | 0.20 | 0.50 | 2.0 | 3.0 | 5.0 |
| | | 10 | 12 | 20 | 40 | 100 |
| 34 | v_0 | 135.36 | 1600 | 1.0 | 1.0 | |
| | | 3.0 | 5.0 | | | |
| 35 | v_0 | 135.36 | 1600 | 2.40 | 1.0 | |

(continued)

Table 1 (continued)

| | | | | | | |
|----|---------------|--------|------|------|------|------|
| 18 | v_0 | 399.60 | 550 | 5.20 | 1.0 | |
| | | 1.0 | 3.0 | | | |
| | | 0.4 | 10 | | | |
| 36 | E_1^*/E_2^* | 135.36 | 16 | | 1.0 | 0.50 |
| | | 1.0 | 2.0 | 10 | 50 | |
| 37 | σ_Y | 135.36 | | 50 | 1.0 | 0.50 |
| | | 4.0 | 8.0 | | | |
| 38 | σ_Y | 135.36 | | 200 | 1.0 | 0.50 |
| | | 0.40 | 0.60 | 0.80 | 1.60 | |
| 39 | v_0 | 135.36 | 0.80 | 200 | 1.0 | 0.50 |
| | | 1.20 | 1.50 | | | |

into 39 impact cases (Impact ID). The detailed introductions of these impact cases can be found elsewhere [53]. Notice that, in later sections, the cited FE simulation is marked, for example, for impact case 1 with $E_1^*/E_2^* = 0.022$, as IC-1 (0.022). The value in the bracket is the variable parameter.

4 Numerical Results and Discussion

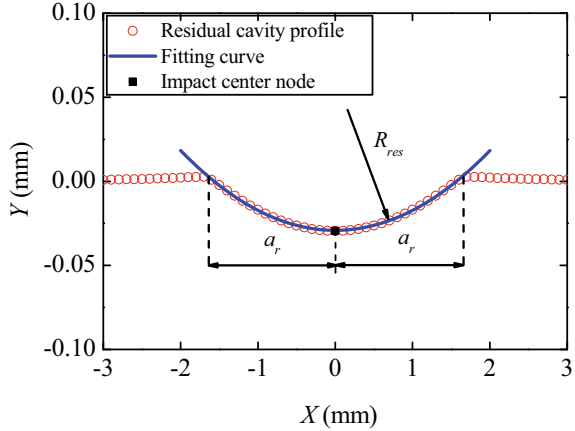
A new revised Hertz unloading model is provided by presenting an accurate solution of R^{*e} in this section. The accurate solution of R^{*e} is determined by combining its physical definition with the best fitting of R_{res} .

4.1 Radius of Cavity Profile

In this section, the method of measuring R_{res} is provided. The unloading curve of force-indentation has been verified to follow Hertz unloading law with a new R^{*e} , which is a crucial parameter to be determined. In the existing unloading models, R^{*e} was almost calculated by the empirical assumptions. The residual cavity profile has been validated to be spherical of a radius R_{res} [53].

To evaluate the accuracy of R_{res} , the curve fitting method is used in the basis of the FE data. The nodes of summit of the deformed half-space after complete unloading are extracted and the nodes within the scope of the truncated residual contact radius a_r are used to fit by a standard equation of circle, for example, as shown in Fig. 3 for IC-11 (2.019). Hence, R_{res} can be evaluated. And the cavity profiles for all FE simulations are measured to reveal the character of the R_{res} of the cavity profile after post-yield impact.

Fig. 3 Method to measure R_{res}



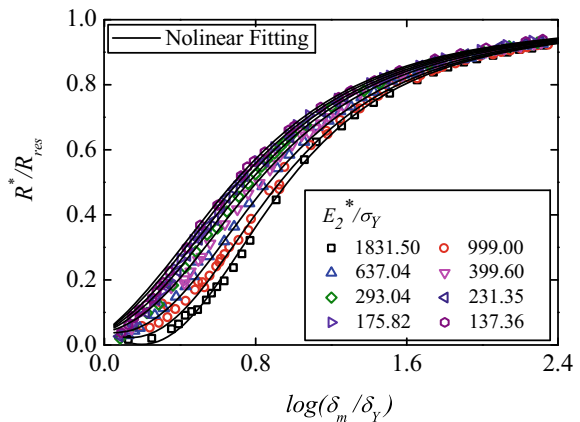
4.2 Determination of R_{res}

The residual radius of contact curvature R^{*e} can be derived from Eq. (4) as follows:

$$R^{*e} = R_1 R_{res} / (R_{res} - R_1) \tag{5}$$

where R^{*e} can be calculated from the given values of R_{res} and R_1 . The radii of residual cavity R_{res} of all impact simulations listed in Table 1 are extracted using the method provided in Sect. 4.1. According to the FE results, an analytical expression of the residual contact radius R_{res} is fitted. To eliminate the influence of the radius size of elastic sphere, R_{res} is normalized by the effective radius R^* to be R^*/R_{res} . Figure 4 plots the variations of R^*/R_{res} with δ_m/δ_Y for all the FE simulations. In Fig. 4, the curves of R^*/R_{res} versus $\log(\delta_m/\delta_Y)$ for the same E_2^*/σ_Y coalesce to

Fig. 4 Relationship between the residual contact radius of curvature and maximum indentation



a single master curve, which illustrates that the relationship R^*/R_{res} with δ_m/δ_Y is dependent on E_2^*/σ_Y .

Figure 4 shows that R^*/R_{res} increases monotonically with δ_m/δ_Y . It is found that R^*/R_{res} strongly depends on E_2^*/σ_Y , while it does not depend upon other parameters, such as ρ_1/ρ_2 and E_1^*/E_2^* . Hence, R^*/R_{res} can be regard as a function of merely these two parameters. The curves of R^*/R_{res} versus $\lg(\delta_m/\delta_Y)$ is nonlinear, which is different to that reported by Etsion et al. [46]. Based on the current numerical results covering a wide range of δ_m/δ_Y up to 220, a best nonlinear curve fit is presented by the solid lines in Fig. 4, and by the following empirical expressions:

$$\begin{aligned} R^*/R_{res} = & 1 - 35/(36.42522 + A \log(\delta_m/\delta_Y)) \\ & + 26.5(\log(\delta_m/\delta_Y))^2 + B(\log(\delta_m/\delta_Y))^3 \end{aligned} \quad (6)$$

$$A = -14.07344 + 41.90465 \exp(-E_2^*/\sigma_Y/493.25814)$$

$$B = 23.35 + 9.451 \exp(-E_2^*/\sigma_Y/172.511)$$

4.3 Unloading Model

The start of unloading phase is at the end of loading phase, when the contact force and indentation are both maximum. The unloading process is assumed to be elastic and the contact force-indentation relationship follows the Hertz theory. A new revised Hertz unloading model is suggested here:

$$F(\delta) = \begin{cases} \frac{4}{3} E^* (R^*)^{\frac{1}{2}} \delta^{\frac{3}{2}}, & \text{if } \delta_m < \delta_Y \\ \frac{4}{3} E^* (R^{*e})^{\frac{1}{2}} (\delta - \delta_r)^{\frac{3}{2}}, & \text{if } \delta_m > \delta_Y \end{cases} \quad (7)$$

where R^{*e} is determined by combining Eq. (5) and the empirical relation Eq. (6), i.e.:

$$R^{*e} = R^* (36.42522 + A \lg(\delta_m/\delta_Y) + 26.5(\log(\delta_m/\delta_Y))^2 + B(\log(\delta_m/\delta_Y))^3) / 35 \quad (8)$$

R^{*e} can be calculated by Eq. (8) for post-yield loading conditions including both the elastic-plastic and fully plastic deformations, which is quite different from the unloading models [20, 25]. By enforcing the continuity between the loading and unloading phases, δ_r , can be derived theoretically as:

$$\delta_r = \delta_m - (3F_m / (4E^* \sqrt{R^{*e}}))^{2/3} \quad (9)$$

The unloading contact force-indentation relationship can be calculated from F_m and δ_m .

Because the residual cavity profile is a perfect spherical surface with a uniform radius R_{res} , the theoretical a_r can be determined according to the geometrical relation shown in Fig. 1 and written as:

$$a_r = (2R_{res}\delta_r - \delta_r^2)^{\frac{1}{2}} \quad (10)$$

where R_{res} can be calculated by the empirical relations Eq. (6). In the study of Chen et al. [53], the difference between a_r and a_c caused by the pile-up deformation is considered and the relative difference is expressed as:

$$(a_c - a_r)/a_c = 997.140355 - 996.893555 * B_1 - 0.171136 * B_2 \quad (11)$$

$$B_1 = 1 - \exp(-\delta_m/\delta_Y/0.13123), B_2 = 1 - \exp(-\delta_m/\delta_Y/10.30736)$$

Combining Eq. (10) with Eq. (11), a_c can be calculated.

In summary, combining the fitting curves (6) for R_{res} and the empirical relation of $(a_c - a_r)/a_c$, the unloading law (7) gives the simple analytical solutions for the unloading contact force-indentation relationship, R^{*e} , R_{res} , δ_r , a_r and a_c , for a given impact case with F_m and δ_m .

5 Validations

In the new revised Hertz unloading model, the key parameter is R^{*e} fitted only in the basis of the FE results of R_{res} . To verify this unloading model numerically for more extensively materials, the FE unloading data such as unloading curve and δ_r can be used for comparison. Here, the new unloading model is validated by numerical and experimental data. Other ten well-known unloading models with F_m and δ_m measured from the present FE data are used for comparisons with the new unloading model. The numerical results are provided by some FE simulations listed in Table 1. The experimental results are provided by the published references [64, 65].

5.1 Numerical Verification

The ten existing unloading models are the Strong [21], LEPM [17], MYC [23], CYM [35], MJG [55], Thornton [18], JG [54], KE [46], KK [39] and DW [59] models.

Figure 5 shows the unloading curves of the impact simulations, IC-1 (0.039), IC-37 (4.0) and IC-16 (20), and the solutions by the new unloading models and the ten unloading models. The three FE simulations cover δ_m/δ_Y from 2.67 to 205.29 and different values of E_2^*/σ_Y . As it can be seen, except for the DW model, other unloading models can ensure the continuity at the transition between loading and unloading. As it can be seen from Fig. 5, the new unloading model can predict the best solutions compared with the FE unloading results and more accurate than other models. This suggests that the new unloading model can predict the unloading curve accurately for a wide range of deformation regimes material properties.

Figure 6a–c show the relations between δ_r/δ_Y and δ_m/δ_Y of the FE data of the three categories of impacts of CNo. 1, 4 and 8, together with the solutions by the new unloading models and the ten unloading models, respectively. All the predictions by the models have the same tendency. As it can be seen, δ_r/δ_Y predicted by the new unloading model agrees well with FE result for different material properties, especially for larger δ_m/δ_Y . However, other models cannot account for the dependence of δ_r/δ_Y on material properties.

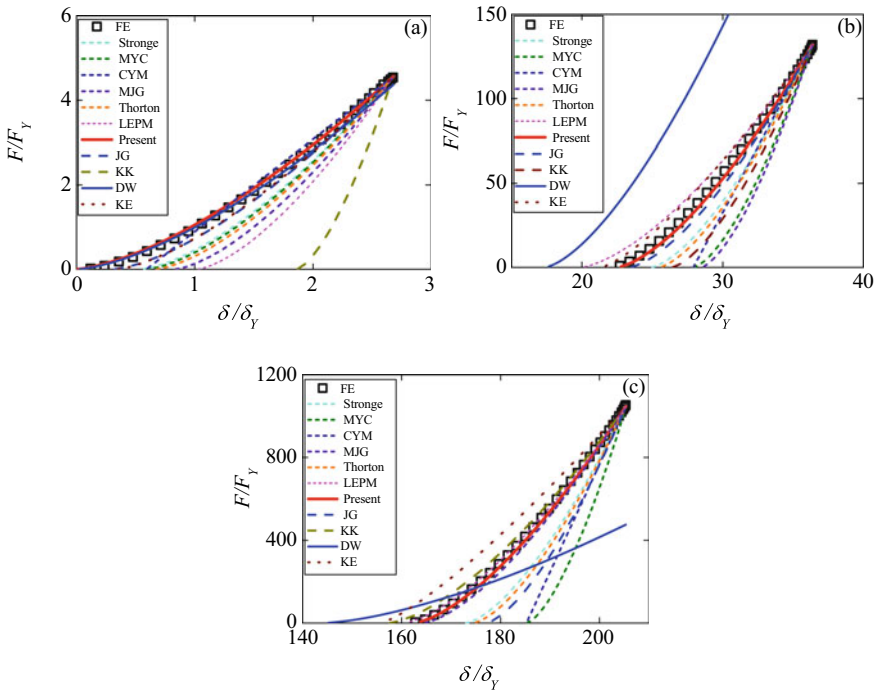


Fig. 5 Unloading curves: **a** IC-1 (0.039), **b** IC-37 (4.0) and **c** IC-16 (20)

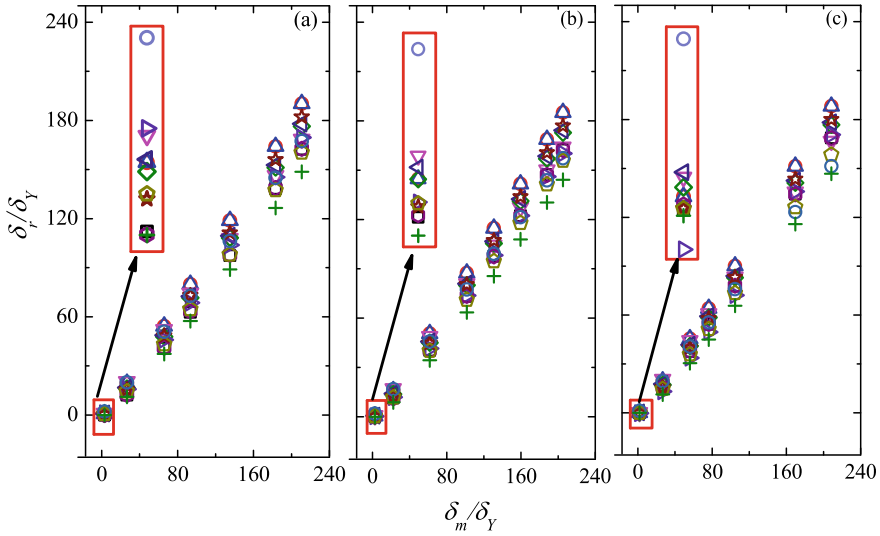


Fig. 6 δ_r/δ_Y of FE (\square), MYC (\circ), CYM (\triangle), MJG (∇), Stronge (\diamond), Thornton (\triangleleft), LEPM (\triangleright), JG (\star), KE (\pentagon), KK (\odot), DW (+), Present (\oplus) for representative impact simulations of three categories of impacts: **a** CNo. 1, **b** CNo. 4 and **c** CNo. 8

5.2 Experimental Validations

Some experimental studies of impact behavior of elastoplastic spheres have been published in the literature. The similar experimental and FE data with the validations in our previous study [53] are used to make comparisons with the solutions by the present unloading model. The experimental data of three types of impact together with the corresponding model results between two elastic-plastic spheres reported in the references [64, 65] are extracted. The material properties of the elastic-plastic spheres are listed in Table 2. The three types of impact include: (1) impacts between identical diameter (12.7 mm) Brass sphere and Aluminum sphere; (2) impacts between two identical material (Brass) spheres with the different diameter combinations as listed in Table 3; (3) impacts between two identical material (Aluminum) and identical diameter (12.7 mm) spheres with the 12.7 mm under the different impact velocity as listed in Table 4.

Table 2 Material properties

| Material | Density (kg/m ³) | Elastic modulus (GPa) | Poisson's ratio | Yield stress (MPa) |
|-----------------|------------------------------|-----------------------|-----------------|--------------------|
| Brass alloy 260 | 8500 | 115 | 0.3 | 550 |
| Al alloy 2017 | 2700 | 70 | 0.3 | 500 |

Table 3 Size combinations for the second impact type

| Material | Size combinations (mm) |
|-----------------|------------------------|
| Brass alloy 260 | 12.7–12.7 |
| | 12.7–9.53 |
| | 12.7–6.35 |
| | 9.53–9.53 |
| | 9.53–6.35 |
| | 9.53–4.76 |

Table 4 Impact velocities for the third impact type

| Material | Impact velocity (m/s) |
|---------------|-----------------------|
| Al alloy 2017 | 1.48 |
| | 3.15 |
| | 3.36 |
| | 4.99 |
| | 5.56 |
| | 5.96 |

The loading and unloading contact force-indentation curves together with the corresponding FE results of the first type impact mentioned above are shown in Fig. 7. For comparison, the prediction of the new unloading model is obtained by using the measured maximum contact force and indentation as shown in Fig. 7. The comparison shows that the prediction agrees well with the experimental and numerical results.

Other six experimental force-indentation curves and the corresponding FE results of the second type impact were also measured in reference [64]. δ_r is calculated by the present unloading model by using the measured results of δ_m and F_m . The

Fig. 7 Comparison of the unloading curve

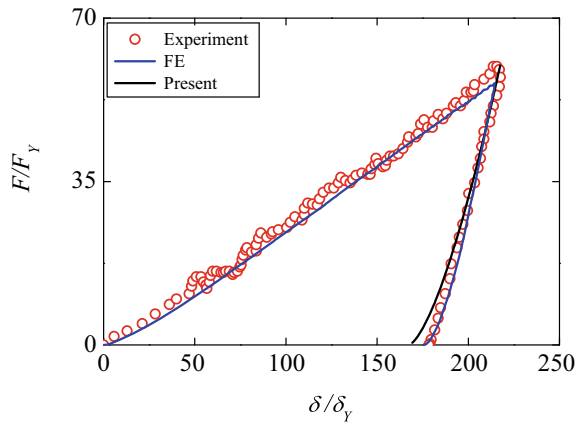
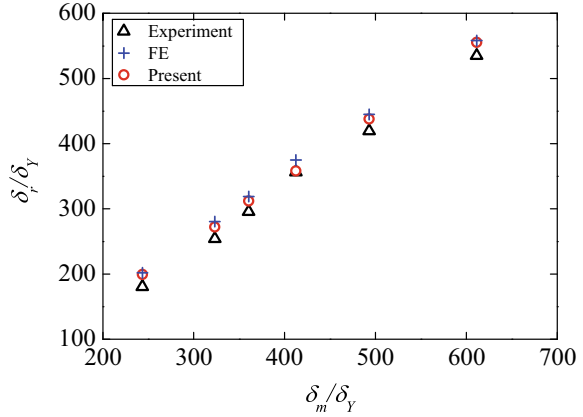


Fig. 8 Comparison of the residual indentation

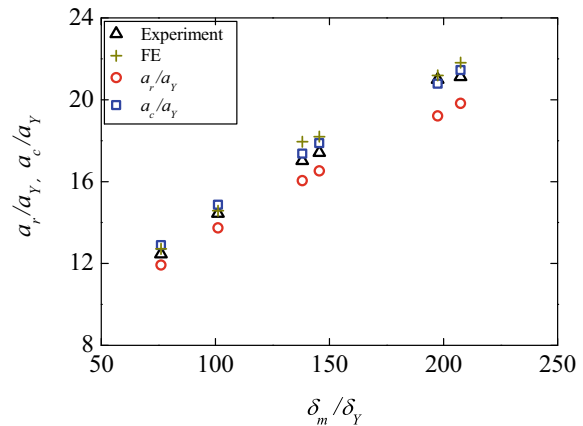


maximum error of the theoretical prediction compared with the experimental results is 9.44% as shown in Fig. 8. Compared with the FE results, the maximum prediction error is only 4.60%.

Wang et al. [65] provided another elastic-plastic impact experimental (the third type impact) measurement of the residual contact radius. a_r and a_c can be calculated by the new unloading geometry by using the measured results of δ_m and F_m . Because the material and geometry size for both two beads are identical, the two beads have the same residual indentation. Hence, $\delta_r/2$ should be used in the geometry relation (12) to predict a_r . Figure 9 shows the experimental results together with the corresponding FE results and the theoretical solutions. As it can be seen, the maximum error of a_r between the predictions and experimental results is 8.46%, and as for a_c , the maximum error is 3.54%.

As shown from the comparisons above, the accuracy and applicability of the new revised Hertz unloading model are validated by FE simulations and existing

Fig. 9 Comparison of the residual contact radius



experiments. It is suggested that the new Hertz unloading model can be applied to accurately predicting the unloading force-indentation relationship, a_r , a_c and δ_r .

6 Conclusion

The unloading process of an elastic sphere impacting an elastic-perfectly plastic half-space under low-velocity is deeply studied in the light of FE method. The unloading of FE simulations is designed to cover extensive impact velocities and material properties. In the basis of the FE analyses, the normalized parameter R^*/R_{res} is found to be dependent on E_2^*/σ_Y and independent of ρ_1/ρ_2 and E_1^*/E_2^* . A new revised Hertz unloading model is suggested to predict the unloading parameters, such as force-indentation relationship, R^{*e} , R_{res} , δ_r , a_r and a_c . The determination of R^{*e} is derived from the physical definition combining with the best fitting of the numerically FE data. The new unloading model is verified by FE simulations and validated by existing experiments. Comparisons show that the new unloading model is coincident well with the FE and experimental data.

References

1. Arakere NK (2009) A review of rolling contact fatigue. *J Tribol* 131(4):041403
2. Li Y et al (2020) Dynamic response of spiral groove liquid film seal to impact conditions. *Tribol Int* 141
3. Li Y et al (2019) Dynamic response of spiral groove liquid film seal to impact conditions. 141:105865
4. Brake MR (2014) The role of epistemic uncertainty of contact models in the design and optimization of mechanical systems with aleatoric uncertainty. *Nonlinear Dyn* 77(3):899–922
5. Arab AZE-A et al (2020) Finite-element analysis of a lateral femoro-tibial impact on the total knee arthroplasty. *Comput Meth Progr Biomed* 192(105446)
6. Ding Y et al (2018) Spherical indentation on biological films with surface energy. *J Phys D* 51(29):295401
7. Lin T et al (2007) A finite element method for 3D static and dynamic contact/impact analysis of gear drives. *Comput Meth Appl Mech Eng* 196(9–12):1716–1728
8. Wang Y et al (2018) Optimal design of gear teeth modification with the minimum value of meshing-in impact. *J Comput Theor Nanosci* 15(1):230–236
9. Deng X et al (2020) A combined experimental and computational study of lubrication mechanism of high precision reducer adopting a worm gear drive with complicated space surface contact. 146(5–6):106261
10. Wei L et al (2020) Investigation on the influence of spalling defects on the dynamic performance of planetary gear sets with sliding friction. 154
11. Yao T-Q et al (2016) Dynamics analysis on ball bearing-mechanism with clearance and impact of cage. *J Aerosp Power* 7:23
12. Branch NA et al (2013) Critical stresses and strains at the spall edge of a case hardened bearing due to ball impact. *Int J Fatigue* 47:268–278
13. Yu Q et al (2004) The examination of the drop impact test method, intersociety conference on thermal and thermomechanical phenomena in electronic systems. 336–342

14. Lee C, Wang C (2019) Drop impact analysis of AMOLED display with buffer designs by using dynamic finite element simulation. In: International workshop on active matrix flatpanel displays and devices
15. Johnson (1987) Contact mechanics
16. Goldsmith W, Frasier JT (1961) Impact: the theory and physical behavior of colliding solids. *J Appl Mech* 28(4):639
17. Dong X et al (2018) Local contact behavior between elastic and elastic-plastic bodies. *Int J Solids Struct* 150:22–39
18. Thornton, (1997) Coefficient of restitution for collinear collisions of elastic perfectly plastic spheres. *J Appl Mech* 64:383–386
19. Brake MRW (2015) An analytical elastic plastic contact model with strain hardening and frictional effects for normal and oblique impacts. *Int J Solids Struct* 62:104–123
20. Brake MR (2012) An analytical elastic-perfectly plastic contact model. *Int J Solids Struct* 49(22):3129–3141
21. Stronge WJ (2000) Impact mechanics. Cambridge University Press
22. Vu-Quoc L et al (2000) A normal force-displacement model for contacting spheres accounting for plastic deformation: force-driven formulation. *J Appl Mech* 67(2):363–371
23. Majeed MA et al (2012) Elastoplastic contact/impact of rigidly supported composites. *Compos B* 43(3):1244–1251
24. Jackson R et al (2005) A finite element study of the residual stress and deformation in hemispherical contacts. *J Tribol* 127(3):484–493
25. Ma D, Liu C (2015) Contact law and coefficient of restitution in elastoplastic spheres. *J Appl Mech* 82(12)
26. Kogut L, Etsion I (2002) Elastic-plastic contact analysis of a sphere and a rigid flat. *J Appl Mech* 69(5):657–662
27. Big-Alabo A et al (2015) Contact model for elastoplastic analysis of half-space indentation by a spherical impactor. *Comput Struct* 151:20–29
28. Bartier O et al (2010) Theoretical and experimental analysis of contact radius for spherical indentation. *Mech Mater* 42(6):640–656
29. Carter CB et al (2015) Superhard silicon nanospheres. *J Mech Phys Solids* 51(6):979–992
30. Majumder S et al (2001) Study of contacts in an electrostatically actuated microswitch. In: Proceedings of the forty-fourth IEEE holm conference on electrical contacts, 1998, 2001, pp 127–132
31. Kadin Y et al (2006) Unloading an elastic-plastic contact of rough surfaces. *J Mech Phys Solids* 54(12):2652–2674
32. Hertz H (1882) Ueber die Berührung fester elastischer Körper. : Journal für die reine und angewandte Mathematik (Crelle's Journal). *Journal Für Die Reine Und Angewandte Mathematik*
33. Apetre NA et al (2006) Low-velocity impact response of sandwich beams with functionally graded core. *Int J Solids Struct* 43(9):2479–2496
34. Managuli V et al (2011) Low velocity impact analysis of composite laminates using linearized contact law. In: International conference on advances in mechanical engineering
35. Yigit A (2013) Low-velocity impact response of structures with local plastic deformation: characterization and scaling. *J Comput Nonlinear Dyn* 8(1):149–156
36. Li LY et al (2002) A theoretical model for the contact of elastoplastic bodies. *Proc Inst Mech Eng Part C* 216(4):421–431
37. Zhang L et al (2018) Transient impact response analysis of an elastic-plastic beam. *Appl Math Model* 55:616–636
38. Jin T et al (2019) Numerical-analytical model for transient dynamics of elastic-plastic plate under eccentric low-velocity impact. *Appl Math Model* 70:490–511
39. Kogut L, Komvopoulos K (2004) Analysis of the spherical indentation cycle for elastic-perfectly plastic solids. *J Mater Res* 19(12):3641–3653
40. Jackson RL, Green I (2005) A finite element study of elasto-plastic hemispherical contact against a rigid flat. *J Tribol* 127(2):343–354

41. Tabor D (1948) A simple theory of static and dynamic hardness. *Proc R Soc A* 192(1029):247–274
42. Kral E et al (1993) Elastic-plastic finite element analysis of repeated indentation of a half-space by a rigid sphere. *J Appl Mech* 60(4):829–841
43. Ye N, Komvopoulos K (2003) Effect of residual stress in surface layer on contact deformation of elastic-plastic layered media. *J Tribol* 125(4):692–699
44. Kral E et al (1995) Finite element analysis of repeated indentation of an elastic-plastic layered medium by a rigid sphere, Part II: Subsurface results. *J Appl Mech* 62(1):29–42
45. Kral ER et al (1995) Finite element analysis of repeated indentation of an elastic-plastic layered medium by a rigid sphere, part I: surface results. *J Appl Mech* 62(1):20–28
46. Etsion I et al (2005) Unloading of an elastic-plastic loaded spherical contact. *Int J Solids Struct* 42(13):3716–3729
47. Ovcharenko A et al (2007) In situ investigation of the contact area in elastic-plastic spherical contact during loading-unloading. *Tribol Lett* 25(2):153–160
48. Li LY, Gu JZ (2009) An analytical solution for the unloading in spherical indentation of elastic-plastic solids. *Int J Eng Sci* 47(3):452–462
49. Yan S, Li L (2003) Finite element analysis of cyclic indentation of an elastic-perfectly plastic half-space by a rigid sphere. *Proc Inst Mech Eng C J Mech Eng Sci* 217(5):505–514
50. Majeed MA et al (2011) Modeling and analysis of elastoplastic impacts on supported composites, key engineering materials. *Trans Tech Publications*, pp 367–372
51. Christoforou AP et al (2013) Characterization and scaling of low velocity impact response of structures with local plastic deformation: implications for design. In: *ASME 2012 International design engineering technical conferences and computers and information in engineering conference*, American Society of Mechanical Engineers Digital Collection, pp 125–135
52. Ibrahim AH, Yigit AS (2013) Finite element modeling and analysis of low velocity impact on composite structures subject to progressive damage and delamination. In: *ASME 2012 International mechanical engineering congress and exposition*. American Society of Mechanical Engineers Digital Collection, pp 719–730
53. Chen C et al (2020) Unloading behavior of low velocity impact between elastic and elastic-plastic bodies. *Tribol Int* 151C
54. Jackson RL et al (2010) Predicting the coefficient of restitution of impacting elastic-perfectly plastic spheres. *Nonlinear Dyn* 60(3):217–229
55. Ghaednia H et al (2015) Predicting the permanent deformation after the impact of a rod with a flat surface. *J Tribol* 137(1):011403
56. Thornton C, Ning Z (1994) Oblique impact of elasto-plastic spheres. In: *Proceedings of the first international particle technology forum*. AIChE Publications, pp 14–19
57. Vu-Quoc L, Zhang X (1999) An elastoplastic contact force-displacement model in the normal direction: displacement-driven version. *Proc Math Phys Eng Sci* 455(1991):4013–4044
58. Wang H et al (2020) The correlation of theoretical contact models for normal elastic-plastic impacts. *Int J Solids Struct* 182–183:15–33
59. Du Y, Wang S (2009) Energy dissipation in normal elastoplastic impact between two spheres. *J Appl Mech* 76(6):061010
60. Jackson RL, I.G., D.B. Marghitu, (2010) Predicting the coefficient of restitution of impacting elastic-perfectly plastic spheres. *Nonlinear Dyn* 60(3):217–229
61. Stevens A, Hrenya C (2005) Comparison of soft-sphere models to measurements of collision properties during normal impacts. *Powder Technol* 154(2–3):99–109
62. Martin CL, Bouvard D (2004) Isostatic compaction of bimodal powder mixtures and composites. *Int J Mech Sci* 46(6):907–927
63. Larsson PL, Olsson E (2015) A numerical study of the mechanical behavior at contact between particles of dissimilar elastic-ideally plastic materials. *J Phys Chem Solids* 77:92–100
64. Wang E et al (2013) An experimental study of the dynamic elasto-plastic contact behavior of dimer metallic granules. *Exp Mech* 53(5):883–892
65. Wang E et al (2013) An experimental study of the dynamic elasto-plastic contact behavior of metallic granules. *J Appl Mech* 80(2):021009

Fracture Micro Mechanism of Cryogenically Treated Ledeburitic Tool Steel



Peter Jurčí , Jana Ptačínová , and Ivo Dlouhý 

Abstract Fracture micro mechanism of cryogenically treated Cr-V ledeburitic tool steel was studied on fracture toughness testing specimens, by using the scanning electron microscopy and microanalysis. Experimental steel has been processed at different combinations of cryogenic temperatures (from the range -75 to -269 °C) and tempering regimes, producing different microstructures (martensite, retained austenite, carbides), hardness- and fracture toughness values (from the ranges 700–1000 HV and 13 – 20 MPa \times m^{1/2}, respectively). Conventionally quenched the same steel was considered as a reference. Generally, the obtained fracture surfaces manifest combined low-energetic ductile/cleavage crack propagation mode. The low-energetic ductile mode is associated with the presence of small globular carbides (size < 0.3 μ m) that are produced by cryogenic treatments. On the other hand, cleavage mode is more pronounced with increased matrix stiffness, which is caused by the precipitation of nano-scaled transient carbides within the martensite. Also, differences in role of crack propagation between various carbides were determined. These differences are caused by crystallography of these phases as well as by their size. While small globular carbides (cementite) and dominant amount of the eutectic carbides (cubic MC-phase) assist more probably (by 50–60%) in ductile micro mechanism the coarser secondary particles (hexagonal M₇C₃-phase) are much more prone to cleavage cracking. This tendency increases with decreasing steel hardness since the matrix becomes more plastic, and the carbides cannot deform together with the matrix as they are much more brittle.

P. Jurčí (✉)

Department of Materials Science, Faculty of Materials Science and Technology in Trnava, Slovak University of Technology, Paulínská 16, 917 24 Trnava, Slovakia
e-mail: p.jurci@seznam.cz

J. Ptačínová

Department of Materials Science, Slovak University, Paulínská 16, 917 24 Trnava, Slovakia

I. Dlouhý

Institute of Physics of Materials, CEITEC-IPM, Academy of Sciences of the Czech Republic, Žitkova 22, 61662 Brno, Czech Republic

Keywords Cryogenic treatment · Ledeburitic steel · Microstructure · Fracture toughness · Fracture micro mechanism

1 Introduction

Cold work tools manufacturers in high-developed countries are continuously enhancing their productivity in order to be competitive and increase their market share and profits. Therefore, the companies are forced to minimize their production costs and achieve more efficient processes by means of improvement in labour productivity, increasing the life time of tools, optimizing the use of available devices, and by developing of new production or treatment routes suitable for existing materials.

Mechanical properties of steels are governed by their microstructure, at grain-and/or at nano-scale levels. Therefore, microstructure plays a crucial role in the service life of tools during the industrial processes. Heat treatment is mostly used as the final operation during which the tools achieve the final microstructure and thereby the mechanical properties. In cold working the tools and dies are made up of chromium (Cr-) or chromium-vanadium (Cr-V) ledeburitic steels. These steels have high hardness, good strength, and excellent wear resistance. On the other hand, they often suffer from insufficient toughness, due to presence of hard and brittle carbides in their microstructure. Also, too high amounts of retained austenite that remain in microstructures of conventionally heat treated ledeburitic steels are undesirable as this phase is soft, and also amenable to transform to brittle martensite during the future service operating conditions. Conventional heat treatment (austenitizing followed by room temperature quenching) is unable to evoke the conversion the austenite into martensite in sufficiently high extent. This is because the characteristic martensite finish temperature of these materials lies far below the zero Celsius temperature. Hence, cryogenic (or sub-zero treatments, SZTs) are done in many heat treatments schedules to convert more austenite into the martensite.

This kind of treatment was introduced into practice in the first half of the twentieth century, and nowadays becomes a great industrial importance in high developed countries like Japan, North America and Europe. Significant increase in wear performance [1–5], better dimensional stability [6, 7], slightly improved corrosion resistance [8] and enhanced fatigue properties [9, 10] are the main benefits of the application of SZTs. However, the effect of SZTs on toughness of high-alloyed tool steels is unclear to date. Some authors reported increased toughness of sub-zero treated tool steels while others claimed less or more significant worsening of this property. For the most commonly used AISI D2 steel (manufactured by classical ingot metallurgy) Collins and Dormer [11], Wierszyllowski [12] and Das et al. [13] reported considerable reduction in toughness while only Rhyim [14] pointed out that the toughness may be also improved, when high-temperature tempering is followed the SZTs. Similar results were published also by Kumar [15], for AISI D3 steel. Conversely, an improvement in toughness was found for the AISI H13 hot work

tool steel [16, 17] and almost no effect or rather slightly positive effect of cryogenic treatment on toughness of PM Vanadis 6 steel has been recorded [18–22].

There is significant lack of detailed fractographical analysis of toughness specimens made of ledeburitic steels in scientific literature. Only Das et al. [13] and the group of investigators Jurčič et al. [18–21] performed careful investigations focused to how the fracture propagates under circumstances of fracture toughness testing. These authors found that the fracture surfaces appear flat and shiny at low magnification of scanning electron microscopes. This appearance is typical for hard materials (steels with hardness 60 HRC and above) whose plasticity is limited. At higher magnifications there were the following typical features of fracture surfaces found: The matrix was cracked by either cleavage or micro-plastic mechanism. The carbides can assist either to plastic deformation of the matrix (by decohesion at carbide/matrix interface whereas the carbide can either be retained in the matrix or is extracted) or are they are cleaved along the fracture plane. Some attempts to make a classification of these carbides according their role in fracture propagation and crystallography have been done. However, there was no attempt made in order to provide comprehensive study of that. The current paper is the first trial to overcome this gap in knowledge. It is focused to the determination of percentage of cleaved vs. plastically deformed carbides in specimens for fracture toughness testing, depending on the K_{IC} values obtained by different regimes of cryogenic treatments and tempering. The same concern the percentage of cleaved/plastically deformed matrix.

2 Experimental

Thick sheet made of commercial Vanadis 6 steel was cut and net-shape machined into 10 × 10 × 55 mm specimens for fracture toughness. The nominal chemical composition of the material was 2.1% C, 1.0% Si, 0.4% Mn, 6.8% Cr, 1.5% Mo, 5.4% V, and Fe as the balance. As-delivered material had a microstructure that consisted of ferrite and different spherical carbides, and its hardness was 281 HV 10.

After the machining the samples were moved into vacuum furnace where they were gradually heated up to the austenitizing temperature of 1050 °C, held there for 30 min., and then cooled down to the room temperature rapidly, by using a 5 bar nitrogen gas pressure. One set of specimens was immediately tempered, in two cycles for 2 h each, at temperatures from the range 170–530 °C. This treatment was denoted “conventional heat treatment”, hereinafter “CHT”. The remaining sets were further processed as shown in Table 1. Cryogenic treatments were conducted at different temperatures, for 17 h each. After that the specimens were re-heated to the room temperature, and immediately tempered by using the same regimes as in CHT. However, selected specimens were further investigated in untempered state.

After the heat treatment the specimens were fine-grinded and polished to the surface roughness R_a lying in interval 0.05–0.07 μm . Then, they were pre-cracked by using a resonance frequency machine (Cracktronic 8024), in four point bending configuration. For the fracture toughness (K_{IC}) measurements the specimens were

Table 1 Parameters of cryogenic treatments and tempering of experimental steel

| Set of specimens | Cryogenic treatment temperature (°C) | Cryogenic medium | Tempering temperature (°C) |
|------------------|--------------------------------------|-------------------|----------------------------|
| 1 | No | – | No, 170, 330, 450, or 530 |
| 2 | –75 | Cold nitrogen gas | No, 170, 330, 450, or 530 |
| 3 | –140 | Cold nitrogen gas | No, 170, 330, 450, or 530 |
| 4 | –196 | Liquid nitrogen | No, 170, 330, 450, or 530 |
| 5 | –269 | Liquid helium | No, 170, 330, 450, or 530 |

loaded in three-point bending. Both the pre-crack manufacturing and the measurements were conducted at room temperature and following the ISO 12137 standard [23]. Details of these procedures are described in [20], for instance. Five samples were tested for each investigated heat treatment state, to ensure the statistical reliability of the obtained data.

The material microstructures as well as fracture surfaces were examined by using a JEOL JSM 7600F scanning electron microscope (SEM) equipped with an Energy Dispersive Spectrometer (EDS), operating at an acceleration voltage of 15 kV. For more detailed examination also transmission electron microscopy was adopted. For the TEM a JEOL 200CX device operating at an acceleration voltage of 200 kV has been used. Thin foils were prepared by electrolytic jet-polisher (Tenupol 5). For details of specimens preparation refer e.g. [24].

In microstructural investigations the carbide particles were categorized as eutectic carbides (ECs), secondary carbides (SCs) and small globular carbides (SGCs). This categorization was done according to the origin, chemistry and size of the particles. For more details refer the [25].

The same categorization was also used in analysis of role of individual carbide particles in fracture propagation. The percentages of cleaved vs. decohesion carbide particles were established on twenty randomly acquired SEM images, at a magnification of 4000 \times . The same micrographs were used for the estimation of percentage of cleaved vs. micro-plastically deformed matrix.

X-ray diffraction was carried out by a Phillips PW 1710 device with filtered $\text{Co}_{\alpha,1,2}$ characteristic radiation. Diffraction spectra were acquired from the range 30–115° of the two-theta angle. The amounts of the retained austenite (γ_R) have been determined following the appropriate ASTM standard [26]. However, personal experience of the authors of the paper indicates that the diffraction peaks of retained austenite are often superimposed by peaks of major carbides present in ledeburitic steels. Therefore, the analyses were complemented with Rietveld refinement of the recorded X-ray spectra.

Macro-hardness HV 10 was measured for the specimens processed with each combination of heat-treatment parameters. On each specimen five readings were made, and the mean values of the obtained values were then calculated.

3 Results and Discussion

Figure 1 shows the obtained prior-to-tempered microstructures of the examined steel after CHT and after different cryogenic treatments (as labelled inside the images). Generally, the microstructure of all the specimens is formed of the matrix and different carbide particles. These particles manifest uniform distribution throughout the matrix.

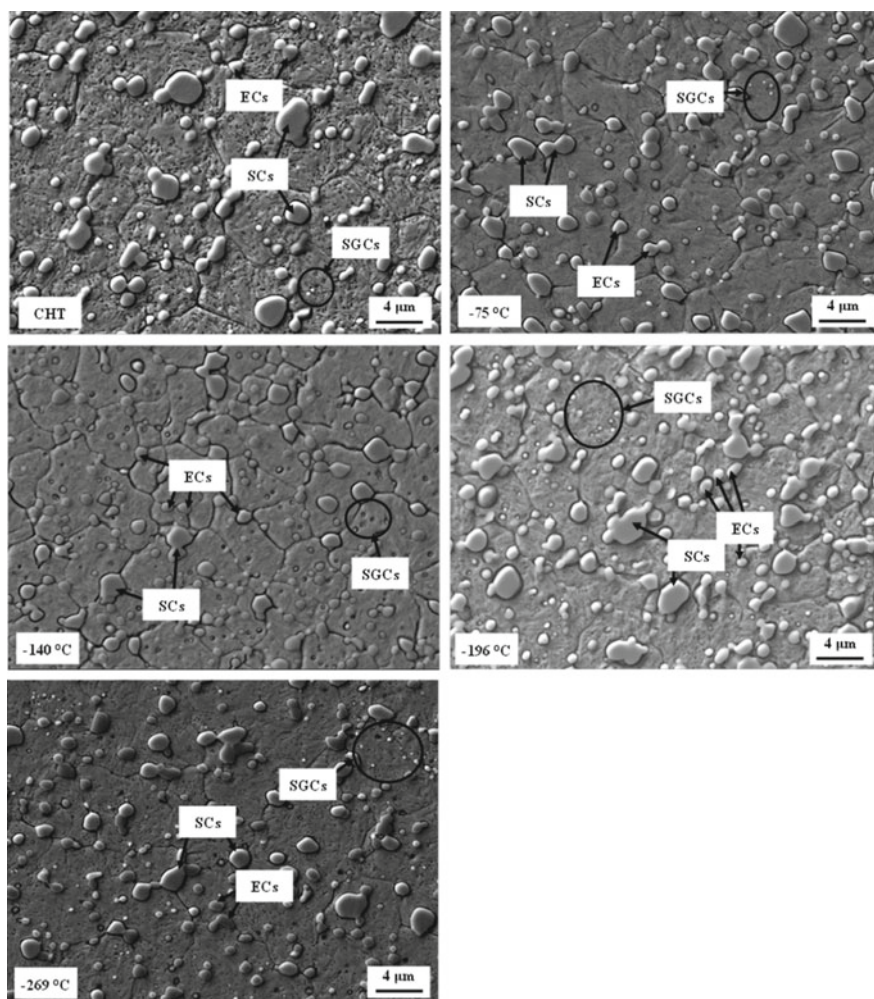


Fig. 1 SEM images of the obtained microstructures of the Vanadis 6 steels after room temperature quenching, and after treatments at different cryogenic temperatures as indicated by labelling inside the images

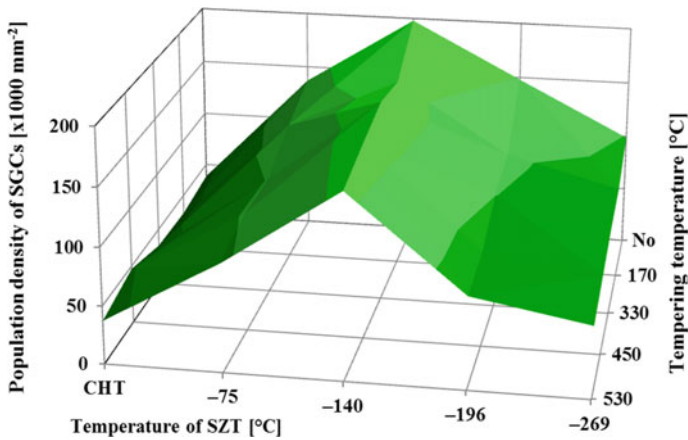


Fig. 2 Population density of SGCs as a function of cryogenic (sub-zero, SZT) treatment temperature and tempering temperature

As abovementioned, three carbides types are present in the examined material. The ECs are insoluble in the austenite during the heat treatment, and their number and population density remain almost constant during all steps of heat treatment schedules applied, see e.g. [21, 24, 25]. Also, these characteristics of secondary carbides (SCs) are unchanged. This is because these particles undergo dissolution in the austenite, and the amount of dissolved SCs depends on the level of the austenitizing temperature (T_A). Since the T_A was constant in our experiments both the number and population density of these particles are also constant for differently cryogenically treated and tempered specimens. The third carbide type in heat-treated Vanadis 6 steel is represented by small globular carbides. A series of SEM images in Fig. 1 demonstrates that cryogenic treatments increase the number and population density of these particles significantly. Summarizing diagram in Fig. 2 shows that the maximum population density of these particles was achieved by -140 °C cryogenic treatment while other processes gave lower population density of SGCs. Tempering evokes moderate decrease in population density of these carbides, despite that it remains higher as compared with the state after CHT.

Increased amounts of SGCs in cryogenically treated steel, as compared with the CHT one, is in line with the observations of other authors, on different tool steels, e.g. [1, 3, 4, 11]. On the other hand, reliable metallurgical background being responsible for their formation during cryogenic treatment was discovered only in recent years [24, 25].

Detailed SEM micrographs, Fig. 3 are focused to the matrix microstructure of untempered, conventionally- and cryogenically treated specimens. It is shown that the martensite manifests clearly visible lath morphology. The retained austenite is localised mainly in-between the martensite laths, as indicated by arrows. In CHT specimen the formations of retained austenite are visible in the form of tiny oblong features, with a thickness of several tens of nm, as well as in more regularly shaped

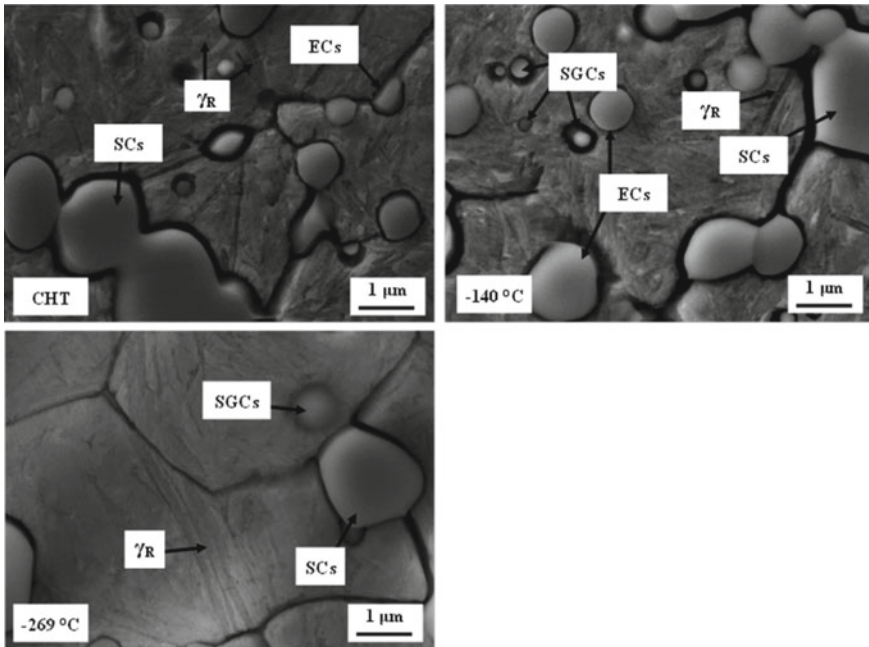


Fig. 3 High-magnification SEM micrographs that are focused to show the obtained matrix microstructures of the Vanadis 6 steels after conventional quenching, and after treatments at different cryogenic temperatures as indicated by labelling inside the images

formations. In cryogenically treated steel the γ_R amount is significantly reduced, and this phase can be distinguished from the martensite as tiny elongated formations.

Figure 4 provides a clear insight on the fact how the application of different cryogenic treatments reduces the retained austenite amounts. Cryogenic treatments at either -75 or -269 °C, for instance, reduce the γ_R amounts by two thirds as compared with the state after CHT. More dramatic reduction of γ_R is allowed by the use of -140 °C for the treatment (approx. to one fifth). The application of liquid nitrogen for the treatment further decreases the γ_R amounts, to almost one tenth of the amounts after CHT. Tempering treatments that are carried out at lower temperatures do not have significant impact on the amounts of retained austenite. But, high-temperature tempering further reduced the amount of γ_R , thus no measurable amounts of this phase are present in cryogenically treated and high-temperature tempered specimens.

Figure 5 presents TEM images and corresponding diffraction patterns of the carbide particle displayed in bright-field image, Fig. 5a. Dark field image, Fig. 5b of the carbide was obtained by using the reflection $(10\bar{1})$ of the M_7C_3 -phase. Diffraction patterns, Fig. 5c disclosed that the particle belongs to the secondary M_7C_3 carbides. Apart from this the diffraction patterns of the retained austenite (from the matrix) is shown.

Figure 6 shows bright-field TEM micrograph of carbide particles in cryogenically

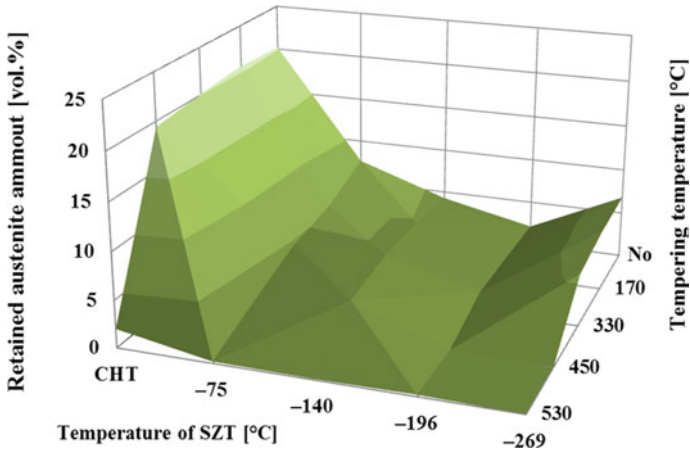


Fig. 4 Retained austenite amounts as a function of cryogenic (sub-zero, SZT) treatment temperature and tempering temperature

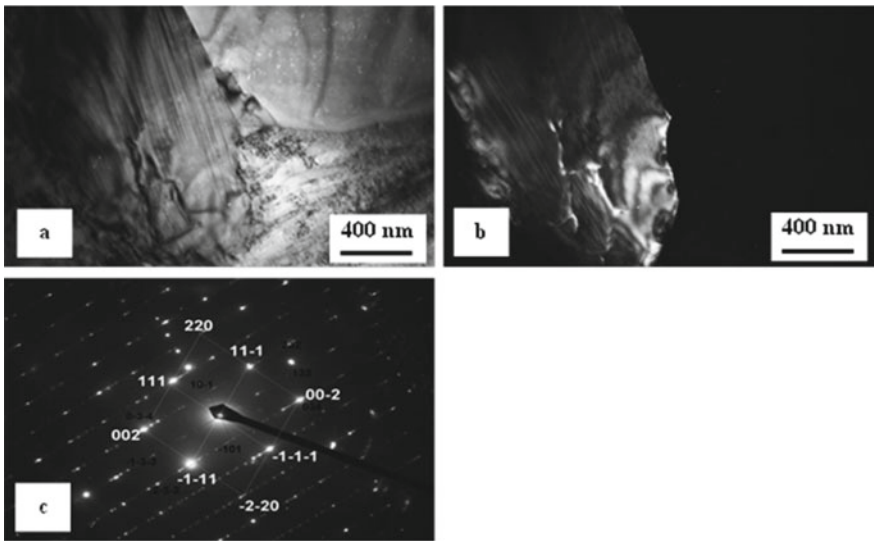


Fig. 5 TEM micrographs showing the matrix and M_7C_3 carbide particle in CHT specimen. **a** bright-field image, **b** corresponding dark-field image, **c** diffraction pattern of carbide on the left side of the micrographs

treated (at $-196\text{ }^\circ\text{C}$) and untempered specimen. The carbides are regularly-shaped, and their size is around $1\text{ }\mu\text{m}$, Fig. 6a. Corresponding diffraction patterns of the carbide particle indicated by arrow disclosed that this particle belongs to the eutectic MC carbides.

Figure 7a shows bright-field TEM micrograph of carbide particle (from the spec-

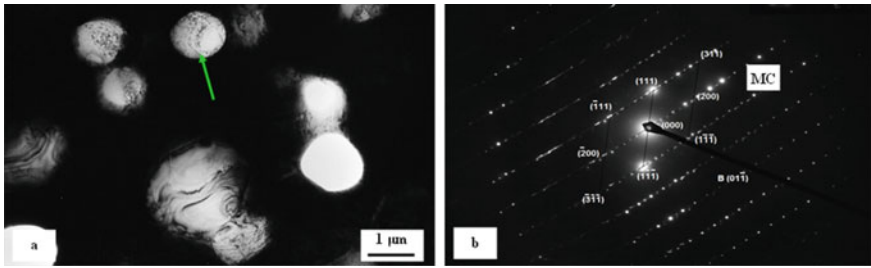


Fig. 6 TEM micrograph and corresponding diffraction patterns showing eutectic carbide MC particle in the steel that was cryogenically treated at $-196\text{ }^{\circ}\text{C}$, **a** bright-field image, **b** diffraction pattern of carbide denoted by green arrow

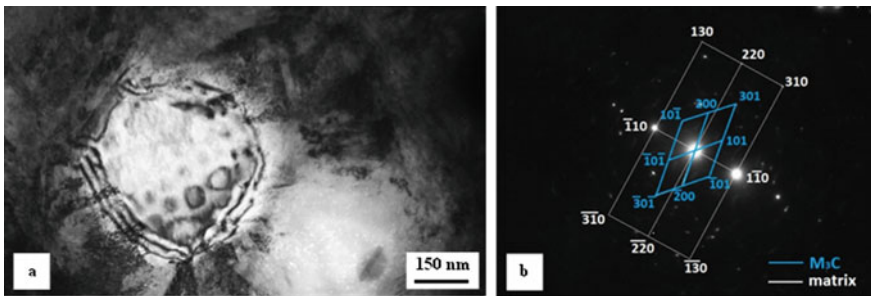


Fig. 7 TEM micrograph and corresponding diffraction patterns showing small globular carbide in specimen that was cryogenically treated at $-140\text{ }^{\circ}\text{C}$, **a** bright-field image, **b** diffraction pattern of carbide particles. *Note* apart from the carbide also the matrix gave diffraction, and it is displayed in Fig. 7b together with diffraction patterns of the carbide

imen that was cryogenically treated at $-140\text{ }^{\circ}\text{C}$) that belongs to the group of small globular carbides. The diameter of this carbide is around 400 nm. Corresponding diffraction patterns of the carbide particle, Fig. 7b revealed that the SGSc are cementite with orthorhombic structure.

Summarizing diagram of the effects of cryogenic temperature and tempering temperature on the bulk hardness of examined steel is in Fig. 8. The as-quenched hardness of the steel was 875 HV 10. Cryogenic treatments increased the average hardness to 930, 933, 942 and 904 HV 10 for the cryogenic temperatures of -75 , -140 , -196 and $-269\text{ }^{\circ}\text{C}$, respectively. Tempering induces a decrease in hardness for CHT steel at lower tempering temperatures, which is succeeded by very slight hardness increase when tempered at approx. $530\text{ }^{\circ}\text{C}$. In cryogenically treated specimens the secondary hardness peak disappeared completely, and the decrease in hardness is monotonic with tempering temperature. Despite that the average hardness values are fully comparable with those achieved by tempering followed the room temperature quenching. On the other hand the as-tempered (at $530\text{ }^{\circ}\text{C}$) hardness is mostly lower than the hardness of CHT steel after application the same tempering. An exception

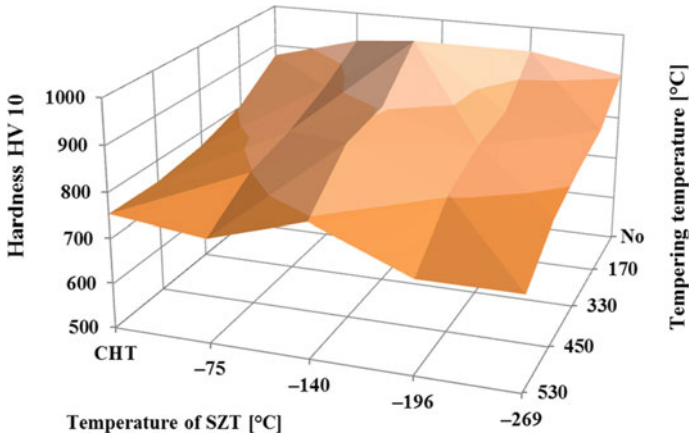


Fig. 8 Relationship between bulk hardness of examined steel, cryogenic (sub-zero, SZT) treatment temperature and tempering

from this general trend is represented by the steel specimens processed at $-140\text{ }^{\circ}\text{C}$. The bulk hardness of these specimens reached up to 1000 HV 10 when tempered at $170\text{ }^{\circ}\text{C}$ and, despite its monotonic decrease its values are maintained higher than what is obtained after CHT, irrespectively to the level of tempering temperature.

The relation between the fracture toughness, temperature of SZT and tempering temperature is in Fig. 9. CHT and untempered material has the average fracture toughness of $16.39\text{ MPa} \times \text{m}^{1/2}$. The application of $170\text{ }^{\circ}\text{C}$ tempering evoked an increase in K_{IC} to $19.65\text{ MPa} \times \text{m}^{1/2}$. But, lowering of the K_{IC} has been recorded in the specimens tempered at higher temperatures. This lowering is first moderate but it

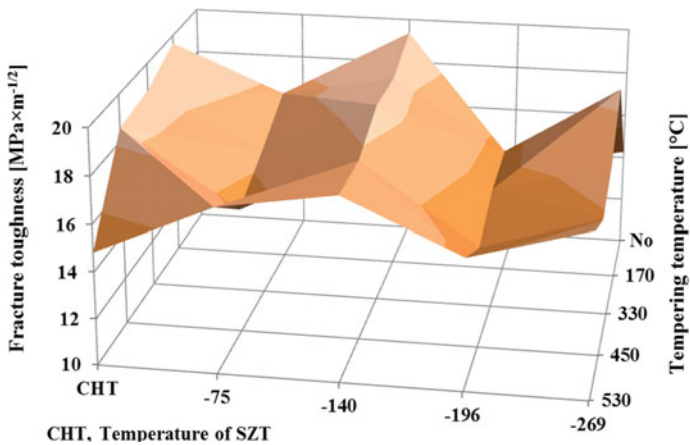


Fig. 9 Dependence of fracture toughness of the examined material on cryogenic (sub-zero, SZT) treatment temperature and on the tempering

is accelerated at tempering temperatures within the secondary hardening temperature range (around 530 °C). The average fracture toughness was $14.84 \text{ MPa} \times \text{m}^{1/2}$ after this kind of tempering.

Generally, the application of cryogenic treatments reduced the fracture toughness of untempered specimens. This trend is maintained also after tempering at 170, 330 or 450 °C. However, after tempering at 530 °C cryogenically treated steel manifests better fracture toughness than the steel after conventional room temperature quenching. It should be noticed that the treatment at $-140 \text{ }^\circ\text{C}$ results in K_{IC} increase as compared with the steel after room temperature quenching, and also the fact that this kind of cryogenic treatment produces comparable (in comparison with CHT steel) K_{IC} values, at significantly improved hardness.

The obtained results of fracture toughness variations (especially that what was obtained after treatment at $-140 \text{ }^\circ\text{C}$) are rather surprising and counterintuitive. One can expect general worsening of this property rather than “no effect” or, even positive influence of cryogenic treatment. However, the literature review gave inconsistent results—some authors reported worsening of toughness [12–15] while others reported rather positive effect of this kind of treatment on toughness [16, 17, 20]. The reason for this can be determined as a competitive effect of different microstructural changes due to the application of cryotreatments:

- reduction of retained austenite amount—this normally leads to worsening of fracture toughness as experimentally proved by Putatunda et al. [27]

- increased population density of SGCs—it was demonstrated that the presence of carbides provides clear obstacles in fracture propagation [13, 17, 20, 28] and thereby improves the material toughness.

- general microstructural refinement—this can, according to well-known Hall-Petch strengthening (e.g. [29]) lead to simultaneous improvement in strength/hardness and toughness precipitation of nano-sized coherent carbides—it was found recently that the precipitation of these particles is rather delayed by SZT at higher tempering temperatures but it is accelerated at low temperatures [24, 25].

Specifically for cryogenically treated SZT Vanadis 6 steel the reduction of retained austenite amounts tends to induce a K_{IC} decrease. The same effect can be expected to be resulted from enhanced precipitation of transient, coherent carbides as these particles increase the matrix stiffness. However, this effect is less or more compensated by general microstructural refinement, and also by considerably enhanced amount of SGCs. Therefore, cryogenic treatments lead to improvement in K_{IC} after the tempering in the normal secondary hardening temperature range. When tempered in the low temperature tempering range the effect of SGCs is insufficient to equilibrate the effect of lowering the γ_R amount as well as the impact of the presence of transient carbides in matrix, thus resulting in K_{IC} reduction. An exception is the SZT temperature of $-140 \text{ }^\circ\text{C}$ where the K_{IC} was either improved as compared with the state after CHT or its values were comparable with this material state. This is attributed to extremely high number of SGCs, see Fig. 2.

Figures 10, 11 and 12 show fracture surfaces and corresponding EDS mapping results of differently heat treated fracture toughness specimens. In Fig. 10a there is the fracture surface of CHT and untempered specimen. This particular specimen had the

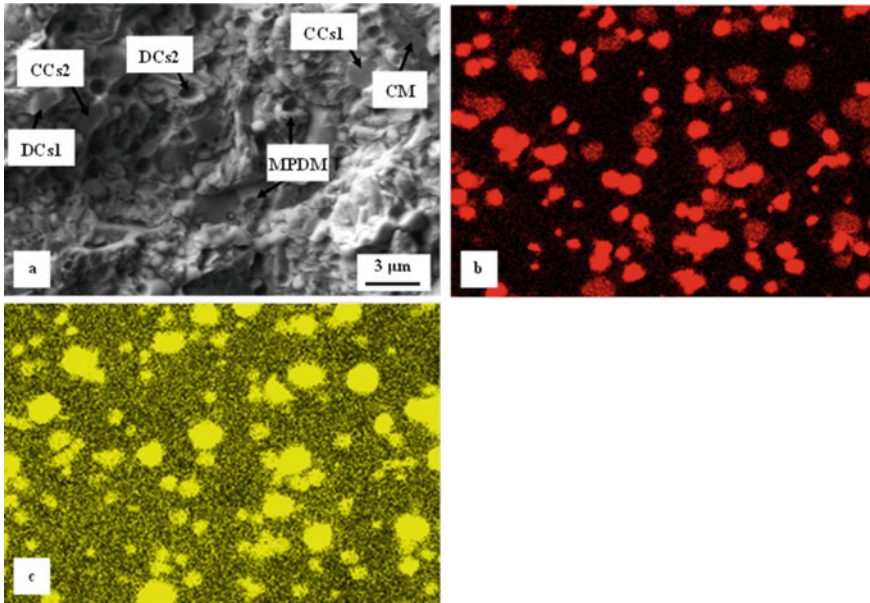


Fig. 10 SEM micrograph and corresponding EDS mapping of main alloying elements of conventionally heat treated and untempered fracture toughness specimen. **a** image, **b** EDS map of vanadium, **c** EDS map of chromium. CM—cleaved matrix, MPDM—micro-plastically deformed matrix, CCs1—cleaved carbides M_7C_3 , CCs2—cleaved carbides MC, DCs1—decohesive carbides M_7C_3 , DCs2—decohesive carbides MC

fracture toughness of $16.58 \text{ MPa} \times \text{m}^{1/2}$ (i.e. relatively low value). It is shown that the matrix manifests two basic fracture modes. The first one is micro-plastic deformation, which is associated with decohesion at carbide/matrix interfaces and thus microvoid coalescence. The second mechanism is cleavage cracking. This is mainly related to high material hardness and, also to high level of matrix stiffness (presence of untempered martensite). Also, the carbides operate in two distinct manners in the fracture propagation. There are cleaved carbides of both (M_7C_3 and MC) particle types as well as carbides that assist the decohesive fracture mechanism visible on the SEM image, Fig. 10a. EDS maps of the main alloying elements, Figs. 10b, c assist to clearly differentiate between these two carbide types, and also between their fracture manner. Moreover, there are also other carbides visible on the image, Fig. 10a. These particles belong to the class of small globular carbides (SGCs), and have size mostly below 300 nm. As shown in Fig. 7 the SGCs are cementite. It was recently demonstrated that they have nearly the same chemical composition (metallic elements contents) as the matrix, as they are developed by diffusion-less transformation, during the hold of the steel at cryogenic temperature [24]. In fracture propagation these particles assist to decohesive propagation mechanism, and are either separated from the material (micro-voids on the fracture surface) or remain embedded into the matrix.

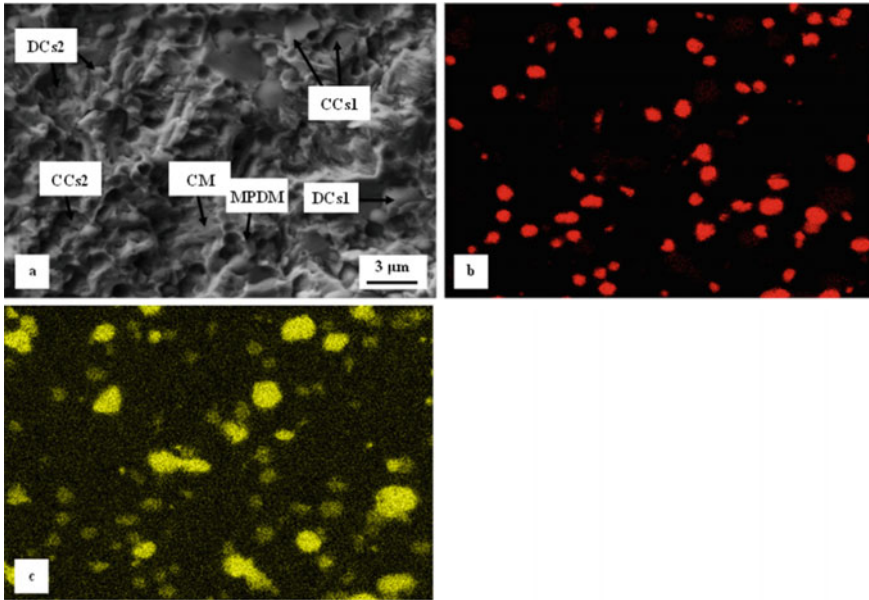


Fig. 11 SEM micrograph of fracture surface and corresponding EDS mapping of main alloying elements of CHT and tempered at 170 °C specimen, **a** image, **b** EDS map of vanadium, **c** EDS map of chromium. CM—cleaved matrix, MPDM—micro-plastically deformed matrix, CCs1—cleaved carbides M_7C_3 , CCs2—cleaved carbides MC, DCs1—decohesive carbides M_7C_3 , DCs2—decohesive carbides MC

The same features can be observed on the fracture surface of the specimen that experienced conventional heat treatment followed by tempering at 170 °C, Fig. 11. This particular specimen had the fracture toughness of $19.7 \text{ MPa} \times \text{m}^{1/2}$ (i.e. relatively high value). However, the fracture surface of this specimen differs from that in Fig. 10a, in terms of the area percentage of cleaved/decohesive crack propagation manner. This is because tempering induces partial stress relief, and also due to the fact that the martensite undergoes tempering, which is associated with moderate drop in hardness.

The fracture surface of the specimen that experienced cryogenic treatment at $-140 \text{ }^\circ\text{C}$ with subsequent tempering at 170 °C is shown in Fig. 12a. The fracture toughness of this particular specimen was $18.7 \text{ MPa} \times \text{m}^{1/2}$ (i.e. relatively high value). Basically, the fracture surface manifests the same features as those of the specimens that were not cryogenically treated (but also those after SZT at other temperatures). However, there also clear differences as compared with conventionally treated samples. First it should be noted that the analysed specimen had the hardness of 1000 HV 10, i.e. much higher than the conventionally treated ones. One can thus expect its very brittle behaviour under circumstances of fracture toughness testing. However, the obtained fracture toughness is comparable with, for instance, conventionally treated specimens that have much lower (by 150 and more Vickers

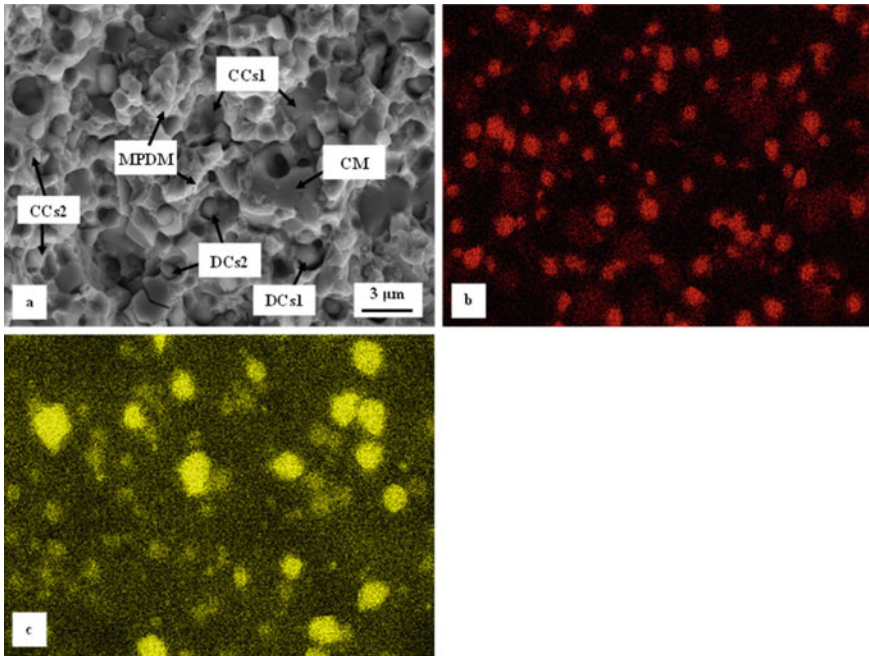


Fig. 12 SEM micrograph and corresponding EDS mapping of main alloying elements of crygenically treated (at $-140\text{ }^{\circ}\text{C}$) and tempered at $170\text{ }^{\circ}\text{C}$ fracture toughness specimen, **a** image, **b** EDS map of vanadium, **c** EDS map of chromium. CM—cleaved matrix, MPDM—micro-plastically deformed matrix, CCs1—cleaved carbides M_7C_3 , CCs2—cleaved carbides MC, DCs1—decohesive carbides M_7C_3 , DCs2—decohesive carbides MC

units) hardness. Figure 12 reveals that the fracture surface contains obviously higher area percentage of cleaved sites as compared with the fracture surface of conventionally treated specimen that was tempered at $170\text{ }^{\circ}\text{C}$, Fig. 11a. Conversely, the fracture surface contains also much more sites where the micro-voids coalescence crack propagation mechanism takes place. This is associated with much higher population density of SGCs, as Figs. 1 and 2 illustrate. These carbides have mostly several tens or hundreds nm in diameter. Also it should be noted that their nature is cementite. This carbide is relatively less brittle as compared with M_7C_3 , for instance. Moreover, its fracture toughness manifests much smaller scatter. Bhadeshia [30], and Coronado and Rodriguez [31] reported the fracture toughness in differently alloyed cementite (with either Cr or V) to be in the range $2.24\text{--}2.74\text{ MPa} \times \text{m}^{1/2}$. Alternatively, this property manifests large scatter for the M_7C_3 -particles. Casellas et al. [32] reported a great level of directional anisotropy of the KIC. Consequently, its values range between 0.5 and $4.5\text{ MPa} \times \text{m}^{1/2}$. One can thus expect that much finer SGCs (cementite) are much less amenable to crack, due to their more uniform toughness values and higher isotropy level as compared with the M_7C_3 . Additionally, it is worth noting the description the carbide size effect on its fracture toughness. Fukaura

et al. [33] found that the material resistance against the fracture initiation is improved owing to the carbide particles refinement for the AISI D2 tool steel. In the Vanadis 6 steel the mean spherical diameter of M7C3 phase particles ranges between 2.5 and 2.8 μm but the SGCs are ten or more times finer. This is, in principle, an explanation of very different carbides behaviour in differently cryotreated and tempered fracture toughness specimens in the present study.

Figure 13 shows the percentages of cleaved and decohesive ECs and SCs, respectively, for CHT steel and for the steel that was cryogenically treated at $-196\text{ }^\circ\text{C}$. It is worth noting that similar variations in percentages of cleaved and decohesive

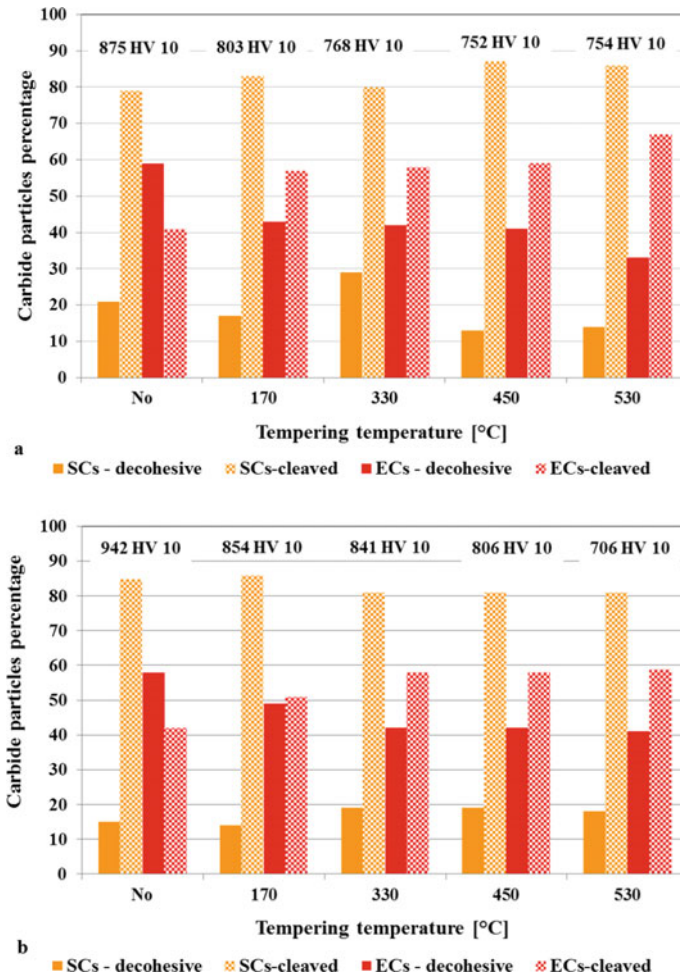


Fig. 13 Role of SCs (decohesion vs. cleavage) and ECs in fracture propagation in differently tempered specimens, **a** after CHT, **b** after cryogenic (sub-zero, SZT) treatment at $-96\text{ }^\circ\text{C}$

carbides were also found for the steel specimens treated at other cryogenic temperatures. First it is shown that the SCs (M_7C_3) undergo much more easily the cleavage fracture than the ECs (MC). This tendency is evident for all the specimens, irrespectively to the application of SZT or to the level of tempering temperature used. Also, the percentages of cleaved and decohesive SCs are practically the same. However, the ECs undergo cleavage in significantly lower extent in untempered specimens, and the percentage of cleaved ECs particles increases with tempering temperature.

To explain the fracture behaviour of mentioned two carbides it is relevant to express a few supplementary comments. As discussed above the M_7C_3 carbides are very brittle, thus prone to cracking. The main reasons are their microstructural anisotropy (hexagonal structure) and greater size than, for instance the MC—phase (eutectic carbides, ECs). In contrast, the MC—carbides manifest much more pronounced isotropic behaviour of the fracture toughness since they crystallize in cubic crystal cell. Even though they have higher hardness compared to M_7C_3 their fracture toughness is mostly from the range $2.7\text{--}3.7 \text{ MPa} \times \text{m}^{1/2}$ [31, 34], i.e. it is generally rather higher than for the M_7C_3 .

The reason for the increase in percentage of cleaved ECs with increasing the tempering temperature may be elucidated by the fact that the matrix (and also the steel in general—see hardness values in Fig. 13) becomes softer, and thus more plastic (less brittle) when tempered. Conversely, the carbides are much harder, and more brittle as compared with the matrix. Therefore they cannot deform with the matrix plastically during the crack propagation and are more amenable to brittle cracking.

4 Conclusions

Specimens for fracture toughness determination manufactured of Vanadis 6 tool steel were conventionally- as well as cryogenically treated at different cryogenic media temperatures, and then differently tempered. These treatments resulted in great variations in both the hardness and the fracture toughness. The principal conclusions of the obtained results are the following:

Cryogenic treatments considerably reduce the retained austenite amounts, increase the number and population density of sub-micron cementitic carbides and generally refine the steel microstructure.

The steel hardness is increased by cryogenic treatments but this kind of treatment leads to loss of the secondary hardening in high-temperature tempering range.

Cryogenic treatments followed by low-temperature tempering lower the fracture toughness except the processing at $-140 \text{ }^\circ\text{C}$ where the K_{IC} vales are comparable with those obtained by conventional heat treatment. Conversely, the K_{IC} is improved for cryogenically treated steel after tempering at temperatures within the secondary hardening temperature range.

The role of individual structural constituents in fracture propagation differs one from others, as a result of their different properties. The M_7C_3 (secondary carbides,

SCs) undergo much more easily brittle cracking because of their largest size and great anisotropy. On the contrary the MC particles assist more probably to decohesive fracture mechanism. But, this probability decreases with increasing the matrix plasticity. Small globular carbides assist only in the decohesive fracture propagation mechanism as they are very small, thus less amenable to brittle cracking.

The matrix of untempered specimens manifests clear indications of cleavage fracture while the plasticity of the matrix slightly increases with tempering treatment.

Acknowledgements The authors would like to acknowledge that the article is an outcome implementation of the following two projects: scientific project VEGA 1/0112/20 and APRODIMET, ITMS: 26220120048, supported by the Research and Development Operational Programme funded by the European Regional Development Fund.

References

1. Das D, Ray KK (2012) Structure-property correlation of sub-zero treated AISI D2 steel. *Mater Sci Eng A* 541:45–60
2. Das D, Ray KK, Dutta AK (2009) Influence of temperature of sub-zero treatments on the wear behaviour of die steel. *Wear* 267:1361–1370
3. Amini K, Akhbarizadeh A, Javadpour S (2012) Investigating the effect of holding duration on the microstructure of 1.2080 tool steel during the deep cryogenic treatment. *Vacuum* 86:1534–1540
4. Akhbarizadeh A, Javadpour S, Amini K, Yaghtin AH (2013) Investigating the effect of ball milling during the deep cryogenic heat treatment of the 1.2080 tool steel. *Vacuum* 90:70–74
5. Yarasu V, Janka L, Jurči P (2020) Začiatok formulára Spodná časť formulára Dry sliding wear behaviour of sub-zero processed Cr-V ledeburitic steel Vanadis 6 against three counterpart types. *Int J Mater Res* 111:894–907
6. Berns H (1974) Restaustenit in ledeburitischen Chromstählen und seine Umwandlung durch Kaltumformen, Tiefkühlen und Anlassen. *HTM J Heat Treat Mater* 29:236–247 (in German)
7. Surberg CH, Stratton P, Lingenhölle K (2008) The effect of some heat treatment parameters on the dimensional stability of AISI D2. *Cryogenics* 48:42–47
8. Bartkowska A, Jurči P (2019) Corrosion resistance of vanadis 6 steel after conventional heat treatment and sub-zero treatment in cold nitrogen gas followed by tempering. *Defect Diffus Forum* 395:16–29
9. Shinde T (2020) Failure analysis of cryogenically treated H13 specimen in rotating bending fatigue. *Eng Fail Anal* 113, Article number 104535
10. Korade D, Ramana KV, Jagtap K (2020) Effect of carbide density on fatigue limit of H21 die steel. *J Mater Eng Perform* 29:230–241
11. Collins DN, Dormer J (1997) Deep cryogenic treatment of a D2 cold-work tool steel. *Heat Treat Meals* 3:71–74
12. Wierszylowski I (2006) The influence of post-quenching deep cryogenic treatment on tempering processes and properties of D2 tool steel. *Studies of Structure, XRD, Dilatometry, Hardness and Fracture Toughness. Defect and Diffusion Forum* 258–260, 415–420
13. Das D, Sarkar R, Dutta AK, Ray KK (2010) Influence of sub-zero treatments on fracture toughness of AISI D2 steel. *Mater Sci Eng A* 528:589–603
14. Rhyim YM, Han SH, Na YS, Lee JH (2006) Effect of deep cryogenic treatment on carbide precipitation and mechanical properties of tool steel. *Solid State Phenom* 118:9–14
15. Kumar S, Nahraj M, Bongale A, Khedkar NK (2019) Effect of deep cryogenic treatment on the mechanical properties of AISI D3 tool steel. *Int J Mater Eng Innov* 10:98–113

16. Molinari A, Pellizzari M, Gialanella S, Straffellini G, Stiasny KH (2001) Effect of deep cryogenic treatment on the mechanical properties of tool steels. *J Mater Process Technol* 118:350–355
17. Pérez M, Rodríguez C, Belzunce FJ (2014) The use of cryogenic thermal treatments to increase the fracture toughness of a hot work tool steel used to make forging dies. *Proc Mater Sci* 3:604–609
18. Sobotová J, Jurčí P, Dlouhý I (2016) The effect of sub-zero treatment on microstructure, fracture toughness, and wear resistance of Vanadis 6 tool steel. *Mater Sci Eng A* 652:192–204
19. Ptačinová J, Sedlická V, Hudáková M, Dlouhý I, Jurčí P (2017) Microstructure Toughness relationships in sub-zero treated and tempered Vanadis 6 steel compared to conventional treatment. *Mater Sci Eng A* 702:241–258
20. Jurčí P, Ďurica J, Dlouhý I, Horník J, Planieta R, Kralovič D (2019) *Appl Metallurg Mater Trans* 50A:2413–2434
21. Kusy M, Rizekova-Trnkova L, Krajcovic J, Dlouhy I, Jurčí P (2019) Can sub-zero treatment at -75 degrees C bring any benefits to tools manufacturing? *Materials* 12, Article number 3827
22. Jurčí P, Ptačinová J, Dlouhý I (2019) Cryogenic treatment of Cr-V die steel in liquid helium—effect on mechanical properties. In: *METAL 2019—28th International conference on metallurgy and materials*, pp 562–568, Tanger, Ltd., Brno, Czech Republic
23. ISO 12137 (2010) *Metallic materials—determination of plane strain fracture toughness*
24. Ďurica J, Ptačinová J, Dománková M, Čaplovič L, Čaplovičová M, Hrušovská L, Malovcová V, Jurčí P (2019) Changes in microstructure of ledeburitic tool steel due to vacuum austenitizing and quenching, sub-zero treatments at -140°C and tempering. *Vacuum* 170. <https://doi.org/10.1016/j.vacuum.2019.108977>
25. Jurčí P, Dománková M, Hudáková M, Ptačinová J, Pašák M, Palček P (2017) Characterization of microstructure and tempering response of conventionally quenched, short- and long-time sub-zero treated PM Vanadis 6 ledeburitic tool steel. *Mater Charact* 134:398–415
26. ASTM E975-13 (2004) Standard practice for X-ray determination of retained austenite in steel with near random crystallographic orientation. *ASTM book of standards*, vol 3.01. West Conshohocken, PA, USA
27. Putatunda SK (2001) Fracture toughness of a high carbon and high silicon steel. *Mater Sci Eng A* 297:31–43
28. Berns H, Broeckmann C (1997) Fracture of hot formed ledeburitic chromium steels. *Eng Fract Mech* 58:311–325
29. Hansen N (2004) Hall-Petch relation and boundary strengthening. *Scripta Mater* 51:801–806
30. Bhadeshia HKDH (2019) Cementite. *Int Mater Rev*. <https://doi.org/10.1080/09506608.2018.1560984>
31. Coronado JJ, Rodriguez SA (2015) Cementite characterization with chromium and vanadium contents using indentation technique. *J Iron Steel Res Int* 22:366–370
32. Casellas D, Caro J, Molas S, Prado JM, Valls I (2007) Fracture toughness of carbides in tool steels evaluated by nanoindentation. *Acta Mater* 55:4277–4286
33. Fukaura K, Yokoyama Y, Yokoi D, Tsuji N, Ono K (2004) Fatigue of cold-work tool steels: effect of heat treatment and carbide morphology on fatigue crack formation, life, and fracture surface observations. *Metallurg Mater Trans* 35A:1289–1300
34. Večko Pirtovšek T, Kugler G, Terčelj M (2013) The behaviour of the carbides of ledeburitic AISI D2 tool steel during multiple hot deformation cycles. *Mater Charact* 83:97–108

Strength of Solder and Adhesive Joints of Copper Sheets



Anna Rudawska , Jakub Szabelski , Izabela Miturska ,
and Elżbieta Doluk 

Abstract In order to compare selected strength aspects of solder and adhesive joints made of M1E z4 copper sheet, destructive tests of load capacity were performed. In the case of solder butt joints, three different fluxes were analysed, while four different adhesive compositions were tested for adhesive lap joints. Different types of joints were also used in both groups. The results of the strength tests of joints' load capacity were subjected to statistical analysis, homogeneous groups and the importance of differences between the various methods of assembly joints made using the same technology were specified, and then adhesive and solder joints with insignificant differences in terms of strength were determined. It was found that in the case of solder joints, the highest and lowest values of load capacity were obtained for joints made with Unifix paste and Fosol as flux, respectively. The highest load capacity value was obtained for the adhesive joints made with the E53/PAC/100:80 composition, while the lowest was obtained for the adhesive joints made with the E5/Z1/100:12 adhesive composition. It was demonstrated that the analysed solder joints are between the strongest and the weakest adhesive joints.

Keywords Solder joints · Adhesive joints · Soft soldering · Copper sheet · Joint load capacity · Epoxy adhesives · Resin · Hardener · Flux

1 Introduction

Solder and adhesive joints are one of the types of permanent assembly joints used in various structures. Both belong to the group of bonded joints and therefore have certain characteristic properties. One of the main advantages of solder and adhesive joints is the ability to join different materials. Despite the emergence and development

A. Rudawska · J. Szabelski (✉) · I. Miturska · E. Doluk
Lublin University of Technology, Nadbystrzycka 36, 20-618 Lublin, Poland
e-mail: j.szabelski@pollub.pl

A. Rudawska
e-mail: a.rudawska@pollub.pl

© The Author(s), under exclusive license to Springer Nature Singapore Pte Ltd. 2022
M. Abdel Wahab (ed.), *Proceedings of the 9th International Conference on Fracture, Fatigue and Wear*, Lecture Notes in Mechanical Engineering,
https://doi.org/10.1007/978-981-16-8810-2_7

of many new metal joining technologies, in the modern technology soldering is widely used as it may help solve even the most complex material and construction problems. This method allows joining elements of various shapes, dimensions and properties, elements made of various modern materials, such as metals, ceramics, glass, and composites. Currently, one of the most important factors determining the development of this technology is the range of additional materials for soldering. The selection of appropriate solder and flux has an impact on the use of these materials, labour and energy consumption in the soldering process and, mainly, the quality and properties of joints [1–4].

The adhesive technology is a valuable complement to other methods for joining construction materials. It is now used in many industries: construction, automotive, aviation, machine building, packaging manufacturing and many others. Joining metals by adhesives is increasingly used due to the high strength of joint, the lack of stresses and low unit costs of work, resulting mainly from the amount of adhesive applied to make a single joint. The advantages of adhesive joints also include: the ability to dampen vibrations, the option to make the joint without using machine tools and expensive, special tools and materials (although the costs of equipment may be high in some cases), and the lack of electrochemical effects usually occurring while joining metals through other methods. It should be emphasized that surface preparation, i.e. the first stage of the adhesive technology, is an important activity during the preparation of adhesive joints. Proper surface preparation, adjusted to the type of material, for example, is an important condition for obtaining an adhesive joint with specific properties [5–10].

This paper analyses the selected issues of joining copper sheets by soldering and adhesive joining. Some of conditions and parameters applied to making joints are the same as those used in real circumstances. The objective was to perform experimental tests, which would then be the basis for analysing the selected strength aspects in individual groups of assembly joints.

2 Research Methodology

2.1 Materials

Solder and adhesive joints of Cu-ETP copper sheet (EN: CW004A) (half hard: R250/H065) were made during the experimental tests. The chemical composition of the tested copper sheet is specified in Table 1, while selected mechanical properties are in Table 2. This material is characterised by high electrical and thermal conductivity, combined with high plasticity and corrosion resistance. This is why it is very often used in industry. Copper rods, sheets, wires and rails are perfect conductors of electricity and parts of electrical devices.

Table 1 Chemical composition of Cu-ETP sheet

| Element | Share (%) |
|---------|-----------|
| Cu | ≥99.9 |
| Bi | ≤0.0005 |
| O | ≤0.04 |
| Pb | ≤0.005 |
| Cu | ≥99.9 |

Table 2 Selected mechanical properties of the M1E z4 copper sheet [11]

| Properties | Value |
|-------------------------------------|-------------------------|
| Min. Rm (MPa) | 250 |
| Min. hardness HB | 65 |
| Max. hardness HB | 90 |
| Density (g/cm ³) | 8.87–8.91 |
| Thermal expansion coefficient (1/K) | 16.5 × 10 ⁻⁶ |

2.2 Solder Joints

Butt solder joints were used for the tests; their diagram is shown in Fig. 1. Dimensions of solder joints (after the soldering process) were as follows: $b = 20 \text{ mm}$, $g = 1 \text{ mm}$, $l = 100 \text{ mm}$, $l_d = 2 \pm 0.5 \text{ mm}$, $l_c = 202 \pm 0.5 \text{ mm}$.

The solder joints were made by soft soldering with an electric soldering iron, whose operating temperature was approx. 400°C. Three types of fluxes were used: rosin, Fosol and Unifix 3 paste. The fluxes used in solder joints were selected according to the type of soldering, meaning soft soldering in this case, and the properties of the material (copper) being soldered. The samples were joined on both sides with a Tin (LC60) solder rod. The joints were cured at the temperature of $20 \pm 2 \text{ °C}$. Eight samples were made for each type of flux. Below is the presentation of operations and their parameters:

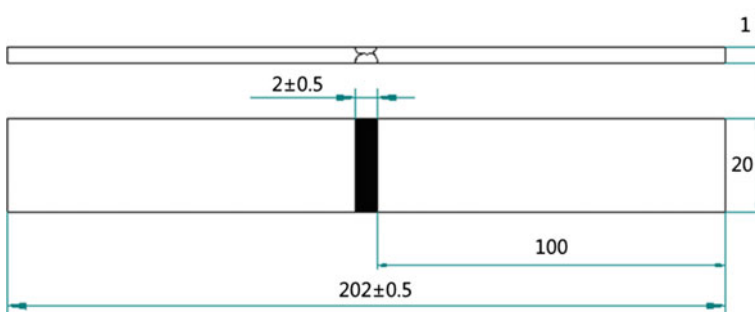


Fig. 1 Solder joint diagram and dimensions

1. Machining of sample faces (P100 grit sandpaper);
2. Priming of samples with an appropriate flux applied to the sample face
 - a. Rosin—transformer soldering iron,
 - b. Fosol—cotton cloth,
 - c. Unifix 3 paste—brush,
3. Priming of samples with tin LC60 using an electric soldering iron, priming time:
 - d. 7–8s—rosin,
 - e. 6s—Fosol, Unifix 3,
4. Double-sided butt soldering of primed samples, soldering time:
 - f. 8s—rosin,
 - g. 6–7s—Fosol, Unifix 3,
5. Curing at room temperature of 20 ± 2 °C, 5–6 s;
6. Dimension control with a 250/0.02 mm caliper – joint thickness and width.

2.3 Adhesive Joints

In the second part of the test, single-lap adhesive joints were made, with the lap length of $l_z = 15$ mm, width of $b = 20$ mm, sheet thickness of $g = 1$ mm, sheet sample length of $l = 92 \pm 1$ mm, $l_z = 15$ mm and $l_c = 77 \pm 1$ mm. The joint diagram and dimensions are shown in Fig. 2.

The following were used for adhesive joints: four two-component epoxy adhesives, made of two types of epoxy resins based on Bisphenol A (Epidian 5 and Epidian 53 trade names, producer: CIECH Resins, Nowa Sarzyna, Poland) and two types of curing agents: polyaminoamide C curing agent (PAC trade name, producer: CIECH Resins, Nowa Sarzyna, Poland) and triethylenetetramine (Z-1 trade name, producer: CIECH Resins, Nowa Sarzyna, Poland). Recommendations for the proper stoichiometric ratio of the specified resin and curing agent were applied. The list thereof and the number of samples made for each set are shown in Table 3.

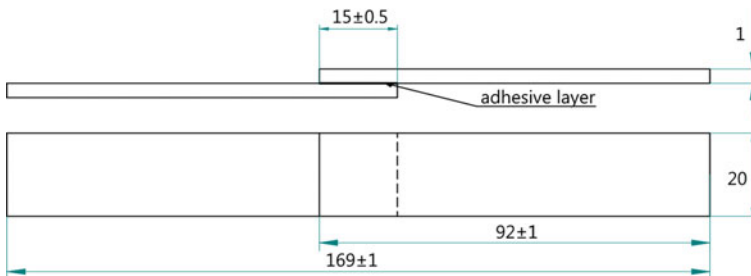


Fig. 2 Adhesive joint diagram and dimensions

Table 3 Types of adhesive compositions used for testing

| No. | Resin | Curing agent | Stoichiometric ratio (%) | Composition name |
|-----|------------|--------------|--------------------------|------------------|
| 1 | Epidian 53 | PAC | 100:80 | E53/PAC/100:80 |
| 2 | | Z-1 | 100:10 | E53/Z1/100:10 |
| 3 | Epidian 5 | PAC | 100:80 | E5/PAC/100:80 |
| 4 | | Z-1 | 100:12 | E5/Z1/100:12 |

Amine curing agent (Z-1) and polyamide curing agent (PAC) are used for curing reactive resins. They are usually applied with low-molecular weight (liquid) epoxy resins or in various compositions based on them. The properties of both the curing agents and epoxy resins were analysed in papers [12–14].

Ingredients of respective epoxy adhesives (Table 3) were agitated mechanically for 90 s with a disc agitator at a speed of 128 m/min in a polymer tank at a mixing station. Before the gluing process, the surfaces of copper sheet samples were machined with P100 grit sandpaper, after which they were cleaned and degreased with an acetone-based degreaser Loctite 7061 (Henkel, Belgium). To clean the surface of the contaminants left after the machining, it was sprayed with a large amount of degreaser and wiped dry with a dust-free cloth. Then the degreasing agent was applied again and the surface was allowed to dry for approx. 10 s. The prepared adhesive compositions were applied manually on one of the joined surfaces. The uniform thickness of the adhesive joint was obtained in the curing process using appropriate equipment. The samples were cured in one step at a temperature of 24 ± 2 °C and humidity of $28 \pm 2\%$ for 8 days, under pressure of 0.18 MPa.

3 Strength Tests

All strength tests were carried out using a Zwick/Roell 150 testing machine (Zwick/Roell GmbH&Co. KG, Ulm, Germany) at a temperature of 24 ± 2 °C and air humidity of $28 \pm 2\%$. The conditioning time for joint samples before strength tests in the above-mentioned conditions was 24 h. The solder joints were subjected to destructive strength tests in accordance with DIN EN 1465 [15] to determine the load capacity in the tensile test. Shear strength tests in accordance with the said standard were also performed on the adhesive joints after a specified curing time to specify the load capacity of adhesive joints.

3.1 Test Results for Solder Joints

Figure 3 shows the load capacity test results for solder joints. Based on the obtained

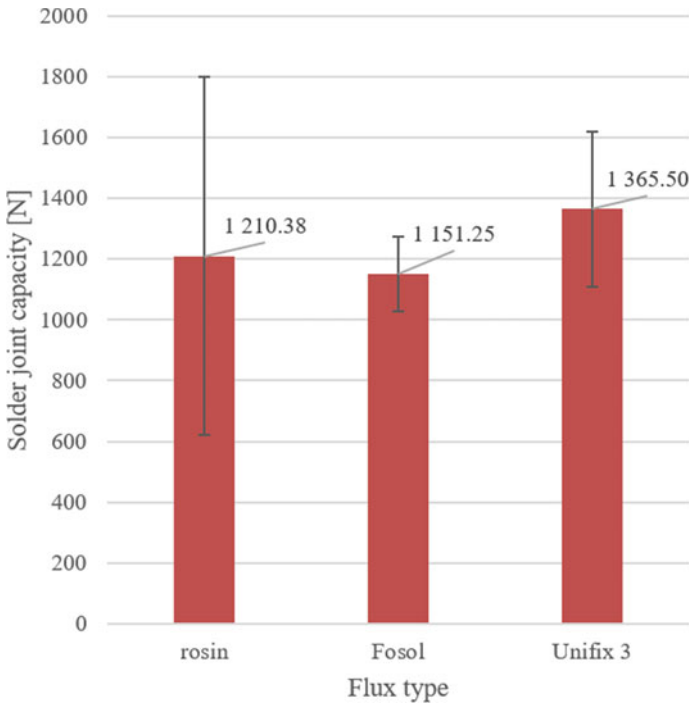


Fig. 3 Strength test results for solder joints

test results, it was observed that the lowest mean value of load capacity was demonstrated by the solder joints made with Fosol flux—1 151.3 N, but in this case the joints showed the best repeatability. The highest dispersion of results were recorded in the joints made with rosin. The highest mean value of load capacity was obtained for the joints made with Unifix 3 paste—1 365.5 N.

In order to comprehensively evaluate and compare the obtained results, it was necessary to conduct a statistical analysis. The Shapiro-Wilk normality test was performed to check the match between the obtained empirical test results for the analysed variables and the normal distribution, distinguished according to the type of flux applied, at the assumed significance level $\alpha = 0.05$. After confirming that the distribution of results was consistent with the normal distribution, ANOVA was then carried out to determine significant differences between the groups. The Tukey's range test was used for different sample sizes in respective groups to specify significant differences. It was shown that in the case of solder joints, no significant differences were found at the significance level $\alpha = 0.05$ for each type of flux, and all groups were within the range of one homogeneous group. This means that the type of flux, chosen from among the three tested ones, does not have a significant impact on the strength of solder joints.

3.2 Test Results for Adhesive Joints

The strength test results for adhesive joints made with the selected adhesive compositions are listed in Fig. 4. The obtained test results indicated that the highest value of the load capacity was obtained for adhesive joints made with composition E53/PAC/100:80—2 585 N, which at the same time was characterised by the highest dispersion of results, while the lowest value was recorded for adhesive joints made with adhesive composition E5/Z1/100:12—257.7 N.

As in the case of the results for solder joints, a statistical analysis was performed for the obtained results. The normality of the distribution was checked for each group of samples, distinguished according to the type of adhesive composition, at the assumed significance level of $\alpha = 0.05$. The normality test results indicated that the distribution of the results was consistent with the normal distribution. The following ANOVA and Tukey’s range test for different sample sizes in individual groups were used for determining homogeneous groups (Table 4).

The results of statistical analyses indicate that the adhesive joints that showed the highest mean value of the load capacity (E53/PAC/100:80) are in one homogeneous group (c) of adhesive joints E5/PAC/100:80, and there were no statistically significant differences were observed between them. The lowest mean value of the load capacity

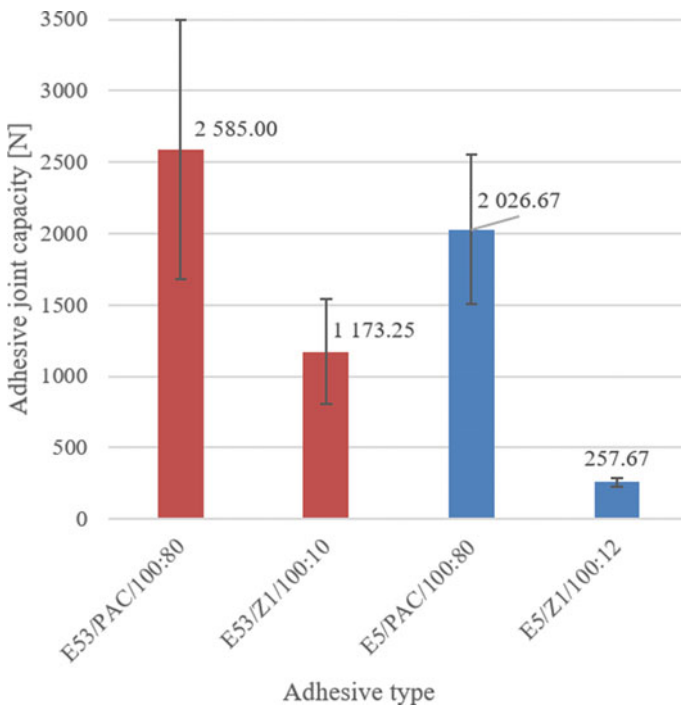


Fig. 4 Strength test results for adhesive joints

Table 4 Tukey’s range test results for different sample sizes

| No. | Adhesive type | Mean joint load capacity (N) | Homogeneous group | | |
|-----|----------------|------------------------------|-------------------|---|---|
| | | | a | b | c |
| 1 | E53/PAC/100:80 | 2 585.0 | * | | |
| 2 | E53/Z1/100:10 | 1 173.3 | | * | |
| 3 | E5/PAC/100:80 | 2 026.7 | * | * | |
| 4 | E5/Z1/100:12 | 257.7 | | | * |

Table 5 Tukey’s range test results for different N

| No. | Joint type | Adhesive/flux | Mean joint load capacity (N) | Homogeneous group | |
|-----|------------|---------------|------------------------------|-------------------|---|
| | | | | a | b |
| 1 | Soldered | Fosol | 1 151.3 | * | |
| 2 | Adhesive | E53/Z1/100:10 | 1 173.3 | * | |
| 3 | Soldered | Rosin | 1 210.4 | * | |
| 4 | Soldered | Unifix 3 | 1 365.5 | * | * |
| 5 | Adhesive | E5/PAC/100:80 | 2 026.7 | | * |

was obtained for the adhesive joints made with E5/Z1/100:12, which are in a separate homogeneous group (a); the result differs significantly from the others. In the case of two groups of adhesive joints—E53/PAC/100:80 and E53/Z1/100:10—there were no statistically significant differences at the assumed significance level.

3.3 Comparative Analysis

The results obtained in the above statistical analysis suggest that it is possible to make a direct comparison of the load capacities of joints made with the two analysed methods, and additional statistical analyses were performed using post-hoc multiple comparison tests, such as Tukey’s test. The analysis included all the solder joints results, as there were no statistically significant differences between them, and the results of the load capacity of selected adhesive joints—those distinguished as a homogenous group after previous statistical analysis, and whose values were similar to the results of solder joints.

The summary of results (Table 5, Fig. 5) shows that the load capacity of the solder joints corresponds directly to the load capacity of the adhesive joint made with one of the compositions, namely E53/Z1/100:10. This places the tested solder joints exactly between the strongest and weakest adhesive joints. Therefore, it is worth considering other criteria for selecting the type of technology for joining the analysed sheets, in addition to strictly strength-related criteria. The starting point will be the operational

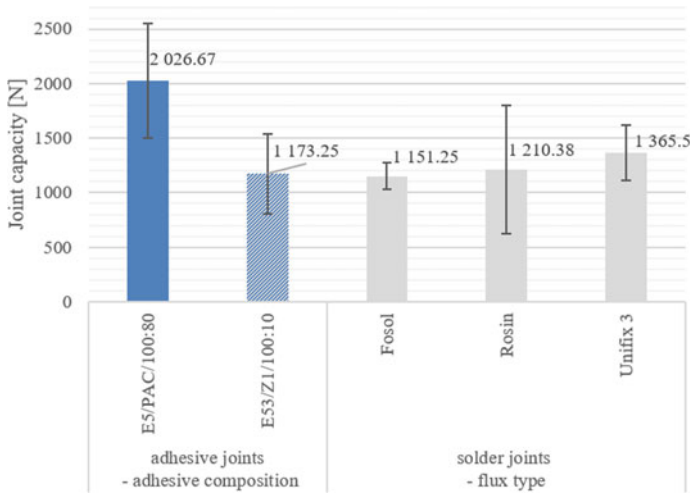


Fig. 5 Summary of a homogeneous group of solder and adhesive joints

requirements for joined materials, i.e. conditions of use (e.g. temperature), expected load capacity or cost-effectiveness criteria for making the joint.

4 Summary and Conclusions

Based on the strength tests of solder joints, prepared under the above-described conditions, it can be observed that the use of various fluxes, such as: rosin, Fosol or Unifix 3 paste, does not indicate statistically significant differences in the load capacity of such joints. The minimal differences in results of individual groups are within one statistically homogeneous group.

In the case of adhesive joints, the following conclusions may be made on the basis of the results:

1. In the group of adhesive joints, the highest value of load capacity was achieved by joints made with adhesive E5/PAC/100:80.
2. The strength properties of adhesive joints indicate that a much better choice for joining copper elements is an adhesive containing a polyamide curing agent (PAC), regardless of the type of resin used. Thanks to the use of a polyamide curing agent, it is possible to make a flexible joint, which is very important in the case of materials such as copper. The above formulation was confirmed by the statistical analysis of the test results, which indicates no significant differences between the groups of adhesive joints E5/PAC/100:80 and E53/PAC/100:80.
3. The lowest load capacity value was recorded for the adhesive joints made with adhesive E5/Z1/100:12 containing an amine curing agent (Z-1). This adhesive joint was also characterized by considerable stiffness.

4. The load capacity of the analysed solder joints corresponds to the load capacity of the adhesive joint of average strength (1 173.25 N).

To sum up, it should be concluded that in both cases of joints it is important to properly prepare the surface, which is one of the basic conditions for making a joint correctly. An additional criterion for adhesives is the selection of a product with good strength properties. This information may have a significant impact on the design of the technology for solder and adhesive joints of analysed construction material. It may be concluded that better results could be obtained if the surface preparation method was changed for solder joints, or a different type of adhesive compositions was selected for adhesive joints.

The project/research was financed in the framework of the project Lublin University of Technology-Regional Excellence Initiative, funded by the Polish Ministry of Science and Higher Education (contract no. 030/RID/2018/19).

References

1. Kroupa A, Andersson D, Hoo N, Pearce J, Watson A, Dinsdale A, Mucklejohn S (2012) Current problems and possible solutions in high-temperature lead-free soldering. *J Mater Eng and Perform* 21:629–637. <https://doi.org/10.1007/s11665-012-0125-3>
2. Pstruś J, Ozga P, Gancarz T, Berent K (2017) Effect of graphene layers on phenomena occurring at interface of Sn-Zn-Cu solder and Cu substrate. *J Electr Mater* 46:5248–5258. <https://doi.org/10.1007/s11664-017-5529-2>
3. Puranik G (2020) Soldering of copper using graphene-phosphoric acid gel. *J Metals Mater Miner* 6067. <https://doi.org/10.14456/JMMM.2020.52>
4. Prach M, Koleňák R (2015) Soldering of copper with high-temperature Zn-based Solders. *Proc Eng* 100:1370–1375. <https://doi.org/10.1016/j.proeng.2015.01.505>
5. Rudawska A, Abdel Wahab M, Szabelski J, Miturska I, Doluk E (2021) The strength of rigid and flexible adhesive joints at room temperature and after thermal shocks. In: Abdel Wahab M (ed) *Proceedings of 1st international conference on structural damage modelling and assessment*. Springer Singapore, Singapore, pp 229–241. https://doi.org/10.1007/978-981-15-9121-1_18
6. Szabelski J (2018) Effect of incorrect mix ratio on strength of two component adhesive Butt-Joints tested at elevated temperature. *MATEC Web Conf* 244:01019. <https://doi.org/10.1051/mateconf/201824401019>
7. Rudawska A, Miturska I, Szabelski J, Abdel Wahab M, Stančeková D, Čuboňová N, Madleňák R (2020) The impact of the selected exploitation factors on the adhesive joints strength. In: Wahab MA (ed) *Proceedings of the 13th international conference on damage assessment of structures*. Springer Singapore, Singapore, pp 899–913. https://doi.org/10.1007/978-981-13-8331-1_72
8. Kendall K, Dahm RH, Packham DE, Cope BC, Allen KW, Greef R, Parker GC, Watson C, Watts JF, Whitehouse NR, Ashley RJ (2005) Epoxide adhesives: curatives. In: Packham DE (ed) *Handbook of adhesion*. John Wiley & Sons, Ltd, Chichester, UK, pp 123–161. <https://doi.org/10.1002/0470014229.ch5>
9. Michels J, Sena Cruz J, Christen R, Czaderski C, Motavalli M (2016) Mechanical performance of cold-curing epoxy adhesives after different mixing and curing procedures. *Compos B Eng* 98:434–443. <https://doi.org/10.1016/j.compositesb.2016.05.054>
10. Rudawska A (2008) Surface free energy and geometric structures of the surfaces of selected epoxy composites. *Polimery* 53:452–456. <https://doi.org/10.14314/polimery.2008.452>

11. EN 13601 (2013) Copper and copper alloys—copper rod, bar and wire for general electrical purposes
12. Rudawska A, Frigione M (2020) Aging effects of aqueous environment on mechanical properties of calcium carbonate-modified epoxy resin. *Polymers* 12:2541. <https://doi.org/10.3390/polym12112541>
13. Rudawska A (2020) The effect of the salt water aging on the mechanical properties of epoxy adhesives compounds. *Polymers* 12:843. <https://doi.org/10.3390/polym12040843>
14. Rudawska A (2019) The impact of the seasoning conditions on mechanical properties of modified and unmodified epoxy adhesive compounds. *Polymers* 11:804. <https://doi.org/10.3390/polym11050804>
15. EN 1465 (2009) Adhesives—Determination of tensile lap-shear strength of bonded assemblies

Design of an Experiment to Analyze Modal Parameters in a Crack and Without Crack Conditions in the Presence of Thermal and Mechanical Vibration



Khangamlung Kamei  and Muhammad A. Khan

Abstract Vibration fatigue is a common phenomenon in structural dynamic due to thermal and mechanical loads. This paper designed an experimental method to access the impact of temperatures on the vibration behavior of crack and without crack beam. This experimental design was considered without crack and with a crack of three crack depth 0.25 mm, 0.5 mm, and 1 mm. To analyze the effect of temperatures, three cases of ramping of temperatures were considered. The first case ramped at 2 °C/min allowing the temperature to increase in a slow and steady state to reach the desired temperature. The second case allotted the temperature to increase at a moderate rate at 5 °C/min. In the third case, the temperature was allowed to increase rapidly at a rate of 8 °C/min. This controlled rate of heating the beam was monitor from a PID temperature controller. The experimental results showed that different ramped of temperature has some influence on modal parameters. The temperature ramped at 2 °C/min has more impact on modal parameters than ramped at 5 °C/min and 8 °C/min. While this effect is negligible for lower temperatures, but it is obvious at elevated temperatures. This suggested heating the beam at different rates affects vibration response. Thus, this indicated the heating rate can make some effect on the vibration response measurement of mechanical structures.

Keywords Thermal analysis · Vibration fatigue · Vibration testing · Modal analysis · Fracture mechanics · Structural response

1 Introduction

Vibration analysis is one of the non-destructive investigation techniques. It is vastly studied for structural health monitoring [1, 2]. Traditionally, vibration-based inspections on structures were performed in absence of a thermal environment. In recent years, the research is focused to include temperature load in structural health analysis.

K. Kamei (✉) · M. A. Khan

School of Aerospace, Transport and Manufacturing, Cranfield University, Bedford MK43 0AL, UK

e-mail: k.kamei@cranfield.ac.uk

This is vital because most of the engineering structures particularly in industries such as automotive, aircraft, power plant, etc. work in thermal environments. The system response may vary depends on the working condition especially during the heating and cooling process. The rate of heating and temperature exposure duration can be one of the sources of the thermal disturbance in dynamic response. Warminska et al. [3] studied that the system response is subjected by mechanical and thermal loads. The change in global temperature fluctuated the vibration and eigen frequencies.

In literature, the thermal effect and its distribution on structures have been studied [4–11]. Khan et al. [12] examined that the global temperature of the structure affects the stress intensity and thereby modifies its structural response. Cao et al. [13] specified that thermal vibration and thermal expansion were due to an increase in inter-atomic bond length at high temperatures. The thermal vibration increases with an increase in temperatures. Silva et al. [14], investigated modal analysis in non-uniform temperature distribution heated rectangular plate with the help of digital image correlation. They found that resonant frequencies of the plate were higher for transverse heating than longitudinal heating. This attenuation rate of dimensionless frequency at high temperatures was also observed in functionally graded material [5, 15]. This suggested that temperatures play a vital role in the structural response. In this paper, the effect of heating rate with different exposure times on structural dynamics was examined. It investigated the modal behavior of the cantilever beam subjected to three heating rates. The first case ramped at $2\text{ }^{\circ}\text{C}/\text{min}$ allowing the temperature to increase in a slow and steady state to reach the desired temperature. The second case allotted the temperature to increase at a moderate rate at $5\text{ }^{\circ}\text{C}/\text{min}$. In the third case, the temperature was allowed to increase rapidly at a rate of $8\text{ }^{\circ}\text{C}/\text{min}$. This controlled rate of heating the beam was monitor from a PID temperature controller. The experimental results showed that different ramped of temperature has some influence on modal parameters. The temperature ramped at $2\text{ }^{\circ}\text{C}/\text{min}$ has more impact on modal parameters than ramped at $5\text{ }^{\circ}\text{C}/\text{min}$ and $8\text{ }^{\circ}\text{C}/\text{min}$. While this effect is negligible for lower temperatures, but it is obvious at elevated temperatures. This suggested heating the beam in different rates affect vibration response. Thus, this indicated the heating rate can make some effect on the vibration response measurement of mechanical structures.

2 Materials and Method

2.1 Experimental Setup

The experimental set-up consists of three modules as shown in Fig. 1. The vibrating mechanism consists of a signal generator, power amplifier, and mechanical shaker. The role of the power amplifier is to amplify the applied voltage generated from the signal generator. This amplified voltage is input to the shaker. The shaker provides the fixed amplitude of 2 mm against the input of 3.2 V. The thermal unit consists

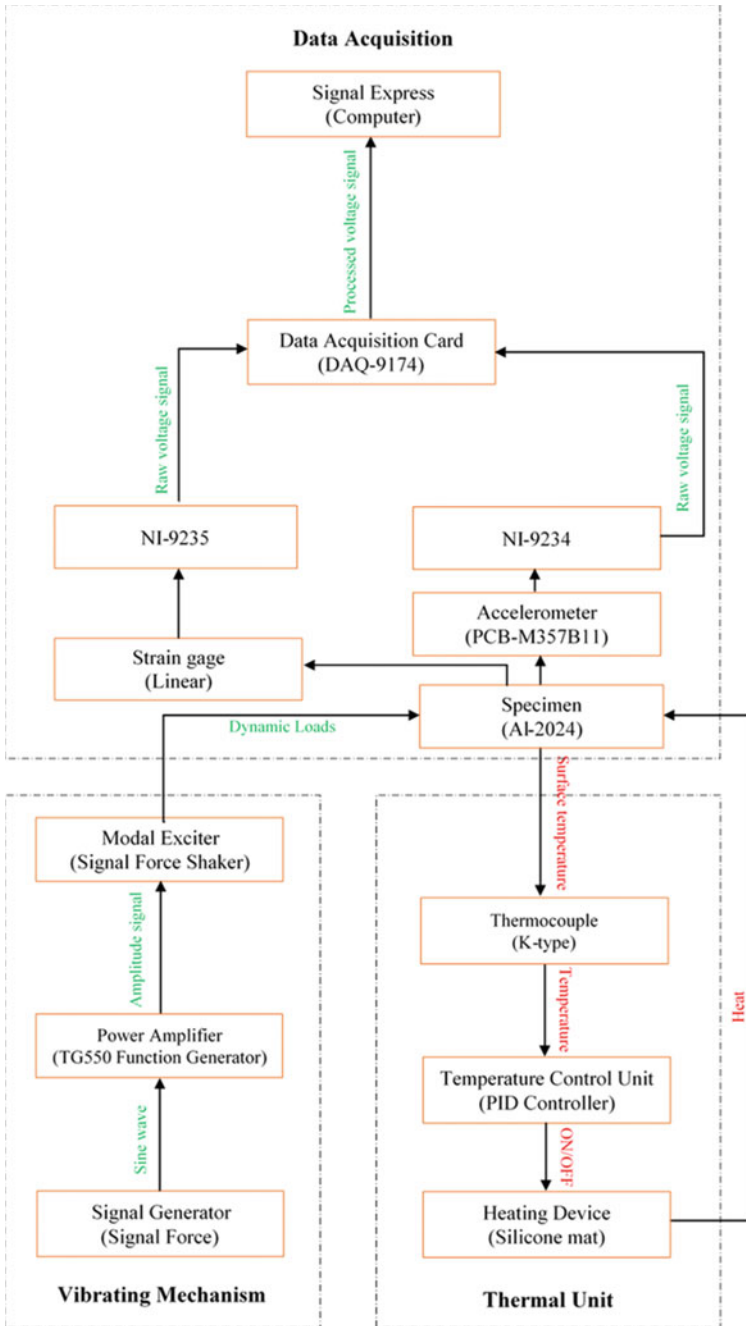


Fig. 1 Experimental layout

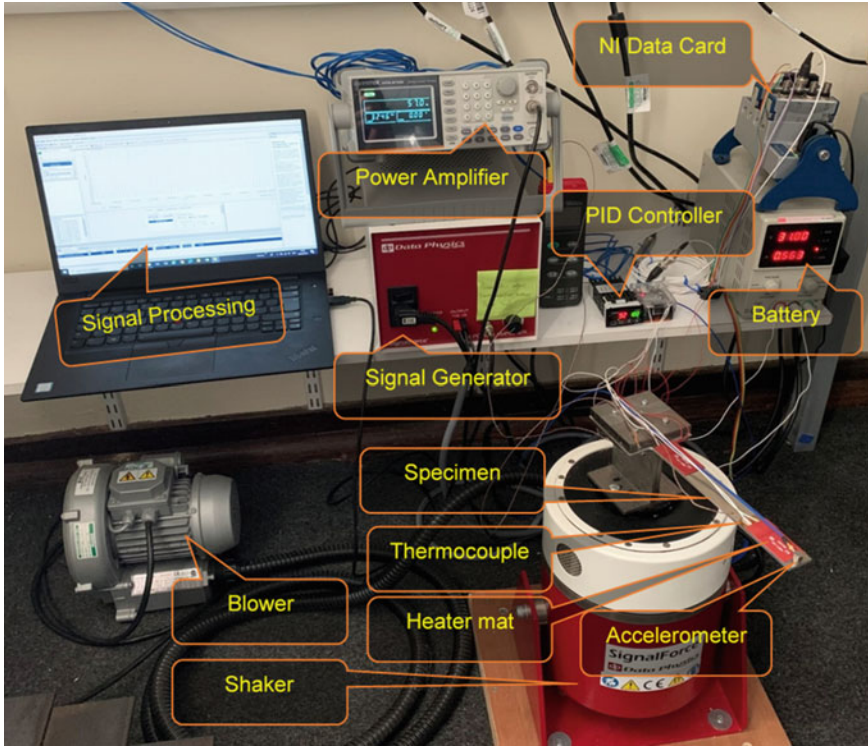


Fig. 2 Experimental set-up

of a thermal couple, a PID temperature controller, and a thermal mat. The K-type thermal couple is used to measure the specimen temperature. Then, this specimen temperature is input to the PID temperature controller to control the heat supplied to the specimen through the thermal mat. The third module is the data acquisition unit. It consists of strain gage, accelerometer, data acquisition card, and software National Instrument Signal Express. The strain gage is fixed near the fixed end of the specimen. The accelerometer is mounted at the free end of the specimen to measure the modal amplitude. The signal express is used to analyze the dynamic response of the specimen. The detail of the experimental set-up is shown in Fig. 2.

2.2 Specimen Preparation

The experimental specimens were prepared from Aluminum 2024-T3. The geometries and their dimensions of without crack and with the crack specimen are shown in Figs. 3 and 4 respectively. Figure 5 shows the test specimens. The specimen has

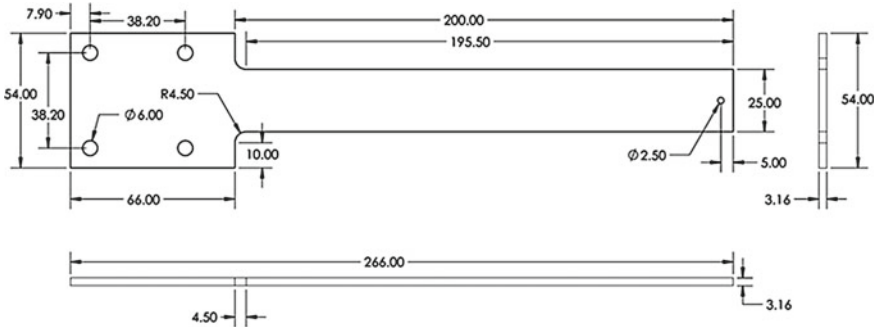


Fig. 3 Geometry of without crack specimen

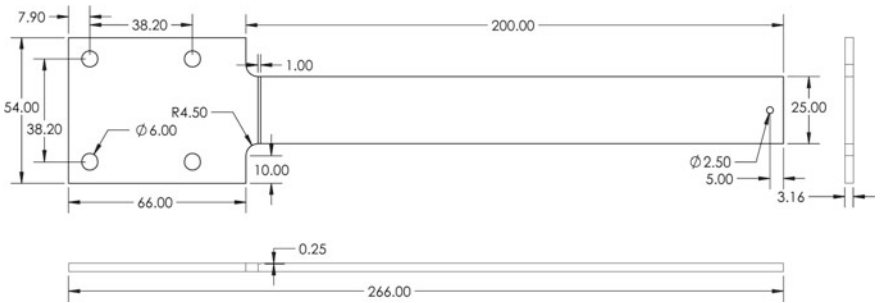


Fig. 4 Geometry of with crack specimen

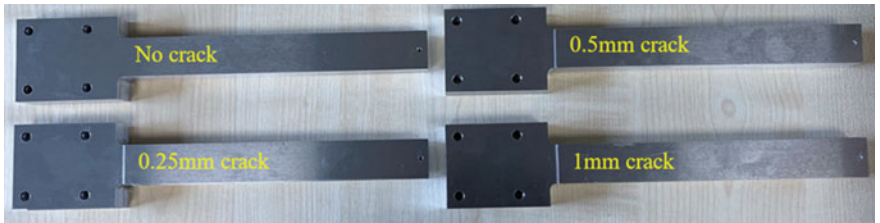


Fig. 5 Test specimens

four holes of 6 mm diameter to fix on the shaker. Another hole of 2.5 mm diameter is provided at the free end to mount the accelerometer. The test specimens were manufactured using a CNC machine to produce accurate dimensions.

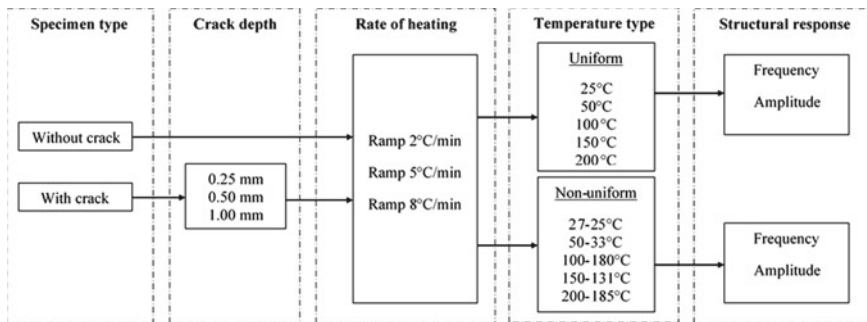


Fig. 6 Experimental scheme

2.3 Experimental Design

In this experimental study, four types of specimens were chosen: without crack, rectangular crack of crack depth 0.25 mm, 0.5 mm, and 1 mm. The specimen without crack was chosen to test the modal response in healthy conditions. While the three crack specimens were selected to analyze the modal behavior under crack conditions. The predefined crack depths were preferred based on the criteria that the initial crack was 0.25 mm and propagated to 1 mm crack depth. The crack location for all the crack specimens is the same which is 4.5 mm away from the fixed end as shown in Figs. 4 and 5. This crack location was kept in the fillet area of the specimen where there is maximum stress concentration during the vibration.

The experimental scheme was designed to examine the modal behavior of the cantilever beam under healthy and crack conditions as shown in Fig. 6. The experiments were conducted for uniform and non-uniform temperatures to a maximum temperature of 200 °C. The beam subjected to three heating rates: 2 °C/min, 5 °C/min, and 8 °C/min were considered. It assumed that heating at the rate of 2 °C/min was slow heating while 5 °C/min, and 8 °C/min were counted as medium and fast heating respectively. This selection of heating rates was considered to monitor the heating effect on the structural response measurement.

3 Results and Discussions

3.1 Time of Heating the Specimen

This research studied the heating effect on the modal response of a cantilever beam. The specimens were assessed in the temperature range of 25–200 °C. The beam was subjected to three types of heating. The first case was heating the beam at the rate of 2 °C/min. The second case was heating at 5 °C/min and the third case

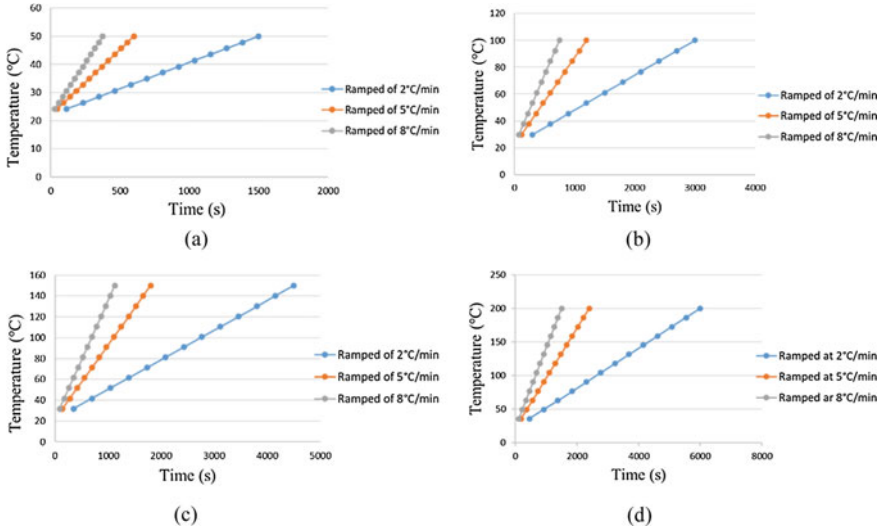


Fig. 7 Time required for different heating rates **a** 50 °C, **b** 100 °C, **c** 150 °C, **d** 200 °C

at 8 °C/min for the same temperatures. This means that slow heating allowed the specimen to expose to temperature for a longer time than medium and fast heating for the same temperatures. Figure 7 shows the time required for different heating rates for the temperature of 50 °C, 100 °C, 150 °C, and 200 °C. It is seen from the graphs that heating at 2 °C/min takes more time to reach the temperatures. While heating at 5 °C/min takes lesser time and heating at 8 °C/min takes least time for all the temperatures. Thus, heating at various rates allowed the specimen to expose to temperatures for a different time. This consequently may adversely affect the material properties especially at higher temperatures leading to deviating modal responses.

3.2 Modal Response of the Cantilever Beam

At first, the experiments were conducted for uniform temperature across the beam. The natural frequency of the cantilever beam with crack and without crack was determined by impact test. The comparison of natural frequency for different heating rates of without crack beam is shown in Fig. 8. It showed that the beam natural frequency decreases with an increase in temperature. The ramping of temperature at different rates has little impact on the natural frequency. Ramping of temperature at the rate of 2 °C/min had more impact on natural frequency by diminishing its frequency.

However, ramping at 5 °C/min and 8 °C/min had little influence compared to ramping at 2 °C/min. This effect of ramping temperature was more significant for higher temperatures. This means that heating at 2 °C/min took more time to reach

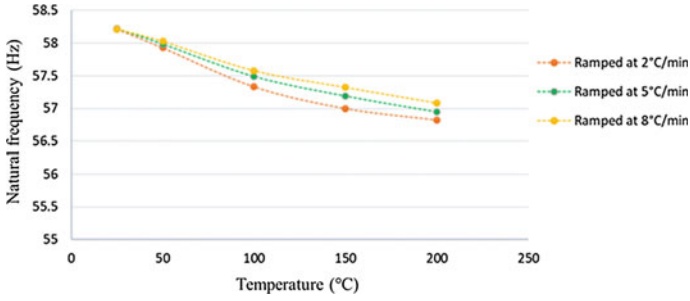


Fig. 8 Natural frequency of without crack in a uniform temperature

the desired temperature as discussed above has affected the structural integrity. This suggested that the beam exposed to a temperature for a longer duration changes the interatomic bond length, especially at high temperatures. Similarly, the natural frequency of crack beams decreases with the increase in temperature and crack depths as shown in Figs. 9, 10 and 11. The heating effect was also apparent for all the crack depths. These experiments aim to verify this by ramped at 2 °C/min, 5 °C/min, and 8 °C/min for all three crack depths. Thus, the effect of heating rates was compared for

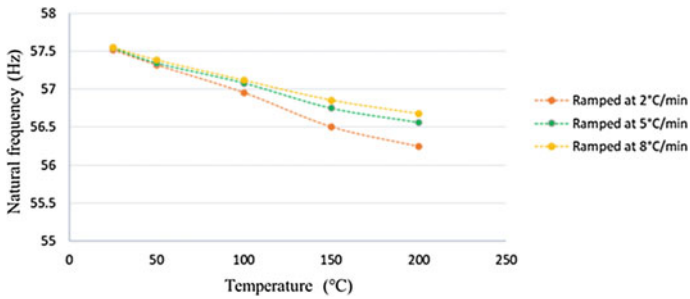


Fig. 9 Natural frequency of 0.25 mm crack depth in a uniform temperature

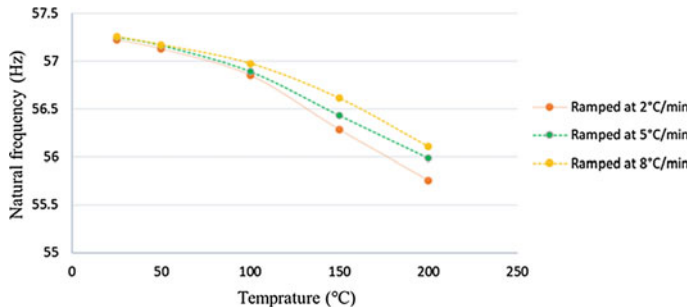


Fig. 10 Natural frequency of 0.5 mm crack depth in a uniform temperature

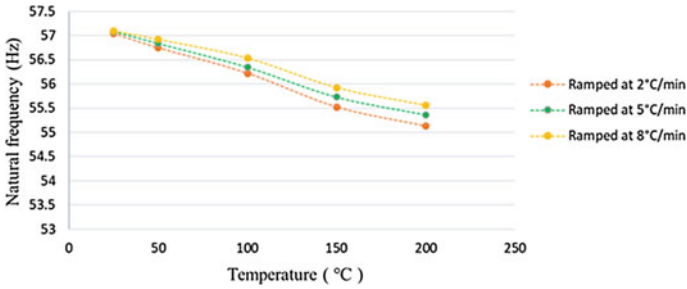


Fig. 11 Natural frequency of 1 mm crack depth in a uniform temperature

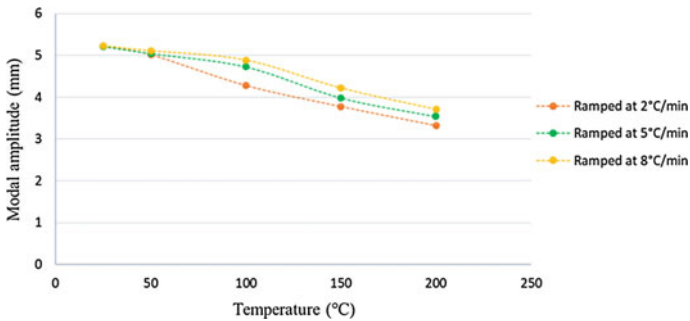


Fig. 12 Modal amplitude of without crack in a uniform temperature

all the specimens as shown in respective figures. It is seen that this effect is minimal at lower temperatures and more noticeable at higher temperatures.

The modal amplitude of without crack for different temperatures is shown in Fig. 12. The graph illustrates that the amplitude decayed as the temperature increased. The drop of amplitude was associated with beam fundamental frequency. Therefore, the modal amplitude displayed a heating effect similar to the fundamental frequency. The heating rate at 2 °C/min showed lower vibration amplitude as compared to the others. This indicates structures went through a more elastic behavior at higher heating rates. This influence of heating rate was quite visible at high temperature values. The modal amplitude for 0.25 mm, 0.5 mm and 1 mm crack depth is presented in Figs. 13, 14 and 15 respectively. Comparatively, the declining trend of amplitude behavior for 1 mm crack depth was more linear than 0.25 mm and 0.5 mm crack depth. This signified the increase in crack depth reduced the beam stiffness.

In non-uniform temperature analysis, the two ends of the beam were allowed to have different temperatures. This temperature difference was achieved by keeping the thermal mat at one end and other end was held without any heat supplied. The temperature of both ends of the specimen was measured by different thermocouples. It was observed that when the applied temperature at one end was 27 °C, the other end was 25 °C. Similarly, the temperature differences on both ends were observed

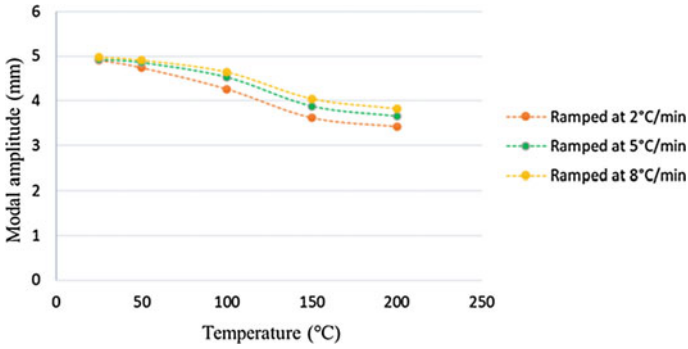


Fig. 13 Modal amplitude of 0.25 mm crack depth in a uniform temperature

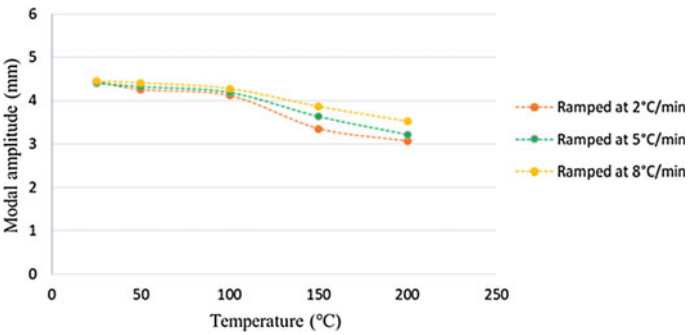


Fig. 14 Modal amplitude of 0.5 mm crack depth in a uniform temperature

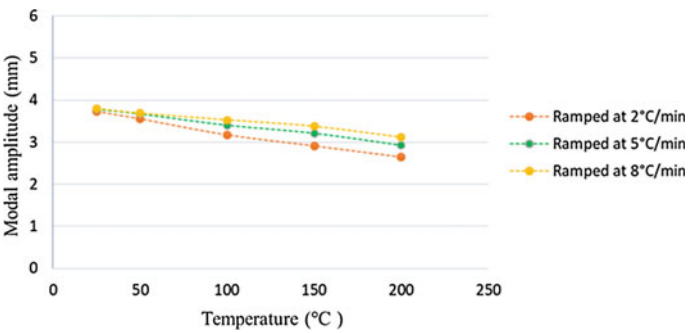


Fig. 15 Modal amplitude of 1 mm crack depth in a uniform temperature

as: 50–33 °C, 100–80 °C, 150–131 °C and 200–185 °C. The natural frequency of without crack beam under non-uniform temperature is shown in Fig. 16 and its modal amplitude in Fig. 17. The results appeared that the respective modal parameters of all

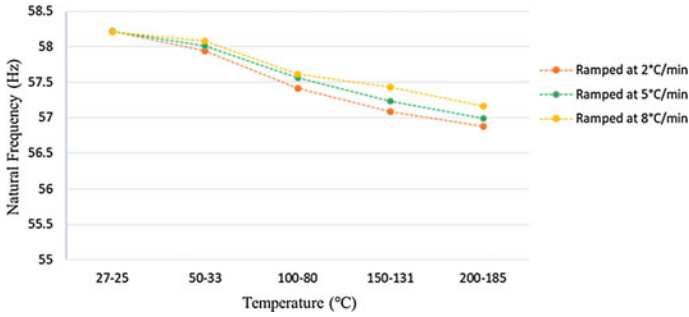


Fig. 16 Natural frequency of without crack in non-uniform temperature

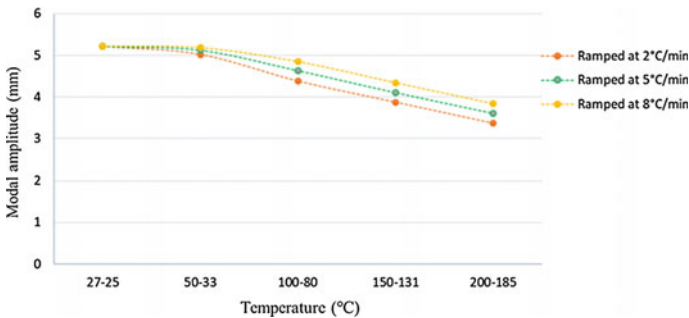


Fig. 17 Modal amplitude of without crack in non-uniform temperature

the experiments of without crack and with crack beams were higher for non-uniform temperature than uniform temperature analysis.

4 Conclusion

The dynamic response of the mechanical structure is frequently used to analyze the structure health monitoring. In the present paper, an experimental design was developed to study the dynamic response of the cantilever beam. The effect of temperature on the modal response of the cantilever was studied by using three heating rates. It was observed that heating rate has influenced the modal behavior of the beam, especially at higher temperatures. The results of the experiments showed that heating at the rate of 2 °C/min has the least fundamental frequency and its amplitude compared to the ramped at 5 °C/min and 8 °C/min. This is because heating at 2 °C/min takes more time to reach the test temperature and thereby accumulating heat on the beam for a longer duration. This heating effect was observed both in a crack and without a crack beam. The results also showed that the modal frequency and its amplitude decrease with the increase in temperature and crack depth. The decreases of modal

parameters indicated the reduction in beam stiffness. Thus, this research established that the rate of heating can impact measuring the dynamic response of the mechanical system.

References

1. Kamei K, Khan MA (2021) Current challenges in modelling vibrational fatigue and fracture of structures: a review. *J Braz Soc Mech Sci Eng* 43
2. Zai BA, Khan MA, Mansoor A, Khan SZ, Khan KA (2019) Instant dynamic response measurements for crack monitoring in metallic beams. *Insight Non-Destr Test Cond Monit* 61:222–229
3. Warminska A, Manocha E, Warminski J, Samborski S (2015) Regular and chaotic oscillations of a Timoshenko beam subjected to mechanical and thermal loadings. *Contin Mech Thermodyn* 27:719–737
4. Ebrahimi F, Jafari A (2016) Thermo-mechanical vibration analysis of temperature-dependent porous FG beams based on Timoshenko beam theory. *Struct Eng Mech* 59:343–371
5. Ebrahimi F, Ghasemi F, Salari E (2016) Investigating thermal effects on vibration behavior of temperature-dependent compositionally graded Euler beams with porosities. *Meccanica* 51:223–249
6. Julien B, Bertrand F, Thierry Y (2013) Probabilistic random vibration fatigue. *Proc Eng* 66:522–529
7. Ghayesh MH, Kazemirad S, Darabi MA, Woo P (2012) Thermo-mechanical nonlinear vibration analysis of a spring-mass-beam system. *Arch Appl Mech* 82:317–331
8. Zhang W, Chen H, Zhu D, Kong X (2014) The thermal effects on high-frequency vibration of beams using energy flow analysis. *J Sound Vib* 333:2588–2600
9. Cui DF, Hu HY (2014) Thermal buckling and natural vibration of the beam with an axial stick-slip-stop boundary. *J Sound Vib* 333:2271–2282
10. Ghadiri M, Shafiei N, Alavi H (2017) Thermo-mechanical vibration of orthotropic cantilever and propped cantilever nanoplate using generalized differential quadrature method. *Mech Adv Mater Struct* 24:636–646
11. Khan MA, Khan SZ, Sohail W, Khan H, Sohaib M, Nisar S (2015) Mechanical fatigue in aluminium at elevated temperature and remaining life prediction based on natural frequency evolution. *Fatigue Fract Eng Mater Struct* 38:897–903
12. Khan KA, Muliana AH, Rajagopal KR, Wineman A (2018) On viscoelastic beams undergoing cyclic loading: Determining the onset of structural instabilities. *Int J Non Linear Mech* 99:40–50
13. Cao G, Chen X, Kysar JW (2006) Thermal vibration and apparent thermal contraction of single-walled carbon nanotubes. *J Mech Phys Solids* 54:1206–1236
14. Santos Silva AC, Sebastian CM, Lambros J, Patterson EA (2019) High temperature modal analysis of a non-uniformly heated rectangular plate: experiments and simulations. *J Sound Vib* 443:397–410
15. Ebrahimi F, Salari E, Hosseini SAH (2016) In-plane thermal loading effects on vibrational characteristics of functionally graded nanobeams. *Meccanica* 51:951–977

Impact of Mechanical Treatment on Strength of Steel Adhesive Joints



Anna Rudawska, Magd Abdel Wahab, Izabela Miturska, Jakub Szabelski, Elżbieta Doluk, and Dana Stančeková

Abstract This article focuses on the surface treatment as a first stage of bonding technology. The aim of the article is to compare several variants of the mechanical treatment of the C45 steel surface and to determine the influence of the surface treatment method on the single-lap joints strength. Seven different variants of mechanical treatment were analyzed with the use of four different abrasive papers: P40, P120, P320 and P500. The geometric structure of the prepared samples was also analyzed by determining selected surface roughness parameters using the HOMMEL TESTER T1000 contact profilometer. Directly before bonding, the surface of the steel samples was degreased with a degreasing agent based on aliphatic hydrocarbons. The two-component epoxy adhesive containing epoxy resin based on Bisphenol A and polyaminoamide curing agent was used to prepare the steel-epoxy adhesive joints. The shear strength tests of the adhesive joints were carried out according to the DIN EN 1465 standard. On the basis of the strength results, it can be concluded that among the tested surface treatment variants, the use of the mechanical treatment with single abrasive papers is more advantageous. The least suitable method of surface treatment

A. Rudawska (✉) · I. Miturska · J. Szabelski · E. Doluk
Faculty of Mechanical Engineering, Lublin University of Technology, Nadbystrzycka 36 St,
20-618 Lublin, Poland
e-mail: a.rudawska@pollub.pl

I. Miturska
e-mail: i.miturska@pollub.pl

J. Szabelski
e-mail: j.szabelski@pollub.pl

E. Doluk
e-mail: e.doluk@pollub.pl

M. Abdel Wahab
Faculty of Engineering and Architecture, Ghent University, Technologiepark Zwijnaarde 903,
B-9052 Zwijnaarde, Belgium
e-mail: magd.abdelwahab@ugent.be

D. Stančeková
Faculty of Mechanical Engineering, University of Žilina, Univerzitná 1, 010 26 Žilina, Slovakia
e-mail: dana.stancekova@fstroj.uniza.sk

© The Author(s), under exclusive license to Springer Nature Singapore Pte Ltd. 2022
M. Abdel Wahab (ed.), *Proceedings of the 9th International Conference on Fracture, Fatigue and Wear*, Lecture Notes in Mechanical Engineering,
https://doi.org/10.1007/978-981-16-8810-2_9

of adherend surface turns out to be the abrasive treatment, in which several abrasive papers are used.

Keywords Mechanical treatment · Abrasive paper · Steel adhesive joints · Strength

1 Introduction

Bonding is one of the techniques of joining various materials using appropriate construction adhesives [1, 2]. Adhesives belong to the type of the adhesive materials that have the ability to generate adhesion forces to the joined elements. The bonding process consists in introducing a thin layer of adhesive between the surfaces to be joined, which sticks them together using the forces of adhesion and cohesion, i.e. the force of internal cohesion of materials [1, 2].

In the bonding process, there are many factors that affect the strength of the adhesive joints. These include *inter alia*: the surface treatment, the parameters of the curing process, type of degreasing agent, the presence of coatings and the surface roughness [3–8]. Changes in the above factors during the bonding process may affect the properties of specific joints in various ways. The influence of these factors on the strength of the adhesive bonds has been described in many studies [9–14].

The surface treatment is one of the most important steps in the bonding process [2, 11, 15]. It consists in proper preparation of the surface layer, i.e. removing all kinds of dirt, dust and other impurities from it, as well as the oxide layer that is on the metal surfaces, as well as on the proper development of the surface, because the high strength of the joints depends on it. The mechanical and the non-mechanical treatment can be used to clean the surface [11, 15, 16].

The mechanical treatment includes several methods, e.g.: sandblasting, machining, abrasive blasting, shot peening, shot blasting, scraping, grinding, wire brushing or sandpaper, and flame firing [17–22]. The use of the mechanical methods makes it possible to shape the geometric structures of the surface and obtain the appropriate development of the surface. The geometric structure of the surface is the set of all real surface irregularities, which include waviness, shape deviations and roughness [23–25]. Excessive surface roughness can reduce the strength of such a joint when the adhesive is not able to adequately moisten all the cavities of the unevenness. When using mechanical methods, special attention should be paid to the structure of surface unevenness and not to generate large residual stresses, which reduce the strength [26–30].

This work focuses on one of these factors, which is the preparation of the surface for bonding using one of the machining methods—treatment with abrasive coating tools. This type of machining is used both in unit production and in works related to, *inter alia*, re-making adhesive connections during repairs or maintenance. The main advantage of this treatment is its availability and the possibility of using it in various conditions and with different accessibility to the prepared surfaces. The paper compares several methods of surface preparation for C45 steel and determines

the influence of the surface treatment method on the value of the destructive force in single-fold joints. Seven different variants of surface treatment were analyzed, including mechanical treatment of surface preparation with four different abrasive papers: P40, P120, P320 and P500.

2 Test Methodology

2.1 Adhesive Joint and Adherend

The subject of the research were the single-lap adhesive joints of the elements made of C45 steel (Fig. 1), with the following dimensions: the adherend samples length 100 ± 0.1 mm, the adherend samples width $b = 20 \pm 0.08$ mm and the adhered samples thickness $g = 2 \pm 0.02$ mm. The samples were made in the single-lap construction with an overlap length $l_z = 15 \pm 0.24$ mm. An exemplary adherend sample is shown in Fig. 2.

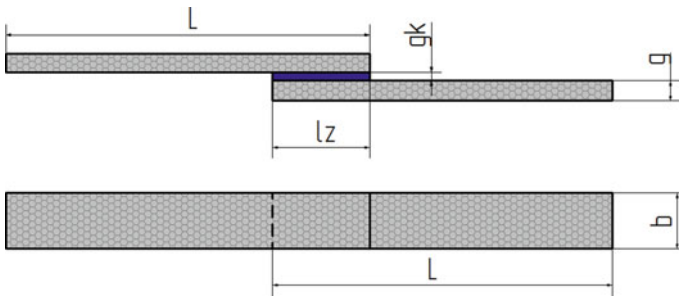


Fig. 1 Scheme of single-lap adhesive joint (designation of symbols in the text)



Fig. 2 Example of a sample made of C45 steel with a thickness of 2 mm

2.2 Characteristics of Surface Treatment Variants

For the treatment of the adherend surface, mechanical processing was used, i.e. grinding, with the use of abrasive paper of the following grain: P40, P120, P320 and P500. Abrasive paper is a thin, flexible carrier (e.g. strong cardboard), covered with an abrasive coating having various grain sizes. The abrasive coating is made of particles of polymeric materials (silicon carbide, aluminum oxide) or natural materials (aluminum oxide, emery). The grains are connected to the support by synthetic resins. There are two main groups of dry and wet abrasive papers. However, regardless of whether they are dry or wet grinding wheels, they have the same grit designation or gradation. Papers with low numbers, such as P40 or P120, mean paper with a coarse grain structure, usually intended for roughing or initial processing of a given material. On the other hand, papers with larger markings, such as P320 or P500, have finer grains and are intended for more precise processing. The higher the number for the abrasive paper marking, the finer the grains. The applied variants of the surface preparation of steel sheet samples are presented in Table 1.

The surface of each sample was treated with approximately 20 circular movements, resulting in unevenness in the structure. Some of the samples were processed with various abrasive papers. This means that the tiles, after being treated with one grinding wheel, were subjected to successive grinding with another abrasive paper with a different grit, and thus the sample combinations as shown in Table 1 were obtained. This was done in order to compare the effect of surfaces with different roughness on the strength of the adhesive joints.

Before bonding, the adherends surfaces were cleaned of contamination with LOCTITE 7063 degreasing agent (Loctite, Henkel Europe). First, the samples were sprayed with a degreaser from a distance of 10 cm, then they were wiped with dust-free swabs to remove dirt, then they were again sprayed and wiped, and the third time—sprayed and allowed to evaporate for approximately 3 min. 112 samples were used in the research, 84 of which were used during the bonding process, and 28 were used to assess the surface structure.

Table 1 Surface treatment variants

| Variants designation | Samples number | Surface treatment variants |
|----------------------|----------------|---|
| V1 | 1–16 | Surface treatment with P40 abrasive paper |
| V2 | 17–32 | Surface treatment with P120 abrasive paper |
| V3 | 33–48 | Surface treatment with P320 abrasive paper |
| V4 | 49–64 | Surface treatment with P500 abrasive paper |
| V5 | 65–80 | Surface treatment with P40 and P120 abrasive papers |
| V6 | 81–96 | Surface treatment with P40, P120 and P320 abrasive papers |
| V7 | 97–112 | Surface treatment with P40, P120, P320 and P500 abrasive papers |

2.3 Adhesive Joints Preparation

Two-component epoxy adhesive containing epoxy resin (trade name Epidian 57, CIECH Resins manufacturer, Nowa Sarzyna, Poland) and a polyamide curing agent (polyaminoamide C, trade name—PAC, CIECH Resins manufacturer, Nowa Sarzyna, Poland) was used to make the adhesive connections. The characteristics of the adhesive components are presented in [31]. Epidian 57 epoxy resin was mixed with a polyamide curing agent in a 1:1 ratio. The designation of the epoxy adhesive used in the work is E57/PAC/1:1. 100 g of the epoxy resin and 100 g of the polyamide curing agent, measured out with electronic scales (OX-8100 type, FAWAG S.A, Lublin, Poland, measurement accuracy 0.1 g, ISO 9001), were thoroughly joined by mechanical mixing with a plate mixer for about 3 min, avoiding the introduction of gas bubbles. Mixing was performed on a mechanical mixing station with a speed of 128 m/min.

Then, after thorough mixing, the adhesive was applied to one of the joined surfaces with a layer thickness of about 0.10 mm. The application of the adhesive was made with a special spatula made of polymer. The made adhesive joints were loaded with the amount 0.18 MPa. The adhesive joints samples were made in one step with the overlap length $l_z \cong 15$ mm. The adhesive joints were cured in one step at an ambient temperature of approx. 25 ± 1 °C and a relative humidity of $28 \pm 2\%$ for 7 days. After preparing the adhesive joints, the samples were conditioned for 24 h (at a temperature of 25 ± 1 °C and a relative humidity of $28 \pm 2\%$) and then subjected to strength tests.

2.4 Experimental Tests

Two types of tests were carried out: (i) measurements of selected parameters of surface roughness of joined materials and (ii) strength tests of adhesive joints.

Measurements of selected parameters of surface roughness, such as: R_a , R_z , R_{max} , R_q and S_m were carried out in accordance with the PN-87M-04251 standard, using the HOMMEL TESTER T1000 contact profilometer (Hommelwerke GmbH, Schwenningen, Germany). During the measurements 0.08 mm the sampling length was used. The description of the individual surface roughness parameters analyzed is presented below:

- R_a —arithmetic mean deviation of the roughness profile,
- R_z —arithmetic mean height of the 5 highest elevations above the mean line, reduced by the arithmetic mean of the 5 lowest pits below the mean line,
- R_{max} —maximum average roughness height,
- R_q —mean square mean of roughness profile ordinates,
- S_m —the average width of the surface roughness intervals.

Strength tests of the prepared adhesive joints were carried out on Zwick /Roell Z150 testing machine (ZwickRoell GmbH&Co. KG, Ulm, Germany), in accordance with DIN EN 1465 standard. The prepared groups of adhesive joints were subjected to the shear strength test in accordance with the test variants (Table 1). The prepared samples were attached to the screw-wedge clamps in the testing machine, and then they were loaded until the samples were broken.

3 Results and Discussion

3.1 Surface Roughness Parameters

Tables 2 and 3 present surface profilograms of steel sheet samples subjected to various variants of surface treatment by mechanical treatment with abrasive coating

Table 2 Profilograms of the surface of samples made of steel sheet depending on the variants of surface treatment—treatment with one type of abrasive paper

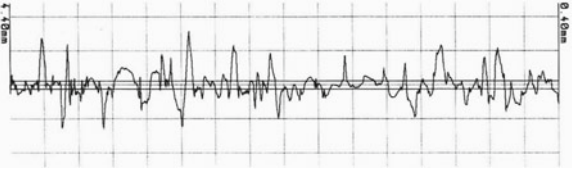
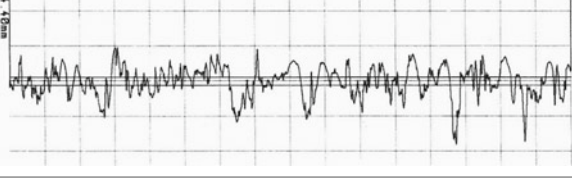
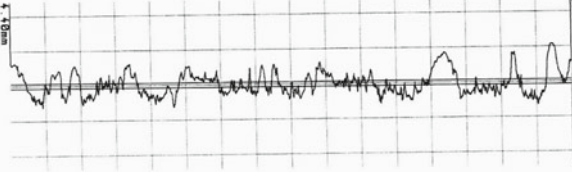
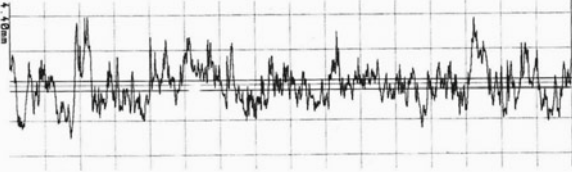
| Surface treatment variants | Surface roughness profiles of adherend sample |
|----------------------------|---|
| V1 |  <p>PROFIL-R Program P2, ISO 11562 (M1) F (1) 0.800 mm LC 0.800 mm VV: 2000 10um= 5.00um VH: 40 10um=250.00um 0.40um</p> |
| V2 |  <p>PROFIL-R Program P2, ISO 11562 (M1) F (1) 0.800 mm LC 0.800 mm VV: 2000 10um= 5.00um VH: 40 10um=250.00um 0.40um</p> |
| V3 |  <p>PROFIL-R Program P2, ISO 11562 (M1) F (1) 0.800 mm LC 0.800 mm VV: 2000 10um= 5.00um VH: 40 10um=250.00um 0.40um</p> |
| V4 |  <p>PROFIL-R Program P2, ISO 11562 (M1) F (1) 0.800 mm LC 0.800 mm VV: 5000 10um= 2.00um VH: 40 10um=250.00um 0.40um</p> |

Table 3 Profilegrams of the surface of samples made of steel sheet depending on the variants of surface treatment—treatment with one several of abrasive paper

| Surface treatment variants | Surface roughness profiles of adherend sample |
|----------------------------|---|
| V5 | |
| V6 | |
| V7 | |

tools (Table 1). Figure 3 shows the effect of the type of abrasive paper used on the average values of selected roughness parameters Ra, Rz and Rmax of samples made of C45 steel.

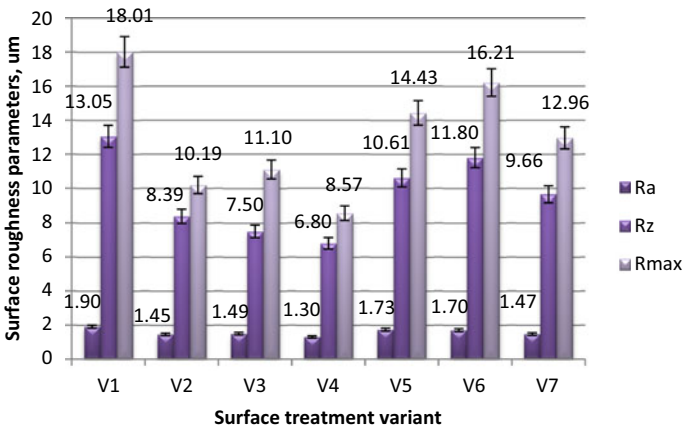


Fig. 3 Influence of the applied mechanical surface treatment on the average values of selected parameters of surface roughness of sheets made of C45 steel

The highest value of the surface roughness parameter Ra was achieved during the preparation of the tile surface with P40 abrasive paper and was 1.90 μm . On the other hand, the lowest value of this parameter was obtained when using P500 abrasive paper. Samples that were subjected to mechanical treatment with the use of various abrasive papers simultaneously obtained a similar value of the Ra parameter. These values were high compared to the use of the single abrasive paper, with the lowest value being 1.47 μm when combined with P40, P120, P320 and P500.

3.2 Adhesive Joints Strength

Figure 4 shows a diagram of the average value of the shear strength of adhesive joints of steel sheets depending on the abrasive paper surface treatment variant used.

From the diagram presented in Fig. 4, it can be seen that the highest shear strength was achieved by joints processed with P500 abrasive paper (V4), which amounted to 11.7 MPa. The adhesive joints made with single papers also obtained high strength and value of the failure force of the joints. The lowest value of the strength of adhesive bonds was obtained when using a combination of P40 and P120 abrasive papers (V5), amounting to only 4.9 MPa, and P40, P120 and P320 (V6)—5.3 MPa. The difference between the highest and the lowest shear strength value of the adhesive joints was 6.8 MPa.

The adhesive joints, after mechanical treatment with P40 abrasive paper (V1), achieved high strength of 10.7 MPa. However, after the next treatment with P120 abrasive paper (P2), this strength decreased by 54% in relation to the strength value of the joints made with the P40 abrasive paper (V1). Then, after another treatment with P320 abrasive paper (V3), this strength also decreased and accounted for almost 50% of the strength value of joints made with P40 (V1). However, when comparing the same method of surface preparation with the treatment with two abrasive papers P40

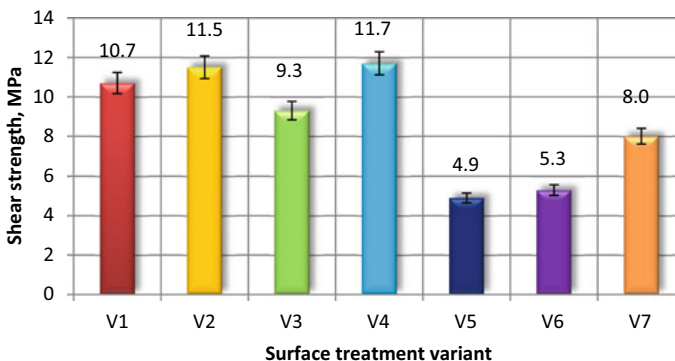


Fig. 4 Shear strength of adhesive joints of steel sheets depending on the abrasive surface treatment variant used

and P120 (V5), it can be seen that after adding another (W6), the strength increases by 8% of the treatment value with P40 and P120 (W5) papers. When one more treatment with P500 abrasive paper (V7) is applied, the strength of the adhesive joints is 75% of the strength of the treatment with a single P40 abrasive paper (V1) and increases by 41% compared to joints made with the use of processing using abrasive papers P40, P120 and P320 (V6) and by 63% for processing with P40 and P120 (V5).

Taking into account the processing with the P500 abrasive paper (V4), which obtained the highest strength, and comparing it with the processing with several abrasive papers P40, P120, P320 and P500 (V7), it can be seen that the strength decreases to 8 MPa, which is 68% highest strength value. On the other hand, when comparing the joints made with one P120 abrasive paper (V2) with those with two types of P40 and P120 abrasive papers (V5), it can be concluded that their strength decreases by 57% of the value of individual papers. The same is true when comparing the treatments with P320 abrasive paper (V3) with V6 variant (P40, P120 and P320), where the strength decreases by 43% compared to the strength value of joints made with only one P320 abrasive paper (V3).

Considering the above data, it can be concluded that too high surface roughness does not increase the strength of such a adhesive joints. The most advantageous method of surface treatment turns out to be the use of mechanical treatments with fine grain size sandpaper such as P500 (V4) and P120 (V2) or grinding the samples with only one type of abrasive paper without additional combinations.

Figure 5 shows a diagram describing the elongation at break depending on the applied surface treatment method.

Based on the analysis of the above results, it was noticed that the highest value of elongation at break was achieved when using abrasive paper P320—V3 (2.1 mm) and P120—V2 (2 mm), and the lowest when using P40 abrasive paper (V1) with an elongation at break of 1.3 mm. The biggest difference between the maximum and minimum value was achieved during surface preparation with P320 abrasive paper

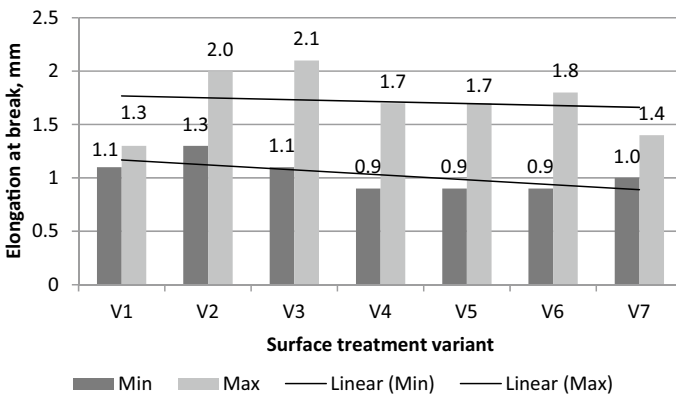


Fig. 5 Elongation at break of adhesive joints depending on the type of abrasive surface treatment used

(V3), which was 1 mm. On the other hand, the smallest difference in elongation at break was achieved when processing with P40 abrasive paper (V1), amounting to 0.20 mm.

The conducted analyzes show that the treatment with single P120 (V2) and P320 (V3) abrasive papers, which are characterized by medium grain size, had the greatest impact on the elongation at break value. Such treatments also obtained high values of shear strength (P120—11.5 MPa, P320—9.3 MPa), close to the highest value of 11.7 MPa.

3.3 Surface Roughness Parameters Versus Adhesive Joints Strength

In order to determine the relationship between the surface roughness parameters and the strength of adhesive joints, a simple correlation was used, and the expression of the correlation was the Pearson correlation coefficient (r), which was in the range $[-1, 1]$. It is a coefficient that determines the level of linear dependence between random variables. If the value of the correlation coefficient is from 0 to 1, then there is a positive correlation, which informs that an increase in the value of one feature is accompanied by an increase in the mean values of the other feature. On the other hand, if the value of the correlation coefficient is from -1 to 0, then there is a negative correlation, which informs that an increase in the value of one feature is accompanied by a decrease in the average values of the other features. The results of the relationship between the surface roughness parameters and the strength of adhesive joints after various mechanical treatments of various adherends were presented in [18, 20, 27].

A statistical analysis was performed on the results from the testing. The TIBCO Statistica 13.3 software suite was used to analyze potential correlations between the selected amplitude surface roughnesses parameters of adherends surface obtained after mechanical treatment. The juxtaposition of these results was presented in Table 4.

The Pearson correlation coefficient PCC ($r(X, Y)$) determined for the all analyzed cases was approximately (-0.44) – (-0.50) which proves a moderate correlation, because on the basis of the strength range of correlation relationships, it is in the range of 0.4–0.6, which means a moderate correlation (significant dependence). However, the value of the correlation coefficient takes a negative value, which means that as the value of the surface roughness parameters increases, the value of the strength of the adhesive bonds decreases. This may mean that with increasing surface roughness parameters, an unfavorable geometric structure is created that does not favor the penetration of the adhesive into micro-unevenness, and therefore a decrease in strength is observed with increasing surface roughness parameters. The type of adhesive was important, or more precisely, its properties, with viscosity as the primary one. Jennings [27] underlined that the degree of roughness of a metallic adherend is frequently a design option for an adhesive joint.

Table 4 Correlation of surface roughness parameters (μm) to adhesive joint strength (MPa)

| X and Y | Values | PCC $r(X, Y)$ | Values | PCC $r(X, Y)$ |
|-------------------------------|------------------------------------|---------------|--|---------------|
| Ra (μm) | Set all values presented in Fig. 3 | -0.44 | Set values presented in Fig. 3 for V1–V4 | -0.29 |
| Adhesive joint strength (MPa) | Set all values presented in Fig. 4 | | Set values presented in Fig. 4 for V1–V4 | |
| Rz (μm) | Set all values presented in Fig. 3 | -0.45 | Set values presented in Fig. 3 for V1–V4 | -0.61 |
| Adhesive joint strength (MPa) | Set all values presented in Fig. 4 | | Set values presented in Fig. 4 for V1–V4 | |
| Rmax (μm) | Set all values presented in Fig. 3 | -0.50 | Set values presented in Fig. 3 for V1–V4 | -0.27 |
| Adhesive joint strength (MPa) | Set all values presented in Fig. 4 | | Set values presented in Fig. 4 for V1–V4 | |

An attempt was also made to determine the correlation between the surface roughness parameters obtained after treatment with single abrasive papers. It was noticed that in the case of the Ra and Rmax parameters, the value of the correlation coefficient is -0.29 and -0.27 , respectively, which is classified as a low correlation (although with a clear relationship). On the other hand, a high correlation was noted -0.61 (the range of high correlation is defined as the range of values from 0.6 to 0.8), i.e. a significant dependence for the Rz parameter and the strength of adhesive connections. However, it should be emphasized that in these cases, there is also a negative correlation. Thus, it can be said that the decrease in the roughness parameters along with the increasing gradation of the sandpaper is accompanied by an increase in the strength of the adhesive joints. Although in the case of processing with many abrasives (V5, V6 and V7) it requires a deeper analysis.

In work [20] The Pearson correlation coefficient (PCC) determined for each case analyzed was approximately 0.98. This was due to a strong linear relationship between each of the surface roughness parameters considered (Ra, Rz, Rt) and the adhesive joint shear strength. The coefficient of determination, R^2 was 0.96–0.97 which meant that the adhesive joint strength could be explained by changes in each of the surface roughness parameters considered (Ra, Rz, Rt). Rudawska et al. [20] was an investigation into the effects of milling on the adhesive joint shear strength in steel sheets, which also found that the highest adhesive joint shear strength was produced by bonding parts with the highest values of selected surface roughness parameters.

It can be assumed, based on the results presented in the literature [17, 18, 20, 21, 23], that also a different type of mechanical treatment contributes to the creation of a different geometrical structure of the surface, which may favor the development of the real surface wetted by the adhesive. At the same time, it should be emphasized that the choice of the type of mechanical treatment is also determined by many factors [3, 5, 14, 19, 27, 28].

4 Conclusion

Based on the test results, it can be concluded that the highest roughness value, considering the Ra parameter, was achieved when the samples were processed with P40 abrasive paper (V1), and it was 1.9 μm . The other methods of surface preparation obtained comparable results ranging from 1.30 μm for processing with P500 abrasive paper (V4) to 1.73 μm for P40 (V1) and P120 (V2) abrasive papers.

Comparing the obtained parameters of the surface roughness and the strength of the adhesive joints, the surfaces of which were subjected to abrasive treatment, it is not possible to clearly indicate the most advantageous and best method of surface development, which contributes to obtaining high strength. The Ra parameter does not fully reflect the unevenness of the surface, which is extremely important for the penetration of the adhesive into micro-unevenness.

Based on the test results, it can be concluded that the highest strength was achieved by the adhesive joints of steel sheets prepared with P500 abrasive paper, which was 11.7 MPa, and using P120 sand paper to treatment it can be obtained a similar strength value of 11.5 MPa. The joints made in this way also obtained a high value of the failure force. A comparable result of the shear strength was also obtained after treatment with the P40 abrasive paper, and it was 10.7 MPa. Among the analyzed methods of surface treatment, the lowest strength of the adhesive joints was obtained during the combination of treatment with P40 and P120 abrasive papers (V5) and amounted to 4.9 MPa and the use of several abrasive papers (V6), equal to 5.3 MPa.

From the obtained results, it can be concluded that the most advantageous among the tested methods of surface preparation is the use of grinding tools with a small grain size, i.e. P500, because too large surface irregularities obtained with several abrasive papers do not increase the strength. Based on the test results, it can also be concluded that the comparatively high strength, equal to 10.7 MPa, is achieved by joints when using coarse-grained abrasive papers, i.e. P120 and P40. The optimal method of surface preparation may also be the use of single sandpaper treatment.

The least suitable method of the surface treatment in the analyzed joints turns out to be the use of any type of abrasive treatment, in which several abrasive paper were used, as it was in the examined tests. Moreover, such surface preparation takes much more time than the preparation of the surface with a single grinding tool and is unjustified and uneconomical, as it does not increase the strength of the adhesive joints.

The different strength of the adhesive joints obtained for all applied abrasive papers may depend on the accuracy of the surface treatment for bonding, as well as on the conditions in which these joints were made. Before selecting the appropriate method of the surface treatment, all the costs, availability of the appropriate machines or the devices and the time needed to perform a given method of the surface treatment should be taken into account, because such an analysis gives the possibility of obtaining the highest strength of adhesive joints with minimal costs associated with it.

References

1. Brockmann W, Geiß PL, Kligen J, Schröder B (2009) Adhesive bonding. Materials, applications and technology. Wiley-Vch Press, Weinheim, Germany
2. Adams RD, Comyn J, Wake WC (1997) Structural adhesive joints in engineering book. Springer, United Kingdom
3. Critchlow GW, Brewis DM (1996) Review of surface pretreatments for aluminium alloys. *Int J Adhes Adhes* 16:255–275
4. Prolongo SG, Ureña A (2009) Effect of surface pre-treatment on the adhesive strength of epoxy-aluminium joints. *Int J Adhes Adhes* 29:23–31
5. Leena K, Athira KK, Bhuvanewari S, Suraj S, Lakshmana Rao V (2016) Effect of surface pre-treatment on surface characteristic adhesive bond strength of aluminium alloy. *Int J Adhes Adhes* 70:265–270
6. Boutar Y, Naïmi S, Mezlini S, Ali MBS (2016) Effect of surface treatment on the shear strength of aluminium adhesive single-lap joint for automotive applications. *Int J Adhes Adhes* 67:38–43
7. Rudawska A (2019) Surface treatment in bonding technology. Academic Press, Elsevier, United Kingdom
8. Rudawska A, Wahab MA (2019) The effect of cathoretic and powder coatings on the strength and failure modes of EN AW-5754 aluminium alloy adhesive joints. *Int J Adhes Adhes* 89:40–50
9. Bockenheimer C, Valeske B, Possart W (2002) Network structure in epoxy aluminium bonds after mechanical treatment. *Int J Adhes Adhes* 22:349–356
10. Lunder O, Lapique F, Johnsen B, Nisancioglu K (2004) Effect of pre-treatment on the durability of epoxy-bonded AA6060 aluminium joints. *Int J Adhes Adhes* 24:107–117
11. Ebnesajjad S (2011) Handbook of adhesives and surface preparation, chap 6. Surface preparation of metals. Plastic Design Library, Elsevier Inc., pp 83–106
12. Borsellino C, Di Bella G, Ruisi VF (2009) Adhesive joining of aluminium AA6082: the effects of resin and surface treatment. *Int J Adhes Adhes* 29:36–44
13. Da Silva LFM, Carbas RJC, Critchlow GW, Figueiredo MAV, Brown K (2009) Effect of material, geometry, surface treatment and environment on the shear strength of single lap joints. *Int J Adhes Adhes* 29:621–632
14. Mandolino C, Lertora E, Gambaro C (2013) Effect of surface pretreatment on the performance of adhesive-bonded joints. *Key Eng Mater* 554–558:996–1006
15. Ebnesajjad S, Ebnesajjad C (2013) Surface treatment of materials for adhesive bonding, 2nd edn. Inc. Norwich, William Andrew, New York
16. Rudawska A (2012) Surface free energy and 7075 aluminium bonded joint strength following degreasing only and without any prior treatment. *J Adhes Sci Technol* 26:1233–1247
17. Harris AF, Beevers A (1999) The effect of grit-blasting on the surface properties for adhesion. *Int J Adhes Adhes* 19:445–452
18. Rudawska A, Danczak I, Müller M, Valasek P (2016) The effect of sandblasting on surface properties for adhesion. *Int J Adhes Adhes* 70:176–190
19. Bhatt RD, Radhakrishnan V (1989) Evaluation of some machining process as adherend surface treatments in bonding aluminium. *J Adhes Sci Technol* 3:383–396
20. Rudawska A, Szabelski J, Wahab MA, Miturska I (2021) Impact of abrasive blasting media on the strength of steel sheets adhesively bonded joints. In: Proceedings of the 8th international conference on fracture, fatigue and wear. Springer, pp 81–95
21. Elbing F, Anagreh N, Dorm L, Uhlmann E (2003) Dry ice blasting as pretreatment of aluminium surfaces to improve the adhesive strength of aluminum bonding joints. *Int J Adhes Adhes* 23:69–79
22. Wang B, Hu X, Lu P (2017) Improvement of adhesive bonding of grit-blasted steel substrates by using diluted resin as a primer. *Int J Adhes Adhes* 73:92–99
23. Staia MH, Ramos E, Carrasquero A, Roman A, Lesage J, Chicot D, Mesmacque G (2000) Effect of substrate roughness induced by grit blasting upon adhesion of WC-17% Co thermal sprayed coatings. *Thin Solid Films* 377–378:657–664

24. Khan AA, Al Kheraif AA, Alhijji SM (2016) Effect of grit-blasting air pressure on adhesion strength of resin to titanium. *Int J Adhes Adhes* 65:41–46
25. Wang B, Hu X, Lu P (2017) Improvement of adhesive bonding of grit-blasted steel substrates by using diluted resin as a primer. *Int J Adhes Adhes* 48:92–99
26. Hirulkara NS, Jaiswalb PR, Alessandroc P, Reis P (2018) Influence of mechanical surface treatment on the strength of mixed adhesive joint. *Mater Today Proc* 5:18776–18788
27. Rudawska A (2014) Selected aspects of the effect of mechanical treatment on surface roughness and adhesive joint strength of steel sheets. *Int J Adhes Adhes* 50:235–243
28. Spaggiari A, Dragoni E (2013) Effect of mechanical surface treatment on the static strength of adhesive lap joints. *J Adhes* 89:677–696
29. Rudawska A, Reszka M, Warda T, Miturska I, Szabelski J, Skoczylas A, Stancekova D (2016) Milling as method of surface pretreatment of steel for adhesive bonding. *J Adhes Sci Technol* 30:2619–2636
30. Gent AN, Lin C-W (1990) Model studies of the effect of surface roughness and mechanical interlocking on adhesion. *J Adhes* 32:113–125
31. Rudawska A (in press) Mechanical properties of epoxy compounds based on Bisphenol A aged in aqueous environments

Modeling of Adhesive Contact of Elastic Bodies with Regular Microgeometry



Yulia Makhovskaya 

Abstract A model of adhesive contact is presented for two nominally flat surfaces, one of which is a plane surface of the elastic half-space and the other is a set of regularly arranged micro-asperities. Adhesion of two different natures is considered—molecular adhesion of dry surfaces associated with van der Waals forces and capillary adhesion of wet surfaces caused by liquid bridges between them. Methods of calculation of the contact characteristics at micro-scale such as real contact area and real pressure are developed, depending on the surface energy of interacting bodies, relative humidity of the atmosphere, mechanical properties of the half-space, and mutual influence of neighbor asperities. A method is proposed to calculate the effective adhesion pressure and effective work of adhesion for two nominally flat surfaces taking into account surface micro-relief. Based on the method proposed, a two-scale contact model is developed which makes it possible to analyze the influence of the characteristics of adhesion and geometric parameters of micro-relief (relative size of asperities and distance between them) on the contact characteristics at macro-scale, such as nominal contact area and load-distance curve.

Keywords Adhesion · Liquid bridges · Regular roughness

1 Introduction

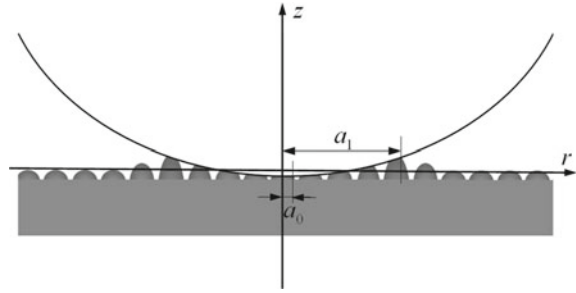
Character of adhesion between two solids depends not only on their surface energy, but also on the microgeometry of their surfaces. Application of artificial surface relief can modify the adhesion properties of surfaces [1, 2]. Thus, an important task is constructing mathematical models that allow one to study the combined influence of the parameters of microgeometry (size and shape of micro-asperities, spacing between them) and adhesion (surface properties of solids and liquid films covering them) on how the solids adhere at macro-scale.

Y. Makhovskaya (✉)

Ishlinsky Institute for Problems in Mechanics RAS, Prospekt Vernadskogo 101-1, Moscow 119526, Russia

e-mail: makhovskaya@mail.ru

Fig. 1 An example scheme of contact taking into account microrelief and adhesion



In order to construct such models, contact problems are considered for two solids, e.g., a spherical indenter and a half-space, one of which is covered by microrelief (Fig. 1), taking into account adhesion attraction. For a surface whose microgeometry has a form of a slight waviness such that the contact stays saturated, the solution of such problem was obtained in the closed form [3]. It was established that application of a regular waviness enhances the adhesion and changes the adhesion hysteresis [4]. If the contact is discrete and real contact area is multiply connected (as is shown in Fig. 1), the solution can be obtained under simplified assumptions [5] or numerically, e.g., by the boundary element method [6].

An alternative approach to deal with such problems is to divide them into two scales. At micro-scale, the contact problem is solved to obtain effective characteristics, which are then used for the problem solution at macro-scale. A method based on calculation of the effective compliance of a rough layer taking into account adhesion was proposed in [7]. Methods of analysis of the adhesive contact problems were also suggested based on calculation of the effective work or adhesion at microlevel [8, 9]. Different values of the effective work of adhesion of rough surfaces in approach and retraction were obtained in [10] and used for modelling the adhesion component of the friction force. In [11], a method was proposed according to which the contact problem is first considered at microlevel for two nominally flat surfaces, one of which has a regular relief. As a result of this problem solution, the effective adhesion pressure as a function of the gap between the surfaces is calculated and then used for the problem solution at macrolevel.

In the present study, the method presented in [11] is used to analyze the two-scale adhesive contact for the cases of both capillary adhesion caused by liquid bridges between surfaces and molecular adhesion associated with van der Waals forces between dry surfaces. Note that for the method to be applicable, it is necessary that the contact spots at micro-level are much smaller than the apparent contact area at macro-level, $a_0 \ll a_1$ (see Fig. 1).

2 Adhesion of Different Nature at Microlevel for a Single Asperity

2.1 Capillary Adhesion

Consider a rigid asperity of hemispherical shape with the radius R_0 in contact with an elastic half-space (Fig. 2). The surfaces of the asperity and elastic half-space are connected by a liquid bridge (meniscus) condensed from the atmosphere and staying in thermodynamic equilibrium with the environment. In this equilibrium state, the capillary pressure inside the liquid meniscus is specified by the Kelvin equation [12]

$$p_c = -\frac{R_{uni}T}{V_m} \ln H \tag{1}$$

where T is the absolute temperature, R_{uni} is the universal gas constant, V_m is the molar volume of the liquid, H is the relative humidity of the environment.

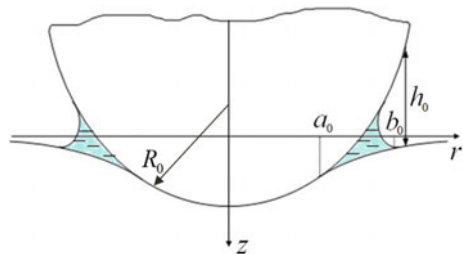
Thus, at specified values of the temperature and humidity, the capillary pressure in the meniscus is known. However, the size of the meniscus, as well as the size of the contact region, are a priori unknown, since these values are dependent on the deformation of the elastic half-space boundary, which in turn depends on the size of the meniscus and capillary pressure in it.

We assume that the stress and strain field in the elastic half-space around the asperity is axisymmetric. Let the asperity make contact with the elastic half-space over a circular region $r \leq a_0$, while the meniscus occupies a ring-shaped region $a_0 \leq r \leq b_0$ (Fig. 2). In accordance with the Laplace equation, the pressure in the meniscus is related to its geometry as [12]

$$p_c = \gamma \left(\frac{1}{r_1} + \frac{1}{r_2} \right) \tag{2}$$

where γ is the surface tension of the liquid, r_1 and r_2 are the meniscus radii in two mutually orthogonal planes:

Fig. 2 Contact of a separate asperity with the elastic half-space in the presence of a liquid bridge



$$r_1 \approx -\frac{h_0(b_0)}{\cos \theta_1 + \cos \theta_2}, \quad r_2 \approx b_0 \quad (3)$$

Here, the radius r_1 in the vertical plane is approximately defined by the gap value $h_0(r)$ between the surfaces and wetting angles θ_1 and θ_2 of the asperity and the half-space surfaces by the liquid. The radius r_2 in the horizontal plane is assumed to approximately coincide with the outer radius b_0 of the meniscus.

The force of surface tension of the liquid film and the friction force between the asperities and the elastic half-space are assumed to be negligible.

2.2 Molecular Adhesion of Dry Surfaces

In the case where the humidity of the atmosphere is low or the interacting surfaces are intentionally dried, the adhesion attraction occurs due to molecular forces. The force of this attraction depends on the value of gap between the surfaces h_0 . To describe this dependence, we use the Maugis model [13] according to which the adhesion pressure p_m is applied outside the contact region:

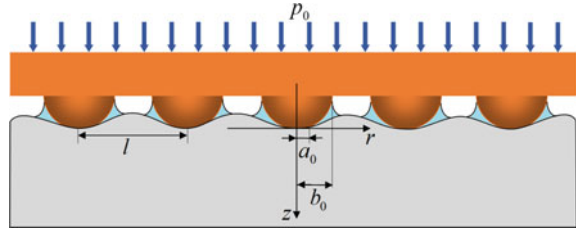
$$p_m(h_0) = \begin{cases} -p_m, & 0 < h_0 \leq h_m \\ 0, & h_0 > h_m \end{cases} \quad (4)$$

The adhesion pressure p_m acts in the ring-shaped region $a_0 \leq r \leq b_0$ around the contact region between the asperity and the elastic half-space. When using the Maugis model of molecular adhesion, the contact problem formulation is similar to the case of capillary adhesion [14]. The values of p_m and h_m are defined by the characteristics of the molecular interaction of two surfaces, and they are related to the specific work of molecular adhesion w as

$$w = \int_0^{+\infty} p_m(h) dh = p_m h_m \quad (5)$$

In the next section, the case of multi-asperity contact will be considered, in which the above contact conditions for the half-space are applied periodically over its infinite boundary.

Fig. 3 Contact between a surface with periodic relief and an elastic half-space in the presence of liquid bridges



3 Adhesion of a Nominally Flat Surface with Periodic Relief to an Elastic Half-Space

3.1 Periodic Problem Formulation

Consider an infinite rigid plane covered by a periodically arranged set of identical hemispherical rigid asperities in contact with an elastic half-space (Fig. 3). The asperities are centered at the nodes of a 2D hexagonal lattice, the spacing between the centers of asperities is l . Let the origin of a local coordinate system (r, z, ϕ) coincide with the top of an asperity. The z -axis is directed vertically inside the half-space. In this coordinate system, the shape of an asperity is given by the function $f_0(r) = r^2/(2R_0)$. The rigid surface covered by asperities is subjected to a uniform pressure p_0 .

We assume that the stress and strain field in the elastic half-space around each asperity is axisymmetric. For each asperity, the half-space is indented by this asperity over the contact region $r \leq a_0$, and it is acted on by either the capillary pressure p_c (1)–(3) or molecular adhesion pressure p_m (4)–(5) over the region $a_0 \leq r \leq b_0$. Note that in the case of capillary adhesion, the molecular forces are assumed to be blocked by the liquid bridges, so these two forces cannot act together.

3.2 Application of the Localization Principle

According to the localization principle [15, 16], to calculate the stress-strain state near a single contact spot, it is sufficient to use the exact contact conditions only for this contact spot and its neighboring contact spots. The effect of more distant contact spots is replaced by the averaged (nominal) pressure acting outside the considered domain. In this study, the simplest version of the localization principle is used, in which only one contact spot is exactly taken into account, while the action of the other contact spots is approximated by the action of the nominal pressure p_0 in the region $r \geq R_{eff}$. The effective radius R_{eff} is determined from the equality condition of the average pressure inside the circle of radius R_{eff} and outside it. For a hexagonal lattice, this

value is defined as $R_{\text{eff}} = 3^{1/4}l/\sqrt{2\pi}$ [15]. Thus, we have the axisymmetric contact problem for the elastic half-space with the boundary conditions:

$$u(r) = -\frac{r^2}{2R_0} - d_0, \quad r \leq a_0, \quad p(r) = \begin{cases} p_{\text{adh}} & a_0 < r \leq b_0 \\ 0 & b_0 < r \leq R_{\text{eff}} \\ p_0 & r > R_{\text{eff}} \end{cases} \quad (6)$$

where $p(r)$ and $u(r)$ are the normal pressure and elastic displacement in z -direction at the boundary $z = 0$ of the elastic half-space, d_0 is the distance between the asperity and the unperturbed surface of the elastic half-space. The adhesion pressure p_{adh} acting outside the contact region equals p_c defined by Eq. (1) for capillary adhesion and p_m defined by Eq. (5) for molecular adhesion.

Within the framework of linear elasticity and axisymmetric formulation, the elastic displacement $u(r)$ is related to the pressure $p(r)$ by the equation [17]

$$u(r) = \frac{4}{\pi E^*} \int_0^\infty p(r') \mathbf{K} \left(\frac{2\sqrt{rr'}}{r+r'} \right) \frac{r' dr'}{r+r'} \quad (7)$$

where $\mathbf{K}(x)$ is the complete elliptic integral of the first kind, $E^* = E/(1 - \nu^2)$, E and ν are the Young modulus and Poisson's ratio of the half-space, respectively.

Equation (7) with conditions (6) serves for determination of the unknown functions—the contact pressure $p(r)$ in the contact region $r \leq a_0$ and the displacement $u(r)$ in the region $a_0 \leq r \leq b_0$. The following conditions are also satisfied—the condition of continuity for the contact pressure at the boundary $r = a_0$ of the contact region:

$$p(a_0) = p_{\text{adh}}, \quad (8)$$

the equilibrium condition for the nominal pressure

$$p_0 = \frac{2}{R_{\text{eff}}^2} \int_0^{R_{\text{eff}}} r p(r) dr, \quad (9)$$

and the adhesion condition which follows from Eqs. (2) and (3) for capillary adhesion and Eq. (4) for molecular adhesion. Those equations contain the value of gap h_0 between the surfaces which is the function of the coordinate r near an asperity and is related to the elastic displacement as

$$h_0(r) = \frac{r^2 - a_0^2}{2R_0} + u(r) - u(a_0), \quad (10)$$

Equation (7) with conditions (6), (8), and (9), (10) taking into account Eqs. (2) and (3) for capillary adhesion and Eq. (4) for molecular adhesion define the problem to be solved below.

3.3 Calculation of Contact Characteristics at Micro Scale Level

The solution to the axisymmetric contact problem formulated in Sect. 3.2 was derived analytically in [18, 19]. In the case of capillary adhesion, in which $p_{adh} = p_c$ and Eqs. (1)–(3) are satisfied, we obtain the nominal pressure p_0 as a function of the normal distance between the two nominally flat surfaces d_0 in the parametric form:

$$\begin{aligned}
 p_0 &= \frac{1}{R_{eff}^2 J(a_0/R_{eff})} \left[\frac{2E^* a_0^3}{3R_0} + p_c b_0^2 J\left(\frac{a_0}{b_0}\right) \right], \\
 d_0 &= -\frac{a_0^2}{R_0} + \frac{2}{E^*} \left(p_0 \sqrt{R_{eff}^2 - a_0^2} - p_c \sqrt{b_0^2 - a_0^2} \right)
 \end{aligned}
 \tag{11}$$

where $J(t) = \arccos(t) + t\sqrt{1 - t^2}$. The unknown contact radius a_0 and outer radius of the meniscus b_0 are related by the equation

$$\begin{aligned}
 d_0 \arccos \frac{a_0}{b_0} + \frac{b_0^2}{2R_0} J\left(\frac{a_0}{b_0}\right) + \frac{2p_c}{E^*} (b_0 - a_0) - \\
 - \frac{2p_0 R_{eff}}{E^*} \left[E\left(\frac{b_0}{R_{eff}}\right) - E\left(\arcsin \frac{a_0}{b_0}, \frac{b_0}{R_{eff}}\right) \right] = \frac{\pi b_0 \gamma (\cos \theta_1 + \cos \theta_2)}{2(\gamma - b_0 p_c)}
 \end{aligned}
 \tag{12}$$

which can be solved numerically for a_0 when b_0 is prescribed.

When the surfaces are not in direct contact but interact only through liquid bridges, the relationship between the nominal pressure p_0 and the distance d_0 has a simpler form and does not require numerical solution:

$$\begin{aligned}
 p_0 &= -p_a \left(\frac{b_0}{R_{eff}} \right)^2, \\
 d_0 &= -\frac{b_0^2}{2R_0} + \frac{4b_0}{\pi E^*} \left[p_c - \frac{R_{eff}}{b_0} \mathbf{E}\left(\frac{b_0}{R_{eff}}\right) \right] + \frac{b_0 \gamma (\cos \theta_1 + \cos \theta_2)}{\gamma - b_0 p_c}
 \end{aligned}
 \tag{13}$$

In Fig. 4a, the dimensionless radius of a contact area a_0/R_0 (red lines) and dimensionless outer radius of a meniscus b_0/R_0 (blue lines) are shown as functions of the dimensionless nominal pressure $p_0 R_0 \rho^3 / \gamma$, where the parameter $\rho = \sqrt{3}l / (2\pi R_0)$ is the dimensionless spacing between asperities. Such parametrization for the nominal pressure is used here to analyze the effect of mutual influence of the asperities

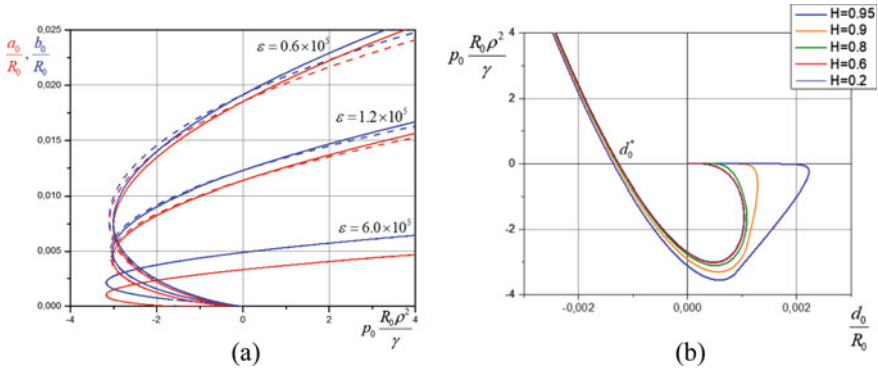


Fig.4 Radii of real contact areas and areas of liquid bridges versus nominal pressure for various elastic modulus and spacing between asperities (a) and nominal pressure versus vertical distance between nominally flat surfaces for various relative humidity (b) in the case of capillary adhesion

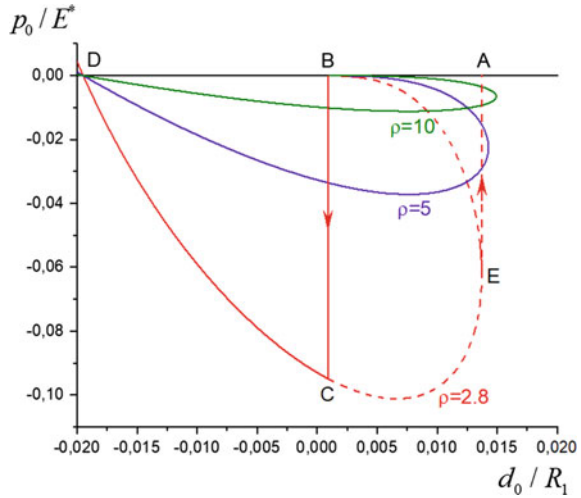
through the elastic half-space. The plots in Fig. 4a are constructed for the dimensionless capillary radius $R_c = V_m \gamma / (R_{uni} T R_0) = 6 \times 10^{-4}$, relative humidity $H = 0.6$, and for three values of the dimensionless elastic modulus $\varepsilon = E^* R_0 / \gamma$. Solid lines correspond to the dimensionless spacing between asperities $\rho = 2$, dashed lines to $\rho = 0.12$. The presented results show that mutual influence of asperities has only small influence on the size of the contact and meniscus areas, but this influence is more significant for lower values of the elastic modulus (for softer materials).

In Fig. 4b, the dimensionless nominal pressure $p_0 R_0 \rho^3 / \gamma$ is presented as a function of the dimensionless vertical distance d_0 / R_0 between the half-space and the surface with regular relief for various values of the relative humidity H . The plots in Fig. 4b are constructed for the dimensionless characteristic capillary radius $R_c = 6 \times 10^{-4}$, dimensionless elastic modulus $\varepsilon = 1.2 \times 10^5$, and dimensionless spacing between asperities $\rho = 2$. The results indicate that the influence of relative humidity manifests itself mostly for $d_0 > d_0^*$, where d_0^* is the equilibrium distance between the bodies. The effect of relative humidity on the pressure-distance curve is more significant for higher values of humidity. An increase in the humidity leads to higher negative pressures that the contact can sustain without breaking.

Relations (11)–(13) can be also used for the calculation of the contact characteristics in the case of molecular adhesion of dry surfaces. For this case, the capillary pressure p_c should be replaced with the molecular adhesion pressure p_m , and the surface tension of the liquid γ should be replaced by $w/2$, where w is the specific work of adhesion of two dry surfaces, also one should set $\theta_1 = \theta_2 = 0$.

In Fig. 5, the dimensionless nominal pressure p_0 / E^* is presented as a function of the dimensionless normal distance d_0 / R_1 between the half-space and the surface with regular relief for the case of molecular adhesion of dry surfaces. The results are calculated for the following values of parameters of molecular adhesion— $p_m / E^* = 10$ and $h_m / R_1 = 10^{-3}$. Here for parametrization, we use the value R_1 which will be introduced in Sect. 4.1 as a radius of curvature at macro-scale, and we take

Fig. 5 Nominal pressure versus vertical distance between nominally flat surfaces for various values of spacing between asperities in the case of molecular adhesion of dry surfaces



$R_0/R_1 = 10^{-2}$. In Fig. 5, the plots are presented in the region $d_0 > d_0^*$, for it is this region where effects of adhesion manifest themselves, and this region of the curves will be used for further calculation at the macro-scale. The three presented curves are calculated for three different values of the dimensionless spacing ρ between asperities of the rigid surface. For more densely arranged asperities ($\rho = 0.028$), the contact can exist under higher negative loads. The curves presented in Figs. 4b and 5 are ambiguous which is characteristic for adhesion of elastic bodies. These curves describe adhesion hysteresis—the work done when the surfaces are brought together (along the path ABCD in Fig. 5) is less than the work done to move the surfaces apart (along the path DCEA).

3.4 Effective Work of Adhesion of Nominally Flat Surfaces with Micro-Relief

For two smooth surfaces, the specific work of adhesion is given by Eq. (5). One can define the effective specific work of adhesion for surfaces with micro-relief as a work done to separate the two surfaces from the equilibrium distance $d_0 = d_0^*$ to infinity:

$$w_{eff} = - \int_{d_0^*}^{\infty} p_0(b) d'_0(b) db \tag{14}$$

In a similar way, one can define the specific work of adhesion when the surfaces are brought together, and this work will be smaller than that done in separating the surfaces, due to adhesion hysteresis.

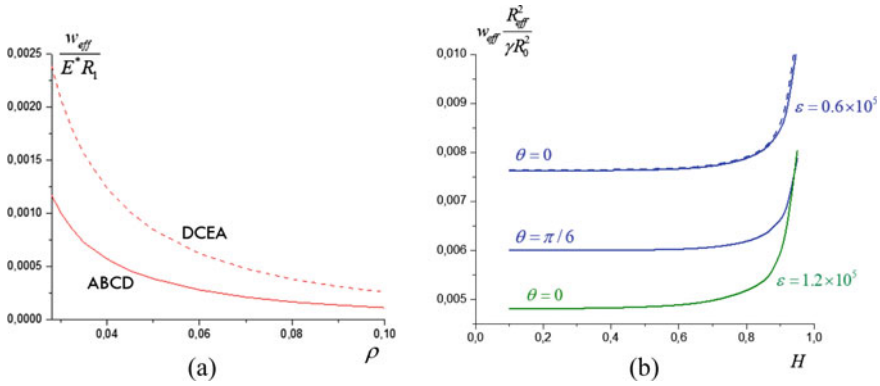


Fig. 6 Effective work of adhesion versus spacing between asperities for dry adhesion (a) and effective work of adhesion as a function of relative humidity for capillary adhesion (b)

In Fig. 6a the dimensionless effective work of adhesion is presented as a function of the dimensionless spacing between surface asperities of the rigid body in the case of molecular adhesion. These results are calculated for the same values of the parameters as the red line in Fig. 5 ($\rho = 2.8$). The solid line in Fig. 6a corresponds to the effective work of adhesion in moving the surfaces together (along the path ABCD in Fig. 5), the dashed line corresponds to the same value in moving the surfaces apart (along the path DCEA in Fig. 5). The results show that both values of the effective work of adhesion decrease as the spacing between surface asperities increases.

In Fig. 6b the dimensionless effective work of adhesion is shown as a function of relative humidity of the surrounding air in the case of capillary adhesion. The effective work of adhesion is calculated by Eq. (14) for retraction of the surfaces. The plots in Fig. 6b are constructed for the dimensionless characteristic capillary radius $R_c = 6 \times 10^{-4}$, two different values of the dimensionless elastic modulus $\varepsilon = 0.6 \times 10^5$ (blue curves) and $\varepsilon = 1.2 \times 10^5$ (green curves), and three different values of the wetting angle θ (it is assumed that $\theta_1 = \theta_2 = \theta$). Solid lines correspond to the dimensionless spacing between asperities $\rho = 2$, dashed lines to $\rho = 0.12$. The results indicate that the effective work of adhesion increases insignificantly for low humidity and raises sharply for humidity close to 100%. Mutual influence of asperities has no significant effect on the effective work of adhesion, while the elastic properties, surface tension, and the wetting angle have substantial effects on the value of the effective work of adhesion.

4 Two-Scale Contact Model

4.1 Problem Formulation at Macro-Scale

At macroscale, we consider a rigid indenter, the shape of which is given by the function $f_1(r) = r^2/(2R_1)$, in contact with the elastic half-space occupying the domain $z \leq 0$ (Fig. 7a). To take into account the adhesion attraction and surface relief at micro-scale, one can use the effective work of adhesion calculated in Sect. 3.4 and apply a simplified model of adhesion, such as JKR model, to calculate the contact characteristics at macro-scale [9, 10].

In this study we use more sophisticated approach suggested in [11]. Let the indenter and the half-space have contact within the circle $r \leq a_1$ in which the pressure acting on the surface of the half-space is positive. And let the adhesion interaction take place in the ring $a_1 \leq r \leq b_1$ inside which the pressure acting on the surface of the half-space is negative. We use the dependence of the nominal pressure on the vertical distance between the nominally flat surfaces, $p_0 = p_0(d_0)$ calculated in Sect. 3.3 to obtain the effective adhesion pressure $p_{eff} = -p_0$ as a function of an effective gap $h_1 = d_0 - d_0^*$. The function $p_{eff} = p_{eff}(h_1)$ thus obtained serves as an input adhesion characteristic at macro-level. The nominal gap h_1 is geometrically defined at macro-level as

$$h_1(r) = \frac{r^2}{2R_1} + u(r) + d_1 \tag{15}$$

where d_1 is the vertical distance between the indenter and the elastic half-space. The conditions on the surface $z = 0$ of the elastic half-space have the form:

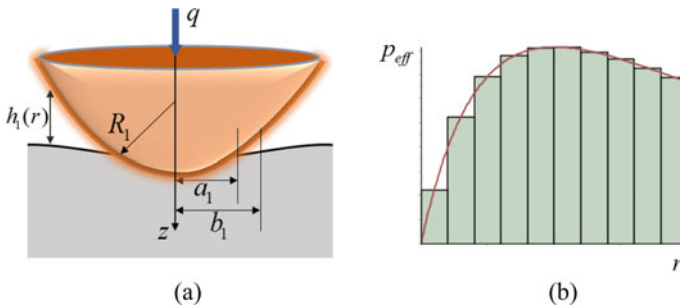


Fig. 7 Scheme of contact at macro-scale (a) and piecewise representation of the effective adhesion pressure (b)

$$\begin{aligned}
h_1(r) &= 0 & r &\leq a_1 \\
p(r) &= -p_{eff}(h_1(r)) & a_1 &\leq r \leq b_1 \\
p(r) &= 0 & r &> b_1
\end{aligned} \tag{16}$$

At the boundary $r = a_1$ of the contact region, the pressure acting on the half-space is continuous:

$$p(r) = 0, \quad r = a_1 \tag{17}$$

The equilibrium condition for the normal load q applied to the indenter is satisfied:

$$q = 2\pi \int_0^{b_1} r p(r) dr \tag{18}$$

For the description of the mechanical properties of the half-space, Eq. (7) is used. Relations (15)–(18) together with Eq. (7) and the function of effective adhesion pressure $p_{eff} = p_{eff}(h_1)$ calculated by the method described in Sect. 3 define the problem at macro-level.

4.2 Method of Solution

To solve the problem at macro-scale, the effective adhesion pressure is considered as a function of the radial coordinate r :

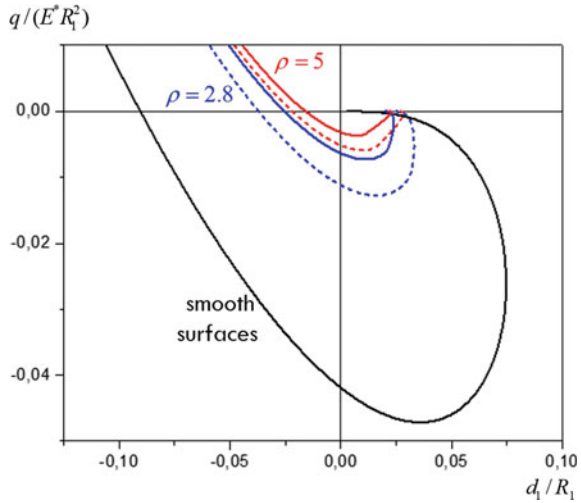
$$p_{eff}(r) = p_{eff}(h_1(r)) \tag{19}$$

In the region of adhesion, $a_1 \leq r \leq b_1$ the function $p_{eff}(r)$ is represented as a piecewise constant approximation (see Fig. 7b):

$$p_{eff}(r) = \begin{cases} p^1, & b^0 \leq r < b^1 \\ p^2, & b^1 \leq r < b^2 \\ \dots & \dots \\ p^N, & b^{N-1} \leq r < b^N \end{cases} \tag{20}$$

where $b^0 = a_1$, $b^N = b_1$. The method of solution of an axisymmetric contact problem with a piecewise constant representation of the adhesion pressure outside the contact region was proposed in [20] and used for calculations at macro-scale in [11]. For a known effective adhesion pressure function $p_{eff} = p_{eff}(h_1)$, we have a system of N nonlinear algebraic equations to be numerically solved for the values b^i , the contact radius being determined automatically as $a_1 = b^0$. After this, the contact

Fig. 8 Load-distance curves for various spacing between asperities in the case of molecular adhesion



pressure and the load-distance dependence are obtained from analytical relations. All these equations with the description of the calculation method at macro-level are given in [11]. Note that the function $p_{eff} = p_{eff}(h_1)$ calculated from the problem solution at micro-level (Sect. 2) is different for the cases of approach and retraction of the surfaces and, thus, the solution at macro-level is different depending on whether the indenter is approaching the elastic half-space or retracting from it.

4.3 Results of Calculation

In Fig. 8, the dimensionless load $q/(E^* R_1^2)$ is presented as a function of the dimensionless distance d_1/R_1 between the indenter and the half-space for the case of molecular adhesion between dry surfaces. Solid lines correspond to approach, dashed lines to retraction. Blue lines correspond to more closely arranged asperities ($\rho = 2.8$) than red lines ($\rho = 5$). Black line corresponds to the adhesion interaction of two smooth surfaces without asperities.

The results presented in Fig. 8 show that taking into account surface microgeometry considerably decreases the maximum negative load (pull-off force), as well as the value of adhesion hysteresis, in comparison to those for smooth surfaces. This effect is accounted for by smaller real contact area in the case of surface microgeometry [2, 9]. Although microgeometry lowers the value of adhesion hysteresis, it also gives an additional contribution into it due to significant difference between approach and retraction curves (solid and dashed lines in Fig. 8).

In Fig. 9a, the approach and retraction load-distance curves are presented for capillary adhesion. The results are calculated for the dimensionless characteristic

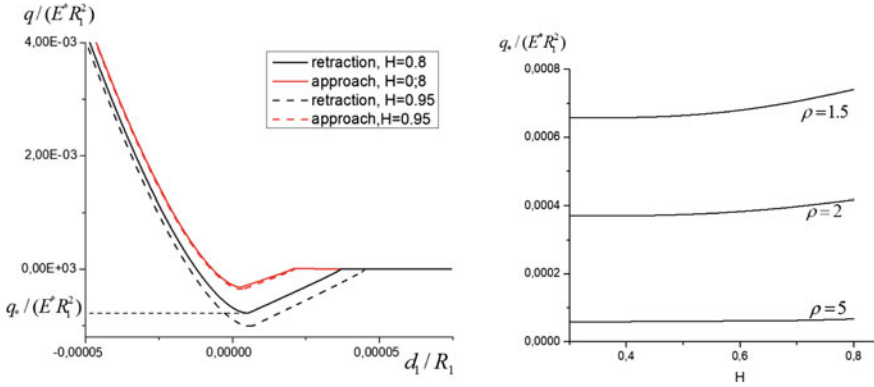


Fig. 9 Load-distance curves for various humidity (a) and pull-off force as a function of relative humidity for various spacing between asperities (b) for the case of capillary adhesion

capillary radius $R_c = 6 \times 10^{-4}$, dimensionless elastic modulus $\varepsilon = 6 \times 10^5$, dimensionless spacing between asperities $\rho = 2$, and two values of relative humidity— $H = 0.8$ and $H = 0.95$. It is seen that an increase in the relative humidity leads to an increase in the adhesion hysteresis associated with surface microgeometry and also to an increase in the pull-off force.

The dimensionless pull-off force $q_*/(E^* R_1^2)$ as a function of the relative humidity H is plotted in Fig. 9b for three different values of dimensionless spacing between asperities. The results indicate that the parameters of surface microgeometry have more significant influence on the pull-off force (and other characteristics at macro-scale) than the value of relative humidity of the surrounding atmosphere.

5 Conclusion

A two-scale model is suggested to describe adhesion of elastic solids with regular relief applied on their surfaces in the case where the contact at micro-scale level is discrete (multiply connected). The model is applicable to describe capillary adhesion associated with liquid bridges between the surfaces and governed by the relative humidity of the atmosphere and molecular adhesion of dry surfaces caused by van der Waals forces.

The contact characteristics at micro-scale such as pressure-distance curve and real contact area are calculated and analyzed depending on the parameters of micro-relief, elastic properties, and relative humidity. Mutual influence of neighbor asperities is taken into account. A method is proposed to calculate the effective adhesion pressure and effective work of adhesion for two nominally flat surfaces taking into account surface micro-relief. It is shown that these values are different in approach and retraction of the surfaces.

The effect of the characteristics of adhesion and geometric parameters of micro-relief (relative size of asperities and distance between them) on the contact characteristics at macro-scale, such as nominal contact area and load-distance curve, are analyzed. In particular, it is shown that an increase in the relative humidity leads to an increase in the pull-off force and adhesion hysteresis in the case of capillary adhesion. For surfaces with larger asperities and larger spacing between them, the effects of adhesion are less significant in the cases of both capillary and molecular adhesion.

The model can be used for control of the adhesion of surfaces through a micro-relief applied on them.

Acknowledgements This research was partially supported by the Russian Science Foundation No. 18-19-00574 (Sections 1, 2, and 3) and the Russian Foundation for Basic Research No. 20-01-00400 (Sections 4 and 5).

References

1. Purtov J, Gorb EV, Steinhart M, Gorb SN (2013) Measuring of the hardly measurable: adhesion properties of anti-adhesive surfaces. *Appl Phys A* 2 111(1):183–189
2. Borodich FM, Savencu O (2017) Hierarchical models of engineering rough surfaces and bio-inspired adhesives. In: Heepe L, Xue L, Gorb S (eds) *Bio-inspired structured adhesives. Biologically-inspired systems*, vol 9. Springer, Cham
3. Guduru PR (2007) Detachment of a rigid solid from an elastic wavy surface: theory. *J Mech Phys Solids* 55(3):445–472
4. Kesari H, Lew AJ (2011) Effective macroscopic adhesive contact behavior induced by small surface roughness. *J Mech Phys Solids* 59(12):2488–2510
5. Ciavarella M (2018) An approximate JKR solution for a general contact, including rough contacts. *J Mech Phys Solids* 114:209–218
6. Li Q, Pohrt R, Popov VL (2019) Adhesive strength of contacts of rough spheres. *Front Mech Eng* 5(7)
7. Galanov BA (2011) Models of adhesive contact between rough elastic solids. *Int J Mech Sci* 53(11):968–977
8. Peressadko AG, Hosoda N, Persson BNJ (2005) Influence of surface roughness on adhesion between elastic bodies. *Phys Rev Lett* 95(12):124301
9. Pepelyshev A, Borodich FM, Galanov BA et al (2018) Adhesion of soft materials to rough surfaces: experimental studies, statistical analysis and modelling. *Coatings* 8(10):350
10. Popov VL, Li Q, Lyashenko IA et al (2021) Adhesion and friction in hard and soft contacts: theory and experiment. *Friction* 9:1688–1706
11. Makhovskaya Y (2020) Adhesion interaction of elastic bodies with regular surface relief. *Mech Solids* 55(7):187–196
12. Israelachvili J (1992) *Intermolecular and surface forces*. Academic, New York
13. Maugis D (1991) Adhesion of spheres: the JKR-DMT transition using a Dugdale model. *J Colloid Interf Sci* 150:243–269
14. Maugis D, Gauthier-Manuel B (1994) JKR-DMT transition in the presence of a liquid meniscus. *J Adhes Sci Technol* 8(11):1311–1322
15. Goryacheva IG (1998) *Contact mechanics in tribology*. Kluwer Academic Publication, Dordrecht

16. Goryacheva IG, Tsukanov IY (2020) Analysis of elastic normal contact of surfaces with regular microgeometry based on the localization principle. *Front Mech Eng* 6:45
17. Johnson KL (1985) *Contact mechanics*. Cambridge University Press
18. Makhovskaya Yu Yu (2003) Discrete contact of elastic bodies in the presence of adhesion. *Mech Solids* 38:39–48
19. Goryacheva IG, Makhovskaya YY (2017) Elastic contact between nominally plane surfaces in the presence of roughness and adhesion. *Mech Solids* 52(4):435–443
20. Goryacheva IG, Makhovskaya YY (2004) An approach to solving the problems on interaction between elastic bodies in the presence of adhesion. *Dokl Phys* 49(9):534–538

Tuning the Mechanical Properties of the Viscoelastic Materials, for the Improvement of Their Adhesive Performance



Elena Pierro , Luciano Afferrante , and Giuseppe Carbone 

Abstract In this paper, the peeling of elastic thin tapes from real-like viscoelastic substrates is investigated by focusing the attention on the damping properties of this kind of materials. We show that the number of relaxation times involved in the physical process, is a key factor to increase the range in frequency where energy dissipation is predominant. This entails several advantages for appropriately managing the detachment process of the elastic tape. Indeed, we show how it is possible to obtain stable release conditions at high loads, so that the peeling force can be employed as control parameter. The practical case of the PMMA (polymethyl methacrylate) is considered as example, as it exhibits high damping at low-frequencies. As a result, stable detachment of the tape occurs at very small peeling velocities, especially with relatively stiff tapes. The results of this study can be exploited in many applications where the adherence of elastic tapes on viscoelastic substrates needs to be suitably designed such as, for example, in bio-medical contexts.

Keywords Energy dissipation · Adhesive properties · Viscoelasticity · Relaxation times

1 Introduction

For several years now, researchers have been observing nature for inspiration, trying to imitate the amazing adhesive abilities of some animals, such as many insects that exhibit an intermittent contact mechanism to adhere and to easily move away from many different substrates. The most recent literature has shown that the shape of the extremity in the contact with the surface is crucial [1–4], but also the distribution of micro-pillars over the interface enables the improvement of the adhesive performance

E. Pierro (✉)
School of Engineering, University of Basilicata, 85100 Potenza, Italy
e-mail: elena.pierro@unibas.it

L. Afferrante · G. Carbone
Department of Mechanics, Mathematics and Management, Polytechnic University of Bari, 70126 Bari, Italy

© The Author(s), under exclusive license to Springer Nature Singapore Pte Ltd. 2022
M. Abdel Wahab (ed.), *Proceedings of the 9th International Conference on Fracture, Fatigue and Wear*, Lecture Notes in Mechanical Engineering,
https://doi.org/10.1007/978-981-16-8810-2_11

139

[5–8]. The peeling mechanism has been thoroughly researched from both a theoretical [9–16] and experimental point of view [17–23], as it finds application in many practical fields, as in the case of the medical bands in adhesion with the human skin, that is a viscoelastic material [24–30]. In this perspective, viscoelasticity has drawn the attention of the scientific community, with particular regards to the adhesion of adhesives on viscoelastic substrates [31–36]. Moreover, several researchers have developed experimental techniques and theoretical models to be able to characterize viscoelastic materials from a mechanical point of view, since a deep knowledge of their properties is crucial for many practical applications [37–39].

In this scenario, the authors proposed an investigation on the interface crack propagation [40], as well as a theoretical model to describe the real-like viscoelastic interfaces [41]. In this paper, the main results of this research are shown, at first by investigating the behavior of a substrate made of PMMA (polymethyl methacrylate) [42], then by proposing a useful approach to design new viscoelastic materials, for adhesive contact applications, focusing the attention on some pivotal mechanical properties.

2 Theoretical Model

The elastic tape shown in Fig. 1 is considered (width b , thickness d), in adhesion with a viscoelastic substrate, with an external force P applied in a stationary peeling process.

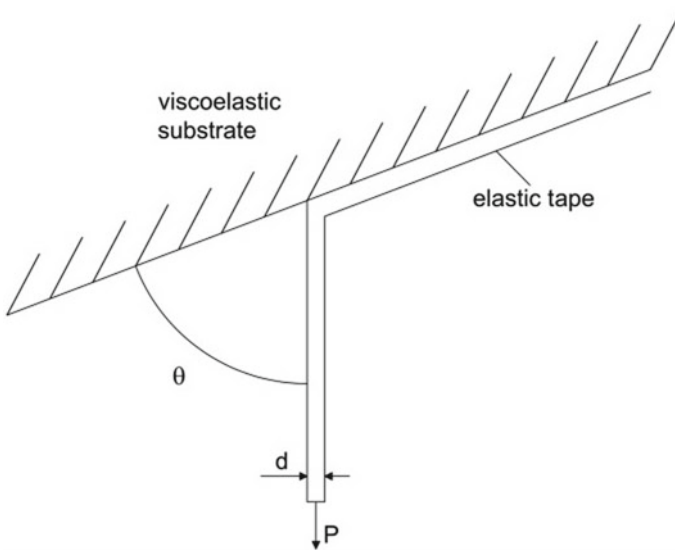


Fig. 1 The peeling of the elastic tape from the viscoelastic substrate

In order to determine the substrate displacements, we employed normal $p_n(x) = p = P \sin \theta / (bd)$ and tangential tractions $p_t(x) = q = -P \cos \theta / (bd)$, with x the direction of the substrate (see Refs. [40, 41] for more details), to which correspond the vector $\mathbf{u}^{el}(x, V) = \int \mathbf{G}(x - x')\sigma(x')dx' = \{u_x^{el}, u_z^{el}\}$, i.e. the surface displacements of an elastic half-plane over a strip ($-a \leq x \leq a$). We can therefore define the viscoelastic normal and tangential displacements [44].

$$\mathbf{u}(x, V) = \int \mathbf{G}(x - x', V)\sigma(x')dx' = \mathbf{J}(0)u^{el}(x) + \int_{0^+}^{\infty} \mathbf{u}^{el}(x + Vt)\dot{\mathbf{J}}(t)dt \quad (1)$$

where the geometrical displacement has been normalized through the stiffness of the substrate.

By considering the generalized viscoelastic model $C(\tau) = \sum_k C_k \delta(\tau - \tau_k)$, made of a spring in series with springs, with elastic compliance C_k , that are in parallel with a dashpot, we can write the creep function $\mathbf{J}(t)$ as

$$\mathbf{J}(t) = \mathbf{H}(t) \left[\frac{1}{E_0} - \sum_{k=1}^N C_k \exp(-t/\tau_k) \right] \quad (2)$$

By substituting Eq. (2) in Eq. (1) [40] one has

$$\mathbf{u}(x, V) = \frac{1}{E_\infty} \mathbf{u}^{el}(x) + \sum_{k=1}^N C_k \int_{0^+}^{+\infty} \mathbf{u}^{el}(x + V\tau_k z_k) \exp(-z_k) dz_k \quad (3)$$

being $\mathbf{J}(+\infty) = E_0^{-1}$ and $\mathbf{J}(0) = E_\infty^{-1}$, where E_∞ is the modulus at high frequencies, and $z_k = t/\tau_k$.

We now consider the energy balance

$$W_{ad} + W_{el} + W_d = W_P \quad (4)$$

being $W_P = PV_P$ the work per unit time of the force P , $W_{ad} = wbV$ the rate of surface adhesion energy, $W_{el} = P^2V/2Ebd$ the rate of elastic strain energy stored in the film and W_d the rate of energy dissipated. In particular, w is the work of adhesion per unit area, E is the Young's modulus of the tape, V is the velocity of the detachment front and V_P is the velocity of the point where the force P is applied. We therefore obtained

$$\hat{w} \delta = \left[\frac{1}{2} - \frac{E}{E_0} f_V(V) \right] \hat{P}^2 + (1 - \cos \theta) \delta \hat{P} \quad (5)$$

having defined the quantities $\hat{w} = w/(E_0d)$, $\hat{P} = P/(E_0bd)$, $\delta = E/E_0$, and θ the peeling angle, $f_V(V)$ a function depending on C_k and τ_k [41]. Let us observe that for $V \rightarrow 0$ and $V \rightarrow \infty$, one gets the Kendall solution $\hat{w} = \frac{1}{2\delta}\hat{P}^2 + (1 - \cos \theta) \hat{P}$.

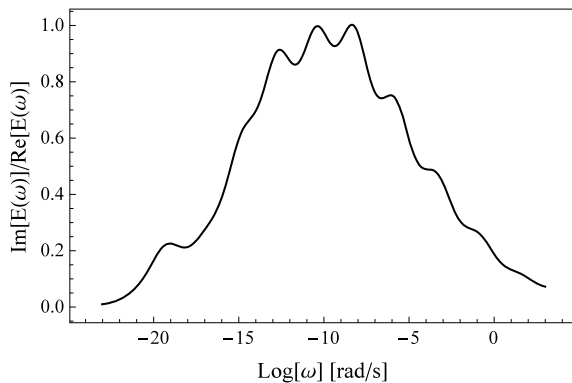
3 Results

A first investigation regards the peeling process of an elastic thin tape in contact with a substrate made of PMMA (polymethyl methacrylate), which has been modeled through a Prony series in Ref. [42] (the constants are given in Table 1). The viscoelastic modulus is shown in Fig. 2, in terms of the ratio between the imaginary and the real parts $Im[E(\omega)]/Re[E(\omega)]$. Since damping is mostly found at low frequencies, we expect to observe stable detachment at small peeling velocities.

Table 1 The constants of the Prony series of PMMA (Ref. [42])

| i | τ_i [sec] | E_i [Pa] |
|---------------------|----------------|---------------|
| 1 | $2 * 10^{-2}$ | $1.94 * 10^8$ |
| 2 | $2 * 10^{-1}$ | $2.83 * 10^8$ |
| 3 | $2 * 10^0$ | $5.54 * 10^8$ |
| 4 | $2 * 10^1$ | $6.02 * 10^8$ |
| 5 | $2 * 10^2$ | $3.88 * 10^8$ |
| 6 | $2 * 10^3$ | $1.56 * 10^8$ |
| 7 | $2 * 10^4$ | $4.1 * 10^7$ |
| 8 | $2 * 10^5$ | $1.38 * 10^7$ |
| 9 | $2 * 10^6$ | $3.68 * 10^6$ |
| 10 | $2 * 10^7$ | $7.9 * 10^5$ |
| 11 | $2 * 10^8$ | $9.6 * 10^5$ |
| $E_0 = 2.24 * 10^6$ | | |

Fig. 2 The viscoelastic modulus of the material considered [42], as the ratio $Im[E(\omega)]/Re[E(\omega)]$



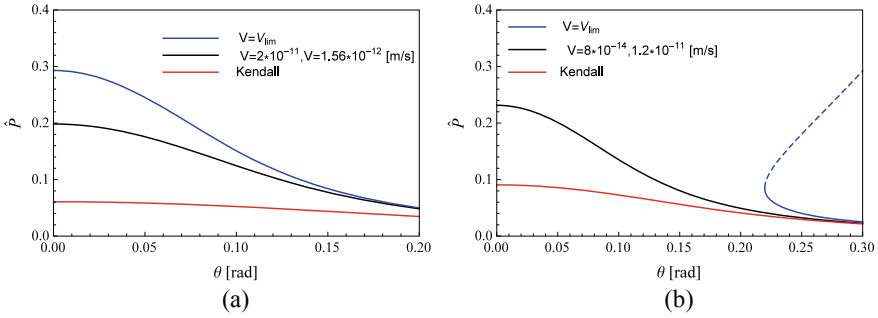


Fig. 3 The external load \hat{P} versus θ , at different velocities V , and the Kendall solution, for a substrate made of PMMA [42]. We considered $\hat{w} = 10^{-3}$, and $\delta = 1.8$ (a), $\delta = 4$ (b), and dashed lines indicate the unstable condition

In Fig. 3 one can observe that the relation between the applied load \hat{P} and the peeling angle θ , is strongly influenced by δ , and this is reasonable since the system increases its toughness with the stiffness of the tape. When a compliant tape is considered ($\delta = 1.8$, Fig. 3-a), and the external load is $\hat{P} < \hat{P}_{Kendall}$, there is no peeling. On the contrary for $\hat{P} > \hat{P}_{Kendall}$ peeling is observed up to the \hat{P}_{lim} ($\hat{P}_{Kendall} < \hat{P} < \hat{P}_{lim}$), which depends on the value of θ where the velocity V_{lim} occurs. In the case of PMMA, we calculated $V_{lim} \cong 3.78 * 10^{-12}$ [m/s], and the tape separates from the substrate at constant velocity, as also observed from experiments [47]. It is evident that for $\hat{P} > \hat{P}_{lim}$, detachment would be unstable, and in case of stiffer tape (Fig. 3-b, dashed lines) it is clearly more tough.

We can also observe that (see Fig. 4) for $\theta \leq \theta_{th} \approx 12.6^\circ$, for every external load, the peeling process is steady-state, while for $\theta > \theta_{th}$ the unstable detachment is established, when $\hat{P} > \hat{P}_{lim}$. This circumstance is related to the viscoelastic modulus of PMMA, which shows high dissipation at low frequencies (see Fig. 2),

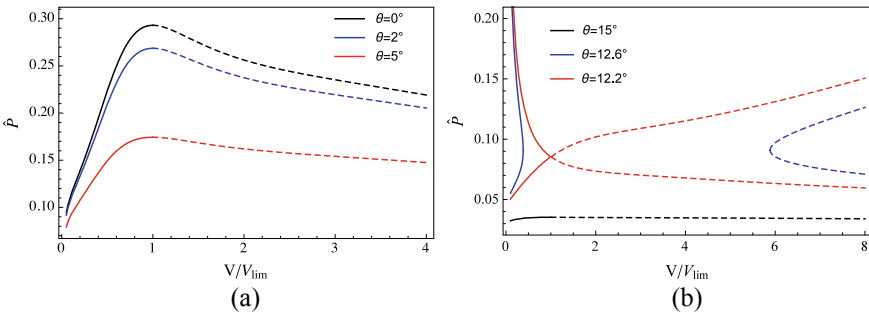


Fig. 4 The external load \hat{P} versus the ratio V/V_{lim} , for the considered substrate in PMMA (Ref. [42]), for different angle θ , and the considered values $\hat{w} = 10^{-3}$, $\delta = 1.8$ (a) and $\delta = 4$ (b). Dashed lines indicate the unstable condition

and therefore it opens scenarios in which it is possible to design material properties of the substrate to obtain ultra-tough peeling behavior.

In this perspective, we compare three materials with 1, 3 and 5 relaxation times. For the first one we take $\tau = 2 * 10^3$ [sec] and $E_0 = 10^5$ [Pa]. For the other two materials, we consider $\tau_i = \tau * 10^k$ [sec], with $i = \{1, 2, 3\}$ and $k = \{-1, 0, 1\}$, and $i = \{1, 2, 3, 4, 5\}$ and $k = \{-2, -1, 0, 1, 2\}$, respectively. The viscoelastic modulus $E(\omega)$ is shown in Fig. 5, as the ratio between the imaginary and real parts.

In Fig. 6a, we plot the peeling force \hat{P} as a function of the peeling angle θ is represented, at fixed values of $\hat{w} = 0.023$, $V = 10^{-8}$ [m/s], and $\delta = 6$. It is quite evident that the materials with 3 and 5 relaxation times exhibit stable equilibrium at arbitrarily small values of the applied force \hat{P} , because of damping occurs in a larger range of frequencies. On the contrary, for the material with 1 relaxation time,

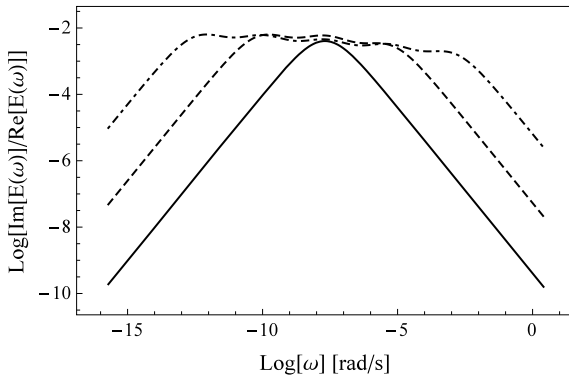


Fig. 5 The viscoelastic modulus of the three different designed materials, with 1 (solid curve), 3 (dashed curve) and 5 (dot-dashed curve) relaxation times

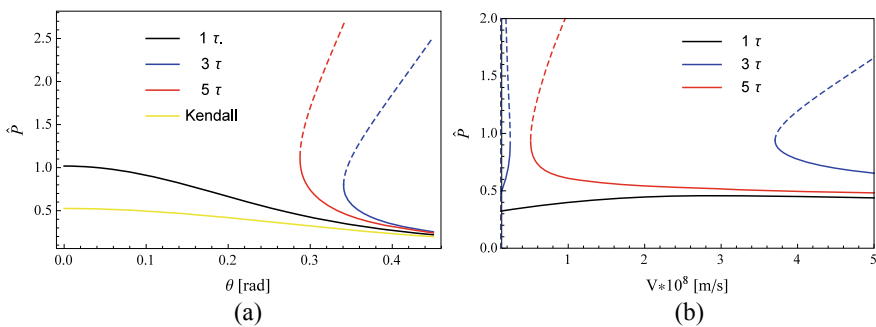


Fig. 6 The external load \hat{P} versus the angle θ , for the 3 ideal materials and the Kendall solution (red curve), with $\hat{w} = 0.023$, $V = 10^{-8}$ [m/s] and $\delta = 6$ (a); the external load \hat{P} versus the velocity V , with $\hat{w} = 0.023$, $\theta = 18^\circ$ and $\delta = 6$ (b). Dashed lines indicate the unstable condition

we observe stable equilibrium is observed only with loads smaller than the threshold value which determines unstable condition (Fig. 6b).

In conclusion, the main result of this study consists in the possibility of conveniently designing viscoelastic materials, in order to optimize the peeling process, making it ultra-tough according to several practical applications.

4 Conclusions

In this paper, we have studied the peeling of an elastic thin tape from a viscoelastic substrate, by focusing the attention on the influence of the mechanical properties of viscoelastic materials on the peeling process. The number of relaxation times plays a crucial role in the material damping distribution over the frequencies, thus affecting also energy dissipation and the relation between the stable peeling process and the external applied loads. In this way, it is possible to control the detachment velocity of the tape by means of the proper choice of the peeling force. We also studied the behavior of the PMMA, a widespread and commonly utilized viscoelastic material, that exhibits high damping at low frequencies. For this material, small peeling velocities are needed in order to get a stable detachment, especially in the case of relatively stiff tapes.

References

1. Gorb SN, Varenberg M (2007) Mushroom-shaped geometry of contact elements in biological adhesive systems. *J Adhes Sci Technol* 21:1175–1183
2. Carbone G, Pierro E, Gorb S (2011) Origin of the superior adhesive performance of mushroom-shaped microstructured surfaces. *Soft Matter* 7:5545–5552
3. Carbone G, Pierro E (2012) Sticky bio-inspired micropillars: finding the best shape. *Small* 8(9):1449–1454
4. Afferrante L, Carbone G (2013) The mechanisms of detachment of mushroom-shaped micropillars: from defect propagation to membrane peeling. *Macromol React Eng* 7:609–615
5. Gorb S, Jiao Y, Scherge M (2000) Ultrastructural architecture and mechanical properties of attachment pads in *Tettigonia viridissima* (Orthoptera Tettigoniidae). *J Comp Physiol A* 186(9):821–831
6. Jiao Y, Gorb S, Scherge M (2000) Adhesion measured on the attachment pads of *Tettigonia viridissima* (Orthoptera, Insecta). *J Exp Biol* 203(12):1887–1895
7. Afferrante L, Carbone C (2012) Biomimetic surfaces with controlled direction-dependent adhesion. *J R Soc Interf* 9:3359–3365
8. Afferrante L, Grimaldi G, Demelio G, Carbone G (2015) Direction-dependent adhesion of micro-walls based biomimetic adhesives. *Int J Adhes Adhes* 61:93–98
9. Huber G, Mantz H, Spolenak R, Mecke K, Jacobs K, Gorb SN, Arzt E (2005) Evidence for capillarity contributions to gecko adhesion from single spatula nanomechanical measurements. *Proc Natl Acad Sci USA* 102(45):16293–16296
10. Pesika NS, Tian Y, Zhao B, Rosenberg K, Zeng H, McGuiggan P, Autumn K, Israelachvili JN (2007) Peel-zone model of tape peeling based on the gecko adhesive system. *J Adhes* 83:383–401

11. Chen B, Wu P, Gao H (2009) Pre-tension generates strongly reversible adhesion of a spatula pad on substrate. *J R Soc Interf* 6(2065):529–537
12. Peng ZL, Chen SH, Soh AK (2010) Peeling behavior of a bio-inspired nano-film on a substrate. *Int J Solids Struc* 47:1952–1960
13. Lepore E, Pugno F, Pugno NM (2012) Optimal angles for maximal adhesion in living tokay geckos. *J Adhes* 88(10):820–830
14. Sauer RA (2011) The peeling behavior of thin films with finite bending stiffness and the implications on gecko adhesion. *J Adhes* 87(7–8):624–643
15. Wu X, Zhang Y, Liu Y, Hu C (2012) Viscoelastic analysis of gecko digital peeling by hyper-extension. In: Proceedings of the 2012 IEEE International conference on mechatronics and automation, August 5–8, Chengdu, China
16. Tian Y, Pesika N, Zeng HB, Rosenberg K, Zhao BX, McGuiggan P, Autumn K, Israelachvili J (2006) Adhesion and friction in gecko toe attachment and detachment. *Proc Natl Acad Sci USA* 103:19320–19325
17. Rivlin RS (1944) The effective work of adhesion. *Paint Technol* 9:215–216
18. Afferrante L, Carbone G, Demelio G, Pugno N (2013) Adhesion of elastic thin films: double peeling of tapes versus axisymmetric peeling of membranes. *Tribol Lett* 52:439–447
19. Misseroni D, Afferrante L, Carbone G, Pugno NM (2017) Non-linear double-peeling: experimental vs. theoretical predictions. *J Adhes* 94(1):46–57
20. Menga N, Afferrante L, Pugno NM, Carbone G (2018) The multiple V-shaped double peeling of elastic thin films from elastic substrates. *J Mech Phys Solids* 113:56–64
21. Putignano C, Afferrante L, Mangialardi L, Carbone G (2014) Equilibrium states and stability of pre-tensioned adhesive tapes. *Beilstein J Nanotechnol* 5:1725–1731
22. Pugno NM (2011) The theory of multiple peeling. *Int J Fract* 171:185–193
23. Peng Z, Chen S (2015) Peeling behavior of a thin-film on a corrugated surface. *Int J Solids Struc* 60(61):60–65
24. Christensen MS, Hargens CW, Nacht S, Gans EH (1977) Viscoelastic properties of intact human skin: instrumentation, hydration effects, and the contribution of the stratum corneum. *J Invest Dermatol* 69:282–286
25. Agache PG, Monneur C, Leveque JL, De Rigal J (1980) Mechanical properties and Young's modulus of human skin in vivo. *Arch Dermatol Res* 269(3):221–232
26. Escoffier C, de Rigal J, Rochefort A, Vasselet R, Leveque J-L, Agache PG (1989) Age-related mechanical properties of human skin: an In vivo study. *J Invest Dermatol* 93:353–357
27. Pereira JM, Mansour JM, Davis BR (1991) Dynamic measurement of the viscoelastic properties of skin. *J Biomech* 24(2):157–162
28. Edwards C, Marks R (1995) Evaluation of biomechanical properties of human skin. *Clin Dermatol* 13(4):375–380
29. Silver FH, Freeman JW, CeVoe D (2001) Viscoelastic properties of human skin and processed dermis. *Skin Res Technol* 7:18–23
30. Boyer G, Lyon CNRS, Zahouani H, Le Bot A, Laquieze L (2007) In vivo characterization of viscoelastic properties of human skin using dynamic micro-indentation. In: Engineering in medicine and biology society, EMBS 2007. 29th Annual international conference of the IEEE
31. Chivers RA (2001) Easy removal of pressure sensitive adhesives for skin applications. *Int J Adhes Adhes* 21:381–388
32. Renvoise J (2006) Rheological and peeling properties on a viscoelastic substrate. Medical applications. PhD Thesis, University of Pau, France
33. Renvoise J, Burlot D, Marin G, Derailb C (2007) Peeling of PSAs on viscoelastic substrates: a failure criterion. *J Adhes* 83:403–416
34. Renvoise J, Burlot D, Marina G, Derailb C (2009) Adherence performances of pressure sensitive adhesives on a model viscoelastic synthetic film: a tool for the understanding of adhesion on the human skin. *Int J Pharm* 368(1–2):83–88
35. Lir I, Haber M, Dodiuk-Kenig H (2007) Skin surface model material as a substrate for adhesion-to-skin testing. *J Adhes Sci Technol* 21(5):1497–1512

36. Plaut RH (2010) Two-dimensional analysis of peeling adhesive tape from human skin. *J Adhes* 86(11):1086–1110
37. Pierro E (2020) Damping control in viscoelastic beam dynamics. *J Vib Control* 26(19–20):1753–1764
38. Pierro E (2019) Viscoelastic beam dynamics: theoretical analysis on damping mechanisms. In: *ECCOMAS Thematic conference on computational methods in structural dynamics and earthquake engineering*
39. Pierro E, Carbone G (2020) Vibration-based identification of mechanical properties of viscoelastic materials. In: *Proceedings of ISMA2020, Leuven, Belgium, September 7–9 2020*
40. Afferrante L, Carbone G (2016) The ultratough peeling of elastic tapes from viscoelastic substrates. *J Mech Phys Solids* 96:223–234
41. Pierro E, Afferrante L, Carbone G (2020) On the peeling of elastic tapes from viscoelastic substrates: designing materials for ultratough peeling. *Tribol Int* 146
42. Park SW, Schapery RA (1999) Methods of interconversion between linear viscoelastic material functions. Part I-A Numer Meth Based Prony Ser Int *J Solids Struct* 36:1653–1675
43. Peng Z, Chen S (2015) Effect of bending stiffness on the peeling behavior of an elastic thin film on a rigid substrate. *Phys Rev E* 91:042401
44. Carbone G, Putignano C (2013) A novel methodology to predict sliding and rolling friction of viscoelastic materials: theory and experiments. *J Mech Phys Solids* 61:1822–1834
45. Christensen RM (1982) *Theory of viscoelasticity*. Academic Press, New York
46. Johnson KL (1985) *Contact mechanics*. Cambridge University Press, Cambridge
47. Kovalchick C, Molinari A, Ravichandran G (2014) Rate dependent adhesion energy and nonsteady peeling of inextensible tapes. *J Appl Mech* 81(4):041016

Numerical and Experimental Analysis of Profile Complexity in Aluminum Extrusion



Josiah Cherian Chekotu, Sayyad Zahid Qamar, and Sayyad Basim Qamar

Abstract In extrusion, shape complexity serves as an indicator of the difficulty in extruding the profile. It can affect the extrusion load and metal flow pattern. Non-homogeneous metal flow and severe pressure conditions can directly influence product quality, die life, and overall productivity. Most of the product defects can be linked to extrusion pressure and flow pattern of the metal. The current paper investigates, experimentally and numerically, how shape complexity influences extrusion load and material flow. Finite element modelling (FEM) is used to simulate and analyze the cold extrusion of various die shapes (nine) having distinct profile complexities. Generated numerical solutions are used to study the influence of geometrical complexity, extrusion ratio, and profile symmetry on dead metal zone (DMZ), metal flow, and extrusion pressure. All of these factors can aid in assessing the possibilities of certain types of product defects. It was observed that higher shape complexity values result in higher pressures and more severe metal flow patterns, which lead to higher chances of product defects. The findings of this study can be of assistance to die manufacturers and extrusion plants in optimizing the die designs, and reducing metal flow related defects.

Keywords Shape complexity · Metal extrusion · Product defects · Extrusion pressure · Metal flow

J. Cherian Chekotu

School of Mechanical & Manufacturing Engineering, Dublin City University, Dublin, Oman
e-mail: josiah.chekotu@dcu.ie

S. Zahid Qamar (✉)

Mechanical & Industrial Engineering Department, Sultan Qaboos University, Muscat, Oman
e-mail: sayyad@squ.edu.om

S. Basim Qamar

Department of Materials Science & Engineering, Texas A&M University, College Station, Texas, USA

1 Introduction

The process of extrusion transforms a billet material into a required geometry by pressing it through a die opening [1]. Cold extrusion (ambient temperature) yields good dimensional precision and improved surface quality in comparison with hot working [2]. However, cold working requires higher pressures, which can reduce the extrudability and can lead to certain product defects [3, 4]. Two major parameters that affecting extrudate quality, die life, and overall productivity are metal flow conditions and extrusion pressure [5–7]. Shape complexity is an indicator of the geometrical intricacy of the die [1, 8–10]. The most well-known and often used definition of shape complexity [11] is based on the perimeter (P_s) and area (A_s) of the section being extruded.

$$C_1 = P_s / A_s \quad (1)$$

Current work involves finite element (FE) simulation of extrusion of solid profiles with different shape complexities, using DEFORM 3D. It provides a better understanding of how shape complexity affects the metal flow and extrusion force, and proposes a method to assess the type and amount of certain extrudate defects. After validating against experimental data of three dies having round, C-shape, and cross profiles, the FE model was employed to numerically explore profiles of different complexities ranging from rectangle, square, triangle to more complex profiles such as I, T, and L-sections. Findings of this study can aid in better design of dies and related tooling, and in minimizing several process-related extrusion product defects.

2 Experimental Work

The experimental setup (Fig. 1) comprised of an extrusion chamber and three dies having solid profiles. All of the parts were designed in-house and fabricated from H13 steel with the help of a local die manufacturer using EDM and high speed milling techniques [12]. The billet material used was aluminum alloy 6063. To visualize the metal flow, the billets were split longitudinally into mirror portions. The whole unit was installed in an Instron testing machine (250kN) that was set to compression mode. An extensometer was connected to a computer through a data logger. Experiments were run at ram speeds of 5 and 10 mm/min, and ram force and displacement information was recorded. Petroleum jelly was used as a lubricant to prevent sticking friction.

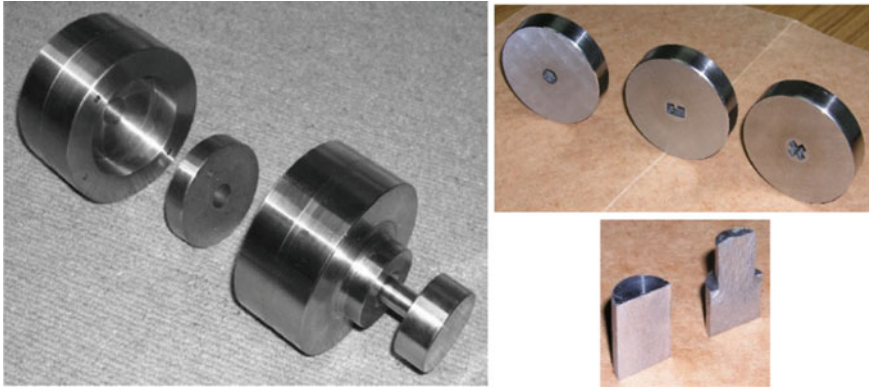


Fig. 1 Extrusion setup (ram, container, die backer); circular, C-channel and cross profile dies; and split billet

3 Numerical Simulation

DEFORM-3D was used in this study especially because of its capability of handling large deformations through automatic re-meshing. The study covers nine different profiles of varying complexity. Geometric details are shown in Fig. 2a, and complexity values are listed in Table 1. The material library of DEFORM-3D was utilized to estimate the mechanical properties for Al-6063 in the annealed state. For cold working, room temperature (30 °C) was set. Triangle, C, T, and L sections

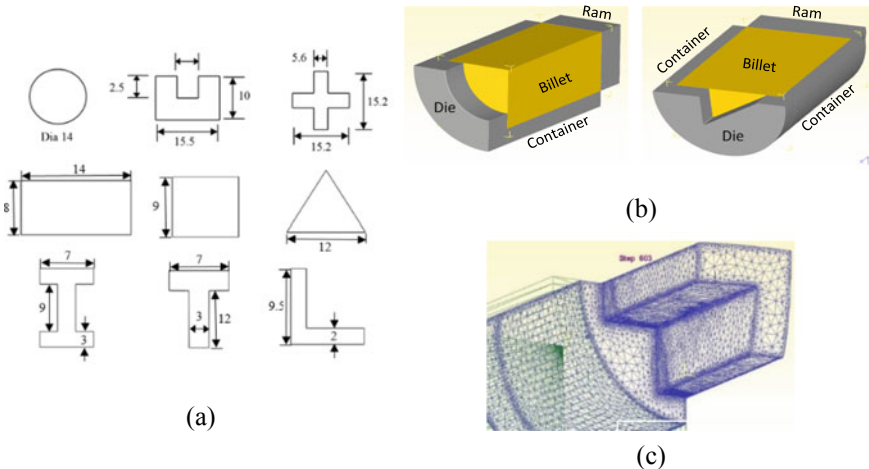


Fig. 2 a Geometry of all die profiles used (dimensions in mm); **b** 3D model of circular (biaxial symmetry) and triangular (uniaxial symmetry) profiles; **c** automatic re-meshing as observed in the cross-shape FE model

Table 1 Complexity indices and extrusion ratios of the nine profiles

| Shape | Complexity index (CI = P_s/A_s) | Extrusion ratio (R = A_0/A_s) |
|-----------|------------------------------------|----------------------------------|
| Circular | 0.286 | 1.842 |
| C-section | 0.376 | 1.906 |
| Rectangle | 0.393 | 2.532 |
| Cross | 0.438 | 2.042 |
| Square | 0.444 | 3.500 |
| Triangle | 0.577 | 4.547 |
| I-section | 0.754 | 4.109 |
| T-section | 0.772 | 4.974 |
| L-section | 1.118 | 8.339 |

are symmetrical about one axis, and were modelled as uni-axisymmetric, while the remaining profiles exhibited bi-axial symmetry, and therefore they were modelled as bi-axisymmetric (Fig. 2b).

Tetrahedral mesh elements were selected because they can handle large deformations very well. Automatic re-meshing was set to re-mesh locally. The billet was initially meshed with an average of about 60,000 elements. For instance, numerical model of cross shape (Fig. 2c) illustrates automated re-meshing. After analyzing convergence patterns, a mesh size of 0.1 mm was selected for all the shapes.

The container-billet interface undergoes sliding friction and therefore a coulomb type friction model was assigned. The value of coefficient of sliding friction was identified as $\mu = 0.1$, after comparing the pressure curves for different values of μ against the experimental pressure curve. The shear friction at the die-billet interface was ignored, as it is almost negligible when compared to friction at the container-billet interface.

4 Results and Discussion

Extrusion forces and velocity profiles were generated using the FE simulation. The simulated (FEM) force curves were found to exhibit minor fluctuations. Higher-order curve fitting and smoothening were used to enhance the readability.

4.1 Model Validation

The force curves generated in the experiment and the simulation were compared for round, C-channel, and cross profiles, at ram speeds of 5 and 10 mm/min. Simulated

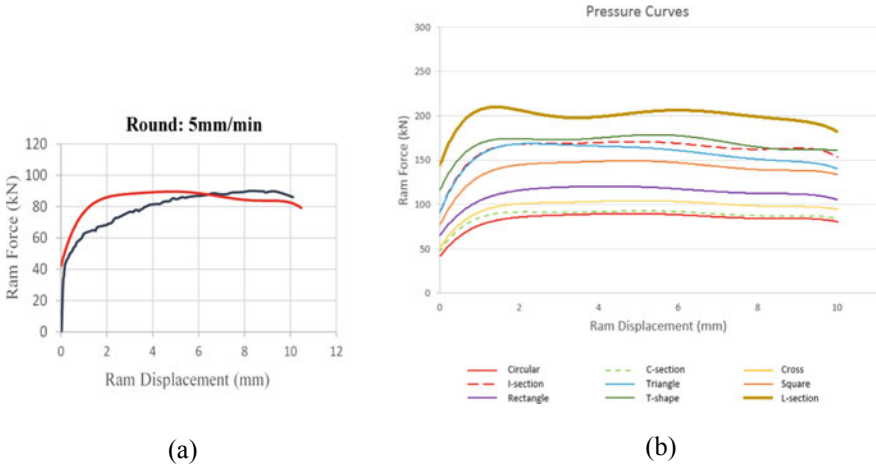


Fig. 3 a Experimental (black) and numerical (red) graphs of extrusion force for circular section (5 mm/min); b Variation of force against ram travel for the nine die geometries

graphs show approximately the same behavior and variations as seen in the experiment (Fig. 3a). The forces at the peak and plateau in both simulation and experiments were found to be almost the same, with a maximum error of less than 7%. A small deviation can be observed between the FE and actual curves in the early stage of pressure rise. This can be attributed to the different effects of machine adjustments and billet upsetting involved in industry or experiment, whereas the FE curves offer only the theoretical behavior of the extrusion process.

4.2 Comparative Analysis of Profiles

4.2.1 Extrusion Force

In Table 1, complexity values of the 9 die shapes are listed, calculated using the “Ps/As” equation. The extrusion force vs ram travel curves for the nine shapes are compiled on one diagram (Fig. 3b). As one would expect, shapes of higher complexity have higher forces. One deviation from this general trend is that the force profile of rectangular shape is higher, while its complexity index is lower (0.393) when compared to more complex profile, such as a cross having 0.438. A vital parameter, extrusion ratio (R), has not been included in definition C1. Higher force curve has been found for the shape having a bigger extrusion ratio (rectangle 2.532, cross 2.042). This points to a necessity of including extrusion ratio along with perimeter-to-area ratio to improve the definition of complexity index.

4.2.2 Material Flow Pattern and Extrusion Defects

Lines of metal flow in extrusion can be investigated by analyzing the velocity profiles in FE simulations as the billet deforms. The direction of metal flow is depicted by the direction of the velocity vectors. These velocity profiles allow us to evaluate whether the metal flow is uniform (homogeneous) or not, along with the accumulation of flow lines in a certain area. The dead metal zone (DMZ), where sliding or shearing takes place, can also be identified using the velocity profile and can help quantify its size. The DMZ resists material flow and contributes to the non-homogeneity in metal flow [12, 13]. The velocity profiles also help to identify symmetry of the metal flow. 2D and 3D views of velocity profiles were analyzed to understand the flow pattern. 2D velocity profiles of circular section and C-section are shown in Fig. 4a, b as examples, while other velocity profiles are discussed but not shown here due to size restrictions.

The simplest (lowest complexity) shape is the round die which has biaxial symmetry and no stress concentration points. The velocity profile in Fig. 4a shows the very symmetric and highly uniform metal flow with no visible concentration of flow lines in any particular region. Length of the DMZ is measured as 2.70 mm, the smallest for all shapes studied. Extrusion pressures will be low due to the very smooth metal flow. This translates into low-power equipment and longer lasting dies and tools.

Lower symmetry is observed in the velocity profile of the C-section (Fig. 4b) along with less homogeneous metal flow. The flow lines are also concentrated in a few areas. The DMZ length (8.50 mm) is also greater and is located near the thinner lip. For the cross-shape, despite the biaxially symmetric profile, the metal flow is less homogeneous because of several stress concentrators. There is higher concentration of flow lines close to the edges and in the axially central portion of the billet, with a DMZ size of around 6.45 mm. Biaxial symmetry also exists for

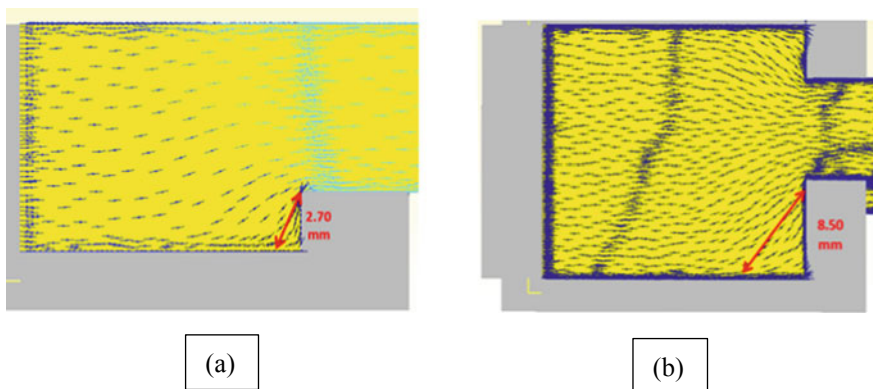


Fig. 4 2D velocity profiles displaying metal flow and DMZ, for **a** double-symmetric round section and for **b** single-symmetry C-shape

profiles of the rectangular and square sections. There is higher concentration of flow lines closer to the shorter dimension for the rectangular shape, with a DMZ length of 7.47 mm. Metal flow is more nonhomogeneous for the square section with the flow lines concentrated near the die cavity. For the triangular shape, the flow is unsymmetrical, non-homogeneous, and highly concentrated near the corners and in the central portion of. With a value of approximately 9.60 mm, the DMZ is larger than all the other shapes described before this. This would lead to larger extrusion pressures and uneven metal flow that is faster on one side.

The metal flow in the I-section is highly unsymmetric, non-uniform, and has a large concentration of flow lines which also bend severely. The length of the DMZ is 10.44 mm (larger compared to the triangle die). This will lead to a higher force requirement and the severity of the metal flow will make the regions of smaller thickness more susceptible to defects. The I- and T-section shapes are similar. However, the T-profile is uni-axisymmetric, whereas the I-section displays bi-axisymmetric but includes higher number of stress raisers. With the T-section, the metal flow is restricted around the tail leading to a larger DMZ size (12.73 mm). This contributes to the slightly higher forces. The highest complexity index belongs to the L-section, which is non-symmetric. As a result, the flow is highly non-homogeneous. Moreover, due to the section being much thinner it yields the highest extrusion ratio. True to form, length of the DMZ (18.30 mm) is also the largest for this shape.

Homogenous material flow (circular section) correlates to good quality of the extrudate, with lower chances of defects. Slightly larger DMZ size (C-shape) can lead to product defects like convex/concave profile, blisters, twists, and out-of-angle. Lower uniformity of material flow and bigger DMZ (cross profile) results in larger extrusion pressure and the likelihood of defects such as pipe formation, tearing and flash-out. Extrusion flaws such as tearing and internal cracking can occur with more inhomogeneous metal flow concentrated near the die cavity (rectangular shape). Higher extrusion forces together with uneven material flow (higher flow speed in one portion of the die compared to the other), as for the triangle section, can lead to defects such as concavity/convexity, tearing, cracking and twists. The L-section combines several detrimental factors (non-symmetric geometry, nonhomogeneous material flow, thin section, big value of ER, big DMZ length) leading to the highest chances of product defects occurring. Large extrusion forces and erratic flow lines commonly lead to funnel and pipe formation, internal cracking, surface cracking, out-of-angle, concave/convex shape, ripping, flash-out, blisters, and twists and bends. More detailed descriptions, reasons, frequency of occurrence, preventative methods, and mitigative actions for extrusion product defects can be found in [14–16].

5 Conclusions

An FEA based numerical model was created, using the package DEFORM 3D, for cold extrusion of solid shape dies. Validation of the FE model was carried out in comparison with experimental results for the circular, C-section, and cross profiles.

Using the FE model, extrusion was then carried out for six other solid-shape dies (rectangular, square, triangular, and I-, T-, and L-sections). Shapes of higher complexity require higher extrusion forces in general, causing more irregular material flow. Along with profile complexity, the extrusion ratio, geometrical symmetry, and DMZ size also contribute to the extrusion process. Larger DMZ values lead to higher resistance to metal flow, causing pressure rise for these shapes. Product defects are highly sensitive to larger values of extrusion force and inhomogeneous metal flow. Therefore, profiles of higher complexity (triangular, I-, T-, and L-sections) are found to be the most susceptible to product defects. These findings can provide an improved understanding of fluctuations in extrusion force and material flow, and aid practitioners and researchers in better design of dies and tools, and in mitigation of product defects.

Acknowledgement Authors acknowledge the support of Sultan Qaboos University; Aluminum Products Co (ALUPCO), Dhahran; and National Aluminum Products Co (NAPCO), Muscat in conducting this investigation.

References

1. Qamar SZ, Arif AFM, Sheikh AK (2003) An investigation of shape complexity in metal extrusion. In: Proceedings of the international conference on advances in materials and processing technologies, Dublin, Ireland, pp 1178–1183
2. Bauser M, Sauer G, Siegert K (2006) Extrusion. ASM International, Materials Park (Ohio), USA
3. Qamar SZ, Arif AF, Sheikh AK (2014) A new definition of shape complexity for metal extrusion. *J Mater Process Technol* 155–156:1734–1739
4. Arif FM, Sheikh AK, Qamar SZ, Al-Fuhaid KM (2001) Modes of die failure and tool complexity in hot extrusion of Al-6063. In: Proceedings of the 16th international conference on production research, Prague, Czech Republic
5. Qamar SZ (2015) Fracture life prediction and sensitivity analysis for hollow extrusion dies. *Fatigue Fract Eng Mater Struct* 38:434–444
6. Qamar SZ, Sheikh AK, Arif AFM, Younas M, Pervez T (2008) Monte Carlo simulation of extrusion die life. *J Mater Process Technol* 202(1–3):96–106. IF 2.66 Oct-2015
7. Arif FM, Sheikh AK, Qamar SZ (2003) A study of die failure mechanisms in aluminium extrusion. *J Mater Process Technol* 134:318–328
8. Qamar SZ, Pervez T, Chekotu JC (2018) Die defects and die corrections in metal extrusion. *Metals* 8:380
9. Laue K, Stenger H (2006) Extrusion: processes, machinery, tooling. American Society for Metals, Metals Park (Ohio), USA
10. Qamar Z, Sheikh AK, Arif AFM, Pervez T (2007) Defining shape complexity of extrusion dies; a reliabilistic view. *Mater Manuf Processes* 22 (7–8):804–810
11. Kargin VR, Deryabin AY (2016) Characteristics of large bars extruding using small extrusion ratio. *Key Eng Mater* 684:211–217
12. Chekotu JC (2017) Analysis of product and tooling defects in extrusion. M.Sc. thesis, Sultan Qaboos University
13. Qamar SZ (2009) FEM study of extrusion complexity and dead metal zone. *Arch Mat Sci Eng* 36:110–117

14. Qamar SZ, Chekotu JC, Pervez T (2017) Mitigation of major product defects in aluminium extrusion. In: Proceedings of the 14th international conference and exhibition on materials science and engineering, Las Vegas, USA, pp 13–15
15. Qamar SZ, Arif AFM, Sheikh AK (2004) Analysis of product defects in a typical aluminium extrusion facility. *Mater Manuf Processes* 19:391–405
16. Qamar SZ (2010) Shape complexity, metal flow, and dead metal zone in cold extrusion. *Mater Manuf Processes* 25:1454–1461

Fatigue

Critical Plane and Critical Distance Approaches to Assess Damage Under Variable Amplitude Fretting Fatigue Loading



C. V. Teuchou Kouanga, D. Nowell, R. S. Dwyer Joyce, and L. Susmel

Abstract This paper summarises an attempt to formulate a design approach suitable for predicting the finite lifetime of mechanical assemblies subjected to constant/variable amplitude fretting fatigue loading. The proposed design methodology makes use of the Modified Wöhler Curve Method (MWCM), applied in conjunction with the Theory of Critical Distance (TCD) and the Shear Stress-Maximum Variance Method (τ -MVM). In particular, the TCD (applied in the form of the Point Method) is used to take into account the damaging effect of the multi-axial stress gradients acting on the material in the vicinity of the contact region. The time-variable linear-elastic stress state at the critical point is then post-processed according to the MWCM which is a bi-parametrical criterion that estimates fatigue lifetime via the plane experiencing the maximum shear stress amplitude. Finally, the τ -MVM is used to calculate the stress quantities relative to the critical plane whose orientation is determined numerically by selecting the plane containing the direction experiencing the maximum variance of the resolved shear stress. Further, this direction is also used to perform the cycle counting by directly applying the classic Rain-Flow Method to post-process the resolved shear stress. The overall accuracy and reliability of the proposed approach is checked against a large number of new experimental results that were generated in the Sheffield Structures Laboratory under variable amplitude fretting fatigue loading.

Keywords Fretting fatigue prediction · Theory of critical distance · Multiaxial fatigue

C. V. Teuchou Kouanga · L. Susmel (✉)

Department of Civil and Structural Engineering, the University of Sheffield, Sheffield S1 3JD, UK
e-mail: l.susmel@sheffield.ac.uk

D. Nowell

Department of Mechanical Engineering, Imperial College London, London SW7 2AZ, UK

R. S. Dwyer Joyce

Department of Mechanical Engineering, the University of Sheffield, Sheffield S1 3JD, UK

1 Introduction

Fretting fatigue damage is a term used to describe those failures occurring in mechanical components at the contact interfaces, with this damage mechanism being active in the presence of combined reciprocating frictional contacts and remote fatigue loading. Over the years, fretting fatigue cracks have been observed in numerous real mechanical assemblies such as, for instance, cylinder block/head gasket of internal combustion engines, threaded pipe connections, riveted/bolted joints and blade-disk attachments in turbines of aero-engines [1]. Hence, the prediction of fretting fatigue lifetime of materials and components is of great interest in situations of industrial interest. This explains the reason why numerous theoretical and experimental systematic studies have been carried out since the early 1960s to quantify and model damage in materials subjected to fretting fatigue loading. Examination of the state of art demonstrates that most fretting fatigue investigations have been conducted under constant amplitude (CA) load histories [2–9]. In particular, the majority of the experimental studies available in the technical literature consist of applying a static load to the testing pads and a CA fatigue load to the specimens. In contrast, very little experimental work has been done to investigate fretting fatigue failures under variable amplitude (VA) loading.

In the scenario briefly described above, the novelty characterising this investigation is twofold. Firstly, to generate new experimental results, where specimens made of cast iron are tested under VA and CA fretting fatigue loading. Secondly, by making use of the “notch analogue” concept [10], the MWCM is used in conjunction with the TCD and the Shear Stress-Maximum Variance Method (τ -MVM) to estimate the finite lifetime of the laboratory specimens tested under both CA and VA fretting fatigue loading.

2 Fundamental of the MWCM Under CA Loading

The MWCM [11, 12] is a critical plane approach which postulates that fatigue damage in materials subjected to fatigue loading can be quantified via the maximum shear amplitude, τ_a , the mean normal stress, $\sigma_{n,m}$, and the normal stress amplitude, $\sigma_{n,a}$, relative to the material plane experiencing the maximum shear stress amplitude (i.e. the so-called critical plane). The stress components associated with the critical plane are used to assess the fatigue damage extent via the following ratio [13]:

$$\rho_{\text{eff}} = \frac{m \cdot \sigma_{n,m} + \sigma_{n,a}}{\tau_a} \quad (1)$$

According to the way this critical plane stress ratio is defined, ρ_{eff} is equal to unity under fully-reversed uniaxial fatigue loading and to zero under fully-reversed torsional fatigue loading [14, 15]. In Eq. (1), m is the mean stress sensitivity index that ranges between 0 and 1. A material is said to be insensitive to the presence of

superimposed static stresses when $m = 0$, whereas $m = 1$ corresponds to a situation where the material is fully-sensitive to the presence of non-zero mean stresses [13]. m is a material property that must be determined by running appropriate experiments.

The MWCM estimates fatigue damage via non-conventional SN curves that are plotted in τ_a versus N_f modified Wöhler diagrams. According to the log–log chart reported in Fig. 1, any modified Wöhler curve is defined via its reference shear stress amplitude, $\tau_{A,Ref}(\rho_{eff})$, extrapolated at N_{Ref} cycles to failure and its negative inverse slope, $k_\tau(\rho_{eff})$. According to the scheme shown in Fig. 1, fatigue damage is seen to increase as ρ_{eff} increases, since the corresponding fatigue curve tends to shift downwards with increasing ρ_{eff} (Fig. 1a). According to the classical log–log scheme used to summarise fatigue data, the position and the negative inverse slope of any Modified Wöhler curve can be defined through the following linear relationships [14]:

$$K_\tau(\rho_{eff}) = (k - k_0)\rho_{eff} + k_0 \text{ for } \rho_{eff} \leq r_{lim} \tag{2}$$

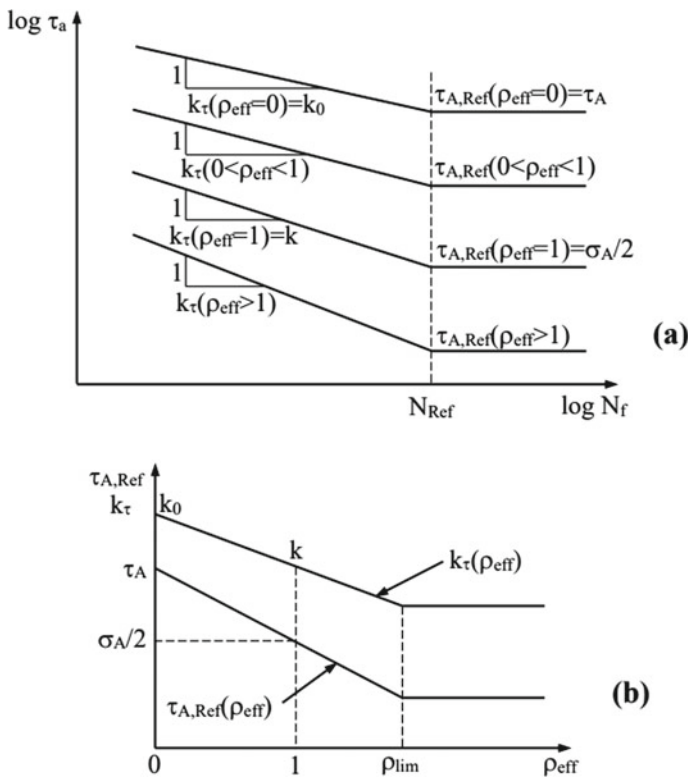


Fig. 1 Modified Wöhler diagram (a) and variation of k_τ and $\tau_{A,Ref}$ with ρ_{eff}

$$\tau_{A,Ref}(\rho_{eff}) = \left(\frac{\sigma_A}{2} - \tau_A \right) \rho_{eff} + \tau_A \text{ for } \rho_{eff} \leq \rho_{lim} \quad (3)$$

The meaning of the symbols used in the above relationships is explained in Fig. 1. For the sake of clarity, Eqs. (2) and (3) are also plotted in Fig. 1b. This schematic diagram can be used to introduce another important assumption that is made to deal effectively with those situations involving large values of ratio ρ_{eff} . In particular, the schematic chart of Fig. 1b makes it evident that when ρ_{eff} is larger than ρ_{lim} , $k_{\tau}(\rho_{eff})$ and $\tau_{A,Ref}(\rho_{eff})$ take on the following values [13, 15]:

$$K_{\tau}(\rho_{eff}) = (k - k_0)\rho_{lim} + k_0 = \text{const for } \rho_{eff} > \rho_{lim} \quad (4)$$

$$\tau_{A,Ref}(\rho_{eff}) = \left(\frac{\sigma_A}{2} - \tau_A \right) \rho_{lim} + \tau_A = \text{const for } \rho_{eff} > \rho_{lim} \quad (5)$$

where [13]:

$$\rho_{lim} = \frac{\tau_A}{2\tau_A - \sigma_A} \quad (6)$$

The above correction, which plays a key role in the overall accuracy of the MWCM, was introduced as a consequence of the fact that, under large values of ratio ρ_{eff} , the estimates obtained via the conventional critical plane approach are seen to become too conservative [15]. According to the experimental results due to Kaufman and Topper [16], such a high degree of conservatism can be ascribed to the fact that, when micro/meso cracks are fully open, an increase of the normal mean stress does not result in a further increase of fatigue damage. This important damage mechanism is incorporated into the MWCM via the use of ρ_{lim} together with relationships (4) and (5) [13].

As far as CA multiaxial fatigue assessment is concerned, the modified Wöhler diagram of Fig. 1a can directly be used to estimate fatigue life via the following trivial relationship:

$$N_f = \left[\frac{\tau_{A,Ref}(\rho_{eff})}{\tau_a} \right]^{K_{\tau}(\rho_{eff})} \quad (7)$$

In Eq. (7), τ_a and ρ_{eff} are to be determined by post-processing the stress components relative to the critical plane, whereas $\tau_{A,Ref}(\rho_{eff})$ and $k_{\tau}(\rho_{eff})$ are directly estimated from Eqs. (2) to (5).

3 The MWCM Applied Along the TCD to Estimate VA Fretting Fatigue Lifetime

In order to increase its computational efficiency, the MWCM is recommended for application by defining the critical plane as that material plane containing the direction experiencing the maximum variance of the resolved shear stress [11, 17, 18]. Accordingly, in this paper, the Shear Stress-Maximum Variance Method (τ -MVM) [19] will be used to calculate the orientation of the critical plane and the associated stress components. Since the algorithm to determine the critical plane according to τ -MVM has already been discussed in detail elsewhere [18, 19], only the definitions used to calculate τ_a , $\sigma_{n,m}$ and $\sigma_{n,a}$ will be recalled briefly below. Further, in what follows, the use of the MWCM applied along with the Theory of Critical Distances (TCD) [20, 21] will be reformulated for the fretting fatigue VA case, with the CA fretting fatigue problem [21] being just a simpler sub-case of the more complex VA solution [22].

The procedure for the in-field usage of the MWCM/TCD is summarised in Figs. 2 and 3. In particular, for the sake of simplicity, consider the flat specimen sketched in Fig. 2. This specimen is loaded by an axial cyclic stress, $\Delta\sigma_b$, and two fretting pads

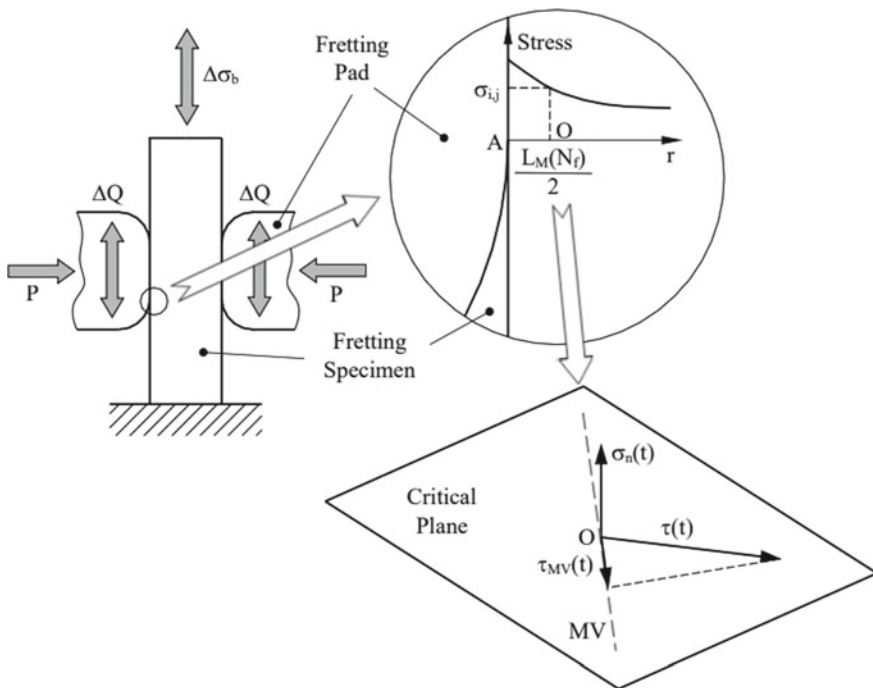


Fig. 2 The MWCM applied in conjunction with the PM and the τ -MVM to estimate, along the focus path, the stress components relative to the critical plane

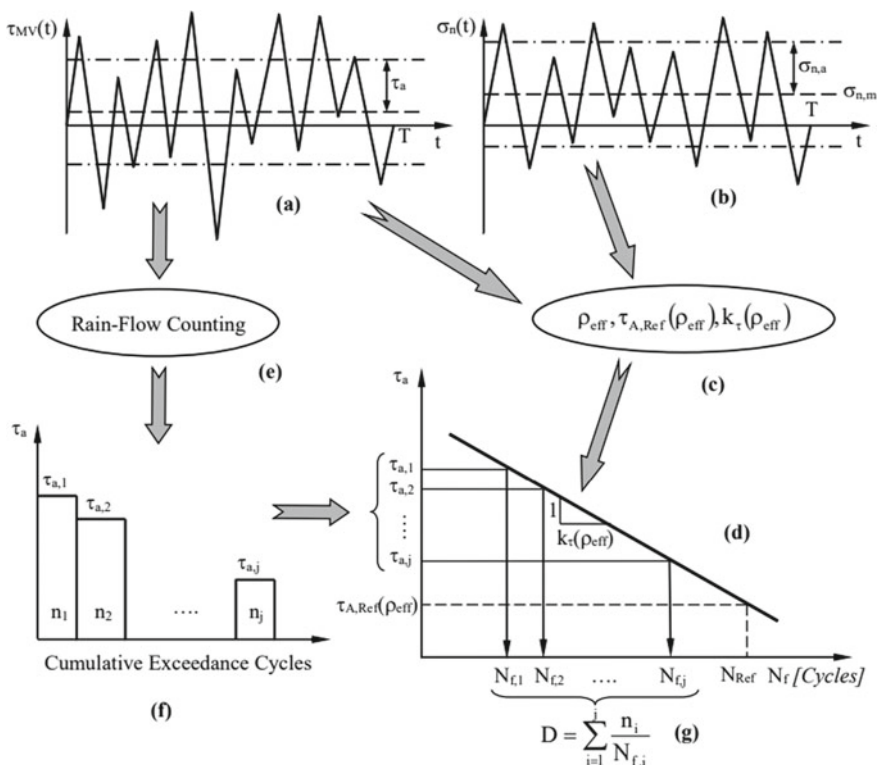


Fig. 3 Procedure to estimate damage under VA fatigue loading according to the MWCM

are pushed against the specimen itself by force, P . The two pads are subjected also to an oscillatory tangential force, ΔQ .

According to the TCD [6, 21–23], the focus path is defined as a straight line that emanates from the trailing edge of the contact zone (point A in Fig. 2) and is perpendicular to the contact surface itself. If the TCD is applied in the form of the Point Method (PM) [24], the linear-elastic stress state to be used to estimate fatigue damage is taken at a distance from the assumed crack initiation point (i.e., point A in Fig. 2) equal to $L_M(N_f)/2$ where [20, 21]:

$$L_M(N_f) = A \cdot N_f^B \tag{8}$$

In Eq. (8), A and B are material fatigue constants to be determined by running appropriate experiments. The experimental strategies suitable for estimating A and B are discussed in detail in Refs. [20, 21].

Since, according to relationship (8), the critical distance, L_M , is a function of the number of cycles to failure, N_f , the design approach proposed in the present section is

applied by adopting suitable recursive procedures so that convergence can be reached effectively and unambiguously [20, 21].

Assume now that the point O along the focus path is the point of interest and its distance from the assumed crack initiation location is equal to $L_M(N_f)/2$. From the linear-elastic stress state at point O, the orientation of the critical plane is determined by locating that material plane containing the direction experiencing the maximum variance of the resolved shear stress (direction MV in Fig. 2) [19, 22]. The shear stress amplitude relative to the critical plane, τ_a , can then be calculated from the variance of the shear stress resolved along direction MV, $\tau_{MV}(t)$, i.e. [19]:

$$\tau_m = \frac{1}{T} \int_0^T \tau_{MV}(t) \cdot dt; \text{Var}[\tau_{MV}(t)] = \frac{1}{T} \int_0^T [\tau_{MV}(t) - \tau_m]^2 \cdot dt \tau_a = \sqrt{2 \cdot \text{Var}[\tau_{MV}(t)]} \tag{9}$$

where T is the time interval over which the assessed load history is defined (Fig. 3a). In a similar way, the mean value, $\tau_{n,m}$, and the amplitude, $\tau_{n,a}$, of the stress, $\tau_n(t)$, normal to the critical plane (Figs. 2 and 3b) take on the following values [19]:

$$\sigma_{n,m} = \frac{1}{T} \int_0^T \sigma_n(t) \cdot dt \text{Var}[\sigma_n(t)] = \frac{1}{T} \int_0^T [\sigma_n(t) - \sigma_{n,m}]^2 \cdot dt; \sigma_{n,a} = \sqrt{2 \cdot \text{Var}[\sigma_n(t)]} \tag{10}$$

As soon as τ_a , $\tau_{n,m}$ and $\tau_{n,a}$ are known, the degree of multiaxiality and non-proportionality of the stress state at point O can directly be evaluated in terms of ratio ρ_{eff} (Fig. 3c), with the position of the corresponding modified Wöhler curve being estimated according to relationships (2) to (5)—(Fig. 3d). By making use of the classical rainflow method [25], the resolved shear stress cycles can now be counted (Fig. 3a and 3e) to build the corresponding load spectrum (Fig. 3f). Finally, the calculated load spectrum has to be used to estimate the damage content associated with any counted shear stress level (Fig. 3f, 3d and 3g), i.e.:

$$D = \sum_{i=1}^j \frac{n_i}{N_{f,i}} \tag{11}$$

Subsequently, total damage D is employed to determine an equivalent number of cycles to failure, $N_{f,eq}$, to be used to estimate the critical distance value via Eq. (8), where [22]:

$$N_{f,eq} = \frac{\sum_{i=1}^j n_i}{\sum_{i=1}^j \frac{n_i}{N_{f,i}}} \tag{12}$$

Accordingly, the L_M versus N_f relationship defined according to Eq. (8) can be rewritten directly as [22]:

$$L_M(N_{f,eq}) = A \cdot N_{f,eq}^B = A \cdot \left(\frac{\sum_{i=1}^j n_i}{\sum_{i=1}^j \frac{n_i}{N_{f,i}}} \right)^B \quad (13)$$

where constants A and B are those estimated for the material being assessed by following the standard procedures being discussed in Refs. [20, 21].

If the L_M value estimated via Eq. (13) assures the following obvious condition:

$$\frac{L_M(N_{f,eq})}{2} - r = 0 \quad (14)$$

where, according to Fig. 2, r is the distance, measured along the focus path, from crack initiation point A, then the number of cycles to failure, $N_{f,e}$, can be estimated directly as [22]:

$$N_{f,e} = \frac{D_{cr}(\rho_{eff}) \cdot n_{tot}}{D} = \frac{D_{cr}(\rho_{eff}) \cdot \sum_{i=1}^j n_i}{\sum_{i=1}^j \frac{n_i}{N_{f,i}}} \quad (15)$$

In Eq. (15), $D_{cr}(\rho_{eff})$ is the critical value of the damage sum. In contrast, if condition (13) is not assured, the same procedure as the one described above has to be re-applied by post-processing the stress state at a different point, O, along the focus path. This recursive procedure has to be re-used iteratively until convergence has occurred.

To conclude, it can be pointed out that in relationship (15) $D_{cr}(\rho_{eff})$ is the critical value of damage sum D and the hypothesis is formed that, in the most general case, $D_{cr}(\rho_{eff})$ can vary as the degree of multiaxiality and non-proportionality of the assessed stress state changes [22]. In contrast, if fatigue lifetime is estimated according to the classical rule due to Palmgren [25] and Miner [26], then the critical value of the damage sum can be taken invariably equal to unity.

4 Experimental Investigation

4.1 Calibration of the MWCM's Governing Equations and the L_M Versus N_f Relationship

In order to validate the fretting fatigue design method summarised in Figs. 2 and 3, a number of experimental results were generated by testing specimens made of a cast iron commonly used in the automotive industry.

To calibrate the MWCM governing equations for the cast iron under investigation, a comprehensive experimental material characterisation was carried out using a 100kN Mayes fatigue testing machine as well as a SCHENCK servo-controlled closed-loop axial-torsion fatigue machine with maximum axial load capacity of 400

kN and maximum torque capacity of 1000 Nm. The force/torque-controlled tests were run using sinusoidal loading signals, with the frequency varying in the range 5–10 Hz. Fatigue failures were defined by 20% stiffness drop.

The results generated under the fully-reversed uniaxial fatigue loading were used to estimate σ_A and k , with fatigue constants τ_A and k_0 being determined from the tests run under fully-reversed torsional fatigue loading. The mean stress sensitivity index, m , for the cast iron under investigation was estimated according to the procedure described in Refs. [21, 24], with this being done by taking full advantage of a further plain fatigue curve experimentally determined under $R = 0.1$.

The strategy summarised in Refs. [20, 24] was used to calculate material constants A and B in the L_M versus N_f relationship, Eq. (8). In more detail, constants A and B were directly estimated from the plain material fully-reversed uniaxial fatigue curve and a fatigue curve generated by testing under tension/compression ($R = -1$) specimens containing a known geometrical feature.

4.2 Fretting Fatigue Experiments

Fretting fatigue experimental tests were carried out using the hydraulic rig located at the Materials Testing Laboratory of the University of Sheffield that is shown in Fig. 4. The testing rig being used comprises of a Moog controller, two horizontal actuators and two vertical actuators. The horizontal actuators were used to apply the

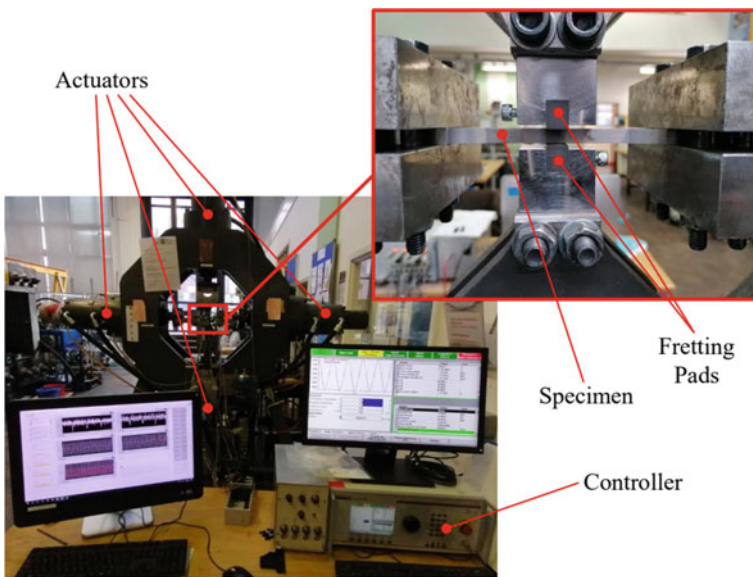
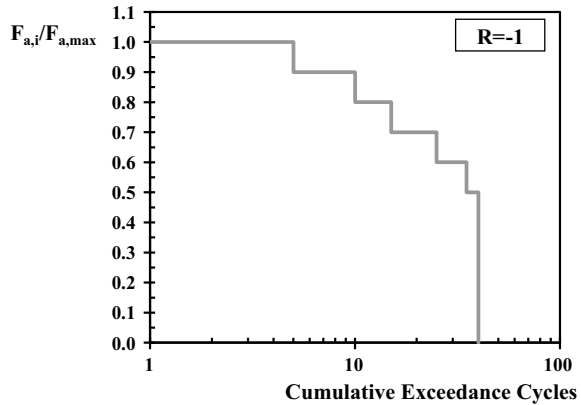


Fig. 4 Fretting fatigue test rig, specimens and pads

Fig. 5 Load spectrum adopted to run the VA fretting fatigue tests ($F_{a,max}$ = maximum value of the amplitude of the force in the load spectrum; $F_{a,i}$ = amplitude of the force associated with the i -th cycle)



CA/VA axial cyclic force, F , to the flat-dog-bone specimens made of the cast iron under investigation.

Two different sets of pads were used. The first set was machined from steel and the second from cast iron. All pads were cylindrical with thickness equal to 12 mm, contact radius, R_p , equal to 75 mm and height equal to 15 mm. The experimental trials were run to investigate the different scenarios described in what follows.

In the first testing configuration, the two cylindrical pads were pushed against the fretting specimen by a static normal load, P . A fully-reversed CA sinusoidal load was then applied (at a frequency of 10 Hz) to one end of the specimen, while the other end was kept fixed.

In the second testing configuration, the two cylindrical pads were instead pushed against the fretting specimen by a CA sinusoidal normal load, with a fully-reversed CA sinusoidal axial load being applied to one end of the specimens. Both the normal and axial fatigue forces were in phase and applied at frequency of 10 Hz.

In the final configuration, the dog-bone specimens were subjected to VA sinusoidal axial load histories, with the pads being used to apply a constant normal force. The VA load spectrum used to run the VA tests is shown in Fig. 5. The VA cycles were applied in random order at a frequency of 10 Hz and all load blocks contained 40 cycles.

5 Validation

The results generated from the fretting fatigue experiments summarised in the previous section were used to check the accuracy of the design methodology sketched in Figs. 2 and 3. In order to predict the number of cycles to failure for each test, ANSYS Workbench® was used to estimate the linear elastic stress fields at the contact interface between pads and specimens. The stress fields obtained at the assumed crack initiation location were then post-processed according to the procedure proposed in

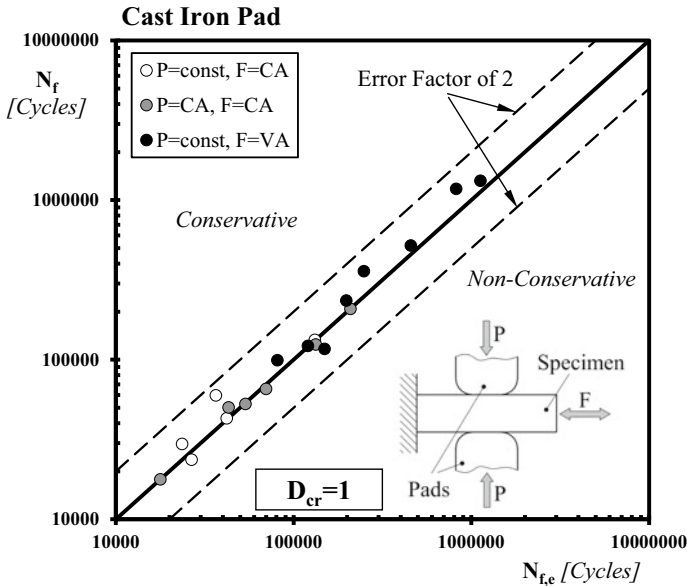


Fig. 6 Accuracy of the MWCM applied along with TCD and τ -MVM in estimating the fretting fatigue results generated by using pads made of cast iron

Sect. 3. In the present investigation, the crack initiation point was taken at the trailing edge of the contact region.

As recommended by Palmgren [25] and Miner [26], the VA design method summarised in Figs. 2 and 3 was applied by setting the critical value of the damage equal to unity.

The experimental, N_f , versus estimated, $N_{f,e}$, number of cycles to failure diagrams reported in Figs. 6 and 7 summarise the overall accuracy obtained by using the proposed fretting fatigue design methodology to post-process the experimental results being generated. The error diagrams of Figs. 6 and 7 confirm that the MWCM applied along with the PM and τ -MVM to predict fretting fatigue lifetime resulted in estimates falling within an error factor (in lifetime) of 2. This result is certainly satisfactory, especially in light of the fact that the proposed approach can be applied by directly post-processing the stress analysis results from conventional linear-elastic FE models.

6 Conclusion

- The MWCM applied in conjunction with the τ -MVM and the PM is seen to be highly accurate in predicting finite lifetime of cast iron subjected to both CA and VA fretting fatigue loading.

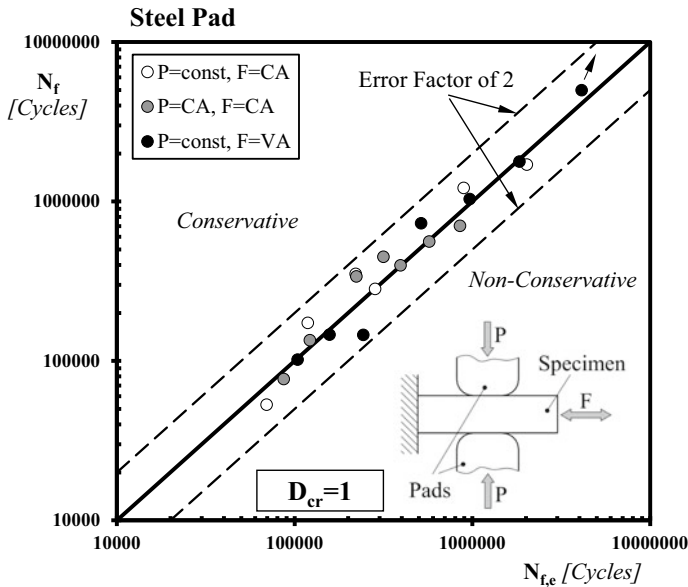


Fig. 7 Accuracy of the MWCM applied along with TCD and τ -MVM in estimating the fretting fatigue results generated by using pads made of structural steel

- The proposed approach is seen to be capable of modelling accurately the detrimental effect of different types of fretting fatigue loading configurations.
- Owing to the fact that the necessary stress analyses can be performed by solving standard linear-elastic FE models, the proposed fretting fatigue design technique is suitable for being used in situations practical interest.

Acknowledgements Support for this work from EPSRC (www.epsrc.ac.uk) and Cummins Inc. (www.cummins.com) through the award of an Industrial CASE project is gratefully acknowledged.

References

1. Jeung HK, Kwon JD, Lee CY (2015) Crack initiation and propagation under fretting fatigue of inconel 600 alloy. *Journal Mechanical Science Technology* 29(12):5241–5244
2. Dini D, Nowell D, Dyson IN (2006) The use of notch and short crack approaches to fretting fatigue threshold prediction: Theory and experimental validation. *Tribol Int* 39(8):1158–1165
3. Dini, D., Nowell, D., Dyson, I.N.: Experimental validation of a short crack approach for fretting fatigue threshold prediction. In: Pappalettere, C. (eds.) *Proceedings of the 12th International Conference on Experimental Mechanics*, Bari, Italy (2004).
4. Noraphaipaksa, L., Manonukul, A., Kanchanomai, C.: Fretting Fatigue with Cylindrical-On-Flat Contact: Crack Nucleation, Crack Path and Fatigue Life. *Materials* (Basel). 2017 10(2) 155, 1–21 (2017) doi: <https://doi.org/10.3390/ma10020155>

5. Araújo JA, Susmel L, Pires M, Castro F (2017) A multiaxial stress-based critical distance methodology to estimate fretting fatigue life. *Tribol Int* 108:2–6
6. Araújo JA, Susmel L, Taylor D, Ferro J, Mamiya E (2007) On the use of the theory of critical distances and the Modified Wöhler curve method to estimate fretting fatigue strength of cylindrical contacts. *Int J Fatigue* 29:95–107
7. Araújo, J.A, Susmel, L., Taylor, D., Ferro, J.C.T, Ferreira, J.L.A.: On the prediction of High-Cycle Fretting Strength. Theory of Critical Distances versus Hot spot Approach. *Engineering Fracture Mechanics* 75, 1763–1778 (2008).
8. Nowell, D.: An analysis of fretting fatigue (D.Phil.thesis). University of oxford, Oxford, UK (1988).
9. Hills D, Nowell D (1994) *Mechanics of Fretting Fatigue*. Kluwer Academic, Dordrecht, The Netherlands
10. Giannakopoulos AE, Lindley TC, Suresh S (2000) Similarities of stress concentrations in contact at round punches and fatigue at notches: implications to fretting fatigue crack initiation. *Fatigue Fract Eng Mater Struct* 23:561–571
11. Susmel L, Tovo R, Benasciutti D (2009) A novel engineering method based on the critical plane concept to estimate lifetime of weldments subjected to variable amplitude multiaxial fatigue loading. *Fatigue Fract Eng Mater Struct* 32:441–459
12. Susmel L, Lazzarin P (2002) A Bi-parametric modified wöhler curve for high cycle multiaxial fatigue assessment. *Fatigue Fract Eng Mater Struct* 25:63–78
13. Susmel L (2008) Multiaxial fatigue limits and material sensitivity to non-zero mean stresses normal to critical planes. *Fatigue Fract Eng Mater Struct* 31(3–4):295–309
14. Lazzarin P, Susmel L (2003) A stress-based method method to predict lifetime under multiaxial fatigue loadings. *Fatigue Fract Eng Mater Struct* 26:1171–1187
15. Susmel L, Tovo R, Lazzarin P (2005) The mean stress effect on the high-cycle fatigue strength from a multiaxial point of view. *Int J Fatigue* 27:928–943
16. Kaufman RP, Topper T (2003) The influence of static mean stresses applied normal to the maximum shear planes in multiaxial fatigue. In: Carpinteri A, de Freitas M, Spagnoli A (eds) *Biaxial and multiaxial fatigue and fracture*. Elsevier and ESIS, Oxford, UK, pp 123–143
17. Macha E (1989) Simulation investigations of the position of fatigue fracture plane in materials with biaxial loads. *Materialwiss Werkstofftech* 20(4):132–136
18. Susmel L, Tovo R (2011) Estimating fatigue damage under variable amplitude multiaxial fatigue loading. *Fatigue Fract Eng Mater Struct* 34:1053–1077
19. Susmel L (2010) A simple and efficient numerical algorithm to determine the orientation of the critical plane in multiaxial fatigue problems. *Int J Fatigue* 32:1875–1883
20. Susmel L, Taylor D (2007) A novel formulation of the Theory of Critical Distances to estimate Lifetime of Notched Components in the Medium-Cycle Fatigue Regime. *Fatigue Fract Eng Mater Struct* 30(7):567–581
21. Susmel L, Taylor D (2008) The Modified Wöhler Curve Method applied along with the Theory of Critical Distances to estimate finite life of notched components subjected to complex multiaxial loading paths. *Fatigue Fract Eng Mater Struct* 31(12):1047–1064
22. Susmel L, Taylor D (2012) A critical distance/plane method to estimate finite life of notched components under variable amplitude uniaxial/multiaxial fatigue loading. *Int J Fatigue* 38:7–24
23. Kouanga CT, Jones JD, Revill I, Wormald A, Nowell D, Dwyer-Joyce RS, Araújo JA, Susmel L (2018) On the estimation of finite lifetime under fretting fatigue loading. *Int J Fatigue* 112:138–152
24. Susmel, L.: *Multiaxial Notch Fatigue: from nominal to local stress-strain quantities*. Woodhead & CRC, Cambridge, UK (2009).
25. Matsuishi M, Endo T (1968) Fatigue of metals subjected to varying stress. Presented to the Japan Society of Mechanical Engineers. Fukuoka, Japan
26. Palmgren A (1924) *Die Lebensdauer von Kugellagern*. *Verfahrenstechnik*, Berlin, Germany 68:339–341
27. Miner, M.A. Cumulative damage in fatigue. *Journal of Applied Mechanics* 67, AI59-AI64 (1945).

Change in Surface Topography of Structural Steel Under Cyclic Plastic Deformation



Aleena Saleem, Hiroshi Tamura, and Hiroshi Katsuchi

Abstract This paper concerns the change in surface topography of structural steel subjected to cyclic plastic deformation considering variable surface conditions and steel types. Notched steel specimens are configured for conducting the experiment under large amplitude cyclic strain. Furthermore, a surface curvature method is proposed for the evaluation of plastic strain from the surface height data obtained by a laser scanner. To this aim, displacement-controlled low cycle fatigue (LCF) tests are performed on mechanically polished and blasted steel specimens. Surface textures are measured at the start and end of fatigue loading cycles and relevant roughness parameters are calculated. Additionally, numerical simulation is conducted for the validation of the strain evaluation method. Regarding the effect of surface finish, blasted specimen showed the lowest fatigue strength with the highest values of surface roughness and plastic strain than the mechanically polished specimens. Analysis results suggest that the roughness parameters can be used for the comprehensive steel surface characterization. Moreover, surface treatment significantly affects the phenomenon of fatigue crack initiation than the types of steel.

Keywords Low cycle fatigue · Cyclic plastic deformation · Plastic strain · Surface roughness

A. Saleem (✉) · H. Tamura · H. Katsuchi
Department of Civil Engineering, Yokohama National University, Yokohama 240-8501, Japan
e-mail: aleena-saleem-ym@ynu.jp

H. Tamura
e-mail: tamura-hiroshi-jg@ynu.ac.jp

H. Katsuchi
e-mail: katsuchi@ynu.ac.jp

1 Introduction

These days, surroundings are full of steel structures consisting of buildings and bridges playing an important role in our lives. Nevertheless, earthquakes can cause significant damages to the structural steel members resulting in loss of lives and properties. Although it is not possible to prevent the occurrence of earthquakes, the collapse of structures can be prevented. This can be achieved by understanding the behavior of steel undergoing earthquakes. In the fatigue process, continuous and repeated damage is confined to a specific area of the member undergoing stress and strain reversals. This phenomenon causes the accumulation of damage inside the material and finally, failure happens when a critical value of the damage is reached [1].

For metals undergoing cyclic plastic deformation, failure often occurs at less than 10^4 cycles and this phenomenon is considered as LCF [2]. This process results in repeated permanent material deformation under fatigue loading involving larger plastic strains and fewer cycles [3, 4]. Due to the recurrent yielding near the areas of higher stress concentrations such as holes, notches, weld toes, end of bridge piers, and beam-column connections, LCF arises. Alternating processes of tension and compression could result in the movement of dislocations. With time, these dislocations get accumulated and the cyclic hardening and softening phenomena occur [5]. In case of LCF, the failure process is governed by the plastic damage, and it can be illustrated by the deterioration of microstructure including void formation, growth, initiation, and propagation of microcracks. Structures experience higher strain rates and larger plastic strain at the local areas of steel members [6]. In the past, brittle fractures originating from ductile crack initiation were observed in beam-column connections and bridge piers during the Kobe earthquake of 1995 in Japan [7, 8]. Also, similar damages were visualized during the Northridge earthquake of 1994 in the United States [9].

Regarding the LCF life prediction, Miner's rule [10] is widely used for the prediction of crack initiation on the steel surface. Additionally, some other studies were conducted on LCF incorporating the variable parameters of strain rates and strain amplitudes by the modification of Miner's rule [11, 12]. However, these formulas were obtained from the experimentation incorporating some of the material constants, and further experimental work is required to cover various conditions of actual steel structures by considering the combined effects of variable surface finishes, steel properties, strain amplitudes, and strain rates. Nevertheless, considering the past literature, limited research is available on conducting LCF testing under large amplitude cyclic plastic strain. Also, it is important to investigate the effect of all the above-mentioned parameters on fatigue life for limiting the brittle fractures of steel structures.

Surface finish is an important parameter influencing the fatigue strength of steel. A component from a structure or machine will have variable surface finishes and various fatigue strengths [13]. Al-Shahrani and Marrow [14] checked the effect of surface modification on the fatigue limit of austenitic stainless steel and it was found that the residual stress on the specimen's surface is a dominant parameter affecting the

fatigue strength. In the LCF regime, cracks often start to initiate from the surface of metals. Therefore, the parameter of surface roughness is important in characterizing the surface geometry and the process of crack initiation [15]. Xiao et al. [16] approximated the power function relationship between fatigue strength and roughness by fitting the experimental data. A quantitative relationship was observed between both the parameters. Additionally, Gao et al. [17] studied the influence of microhardness, surface roughness, and residual stress of nickel aluminum bronze alloy on the fatigue life. The results highlighted that not only the compressive residual stress but also the factor of surface roughness induced by laser shock peening were the major parameters that affected the strength of the bronze alloy.

Furthermore, other investigations and analyses were done on the process of crack initiation in notched specimens. In the study of Leidermark et al. [18], fatigue life function was determined by conducting experiments on smooth and notched specimens. It was concluded that the fatigue notch factor should be well addressed to get a better comparison of numerical and experimental results. Hsu and Wang [19] examined the effects of crack initiation on specimens with variable heat treatments by employing finite element modeling. Experimental results demonstrated that the process of crack initiation was associated with the localization of plastic deformation. The above review signifies that the phenomenon of change in steel surface geometry leading to the initiation of cracks under LCF is needed to be further explored.

This paper focuses on topographic changes occurring on steel surfaces under repeated cyclic plastic deformation. Notched steel specimens with different loading conditions are designed for the application of large amplitude cyclic strain. Also, a surface curvature method is proposed for the evaluation of plastic strain from the surface height data. Specimens consisting of two types of test steels, S400 and S490 with mechanically polished and blasted finishes are used to study the variations in surface geometries under cyclic loading. To reveal the significant change in fatigue life, roughness parameters are evaluated at the start and end of loading cycles. Subsequently, the numerical simulation is done for the validation of experimental results.

2 Experiment Generating Large Cyclic Deformation

2.1 Material and Surface Finish

The materials used for the development of specimens are S400 and S490 test steels taken from Japanese Industrial Standards (JIS) [20]. For the test steels S400 and S490, the steel grades of SM400A and SM490A are used, respectively. Tensile tests are conducted on coupons for determining the mechanical properties. Table 1 enlists the mechanical and chemical properties of steels to be examined in the experimentation.

Table 1 Material properties of SM400A and SM490A steels

| Steel grade | Yield stress (MPa) | Tensile stress (MPa) | Chemical Composition (%) | | | | |
|-------------|--------------------|----------------------|--------------------------|------|-------|------|-------|
| | | | C | Mn | S | Si | P |
| SM400A | 321 | 449 | 0.16 | 0.51 | 0.05 | 0.19 | 0.23 |
| SM490A | 367 | 539 | 0.16 | 1.49 | 0.002 | 0.35 | 0.016 |

Regarding the surface finish, specimens with mechanically polished and blasted surfaces are examined in this research study. In the first case, surfaces are mechanically polished by using White Alundum with abrasive count #46 in order to get a smooth surface. In the second case, blasting is done to remove corrosion from the metal’s surface. Steel grit with abrasive count #100 is used for blasting treatment. Both the surface finishes are applied in the high strain region (at the center) of the specimen and the impact of initial residual stress is considered to be negligible.

2.2 Design Concept and Configuration of Testing Specimens

To produce the buckling phenomenon, notched steel specimens are developed for the current study. Figure 1 shows the top and side views of the designed specimen comprising of arc-shaped notches with a length of 280 mm and a width of 44 mm. Surface height measurements are done at the middle notch because of having no contact with side notches. In this study, cyclic compressive strain with a large amplitude is locally applied by using the buckling deformation of the steel specimens. This is done by grasping both ends of the flat plate specimens and then applying the repeated forced displacement. In this way, the large plastic strain will cause the formation of LCF cracks only at the center of steel specimens.

By the fatigue loading of the specimen, the phenomenon of surface geometry change leading to crack formation can be observed in detail since the largest strain will occur in the region (B) in each loading cycle. The following factors are considered for deciding the shape of the test specimen:

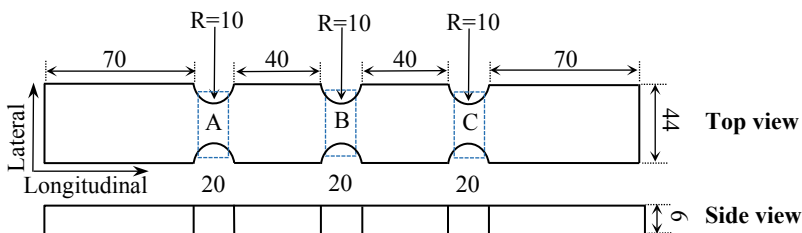


Fig. 1 Geometry of notched steel specimen (all dimensions are in mm)

1. To ensure the width of the specimen in the target area

The width of the specimen in the notched part is chosen to be 20 mm so that the specimen remains in a uniaxial state of stress and the strain distribution is uniform in the width direction. Otherwise, the lesser width of the plate may cause the unequal distribution of strain and the specimen will be in a biaxial state of stress.

2. To fix the maximum strain amplitude generation region

The surface finish is done at the center of the specimen on an area of $20 \times 44 \text{ mm}^2$, so it is necessary to generate large amplitude plastic strain in the region (B) for the initiation of cracks at the same location. For this purpose, semicircular notches of similar dimensions are made in regions (A, B, and C) as marked in Fig. 1. After buckling, plastic hinges are formed in regions (A and C), and a significantly larger plastic strain occurs at the central notch in region (B). Since the maximum plastic strain due to bending is generated at the compression side of the central notch, surface geometry change can be easily observed in the area of interest.

3. To prevent the occurrence of fatigue cracks outside the focused region

Since the large plastic strain is repetitively generated at the notches under fatigue loading, the radius of the notch is chosen not to be so small. If a fatigue crack initiates firstly in areas other than the focused region of interest, the behavior of the targeted area can be affected, or loading may be disturbed.

4. To reproduce the buckling deformation

During the installation of the specimen in the testing machine, the buckling length of the specimen is kept constant irrespective of the depth of gripping the specimen's edge, so that the reproducibility of buckling deformation can be protected. This is achieved by developing arc-shaped notches with a radius of 10 mm.

2.3 Experimental Testing Procedure

Uniaxial and displacement-controlled fatigue loading having a triangular waveform with a constant amplitude of 5 mm is applied to the specimens. The history of input displacement with a triangular pattern is demonstrated in Fig. 2. The displacement rate is taken as 0.012 mm s^{-1} , so that the average strain rate is about $9.97 \times 10^{-5} \text{ s}^{-1}$ for the whole specimen. The lower end of the specimen is fixed, and the top end is movable in the longitudinal direction. The rotational freedom along the longitudinal direction at the top is relaxed, while the other two rotational degrees of freedom are fixed. Specimens are loaded using an MTS universal testing machine (810 Material Test System) having a loading capacity of 50 kN. Specimens are continued to be loaded until the appearance of visible cracks on the steel surface. A laser scanning

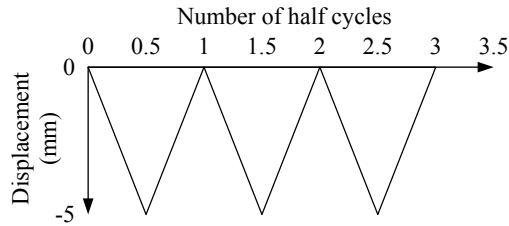


Fig. 2 History of input displacement for notched specimens

device (KEYENCE, LJ-V7080) is used to record the surface height data at the center of the specimen. The experimental testing setup is shown in Fig. 3.

For evaluating the combined effects of surface finish and steel type on LCF life and the process of crack initiation, different combinations of specimens are prepared as listed in Table 2. Specimens are named as FM-40-5 T, FM-49-5 T, and FB-49-5 T, where “FM” and “FB” represent the flat mirrored and flat blasted specimens respectively, “40” and “49” denote the SM400A and SM490A steels respectively, “5” is the displacement amplitude, and “T” represents the triangular loading waveform.

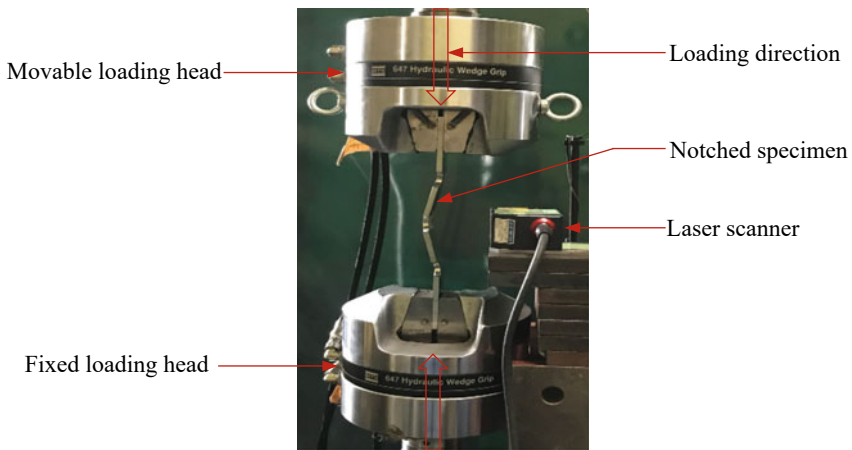


Fig. 3 Testing setup of the notched steel specimen

Table 2 Conditions of the test specimens

| Specimen name | Steel type | Surface finish | Disp. amplitude (mm) |
|---------------|------------|----------------------|----------------------|
| FM-40-5 T | SM400A | Mechanical polishing | 5 |
| FM-49-5 T | SM490A | Mechanical polishing | 5 |
| FB-49-5 T | SM490A | Blasting | 5 |

3 Results and Discussions

As already described, all three specimens were loaded until the appearance of visible cracks at the middle notch. Table 3 enlists the number of cycles required for the initiation of cracks on all the test specimens. In the case of FB-49-5 T, cracks started to appear very earlier at 12.5 cycles than the mechanically polished specimens on which the cracks nucleated at 30.5 cycles.

3.1 Surface Curvature Method for Plastic Strain Evaluation

In the current experimentation, it was difficult to measure the plastic strain at the focused region (B) of the specimen because the strain gauge cannot be attached to the observation surface and the treated surfaces may also get damaged. Therefore, a surface curvature method is proposed for the evaluation of longitudinal strain from the surface height data obtained by the laser scanner. Data measurements are done on the compression side of the middle notch after each half cycle and then plastic strains are calculated. The point of strain evaluation is highlighted in Fig. 4.

The strain evaluation method is based on Euler–Bernoulli beam theory [21] and it can be given by following expressions:

$$\text{Radius of curvature} = R = \frac{(1 + (z')^2)^{3/2}}{|z''|} \tag{1}$$

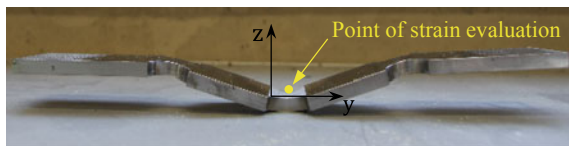
$$\text{Bending strain} = \frac{b}{R} \tag{2}$$

where “z” is the surface height and “b” is the distance between the surface of steel from the neutral axis. In this method, firstly the surface height data at the compression side of the central notch is captured and then a polynomial fit is applied to the curve (in this research, an 8th-degree polynomial is used). After that the radius of curvature at the bottom of the curve is calculated and, ultimately the plastic strain is obtained

Table 3 Number of cycles required for the initiation of cracks

| Specimen name | FM-40-5 T | FM-49-5 T | FB-49-5 T |
|------------------|-----------|-----------|-----------|
| Number of cycles | 30.5 | 30.5 | 12.5 |

Fig. 4 Location of strain measurement at the compressive side of the middle notch



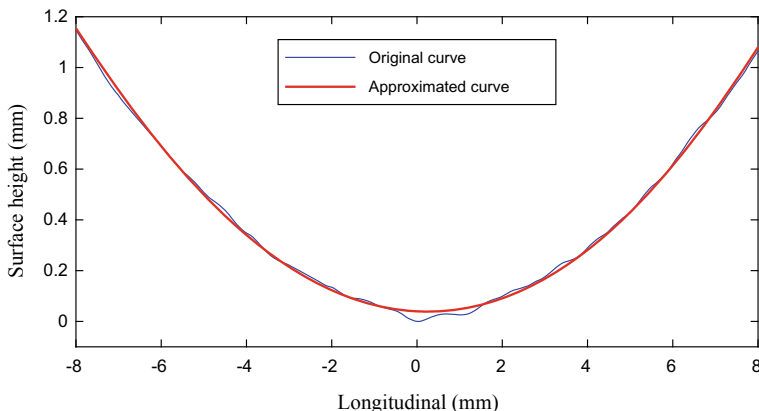


Fig. 5 An 8th order approximation of experimental surface height data (“Original curve” shows the original data and “Approximated curve” is used data for the evaluation of strain)

at the radius of curvature. However, the effects of axial strain and Poisson’s ratio are ignored. By taking FM-40-5^T as an example, the original and 8th order approximated curves after 1.5 fatigue loading cycles are shown in Fig. 5. Here the horizontal axis with a longitudinal value of zero represents the center of the specimen.

Figure 6 explicates the histories of evaluated plastic strains for all the test specimens after each half cycle until the initiation of cracks. Black circles highlight the instant of crack identification on steel surfaces. In these figures, the “0.5” cycle is referred to as “compressive loading” and the “0.0” cycle is considered as “tensile loading”. It is obvious from these results that the value of the plastic strain keeps on increasing with the progression in the number of loading cycles until the cracks appeared on the steel surface. This may be due to the residual plastic deformation accumulated after each fatigue loading cycle. Also, this increase can be attributed to the growing number of microcracks or the formation of cracks. After comparing the strain histories of FM-40-5 T and FM-49-5 T having the same surface finishes but different steel grades, it is observed that cracks appeared at 30.5 loading cycles for both the specimens. Also, the difference in strain values for both the specimens at the end of fatigue loading is very small showing that steel grade has less influence on fatigue life than that of surface finish. In the case of FB-49-5 T, cracks appeared earlier at 12.5 loading cycles with a plastic strain value of 17.97%. Surface blasting reduced the fatigue life by around 2.4 times that of mechanically polishing highlighting that surface treatment is an important parameter affecting the fatigue strength of steel structures. So much attention should be paid to the effect of surface finish for avoiding brittle failures.

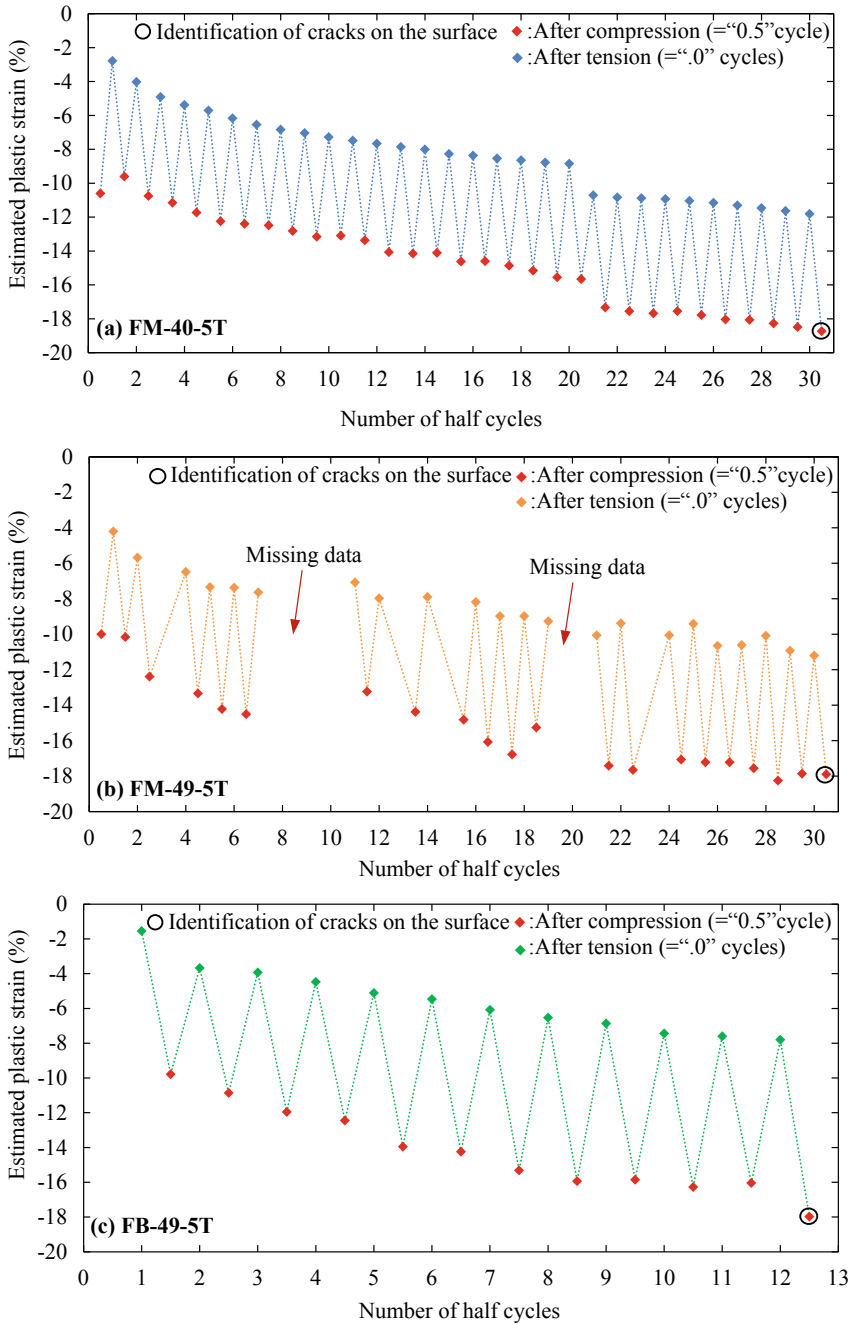


Fig. 6 Evaluated plastic strain histories for a FM-40-5 T, b FM-49-5 T and c FB-49-5 T

3.2 Surface Roughness Characterization

Fatigue cracks usually start to appear on the surface of the metals: thus, the surface treatment can greatly affect the fatigue life. Surface roughness parameters are commonly used for characterizing the topography of processed surfaces and their functionality-related properties can also be evaluated [22]. For the current experiment, surface textures are measured at the start and end of fatigue loading cycles by using a laser displacement meter from KEYENCE, Corporation, Japan. “Vision 64 Map” software by Bruker is used to conduct the surface topographic analyses over an area of $2 \times 2 \text{ mm}^2$ at the center of the specimens. In the analysis process, after obtaining the raw surface height data, it is processed to remove outlier and waviness components in order to obtain a rough surface [23]. A Gaussian filter with a cutoff wavelength of 0.8 mm is applied both in longitudinal and lateral directions for eliminating the outlier, where the slope between the measured data points is 72.5° or more by using a Gaussian function. After that 4th-degree polynomial is applied for removing the curvature and finally the rough surface is attained.

Figure 7 demonstrates the three-dimensional (3D) steel surface topographies at the start and end of fatigue loading cycles. In these images, dominant peaks are marked with solid boundary shapes and valleys are marked with dashed boundary shapes. Figure 7a, b exhibit the surface textures of FM-40-5 T at 0.5 and 30.5 loading cycles, respectively. These figures show that surface texture is perpendicular to the axial direction of the specimens. No clear features are apparent at 0.5 cycle while two dominant ridges and one pit are detected at 30.5 cycles. This deeper pit shows the formation of cracks nucleated from the valley of ridges. Figures 7c and d explicate the 3D surface textures of FM-40-5 T. At 0.5 loading cycle, comparatively smooth surface texture with minor undulations is detected than FM-40-5 T. Moreover, a uniform distribution of peaks and valleys is observed. At 30.5 cycles, two characteristics zones are spotted on the surface: one zone comprises clear ridges and the other zone consists of dales representing the formation of cracks. Surface topographic images for FB-49-5 T are shown in Figs. 7e and f. Blasted specimen represented irregular rough surface due to the wear and plastic deformation of the material. A number of significant pits and summits can also be seen without any periodical features, but no visible cracks are found on the topographic images of the blasted specimen due to its highest surface roughness. However, prominent cracks were physically detected by the naked eye on all the steel specimens at the end of fatigue loading cycles.

3.2.1 Calculation of 3D Surface Roughness Parameters

3D surface roughness parameters are effectively used for analyzing the characteristics of the processed surfaces [24]. The following seven roughness parameters are calculated here to describe the morphology of the steel surface at the start and end of fatigue loading cycles: S_a (arithmetic mean height of the surface), S_q (root mean square height of the surface), S_p (maximum height of peak), S_v (maximum depth of

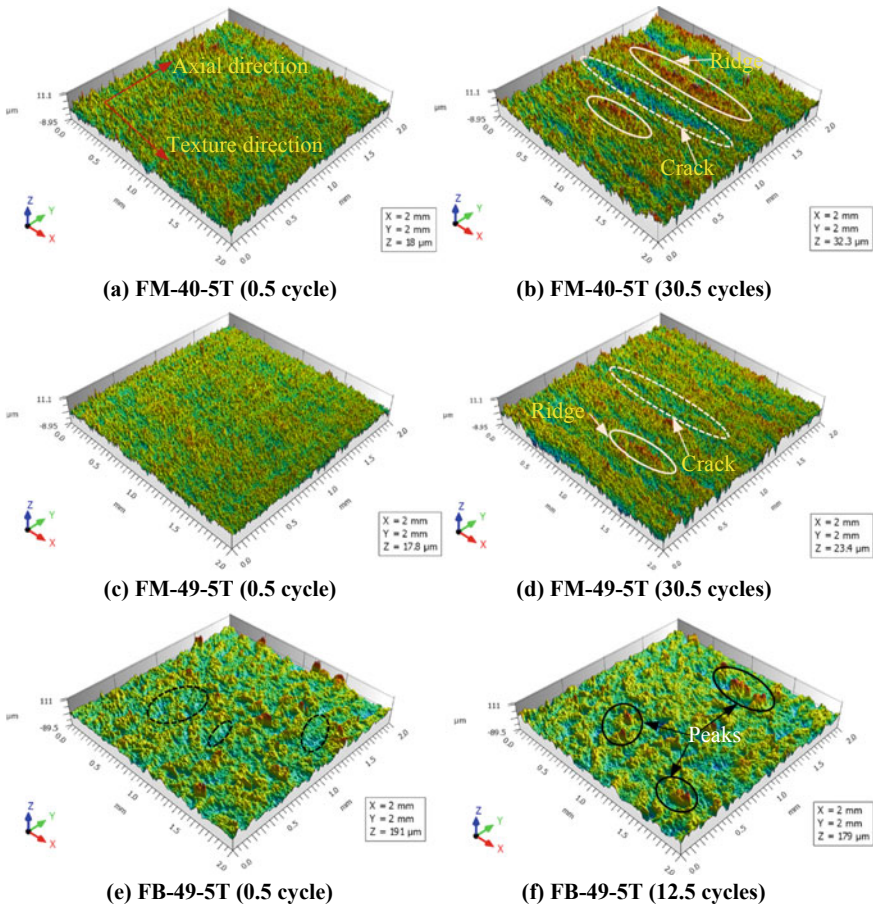


Fig. 7 Surface topographic analyses at the start and end of loading cycles for all test specimens

valley), S_z (maximum surface profile height), S_{sk} (skewness), S_{ku} (kurtosis). For the evaluation of all the above parameters, an algorithm is developed by employing the programming language “MATLAB” [25] and the results are enlisted in Table 4.

The calculation results demonstrate that surface roughness increases with the increase in fatigue loading cycles. S_a value of FB-49-5 T is 6.38 and 7.51 times higher than FM-40-5 T and FM-49-5 T respectively. S_a , S_q , S_p , S_v and S_z parameters indicated an increase at the end of fatigue loading for mechanically polished specimens. But for the blasted specimen, S_p , S_v and S_z values showed a slight decrease at the end of fatigue loading due to the formation of micro pits as a result of the wear process. S_{sk} denotes the deviation of surface about the mean plane and this parameter is effectively used for describing the shape of surface height distribution [24]. S_{sk} values are positive for all the specimens representing the more height of ridges from the mean plane. S_{sk} represents the peakedness of surface height data and S_{ku} values

Table 4 3D surface roughness parameters at the start and end of fatigue loading cycles

| Roughness parameters | FM-40-5 T | | FM-49-5 T | | FB-49-5 T | |
|-------------------------|-----------|-------------|-----------|-------------|-----------|-------------|
| | 0.5 cycle | 30.5 cycles | 0.5 cycle | 30.5 cycles | 0.5 cycle | 12.5 cycles |
| S_a (μm) | 1.44 | 2.07 | 1.22 | 1.76 | 12.35 | 13.21 |
| S_q (μm) | 1.81 | 2.64 | 1.54 | 2.21 | 16.21 | 17.48 |
| S_p (μm) | 10.20 | 17.84 | 10.18 | 10.95 | 102.93 | 93.61 |
| S_v (μm) | 7.80 | 14.44 | 7.60 | 12.47 | 87.75 | 85.31 |
| S_z (μm) | 17.99 | 32.28 | 17.77 | 23.42 | 190.68 | 178.92 |
| S_{sk} | 1.62 | 1.68 | 1.64 | 1.62 | 1.85 | 1.85 |
| S_{ku} | 3.13 | 3.44 | 3.21 | 3.16 | 4.46 | 4.33 |

for all the specimens are greater than 3 indicating the surface is distributed centrally with the occasional deep valleys or high peaks. With the comparison and use of the above calculated 3D surface roughness parameters, it is possible to differentiate the materials with variable surface treatments and the damage assessment can also be done considering the progressive change in surface roughness.

3.3 Finite Element Modeling of Notched Steel Specimens

In this study, the finite element (FE) software “Abaqus version 6.14” is employed to carry out the numerical simulation of notched steel specimens for the verification of the surface curvature method. Linear and nonlinear buckling analyses are performed by incorporating the material and geometric nonlinearities. The computation took hours on a 2.9 GHz PC. A schematic representation of the 3D finite element model of the notched specimen made by employing solid modeling technique is demonstrated in Fig. 8. Since the gripping region is around 40 mm, so for the simplification of the model, the remaining part is only used for conducting the analysis.

3.3.1 Material Properties

Numerical modeling is done on FM-40-5 T and FM-49-5 T specimens consisting of SM400A and SM490A steels. Since steel is a homogenous material, so the linear material properties are assigned to the model as elastic isotropic by defining the values of Poisson’s ratio as 0.3, the density of 7850 kg/m^3 and young’s modulus of 200 GPa. For defining the nonlinear behavior of the material, the rate-independent isotropic hardening plasticity model is adopted. The plastic data for both steel types are obtained from the tension test of coupon specimens.

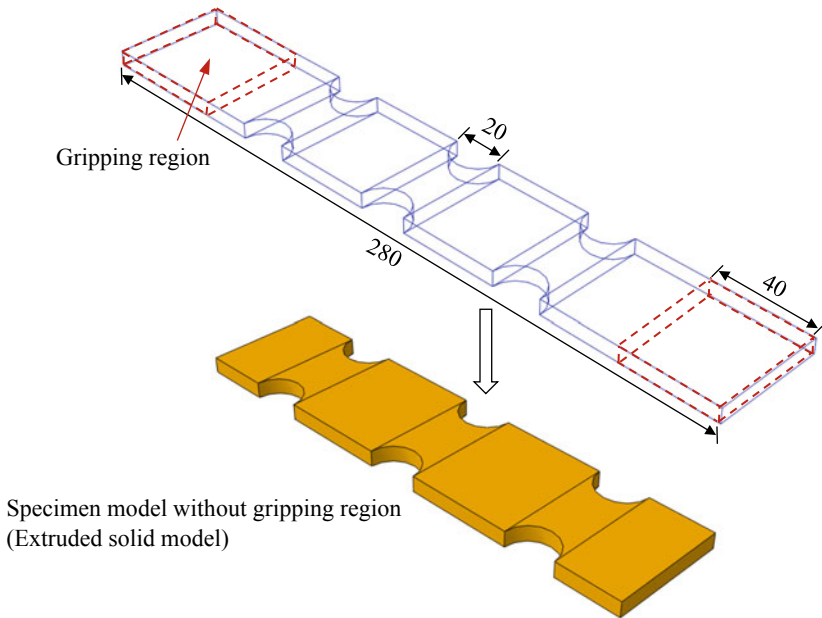


Fig. 8 FE model of notched steel specimen (all dimensions are in mm)

3.3.2 Loads and Boundary Conditions

To simulate the buckling phenomenon, displacement-controlled loading with an amplitude of 5 mm is applied at the top corner of the specimen and a tie constraint is provided for the load distribution from the corner to the whole top surface. Boundary conditions are applied to the specified regions of the model by restraining the movement in a particular degree of freedom. For the current study, it was difficult to correctly simulate the boundary conditions and the problem of instability can also arise in notched components. So, considering the expected buckling behavior, hinge supports are provided at the bottom by constraining the translational degrees of freedom (U_X , U_Y and U_Z) and the top part is free in the axial direction by the restraining U_Y and U_Z .

3.3.3 Meshing

For representing the steel section in the current analysis, solid elements are used for simulating the behavior of notched specimens under the application of axial load. The 3D solid model is discretized with a hexahedral mesh consisting of 8-node “C3D8R” elements with reduced integration to simulate the buckling behavior of global models. This element type is chosen because of its general usage in solving linear and nonlinear problems, and it also offers hourglass control. Based on the

results of convergence analysis, a mesh size of 1 mm is selected for the solid elements in order to achieve accuracy in simulation results.

3.3.4 Nonlinear Buckling Analysis

After defining the required parameters, FE models are developed, and nonlinear buckling analysis is done following two stages. In the first step, linear eigenvalue buckling analysis is performed to obtain the mode shapes and then the nodal coordinates for the desired mode shapes are written as an output for the next step. In the second step, nonlinear buckling analysis is executed by using the Static, General method by incorporating the material nonlinearity, and finally, the geometric imperfections are introduced corresponding to 1st eigenmode. Figure 9 depicts the flow chart containing the steps of conducting nonlinear buckling analysis.

The results of nonlinear buckling analysis after 0.5 loading cycle for “FM-40-5 T and FM-49-5 T” specimens are illustrated in Figs. 10 and 11. Figure 10 indicates that

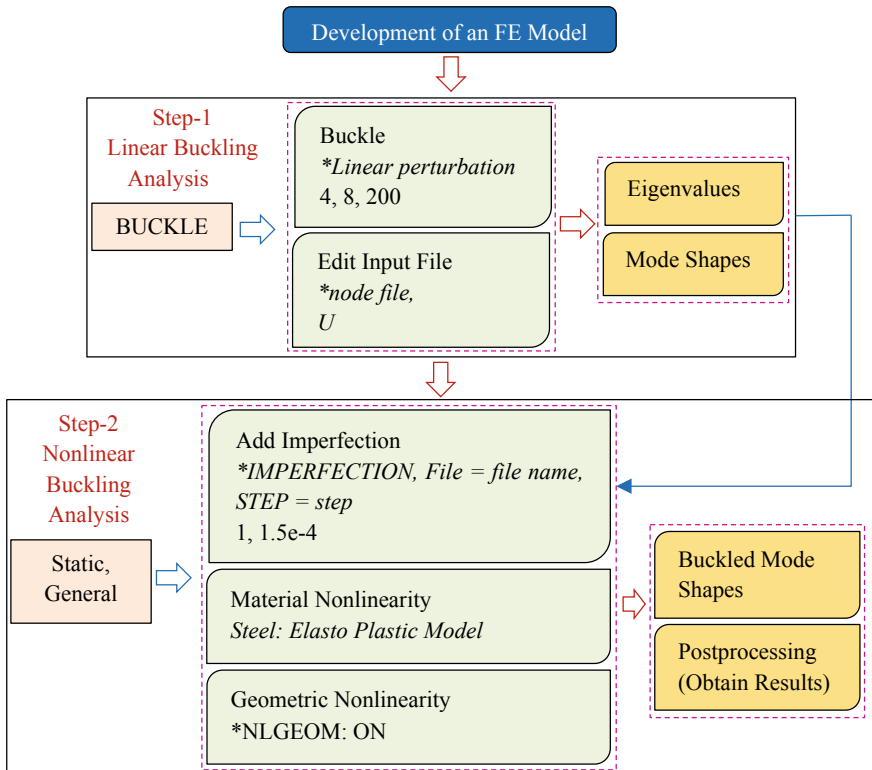


Fig. 9 Flow chart depicting the steps of conducting nonlinear buckling analysis in Abaqus

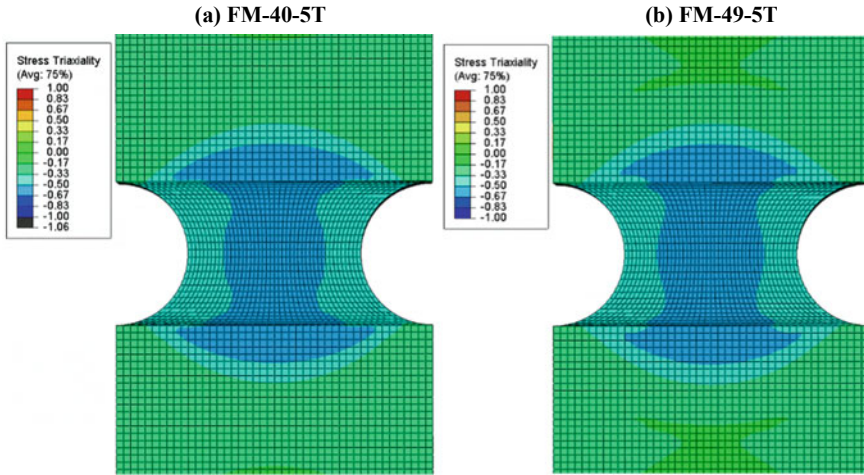


Fig. 10 Stress triaxiality at the center of **a** FM-40-5 T **b** FM-49-5 T specimens

there is a uniform distribution of stress triaxiality at the center of both the specimens on which the cracks are identified.

Figures 11a and b illustrate the equivalent plastic strain (PEEQ) distributions for “FM-40-5 T and FM-49-5 T” specimens, respectively along with the zoomed views of the central part of the specimens. Maximum plastic strain values of 16.06% and 15.85% are obtained at the central notches for FM-40-5 T and FM-49-5 T respectively. Since SM490A is high-strength steel, that is why the lesser strain is developed in FM-49-5 T. Also, there is a minor difference in plastic strain values for both the specimens concluding that the variable steel types have a minor influence on fatigue strength of steel than the effect of surface finish.

For the validation of the surface curvature method of strain evaluation, experimentally obtained strain values are compared with the numerical values. Strain values from the simulation are calculated on the compression side of the middle notch of the specimens (represented by cross sign in the above figures). The area in Fig. 11 with blue color is having PEEQ value equal to zero, indicating that the material is still having the elastic behavior. Table 5 highlights the comparison of numerical and experimental strain values calculated at the center of the middle notch after 0.5 loading cycle for FM-40-5 T and FM-49-5 T specimens. A difference in experimental and numerical strain values of about 6.30% and 11.0% is found for FM-40-5 T and FM-49-5 T, respectively. This might be due to ignoring the effects of axial strain and Poisson’s ratio because the distance of the neutral axis from the surface keeps on changing due to the bending effect. Also, a minor difference in experimental and simulation results shows the validity of the proposed surface curvature method.

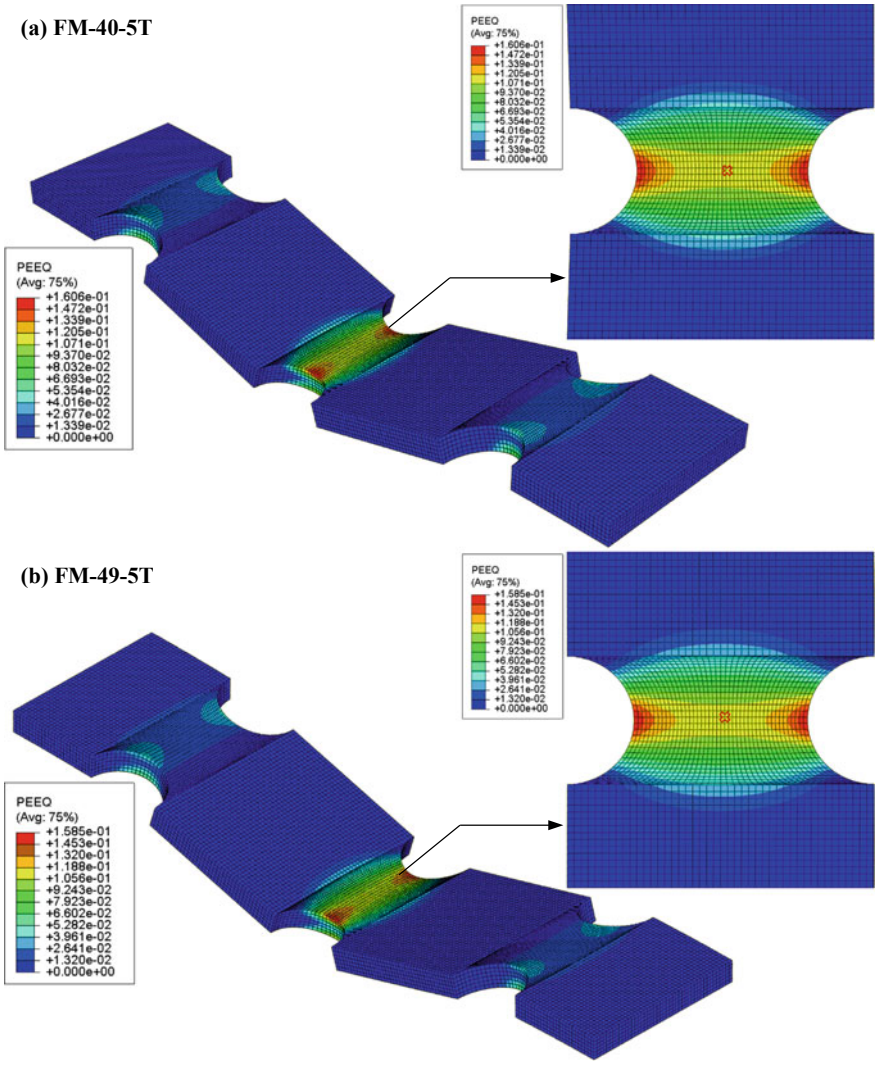


Fig. 11 Equivalent plastic strain distribution in **a** FM-40-5 T **b** FM-49-5 T specimens

Table 5 Comparison of numerical and experimental plastic strain values

| Specimens | Strain from numerical analysis (%) | Strain from experimental data using surface curvature method (%) |
|-----------|------------------------------------|--|
| FM-40-5 T | 11.322 | 10.608 |
| FM-49-5 T | 11.237 | 10.000 |

4 Summary and Conclusions

This study deals with the topographic changes occurring on the steel surfaces undergoing cyclic plastic deformation. Three different types of specimens consisting of SM400A and SM490A steels with mechanically polished and blasted finishes are investigated. The topographic analysis is done for observing the variations in surface geometries at the start and end of fatigue loading cycles. The combined effects of surface finish and steel type on LCF life are also examined. Based on the experimental and simulation results, the following conclusions are drawn:

- From the experimentation, it is concluded that variable surface treatments significantly affect the process of crack initiation than the types of steel. In the case of the blasted specimen, cracks nucleated earlier at 12.5 cycles than the mechanically polished specimens on which cracks appeared at 30.5 cycles. Moreover, blasting treatment caused a reduction in fatigue strength, about 2.4 times that of mechanical polishing showing that the vulnerability of blasted surface to fatigue damage.
- The proposed surface curvature method is capable enough to evaluate the plastic strain from the surface height data. The validity of this method is verified by conducting numerical simulations on notched steel specimens.
- Strain histories depicted an increase in plastic strains with the progression in fatigue loading cycles due to the accumulation of residual plastic deformation. This increase can also be attributed to the increase in the number of microcracks formations and the growth of cracks.
- Evaluation of surface characterization parameters for all the three specimens depicted that the blasted specimen is having the highest value of average roughness. At the start of fatigue loading cycles, surface textures represented very minor undulations, while at the end of loading cycles, all the specimens showed a significant variation in surface topographies.
- The results of nonlinear finite element analysis are in good agreement with the experimental results indicating that numerical simulation is efficient enough to produce the same buckling behavior as detected in the experiment. Also, a slight difference in numerically and experimentally obtained plastic strain values confirms the validity of the proposed surface curvature method.

References

1. Cui W (2002) A state-of-the-art review on fatigue life prediction methods for metal structures. *J Mar Sci Technol* 7:43–56. <https://doi.org/10.1007/s007730200012>
2. Xue L (2008) A unified expression for low cycle fatigue and extremely low cycle fatigue and its implication for monotonic loading. *Int J Fatigue* 30:1691–1698. <https://doi.org/10.1016/j.ijfatigue.2008.03.004>

3. AM Kanvinde GG Deierlein 2005 Continuum based micro-models for ultra low cycle fatigue crack initiation in steel structures *Struct Congr* 1–1 [https://doi.org/10.1061/40753\(171\)192](https://doi.org/10.1061/40753(171)192)
4. Miki C, Aizawa T, Anami K (1998) Brittle fracture at beam-to-column connection during earthquake. *J JSCE* 591 (1–43):273–281. https://doi.org/10.2208/jscej.1998.591_273
5. Wei W, Han L, Wang H et al (2017) Low-Cycle fatigue behavior and fracture mechanism of HS80H steel at different strain amplitudes and mean strains. *J Mater Eng Perform* 26:1717–1725. <https://doi.org/10.1007/s11665-017-2575-0>
6. Tamura H, Sasaki E, Hitoshi Y, Katsuchi H (2012) Study on the casue of brittle fracture during earthquakes in steel bridge bents focusing on dynamic load effect. *J JSCE* 68:226–241. <https://doi.org/10.2208/jscejsee.68.226>
7. H Tamura E Sasaki S Tominaga 2018 Modified-Weibull-stress-based evaluation of brittle fracture occurrence during earthquakes in steel members *Eng Fract Mech* 202 375 393 <https://doi.org/10.1016/j.engfracmech.2018.08.005>
8. Nakashima M, Inoue K, Tada M (1998) Classification of damage to steel buildings observed in the 1995 Hyogoken-Nanbu earthquake. *Eng Struct* 20:271–281. [https://doi.org/10.1016/S0141-0296\(97\)00019-9](https://doi.org/10.1016/S0141-0296(97)00019-9)
9. Miller DK (1998) Lessons learned from the Northridge earthquake. *Eng Struct* 20:249–260. [https://doi.org/10.1016/S0141-0296\(97\)00031-X](https://doi.org/10.1016/S0141-0296(97)00031-X)
10. Miner MA (1945) Cumulative damage in fatigue. *J Appl Mech* 12:A159–A164. <https://doi.org/10.1115/1.4009458>
11. Tateishi K, Hanji T, Minami K (2007) A prediction model for extremely low cycle fatigue strength of structural steel. *Int J Fatigue* 29:887–896. <https://doi.org/10.1016/j.ijfatigue.2006.08.001>
12. Sinsamutpadung N, Sasaki E, Tamura H (2016) Effects of high strain rate on low-cycle fatigue behavior of structural steel in large plastic strain region. *J JSCE* 4:118–133. https://doi.org/10.2208/journalofjsce.4.1_118
13. Bayoumi MR, Abdellatif AK (1995) Effect of surface finish on fatigue strength. *Eng Fracture Mech* 51:861–870. [https://doi.org/10.1016/0013-7944\(94\)00297-U](https://doi.org/10.1016/0013-7944(94)00297-U)
14. Al-Shahrani S, Marrow TJ (2009) Effect of surface finish on fatigue of stainless steels. In: 12th International Conference on Fracture 2009, ICF-12. pp 861–870
15. Maiya PS, Busch DE (1975) Effect of surface roughness on low-cycle fatigue behavior of type 304 stainless steel. *Metall Trans A* 6:1761–1766. <https://doi.org/10.1007/BF02642305>
16. Xiao WL, Chen HB, Yin Y (2012) Effects of surface roughness on the fatigue life of alloy steel. *Key Eng Mater* 525–526:417–420. <https://doi.org/10.4028/www.scientific.net/KEM.525-526.417>
17. Y Gao W Yang Z Huang Z Lu 2021 Effects of residual stress and surface roughness on the fatigue life of nickel aluminium bronze alloy under laser shock peening *Eng Fract Mech* 244 <https://doi.org/10.1016/j.engfracmech.2021.107524>
18. Leidermark D, Moverare J, Simonsson K et al (2010) Fatigue crack initiation in a notched single-crystal superalloy component. *Procedia Eng* 2:1067–1075. <https://doi.org/10.1016/j.proeng.2010.03.115>
19. Hsu TY, Wang Z (2010) Fatigue crack initiation at notch root under compressive cyclic loading. *Procedia Eng* 2:91–100. <https://doi.org/10.1016/j.proeng.2010.03.010>
20. JIS G 3106 (2004) Rolled steels for welded structure. Japanese Standards Association
21. Zhao B, Liu T, Chen J et al (2019) A new Bernoulli-Euler beam model based on modified gradient elasticity. *Arch Appl Mech* 89:277–289. <https://doi.org/10.1007/s00419-018-1464-9>
22. Jouini N, Gautier A, Revel P et al (2009) Multi-scale analysis of high precision surfaces by Stylus Profiler, Scanning White-Light Interferometry and Atomic Force Microscopy. *Int J Surf Sci Eng* 3:310. <https://doi.org/10.1504/IJSURFSE.2009.027418>
23. Le Roux S, Deschaux-Beaume F, Cutard T, Lours P (2015) Quantitative assessment of the interfacial roughness in multi-layered materials using image analysis: Application to oxidation in ceramic-based materials. *J Eur Ceram Soc* 35:1063–1079. <https://doi.org/10.1016/j.jeurceramsoc.2014.09.027>

24. Zeng Q, Qin Y, Chang W, Luo X (2018) Correlating and evaluating the functionality-related properties with surface texture parameters and specific characteristics of machined components. *Int J Mech Sci* 149:62–72. <https://doi.org/10.1016/j.ijmecsci.2018.09.044>
25. MATLAB. Version 9.3.0.713579 (R2017) Natick: The MathWorks Inc. 2017

Comparative Study of Crack Initiation Criteria for Flat–Flat Contacts Subjected to Fretting Fatigue of Drive-Train Components



Denny Knabner, Sebastian Vetter, Lukáš Suchý, and Alexander Hasse

Abstract From the literature, we know that the location of failure (in relation to the specimen geometry) in fretting fatigue problems changes significantly depending on the material pairing selected and the prevailing contact parameters. Previous calculation methods were unable to determine the location of failure with sufficient accuracy. A major challenge in the strength assessment of fretting fatigue is to find a criterion that correctly predicts the location of failure. Therefore, experimental tests in the high-cycle-fatigue domain were performed on two different set-ups: a realistic component-connection and its abstraction by fretting pads. The set-ups were then numerically modelled to evaluate the local stresses. For the realistic component-connection tests, the piston rod with shrink-fitted bushing was chosen based on its numerous mentions in the subject-specific literature. The dynamic axial load on the piston rod causes a relative movement between the piston rod and the bushing, which results in fretting fatigue failure. In addition to the piston rod tests, the corresponding contact conditions were then tested using a flat–flat contact in a fretting pad experiment by using a test bench with slip control. The constant slip and pressure conditions determined in the piston-rod tests was applied to the contact between the tensile specimen and the fretting pads. Both tests were performed with the material pairings 34CrNiMo6 + QT/34CrNiMo6 + QT and 34CrNiMo6 + QT/CuSn8 (designation: base-body material/counterbody material) and revealed significantly different locations of failure. Numerical analyses of the experimental tests were then performed. The local coefficients of friction based on the frictional work were considered in the model contacts. Various crack-initiation criteria were then reviewed using the results presented. For the set-ups presented, the McDiarmid criterion gives the smallest error.

Keywords Fretting fatigue · Crack initiation · Local CoF · High cycle fatigue · Flat–flat-contact

D. Knabner (✉) · S. Vetter · L. Suchý · A. Hasse
Institut of Design Engineering and Drive Technology, Technische Universität Chemnitz, 09107
Chemnitz, Germany
e-mail: denny.knabner@mb.tu-chemnitz.de

© The Author(s), under exclusive license to Springer Nature Singapore Pte Ltd. 2022
M. Abdel Wahab (ed.), *Proceedings of the 9th International Conference on Fracture, Fatigue and Wear*, Lecture Notes in Mechanical Engineering,
https://doi.org/10.1007/978-981-16-8810-2_15

195

1 Introduction

Fretting fatigue is a phenomenon that critically reduces the service lives of assemblies and can induce catastrophic damage [1, 2]. It can occur whenever two or more components are in contact and, apart from the prevailing contact pressure, there is a very small relative motion. In combination with a dynamic load on at least one of the components, this tribological stress leads to fatigue cracks, and crack propagation can result in failure. Fretting fatigue occurs mainly in frictionally connected assemblies, such as bolted joints [3, 4] or shrink-fitted shafts [5, 6], but also in form-fitted assemblies, such as dovetail joints in turbomachines [7, 8]. Vibrations or cyclical elastic deformations due to dynamic loads on the components result in a small relative motion as a side effect. Because of the severe negative impact of fretting fatigue on service life, it is important to be able to predict its occurrence and the vulnerability of components to fretting fatigue. In an arbitrarily shaped component contact, the damage parameters (slip amplitude, contact pressure and cyclical stress) vary from location to location, as does the vulnerability to fretting fatigue. This requires a local approach that correctly determines the location of failure.

This paper describes the execution of fretting fatigue tests in the high-cycle-fatigue domain with two different set-ups and two different material pairings, as well as the subsequent corresponding numerical investigations and evaluations by local failure criteria.

In the first set-up, a piston rod with shrink-fitted bushing was used to represent a realistic component connection with an arbitrarily shaped contact surface. Material combinations 34CrNiMo6 + QT/34CrNiMo6 + QT and 34CrNiMo6 + QT/CuSn8 (piston rod material/bushing material) were used. Staircase tests were performed to quantify the fatigue limit and the location of failure for each material combination. Different failure locations were observed in the two cases. The main influences were assumed to be the different Young's moduli of the bushing materials and the dynamic CoF depending on the material pairing and the frictional work. To determine the correct local damage parameters, numerical investigations were performed on a 3D-model. The local CoF was determined by an iterative simulation process.

Subsequently, tests were performed using a flat-pad set-up. The same material combinations as in the piston-rod tests were used (tensile-specimen material = piston-rod material; pad material = bushing material). By using a test bench with slip control, the same tribological parameters as determined at the failure location of the piston rod tests could be applied here. The fatigue limit was quantified and the location of failure was determined by staircase tests. Subsequently, numerical 2D-modeling of the pad tests was used to determine the local damage parameters.

Finally, a study of crack-initiation criteria was carried out on the basis of the numerical investigations. For this purpose, various criteria mentioned in connection with fretting fatigue were examined, as were criteria related to other problems. The study included an empirical criterion (mFFDP [11]) as well as classical Rankine, Tresca and Mises criteria [12, 13], the critical plane criteria of McDiarmid [14], SWT [15] and FS [16], and the SIH [17] and PIN [18] criteria with integral approaches.

2 Material Properties

The materials used in this work were 34CrNiMo6 + QT as the base-body material (for the piston rod and tensile specimen) and 34CrNiMo6 + QT or CuSn8 as counterbody materials (for the bushing and flat pad). To ensure consistent material properties for all specimens manufactured from the base-body material as well as the two counterbody materials, the bar stock of each material was ordered from a single melt. The bar stock of the base-body material was ordered in several cuboid sections of dimensions $330 \times 160 \times 40$ mm. From these sections, the piston rod (see Fig. 1a, one per section), the tensile specimen for the flat pad tests (see Fig. 4a) and the tensile specimen for the static and dynamic material tests were manufactured. To avoid any anisotropic influences, the specimens were manufactured from the bar stock in such manner that the tensile direction always had the same orientation. For the counterbody material, cylindrical bar stock sections of diameter 110 mm and height 50 mm were ordered for each of the two selected materials. The bushings (see Fig. 1b, one per section) and the flat pads (see Fig. 4b) were manufactured from these sections. To avoid any anisotropic influences, the contact surface of both specimen types was oriented

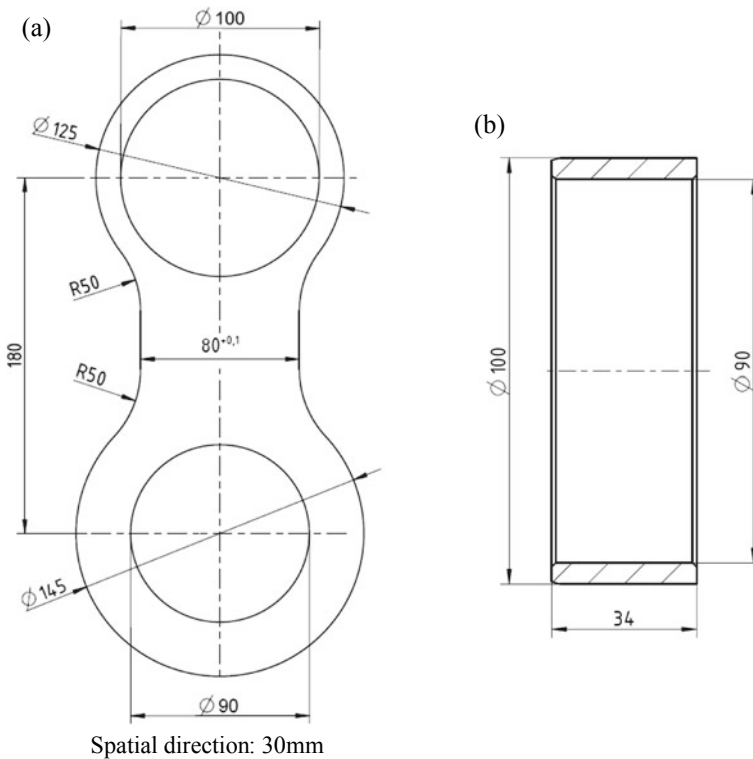


Fig. 1 Geometry of the piston rod (a) and bushing (b)

Table 1 Material properties of the used materials and bar stocks

| Material | Bar stock | S_y (MPa) | S_u (MPa) | f_{-1} (MPa) | f_0 (MPa) | E (GPa) |
|----------------------------|-----------|-------------|-------------|----------------|-------------|-----------|
| 34CrNiMo6 + QT (1.6582) | Cuboid | 1092 | 1172 | 521 | 387 | 207 |
| 34CrNiMo6 + QT (1.6582) | Cylinder | 962 | 1066 | – | – | 207 |
| CuSn8 (2.1030) | Cylinder | 284 | 382 | – | – | 98 |

parallel to the bar-stock axis. Furthermore, tensile specimens for static material tests were manufactured from these sections. Each batch of material was characterized by the tensile strength, S_u , the yield strength, S_y , and the Young's modulus, E . The batch of the base-body material was additionally characterized by the fatigue limit in fully reversed axial loading, f_{-1} , and the fatigue limit in repeated axial loading, f_0 , based on its fatigue-stressed failures in the experiments. The material properties for the various materials and bar stocks are shown in Table 1.

3 Experiments

The experiments described in the following sections are the basis of the numerical investigations addressed later in this paper. The experiments determine the fretting fatigue limits of the components and materials for the high-cycle-fatigue domain and thus the loads that will be introduced in the simulation models. The failure locations, against which the failure criteria will be validated, will also be determined.

3.1 Piston-Rod Tests

As shown by the authors in [19, 20], the piston-rod–bushing connection in engines is highly vulnerable to fretting-fatigue-induced failure. The tension on the piston rod leads to an elastic deformation of the parts, and so a small relative motion (slip) occurs at the contact. Because of the irregular cross section of the piston rod, the stress varies from location to location, and with it the strain and the induced slip.

For the piston-rod tests performed in this paper, the specimen geometry shown in Fig. 1 was used.

The piston rods and bushings were shrink-fitted with the $\text{Ø}100$ mm bore of the piston rod (see also Fig. 2). The shrink fit was calculated in accordance with German standard DIN 7190 [21] for a nominal contact pressure of 10 MPa. Therefore, the diameter of each rod bore was measured on three cross sections in the axial direction with a mechanical coordinate-measuring machine. Subsequently, the outer diameter of the raw bushings were ground to the exact fit. For the 34CrNiMo6

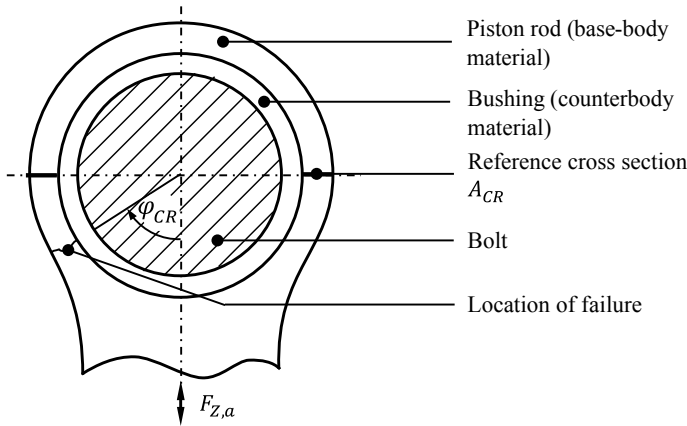


Fig. 2 Piston-rod-bushing assembly, definition of the reference cross section, A_{CR} , and the location of failure, φ_{CR}

+ QT/34CrNiMo6 + QT material pairing, a radial interference $U = 37.5 \mu\text{m}$ was used, and for the 34CrNiMo6 + QT/CuSn8 material pairing, a radial interference $U = 61.5 \mu\text{m}$ was used. The maximum roughness of the contact surfaces was set to $Rz = 4 \mu\text{m}$. The loads were introduced via two bolts in the bores of the piston-rod-bushing assembly. The bolt-bore-fit was set to a nominal radial clearance of approximately $35 \mu\text{m}$.

The fatigue limit, σ_{CR} , was calculated for a maximum number of load cycles of 10,000,000 according to the staircase method of Hück [22], which corresponds to a 50% survival probability, and is calculated by

$$\sigma_{CR} = \sigma_{a0} \cdot d^{A/F} \tag{1}$$

where σ_{a0} corresponds to the lowest level of the load staircase, and d is the logarithmic step interval. The values of F and A are summarized for all events at staircase levels evaluated according to [22] and [23].

For this purpose, each event on the repeated stress level is considered independently of the result (failure or run-out). Therefore, one fictive result on the level of the potential last step can be taken into account.

Table 2 shows the experimental results for each specimen and each material pairing.

With the reference cross section A_{CR} as defined in Fig. 2, the axial force induced by the test bench can be translated to the nominal stress, $\sigma_{CR,a}$, as follows:

$$\sigma_{CR,a} = \frac{F_{z,a}}{2 \cdot A_{CR}} \tag{2}$$

Table 2 Results of fretting fatigue experiments on piston rods made of 34CrNiMo6 + QT

| Test | Bushing material | Tensile stress $\sigma_{CR,a}$ (MPa) | Stress Ratio R | Radial interference U (μm) | Number of cycles N |
|------|------------------|--------------------------------------|------------------|---|----------------------|
| 1 | 34CrNiMo6 + QT | 62 | 0.03 | 37.5 | 2,481,662 |
| 2 | 34CrNiMo6 + QT | 54 | 0.03 | 37.5 | 10,000,000 |
| 3 | 34CrNiMo6 + QT | 62 | 0.03 | 37.5 | 5,643,991 |
| 4 | 34CrNiMo6 + QT | 54 | 0.03 | 37.5 | 1,327,128 |
| 5 | 34CrNiMo6 + QT | 47 | 0.03 | 37.5 | 10,000,000 |
| 6 | 34CrNiMo6 + QT | 54 | 0.03 | 37.5 | 10,000,000 |
| 7 | 34CrNiMo6 + QT | 62 | 0.03 | 37.5 | 1,973,500 |
| 9 | CuSn8 | 82 | 0.03 | 61.5 | 2,658,190 |
| 10 | CuSn8 | 71 | 0.03 | 61.5 | 10,000,000 |
| 11 | CuSn8 | 82 | 0.03 | 61.5 | 982,491 |
| 12 | CuSn8 | 71 | 0.03 | 61.5 | 6,783,360 |
| 13 | CuSn8 | 62 | 0.03 | 61.5 | 10,000,000 |

Table 3 Fatigue limit, σ_{CR} , averaged location of failure, φ_{CR} , and range of measured slip amplitudes, s_a , for each material pairing (piston-rod material is 34CrNiMo6 + QT)

| Bushing material | Slip amplitude s_a (μm) | Location of failure φ_{CR} ($^\circ$) | Fatigue limit σ_{CR} (MPa) |
|------------------|--|---|-----------------------------------|
| 34CrNiMo6 + QT | 7–8 | 65 | 56 |
| CuSn8 | 8–9 | 55 | 72 |

The failure location was detected for each failed specimen and defined with respect to the specimen geometry as shown in Fig. 2.

After performing a few tests and identifying a tendency for the location of failure, the slip in the piston-rod-bushing contact was measured at that location by means of a capacitive displacement encoder. Several measurements showed only a marginal difference between the tests for one material pairing. Table 3 summarizes the results of the piston-rod tests.

Figure 3 shows an example of a piston rod from the tests. The fretting scars are clearly identifiable in (a). The stained appearance results from surface undulations arising from the manufacturing process. In (b), the tribologically induced cracks starting from fretting scars are clearly visible.

3.2 Flat-Pad Tests

In contrast to the real-component tests with arbitrary contact surfaces and locally changing damage parameters, flat-pad testing permits the precise adjustment of mechanical and tribological damage parameters due to the purely tensile load and the

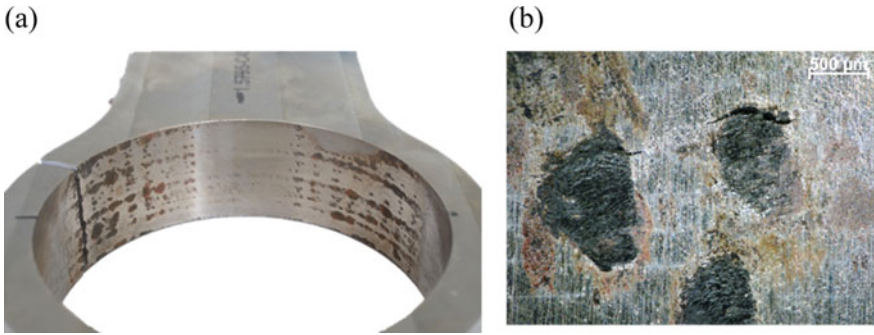


Fig. 3 Fretting scars on a piston rod (a) and cracks induced by fretting fatigue (b)

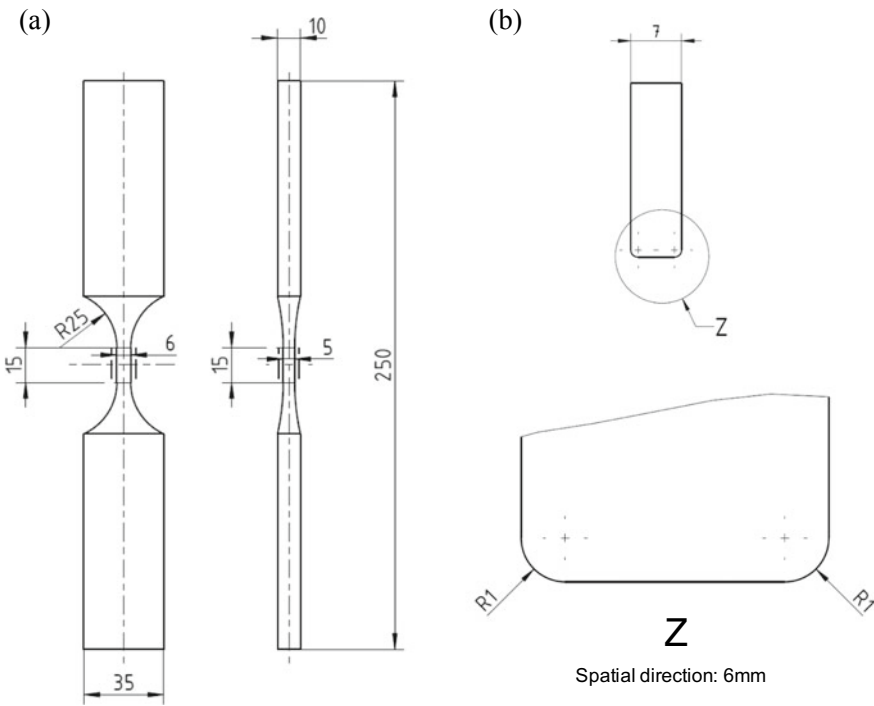


Fig. 4 Geometries of the tensile specimen and flat pads

small contact surface. The specimen geometry used in the tests presented is shown in Fig. 4.

The tests were performed on a high-frequency pulsator, which applied a cyclical tensile load to the specimen. This set-up was suitable for simple fatigue-strength tests. The fretting-fatigue tests required an additional test-bench structure. The test bench and the additional structure are shown in Fig. 5.

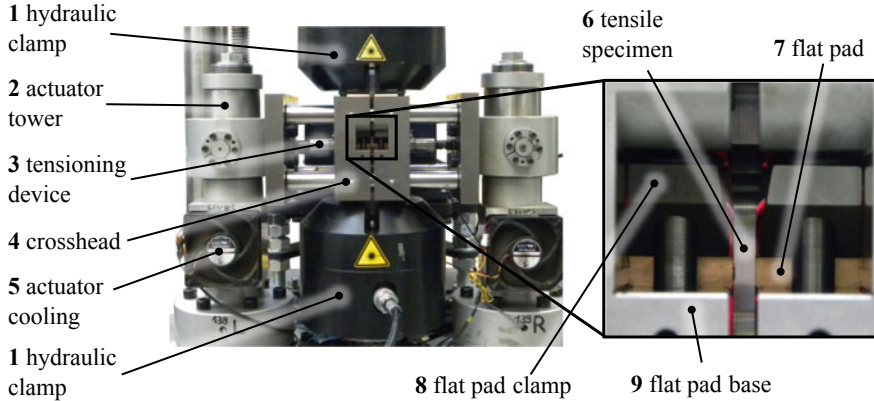


Fig. 5 Double actuated flat-pad test bench with slip control

The additional test bench structure, used to create the contact pressure and slip, consists of two actuator towers and a crosshead. During the test period, the two flat pads are mounted on the crosshead and serve as counterbodies for the flat specimen. The normal force is applied by a mechanical tensioning device and is measured throughout the test. The slip between the flat specimen and the two fretting pads is measured by a laser extensometer, making it possible to detect slip near the contact. Two piezoelectric actuators are used to regulate the slip between the flat specimen and the fretting pad. The piezoelectric actuators are located in the actuator towers to the left and right of the testing axis and can influence the movement of the crosshead. The piezoelectric actuators are actuated at the test frequency of the resonance test bench. The slip at the contact can be kept constant throughout the test period by means of an additional phase shift of the actuator-control signal as well as the adaptation of the actuator voltage.

Due to the stained fretting-scar appearance in the piston rod tests (Fig. 3) and the resulting locally increased unknown contact pressure, the flat-pad tests were performed at a critical contact pressure corresponding to the worst-case concept from [29]. To determine the fatigue limit for a survival probability of 50%, the staircase method according to Hück [22] was applied as described in the previous section. The experimental results of the flat-pad tests for each specimen and each material pairing are shown in Table 4.

Figure 6 shows an exemplary fretting scar on a tensile specimen and the determination of the location of failure, defined as the distance x_{FP} of the fracture edge from the top edge of the fretting scar. Unlike cases reported in many literature references, the crack here does not occur at the contact edge, but mainly at the contact surface. This can be explained by the actuated fretting pads. In contrast to the stick and slip zones of fretting in force-actuated fretting-fatigue tests—in [9, 10], for example—the dual-actuated test system causes a slippage over the entire contact surface.

Table 5 summarizes the results of the flat-pad tests.

Table 4 Results of fretting fatigue experiments with flat pads (material of the tensile specimen is 34CrNiMo6 + QT)

| Test | Mating material | Contact pressure p (MPa) | Slip amplitude s_d (μm) | Tensile stress σ_a (MPa) | Stress ratio R | Number of cycles N |
|------|-----------------|----------------------------|--|---------------------------------|------------------|----------------------|
| 1 | 34CrNiMo6 + QT | 40 | 10 | 93 | 0.03 | 1,060,858 |
| 2 | 34CrNiMo6 + QT | 40 | 10 | 86.7 | 0.03 | 10,000,000 |
| 3 | 34CrNiMo6 + QT | 40 | 10 | 93 | 0.03 | 10,000,000 |
| 4 | 34CrNiMo6 + QT | 40 | 10 | 99.3 | 0.03 | 985,452 |
| 5 | 34CrNiMo6 + QT | 40 | 10 | 93 | 0.03 | 10,000,000 |
| 6 | 34CrNiMo6 + QT | 40 | 10 | 86.7 | 0.03 | 10,000,000 |
| 7 | CuSn8 | 40 | 10 | 46 | 0.03 | 2,567,113 |
| 8 | CuSn8 | 40 | 10 | 35 | 0.03 | 10,000,000 |
| 9 | CuSn8 | 40 | 10 | 46 | 0.03 | 2,871,530 |
| 10 | CuSn8 | 40 | 10 | 35 | 0.03 | 10,000,000 |
| 11 | CuSn8 | 40 | 10 | 46 | 0.03 | 4,297,765 |
| 12 | CuSn8 | 40 | 10 | 35 | 0.03 | 10,000,000 |

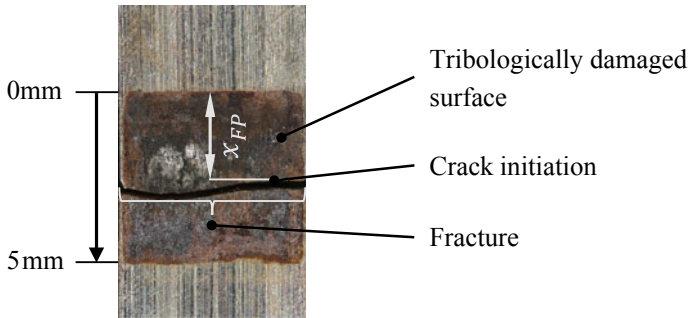


Fig. 6 Fretting scars on a tensile specimen and definition of the location of failure

Table 5 Location of failure, x_{FP} , and fatigue limit, σ_{FP} , of the flat-pad tests (tensile specimen material is 34CrNiMo6 + QT)

| Pad material | Location of failure x_{FP} (mm) | Fatigue limit σ_{FP} (MPa) |
|----------------|--|-----------------------------------|
| 34CrNiMo6 + QT | $2.5 \text{ mm} < x_{FP} < 3.5 \text{ mm}$ | 92 |
| CuSn8 | $2.5 \text{ mm} < x_{FP} < 4.7 \text{ mm}$ | 41 |

4 Numerical Investigations

The determination of the direction- and time-dependent local damage parameters for stress and strain, as well as the tribological parameters, was performed by finite element analysis (FEA) as described below. Commercially available FEA software ABAQUS (version 6.14) was used.

4.1 Piston-Rod Simulations

As shown in Fig. 7, the components of the piston-rod assembly were modelled in full scale by simplifying the geometry in less significant areas (e.g. second bolt bore) and using a symmetry condition to reduce the computational complexity. The analyses were performed in the linear elastic region with the Young's moduli from Table 1. Poisson's ratio was set to 0.34 for CuSn8 and to 0.3 for 34CrNiMo6 + QT. The properties of the steel bolt were set to 210 GPa as Young's modulus and 0.3 as Poisson's ratio. The whole model used C3D8I elements (8-node linear bricks with incompatible modes). The element edge length in the contact regions of the model were set to 0.5 mm in the circumferential direction and 1 mm in the axial-bore direction. At the piston-rod-bushing contact (K1 in Fig. 7), the penalty friction

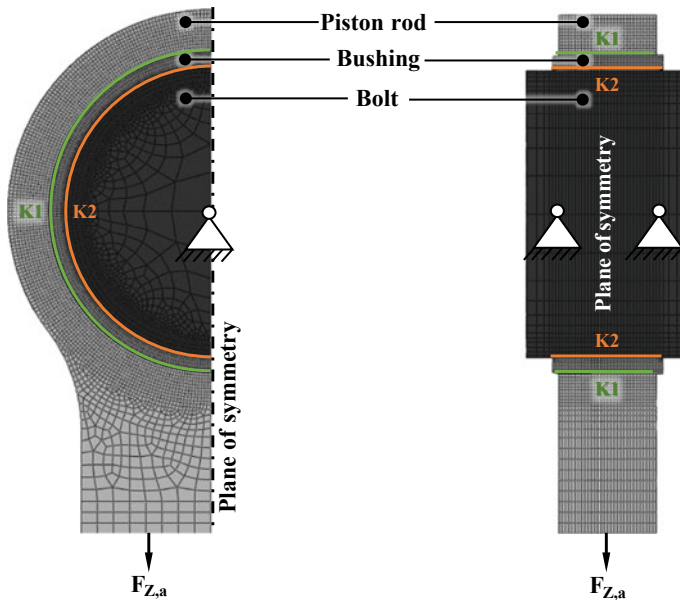


Fig. 7 FE model of the piston-rod assembly with the contacts K1 (piston-rod-bushing contact) and K2 (bushing-bolt contact)

formulation was chosen for the tangential behavior and the maximum elastic slip was set to an absolute value of $0.1 \mu\text{m}$. The bushing-bolt contact (K2 in Fig. 7) was defined to be frictionless. The normal contact behavior was set to “hard” for both contacts and linear contact-stiffness behavior was chosen. The stiffness value was set to 10^7 . Depending on the material pairing (34CrNiMo6 + QT/34CrNiMo6 + QT or 34CrNiMo6 + QT/CuSn8) different averaged interference values ($37.5 \mu\text{m}$ or $61.5 \mu\text{m}$) were used for contact K1 (see also Table 2). The clearance of contact K2 was set to an average value of $35 \mu\text{m}$.

To fix the bolt, the nodes of the plain surfaces were constrained by a kinematic coupling with a fixed reference node in the middle of the bolt. The dynamic load was also applied to a reference node kinematically coupled with the plain end-face nodes of the lower end of the piston-rod model. Each of the two material pairings was computed with the load determined from the staircase method (Sect. 3.1) for a survival probability of 50%. The models were computed over two cycles, each cycle in one step. The last step (cycle) was used for the evaluation.

According to [24], the value of the CoF evolves due to the mechanisms in fretting contacts. To account for this effect, the CoF was determined iteratively for each node based on the locally present frictional work (see Fig. 8, right hand side). The CoF curves from previously performed tests (see Fig. 8, left) were used as a basis. The location of the high local CoF plateau (Fig. 8, red area) corresponds well with the area of the fretting scars on the experimental specimen (Fig. 3).

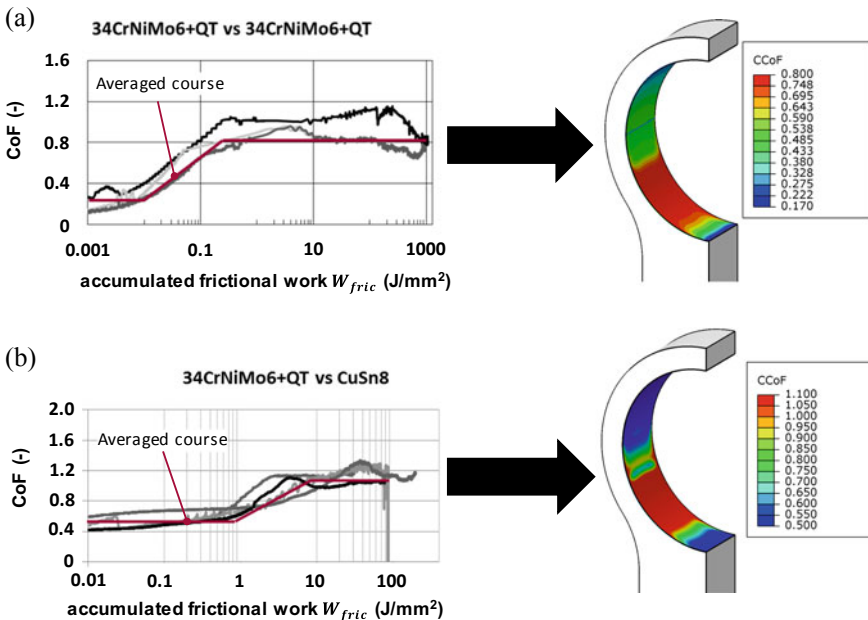


Fig. 8 Piston-rod-bushing contact with iteratively determined CoF conditions for 34CrNiMo6 + QT/34CrNiMo6 + QT (a) and 34CrNiMo6 + QT/CuSn8 (b)

4.2 Flat-Pad Simulations

Because of the regular cross sections of the flat pad and the tensile specimen (at the test cross section) and the negligible strain in the spatial direction, the flat-pad tests were modelled in 2D with a planar strain assumption. To account for the stiffness of the flat-pad mounting, the flat-pad base and flat-pad clamp were also modeled. The bolt-tensioning force of the flat-pad clamp (F_B in Fig. 9) was applied to its surface by means of a coupling. A symmetry condition made it possible to reduce the computational complexity. Figure 9 shows the whole model for the flat-pad simulation.

Linear elastic analyses were performed. As in the piston-rod simulation, the Young's moduli of the base-body and counterbody materials were set according to Table 1 and Poisson's ratio was set to 0.3 for 34CrNiMo6 + QT and to 0.36 for CuSn8. The material properties of the flat-pad base and flat-pad clamp were set to 210 GPa for Young's modulus and 0.3 for Poisson's ratio, corresponding to typical values for steel.

The whole model used CPE4I elements (4-node bilinear planar strain quadrilaterals with incompatible modes). The fretting-contact area was meshed with an element edge length of 20 μm .

Three contacts are defined in the model: K1 (flat-pad–flat-pad-base contact), K2 (flat-pad–flat-pad-clamp contact) and K3 (flat pad–tensile specimen–contact). Normal contact behavior was set to “hard” for all contacts and a linear contact stiffness

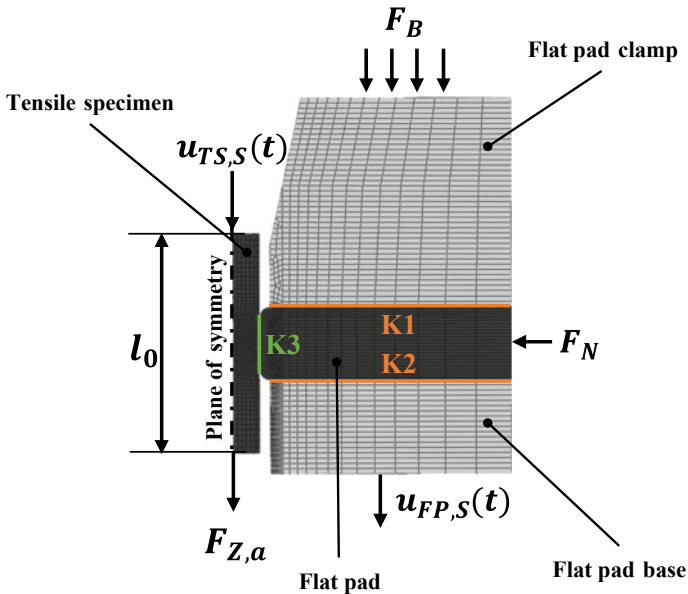


Fig. 9 FE-model of the flat-pad assembly with applied loads and displacements and the definitions of contacts K1 to K3

behavior was chosen. The stiffness value was set to 10^7 . While the tangential contact behavior of K1 and K2 was set as frictionless, for K3 the penalty friction formulation was chosen and the maximum elastic slip was set to an absolute value of $0.1 \mu\text{m}$. The CoF was globally set to 0.8 [24] (34CrNiMo6 + QT/34CrNiMo6 + QT) or 1.1 (34CrNiMo6 + QT/CuSn8).

For setting the contact pressure to 40 MPa, the normal force, F_N , was applied to the back face of the flat pad via a kinematic coupling. The dynamic load, $F_{Z,a}$, was also applied to the tensile specimen via a kinematic coupling. Each of the two material pairings was computed with the load determined from the staircase method (Sect. 3.2) for a survival probability of 50%. The models were computed over two cycles, each cycle in one step. The last step (cycle) was used for the evaluation.

In order to implement the real kinematic conditions of the tests in the simulation, real-time signals recorded by laser extensometer during the test over a few exemplary load cycles were implemented in the model as displacement boundary conditions on the flat-pad base and the tensile specimen. While the real-time displacement signal, U_{FP} , of the flat pad can be implemented directly as $U_{FP,S}(t)$ in the model, the real-time signal of the tensile specimen U_{TS} must be modified by eliminating the elongation of the tensile specimen:

$$U_{TS,S}(t) = U_{TS}(t + \Delta t) - \frac{\sigma_z(F_{Z,a})}{E} \cdot \frac{l_0}{2} \quad (3)$$

5 Evaluation

After performing the FEA, the local stress and strain states as well as the tribological parameters of contact pressure, slip and frictional shear stresses related to a fixed global coordinate system are known. Post-processing of these raw data (to calculate the frictional work or determine the stress states on the different cutting planes, for example), was performed with the MATLAB software (version R2019a). The post-processing was intended to verify several crack-initiation criteria and evaluate their accuracy with regard to the experimental location of failure. The evaluation was conducted for the nodes of the contact surface of the piston rod and tensile specimen, since, in practice, crack initiation also occurs at the surface [25].

In order to select criteria suitable for evaluation, the stress state at the experimental location of failure was considered first. Figure 10 shows this for the two set-ups and the two material pairings.

In both cases, a near-synchronous multiaxial stress state prevails at the failure location. According to [13, 31], the classical approaches of Rankine, Tresca and Mises can be applied. Because of the lack of knowledge of which material behavior (brittle or ductile) prevails at the corrosive boundary layer where cracking occurs, all three criteria were evaluated. According to [26], four criteria that are frequently associated with fretting fatigue were verified: mFFDP [11], McDiarmid [14], SWT

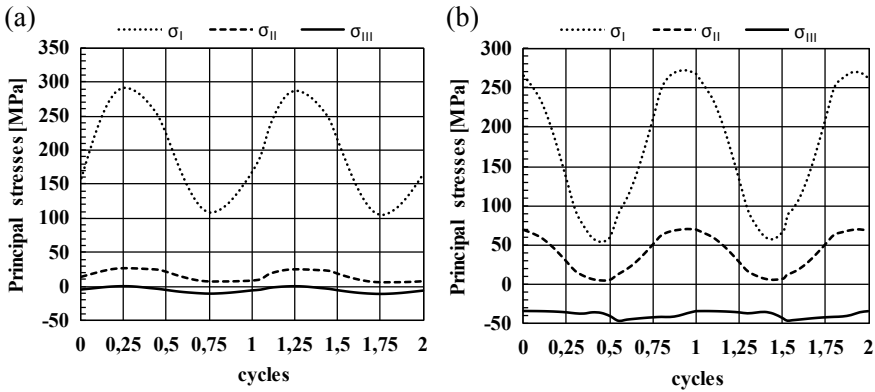


Fig. 10 Principal stress states at the locations of failure for the piston rod (a) and tensile specimen (b) for material pairing 34CrNiMo6 + QT/34CrNiMo6 + QT

[15] and FS [16]. In addition, the two integral approaches—SIH [17] and PIN [18]—were used because of their superior accuracy for free-surface problems [30]. Figure 11 shows a methodical overview of the criteria evaluated in this work.

mFFDP

The mFFDP criterion formulated by Ziaei [11] is a modification of the FFDP criterion by Ruiz [27]. By using a spatial (equivalent) stress, Ziaei adapts the FFDP criterion for 3D contact surfaces, where the largest tangential tensile stress no longer corresponds to the direction or orientation of the relative motion, as assumed by Ruiz. The mFFDP criterion is defined as

$$mFFDP = \sigma_{1,max} \cdot W_{fric} \tag{4}$$

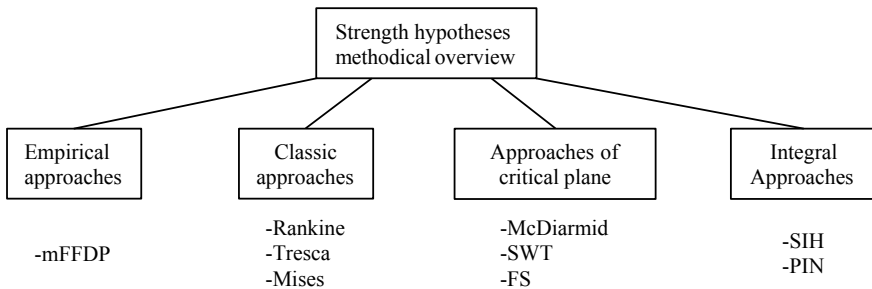


Fig. 11 Used criteria in this work

Rankine, Tresca, Mises

The Rankine [12], Tresca [13] and Mises [13] criteria are formulated for static strength assessment. The criteria consider different failure mechanisms based on the mechanical properties of materials. Rankine (for brittle materials) uses the maximum principal stress, Mises (for ductile materials) uses the maximum octahedron shear stress and Tresca (for ideal ductile materials) uses the maximum shear stress as failure criterion. For the cyclic strength assessment, the approaches can be used—with the restrictions described earlier in this section—as follows:

$$\text{Rankine : } \sigma_{va(\text{Rankine})} = \frac{\max_{(t)}[\sigma_I(t)] - \min_{(t)}[\sigma_{III}(t)]}{2} \quad (5)$$

$$\text{Tresca : } \sigma_{va(\text{Tresca})} = \max_{(t)}[\tau_{\max}(t)] - \min_{(t)}[\tau_{\max}(t)] \quad (6)$$

$$\text{Mises : } \sigma_{va(\text{Mises})} = \sqrt{\frac{\sigma_{xa}^2 + \sigma_{ya}^2 + \sigma_{za}^2 - \sigma_{xa} \cdot \sigma_{ya} - \sigma_{xa} \cdot \sigma_{za} - \sigma_{ya} \cdot \sigma_{za} + 3 \cdot (\tau_{xy}^2 + \tau_{xz}^2 + \tau_{yz}^2)}{3}} \quad (7)$$

McDiarmid

The criterion formulated by McDiarmid [14] uses the plane with the maximum shear-stress range as the critical plane for strength assessment. In the original formula, the factors t_A and t_B differ between two cracking modes, A and B. Due to the lack of knowledge about the prevailing crack mode, the torsional fatigue limit, t_{-1} , was used instead of the factors, so that following formula results:

$$\sigma_{va(\text{McDiarmid})} = \frac{f_{-1}}{t_{AB}} \cdot C_a + \frac{f_{-1}}{2 \cdot S_U} \cdot \sigma_{n,\max} \quad (8)$$

Smith–Watson–Topper and Fatemi–Socie

The damage parameter named for Smith, Watson and Topper (SWT) [15] is obtained as the product of the maximum normal stress, $\sigma_{n,\max}$, and the normal strain amplitude $\Delta\epsilon_n/2$, and thus rests on the physical basis of the specific mechanical-deformation work:

$$SWT = \frac{\Delta\epsilon_n}{2} \cdot \sigma_{n,\max} \quad (9)$$

The Fatemi and Socie (FS) [16] failure criterion includes as its main component the shear-strain amplitude, $\Delta\gamma/2$, which is multiplied by the maximum of the normal stress, $\sigma_{n,\max}$.

$$FS = \frac{\Delta\gamma}{2} \cdot (1 + k \cdot \frac{\sigma_{n,\max}}{S_Y}) \quad (10)$$

SIH and PIN

SIH [17] and PIN [18] take into account the damage contribution of all spatial planes and form a scalar equivalent stress with the help of spatial stress integration. Both investigated fatigue criteria are of similar design but of different arrangement, and consider all four stress components acting on the cutting plane: the shear stress amplitude, $\tau_{\varphi\vartheta a}$, and mean stress, $\tau_{\varphi\vartheta m}$, as well as the normal stress amplitude, $\sigma_{\varphi\vartheta a}$, and mean stress $\sigma_{\varphi\vartheta m}$. Each stress component is weighted by material parameters a , b , m and n , which are derived from reversed and repeated torsional and axial fatigue limits.

$$\sigma_{va(SIH)} = \sqrt{\frac{15}{8\pi} \cdot \int_{\varphi=0}^{2\pi} \int_{\vartheta=0}^{\pi} [a_{SIH} \tau_{\varphi\vartheta a}^2 (1 + m_{SIH} \cdot \tau_{\varphi\vartheta m}^2) + b_{SIH} \sigma_{\varphi\vartheta a}^2 (1 + n_{SIH} \sigma_{\varphi\vartheta m}^2) \sin\vartheta] d\varphi d\vartheta} \quad (11)$$

$$\sigma_{va(PIN)} = \sqrt{\frac{1}{4\pi} \cdot \int_{\varphi=0}^{2\pi} \int_{\vartheta=0}^{\pi} [a_{PIN} \tau_{\varphi\vartheta a} (\tau_{\varphi\vartheta a} + m_{PIN} \tau_{\varphi\vartheta m}) + b_{PIN} (\sigma_{\varphi\vartheta a} + n_{PIN} \sigma_{\varphi\vartheta m}) \sin\vartheta] d\varphi d\vartheta} \quad (12)$$

5.1 Piston-Rod Simulations

The verification of the presented criteria on the nodes of the contact surfaces of the piston rods can be seen in Figs. 12 and 13 for the two material pairings. The white spots in the plots represent the location of the maximum value of the respective criterion.

In Figs. 12 and 13, the criteria quantities are normalized to their maximum value that occurs. Subsequently, it was checked whether the maximum corresponds to the experimental location of failure. While for the 34CrNiMo6 + QT/34CrNiMo6 + QT pairing, the purely stress-based criteria give the best agreement—especially SIH, with an absolute error of $\Delta\varphi_{CR} = 0^\circ$. For the 34CrNiMo6+QT/CuSn8 pairing, the combined stress- and frictional-work-based mFFDP gives the best fit, with an absolute error of $\Delta\varphi_{CR} = 0.5^\circ$. On average, the McDiarmid criterion fits best for both cases, with an error of $\Delta\varphi_{CR} = 4.0^\circ$.

5.2 Flat-Pad Simulations

The flat-pad simulations were evaluated in the same way as the piston-rod simulations. Figures 14 and 15 show the evaluations of the flat-pad simulations. The contact area ranges from 0 to 5 mm (see also Fig. 6). The mFFDP criterion, the classical criteria and the critical-plane criteria all show an increased deflection at the contact edges in both material pairings. This results from increased edge pressures and the

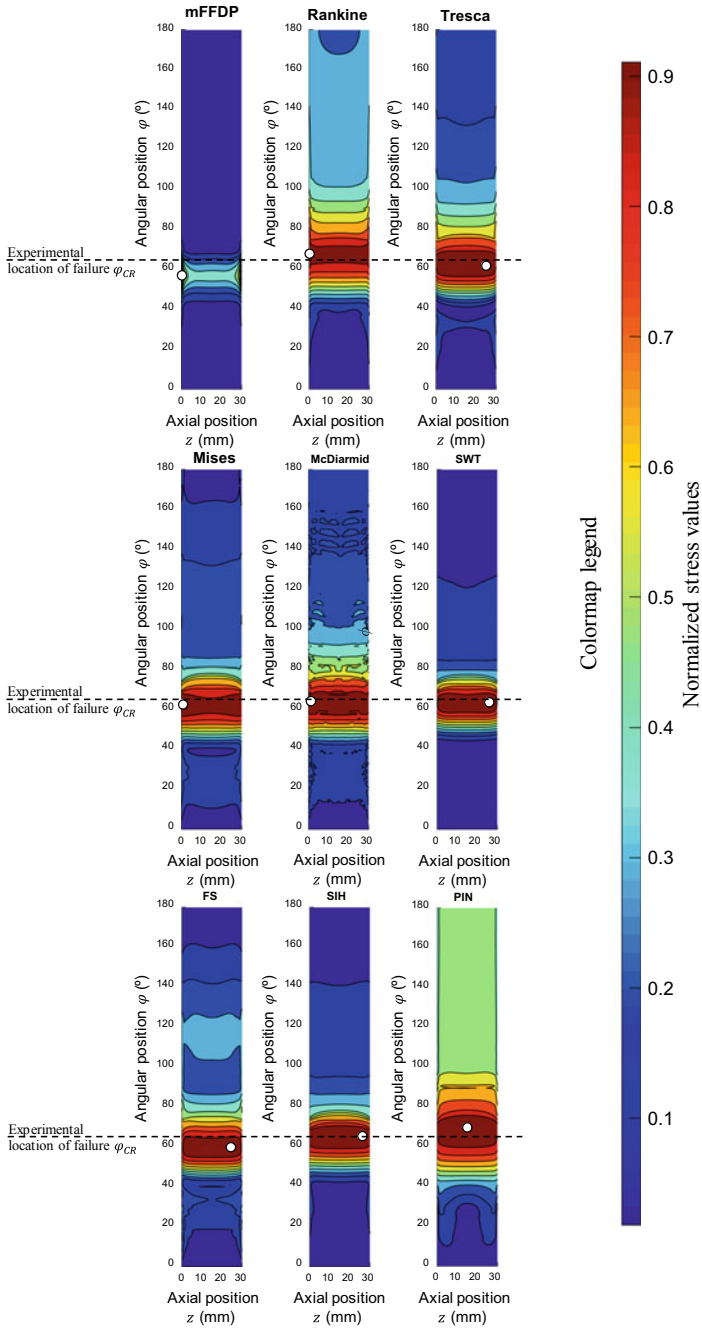


Fig. 12 Simulation results for piston rod for material pairing 34CrNiMo6 + QT versus 4CrNiMo6 + QT

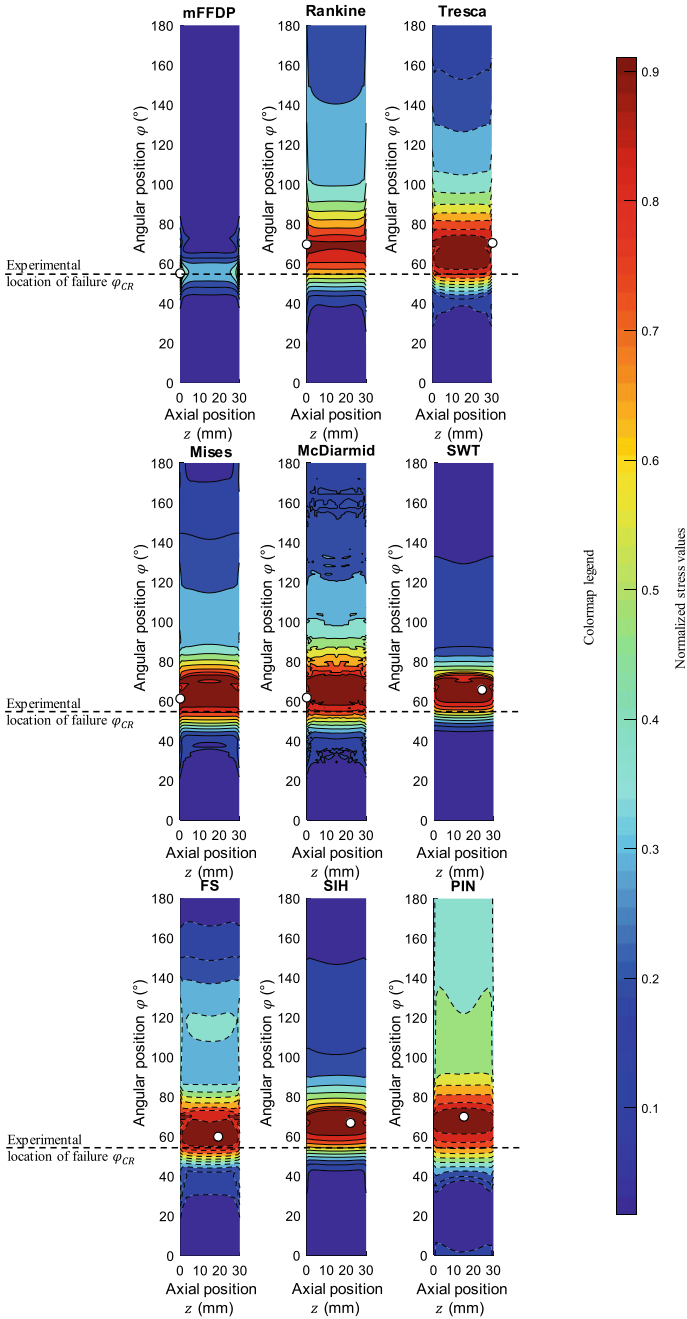


Fig. 13 Simulation results for piston rod for material pairing 34CrNiMo6 + QT versus CuSn8

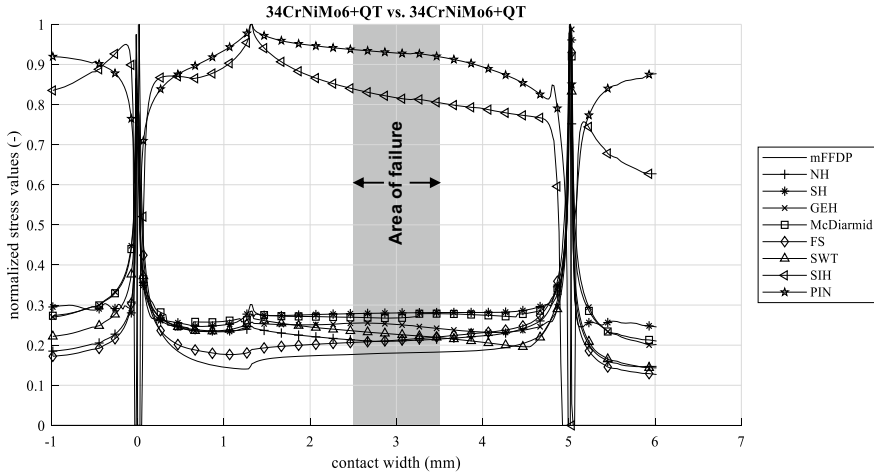


Fig. 14 Simulation results for tensile specimen for material pairing 34CrNiMo6 + QT/34CrNiMo6 + QT

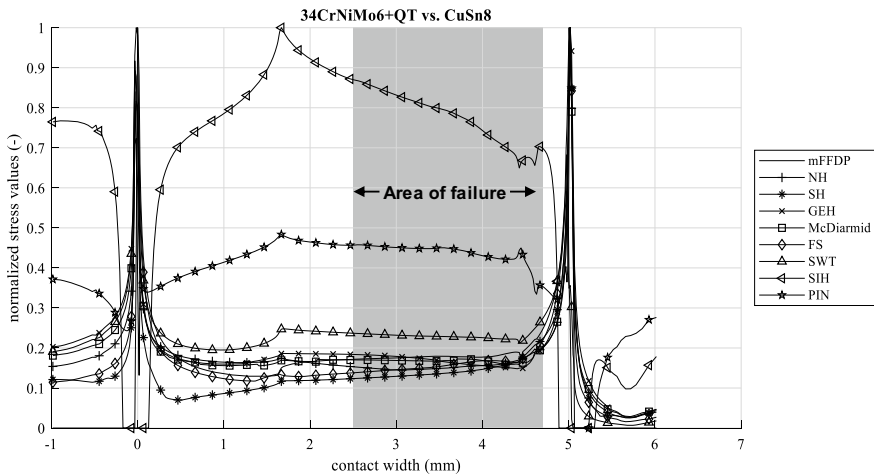


Fig. 15 Simulation results for tensile specimen for material pairing 34CrNiMo6 + QT versus CuSn8

high normal stresses induced by them. For the integral approaches—as can be seen in Fig. 14 for both approaches and in Fig. 15 for SIH—this can result in complex numbers for the equivalent stress (with equivalent stress set to zero in areas where complex numbers occur, because no reliable statement is possible for these areas). The reason is the negative sign of the compression stresses. Since the normal mean stresses are not squared in the integral approaches (see $\sigma_{\varphi\vartheta m}$ in Eqs. 11 and 12), high compressive mean stresses can lead to negative values of the root argument and

thus lead complex-number values. This limiting aspect of the integral approaches is already known from other fields and authors, such as [28]. Neglecting these contact end regions, all criteria for both material pairings show an increased deflection in the area 1 to 2 mm from the upper contact edge. However, with reference to Table 5 (see also Fig. 6), failure is expected in the lower half. The mFFDP, Treca, Mises, McDiarmid and Fatemi/Socie criteria have an elevated plateau in this area, but none has a clear peak at the failure location.

6 Summary and Conclusion

The present paper concerns a verification of crack-initiation criteria for component failures caused by fretting fatigue. The location of failure in relation to specimen geometry was investigated for two set-ups by changing the material pairing. The first set-up—a shrink-fit piston-rod-bushing connection—represents a realistic component connection, with variation of stresses by location due to its irregular cross section. The second set-up—a flat-pad set-up—is a laboratory model. The test bench with slip control presented made it possible to set all parameters independently. The fatigue limit and the location of failure was determined for each set-up and material pairing. Contrary to results frequently reported in the literature, cracks in the flat-pad tests did not occur at the contact edge, but clearly at the contact. The cause is seen in the actuated pads. Due to the actuation, no sticking zone forms, thus there is no trailing edge where cracks can start.

Using the estimated results, FEAs were performed to obtain local stresses. Considering the local stress state at the location of failure, a selection of the criteria to be used was made. Because of the synchronous stress state, the classical criteria of Rankine, Tresca and Mises were used. Furthermore, following the literature preview, criteria related to crack initiation caused by fretting fatigue were verified. These included the empirical mFFDP criterion of Ziaei, as well as the critical-plane criteria of McDiarmid; Smith, Watson and Topper; Fatemi and Socie. Because of their superior accuracy in free-surface problems, two integral approaches—SIH (Liu/Zenner) and PIN (Papuga)—were included to the verification.

The various criteria result in significantly different trends for the different material pairings. Whereas purely stress-based criteria show the best matching with the experimental location of failure for the piston-rod set-up and the 34CrNiMo6 + QT/34CrNiMo6 + QT pairing, mFFDP based on the frictional work gives the smallest error for the 34CrNiMo6 + QT/CuSn8 pairing. On average, McDiarmid's criterion gives the best matches for both cases, with an error of $\Delta\varphi_{CR} = 4.0^\circ$ relative to the angular coordinate of the cylindrical piston-rod bore. The increased compressive stresses at the contact edges of the flat-pad set-up made pure verification of the criteria over the entire contact area difficult. The increased deflection shown by the criteria here fails to agree with the experimental failure location, which is predominantly near the center of the contact. Furthermore, the integral approaches suffer from a problem known from the literature: they cannot handle high mean compressive

stresses. Neglecting these regions at contact ends, the mFFDP, Treca, Mises, MicDiarmid and Fatemi/Socie criteria have an elevated plateau at the failure area, but none has a clear peak at the failure location. Nevertheless, the prediction of the component strength was not evaluated in this work. Therefore, subsequent research will focus on determining or developing an appropriate strength-assessment method. With this aim, the database is expanded by including further experimental results and further criteria, and by investigating further material pairings using the set-ups presented.

Acknowledgements The CORNET promotion plans (Nr. 17761 BR/1 and Nr. 18692 BR/1) of the Research Community for combustion engines (FVV), Lyoner Straße 18, 60528 Frankfurt/Main has been funded by the AiF within the programme for sponsorship by Industrial Joint Research (IGF) of the German Federal Ministry of Economic Affairs and Energy based on an enactment of the German Parliament.

References

1. Waterhouse RB (1981) *Fretting fatigue*, Elsevier Science & Technology
2. Hills DA (1994) *Mechanics of fretting fatigue*. *Wear* 175:107–113
3. Buch A (1977) Fatigue and fretting of pin-lug joints with and without interference fit. *Wear* 43:9–16
4. Juoksukangas J, Lehtovaara A, Mäntylä A (2016) Experimental and numerical investigation of fretting fatigue behavior in bolted joints. *Tribol Int* 103:440–448
5. Juuma T (2000) Torsional fretting fatigue strength of a shrink-fitted shaft with a grooved hub. *Tribol Int* 33:537–543
6. Bertini L, Santus C (2015) Fretting fatigue tests on shrink-fit specimens and investigations into the strength enhancement induced by deep rolling. *Int J Fatigue* 81:179–190
7. Rajasekaran R, Nowell DÅ (2006) Fretting fatigue in dovetail blade roots. *Experiment and analysis* 39:1277–1285
8. Shi L, Wei DS, Wang YR, Tian AM, Li D (2016) An investigation of fretting fatigue in a circular arc dovetail assembly. *Int J Fatigue* 82:226–237
9. Fouvry S, Kubiak K (2009) Development of a fretting–fatigue mapping concept: The effect of material properties and surface treatments. *Wear* 267:2186–2199
10. Sadeler R, Sengül AB (2006) Influence of induction hardening on fretting fatigue behavior of AISI 1045 steel under two different contact pressures. *Kovove Mater* 44:235–241
11. Ziaei M (2003) analytische Untersuchung unrunder Profilmfamilien und numerische Optimierung genormter Polygonprofile für Welle-Nabe-Verbindungen. Technische Universität Chemnitz, Habilitation
12. Radaj D., Vormwald M.: *Ermüdungsfestigkeit: Grundlagen für Ingenieure*, Springer (2007)
13. Fesich T. M.: *Festigkeitsnachweis und Lebensdauerberechnung bei komplexer mehrachsiger Schwingbeanspruchung*, doctoral thesis, Universität Stuttgart (2012)
14. McDiarmid DL (1994) A shear stress based critical-plane criterion of multiaxial fatigue failure for design and life prediction. *Fatigue Fract Engng Mater Struct* 17:1475–1484
15. Smith KN, Watson P, Topper TH (1970) A Stress-Strain Function for the Fatigue of Metals. *J Mater* 5(4):767–778
16. Fatemi A, Socie D (1988) *Fatigue Fract. Engng Mater Struct.* 11:145–165
17. Liu J, Zenner H (1993) Estimation of Endurance Limit under Multiaxial Loading. *Mat.-wiss. u. Werkstofftech.* 24:240–249
18. Papuga J, Suchý L, Růžička M (2019) Mean shear stress effect built into the multiaxial fatigue strength estimation method of an integral type. *MATEC Web Conf.* 300:16010

19. Chao J (2019) Fretting-fatigue induced failure of a connecting rod. *Eng Fail Anal* 96:186–201
20. Merrit D, Zhu G (2004) The Prediction of Connecting Rod Fretting and Fretting Initiated Fatigue Fracture. *Journal of engines* 113:1633–1638
21. DIN 7190–1:2017–02 (2017) Interference fits—Part 1: Calculation and design rules for cylindrical self-locking pressfits“, Beuth Verlag GmbH
22. Hück M (1983) Ein verbessertes Verfahren für die Auswertung von Treppenstufenver-suchen. *Materialwiss Werkstofftech* 14(12):406–417
23. DIN 50100:2016–12 (2016) Load controlled fatigue testing—Execution and evaluation of cyclic tests at constant load amplitudes on metallic specimens and components“, Beuth Verlag GmbH
24. Hintikka J, Lehtovaara A, Mäntylä A (2015) Fretting-induced friction and wear in large flat-on-flat contact with quenched and tempered steel. *Tribology Inter-national* 92:191–202
25. Chambon L, Journet B (2006) Modelling of fretting fatigue in a fracture-mechanics framework. *Tribol Int* 39(10):1220–1226
26. Bhatti NA, Wahab MA (2018) Fretting fatigue crack nucleation: A review. *Tribol Int* 121:121–138
27. Ruiz C, Boddington PHB, Chen K (1984) An investigation of fatigue and fretting in a dovetail joint. *Exp Mech* 24:208–217
28. Hertter T (2003) Rechnerischer Festigkeitsnachweis der Ermüdungstragfähigkeit vergüteter und ein-satzgehärteter Stirnräder, doctoral thesis, Technische Universität München
29. Hauschild S (2020) Reibdauerbeanspruchte Stahl-Kontakte – Auslegung und Bewertung mittels systemspezifischer Reibkorrosionsfaktoren, doctoral thesis Technische Universität Chemnitz
30. Suchý L (2020) Fatigue of multi-axially loaded shaft-hub connection under different load parameters. In: *Proceedings of the 8th international conference on fracture, fatigue and wear*, pp 473–487
31. Bauer C (2017) Untersuchungen der Tragfähigkeit von Verzahnungen bezüglich zahninternen Versagens, doctoral thesis, Technische Universität Dresden

Assessment of a Thermal Fatigue Test Using Open Source CAE and Elastic FEA-Based Simplified Method



Shosuke Miyahira and Terutaka Fujioka

Abstract The assessment of thermal fatigue is often required for high-temperature components such as those in thermal power and chemical plants. The procedures of thermal fatigue assessment are complicated, and in many cases, difficult to carry out. In addition, the verification and validation of thermal fatigue assessment using FEM are rarely carried out due to the high cost and long duration of the tests. In the fatigue-life assessment of high-temperature components, the strain range for thermal fatigue-life consumptions must be estimated using an inelastic analysis. Neuber's rule has been used to estimate the strain range. The stress redistribution locus (SRL) approach is thought to lead to a more realistic behavior than Neuber's rule. This paper describes the numerical confirmation of the SRL behavior under thermal loadings. In addition, this paper describes the fatigue assessment of components subjected to cyclic thermal loadings by the alternate injection hot and cold sodium flow, referring to a previously reported thermal fatigue test performed by Japan Atomic Energy Agency on a tapered cylindrical specimen. Finite element analysis (FEA) and non-steady-state thermal transient and stress analyses were performed to evaluate the thermal stress changes by using an open source FEA software (Salome-Meca, Code-Aster). The results of thermal fatigue assessments obtained by inelastic and elastic FEA route assessments using the SRL approach were compared with each other. The results of thermal fatigue assessments obtained by using the SRL approach were more realistic than those obtained by Neuber's rule. In addition, the SRL can be used to carry out a more simplified evaluation procedure than the conventional evaluation procedure defined by ASME Section III Division 5.

Keywords Thermal fatigue · Stress redistribution locus · Open-source CAE · Finite element analysis · Verification and validation

S. Miyahira (✉)

Course of Advanced Mechatronics System, Graduate School of Science and Engineering, Toyo University, Tokyo, Japan
e-mail: s36a02000154@toyo.jp

T. Fujioka

Department of Mechanical Engineering, Faculty of Science and Engineering, Toyo University, Tokyo, Japan

1 Introduction

1.1 Objective

An assessment of thermal fatigue is often required in the design and/or maintenance of high-temperature components, such as thermal power plant components. The low-cycle fatigue failure of these components may occur when they are subjected to cyclic thermal stress caused by the temperature changes of frequent start-up and stop operations. Such stress changes can be estimated by performing heat transfer and stress analyses with finite element analysis (FEA) software. The fatigue-life consumption evaluation procedures are given in ASME Section III Division 5 [1], which describes inelastic FEA-route assessment procedures for determining the maximum equivalent strain range. Japanese fast breeder reactor design code [2] describes an elastic FEA-route method that is equivalent to those in the ASME code. These methods require the analyst to specify a pair of time steps in a given thermal cycle that maximizes the stress or strain range at a specific location. However, this task is troublesome and requires a large computer memory when surveying a broad section of the component surface.

The lack of experimental verification and validation data presents another difficulty in thermal fatigue assessments. The generation of high stress changes requires a large-sized specimen, and therefore, the test becomes costly and time consuming. Several experimental studies have been carried out at the Japan Atomic Energy Agency (JAEA) using their sodium loop test facilities. The test data obtained in the agency are costly but extremely valuable and should be used as a reference for analysts to evaluate their skills and expertise. In a previous paper [3], a sodium loop test was evaluated by various elastic and inelastic FEA-route fatigue assessment procedures, which ultimately produced results equivalent to those obtained by the ASME method. A previous study employed simplified methods, in which the determination procedures for the time step pair requires less memory and a shorter computation time.

In the fatigue-life assessment of high-temperature components, the strain range for thermal fatigue-life consumptions must be estimated using an inelastic analysis. Neuber's rule has been used to estimate the strain range. However, Neuber's rule results in a conservative assessment. The stress redistribution locus (SRL) approach is thought to lead to more realistic behavior than Neuber's rule.

The objectives of this paper are to validate the previously proposed simplified methods by simulating the thermal fatigue test of a specimen. The test considered was also performed by JAEA [3]. Unlike in the design codes [1, 2], this study employed the von Mises equivalent stress and separately studied SRL methods, as simplified inelastic strain range estimates, without performing stress categorizations. In addition, a more simplified evaluation procedure than the conventional evaluation procedure defined by the ASME Section III Division 5 was carried out.

2 Thermal Transient Test Methods

2.1 Overview of Previously Conducted Thermal Transient Test

This study considered a previously performed thermal fatigue test that used an axisymmetric type 304 stainless steel (304SS) specimen. The test was performed by Ishizaki et al. [3] in JAEA in their sodium flow-test facilities. Figure 1 shows the specimen configuration and dimensions. Thermal cycles were applied to the specimen by alternately injecting hot (600 °C) and cold (300°C) sodium flows into the specimen. The hot sodium flow was maintained for 10 min, whereas the cold sodium flowed for 4 min, with a maximum flow rate of 100 L/min. This thermal transient test was repeated for 2000 cycles. During the cycles, the temperatures were measured at a point of sodium temperature at the entrance. After completing the test, the specimen was cut, and the initiated cracks were observed. The measured temperature history of sodium during one thermal cycle is shown in Fig. 2, and it was used to set the boundary conditions for the thermal transfer analysis. Figure 3 shows the crack observations reported in [3]. The image in Fig. 3 was digitally processed from the photographs in [3].

3 Assessment of Thermal Fatigue Using Simplified Methods

3.1 FEA

Before performing the thermal fatigue analysis, the numerical confirmation of the SRL behavior was described. The stress–strain relation, which is a nondimensionalized inelastic solution with an elastic solution, has the SRL. Supported by theoretically proved the SRL approaches a straight line under displacement control loadings [4], Whereas the SRL curve approaches a straight line under thermal stress. In this study, an apparent elastic follow-up factor [4] was used to confirm that the SRL approaches a straight line. Given that the apparent elastic follow-up factor [4] is independent of dimension, the same value can be possibly used for the same-shape models.

Thermal transient, elastic, and inelastic analyses were performed to confirm the SRL behavior and apparent elastic follow-up factor by using an open source FEA software (Salome-Meca, Code Aster [5]). First, thermal transient analysis was performed by giving three types of gradients up to 5000 °C. Next, elastic and inelastic analyses were performed. Ramberg–Osgood law (1) is defined as the constitutive equations ($n = 3, 5, 10$). Table 1 shows the material properties. Figure 4 presents the thermal loadings for the numerical validation of the SRL behavior. After confirming the SRL behaviors, the thermal transient analysis was performed to examine the temperature

distribution in the analyses model. Next, elastic and inelastic stress analysis were performed to evaluate the changes in the thermal stress and strain using the temperature distribution obtained by thermal transient analysis. The material properties of 304SS and the heat transfer coefficient considered temperature dependence were used in the FEA analyses. Figure 5 shows the analysis model used in the simulation and conditions. Tables 2 and 3 present the mechanical and material properties, respectively.

$$\varepsilon = \frac{\sigma}{E} + \kappa \left(\frac{\sigma}{\sigma_y} \right)^n \quad (1)$$

3.2 Simplified and ASME-Based Methods for Strain Range Estimation

The fatigue-life consumption evaluation procedures are given in the ASME Section III Division 5 [1]; the procedures describe the inelastic FEA-route assessment procedures for determining the maximum equivalent strain range. These methods require the analyst to specify a pair of time steps in a given thermal cycle that maximizes the stress or strain range at a specific location. However, this task is troublesome and requires a large computer memory when surveying a broad section of the component surface.

A previous study proposed three simplified methods which do not consume large computer memory and long calculation time for the calculation of stress and strain ranges. The calculation of the maximum stress range required to determine the pair of time steps can be estimated using the following von Mises equivalent stress range (2) and equivalent strain range (3):

$$S_p = \frac{1}{\sqrt{2}} \{ (\Delta\sigma_z - \Delta\sigma_r)^2 + (\Delta\sigma_r - \Delta\sigma_\theta)^2 + (\Delta\sigma_\theta - \Delta\sigma_z)^2 + 6\Delta\tau_{zr}^2 \}^{1/2} \quad (2)$$

$$\Delta\sigma_z = \sigma_{z_t1} - \sigma_{z_t2}$$

$$\Delta\sigma_r = \sigma_{r_t1} - \sigma_{r_t2}$$

$$\Delta\sigma_\theta = \sigma_{\theta_t1} - \sigma_{\theta_t2}$$

$$\Delta\tau_{zr} = \tau_{zr_t1} - \tau_{zr_t2}$$

$$\Delta\varepsilon = \frac{\sqrt{2}}{2(1 + \nu)} \left\{ (\Delta\varepsilon_z - \Delta\varepsilon_r)^2 + (\Delta\varepsilon_r - \Delta\varepsilon_\theta)^2 + (\Delta\varepsilon_\theta - \Delta\varepsilon_z)^2 + \frac{3}{2} \Delta\gamma_{zr}^2 \right\}^{1/2} \tag{3}$$

$$\Delta\varepsilon_z = \varepsilon_{z_{t1}} - \varepsilon_{z_{t2}}$$

$$\Delta\varepsilon_r = \varepsilon_{r_{t1}} - \varepsilon_{r_{t2}}$$

$$\Delta\varepsilon_\theta = \varepsilon_{\theta_{t1}} - \varepsilon_{\theta_{t2}}$$

$$\Delta\gamma_{zr} = \gamma_{zr_{t1}} - \gamma_{zr_{t2}}$$

The evaluation procedures in the ASME-based FEA-route method are complicated and difficult to carry out because the pair of time steps, namely, t_1 and t_2 , must be selected from all the possible time-step combinations in a load cycle. In addition, the calculated stress and strain components and temperatures must be stored while the FEA is being performed. However, in Method 1, time step t_1 is determined first when the instantaneous equivalent stress reaches its largest in the 2nd cycle. Subsequently, time step t_2 is determined at the point that produces the maximum equivalent stress range in the 2nd cycle. These procedures are undertaken in Method 1 for representative evaluation points.

In Method 2, a pair of time steps t_1 and t_2 is determined for each stress component, after which the identified pair for the component with the largest stress range is selected for estimation of the equivalent stress range. In Method 3, the equivalent stress range is defined as one-half of the stress history path. Method 3 does not need to specify a pair of time steps, similar to the previously proposed method for strain range estimation for a multi-axial fatigue test conducted under non-proportional loadings [6]. Figure 6 describe the conceptual schematics of the simplified method and the ASME-based method.

3.3 Fatigue-Life Consumption

The strain range is required to calculate the fatigue-life consumption N/N_f , where N is the number of thermal loading cycles, and N_f is the corresponding fatigue-life. In the case of elastic analysis, the strain range for thermal fatigue-life consumptions must be estimated using an inelastic analysis. Neuber’s rule has been used to estimate the strain range from elastic FEA. The SRL approach [7] is thought to lead to a more realistic behavior than Neuber’s rule-based method.

In this study, stress categorization was not performed, and the simple criteria given in Eqs. 4 and 5 were employed for the elastic limit. In the following equations, $3S_m$ represents the elastic domain limit, S_p denotes the maximum equivalent stress range

at an evaluation point, and E is the Young's modulus.

$$\Delta\varepsilon = \frac{S_p}{E}(S_p \leq 3S_m) \quad (4)$$

$$\Delta\varepsilon = \frac{S_p^2}{3S_mE}(S_p > 3S_m) \quad (5)$$

For estimating the strain range, one method uses an apparent elastic follow-up factor [4]. This method is an inelastic estimation that is close to the actual behavior. The apparent elastic follow-up factor can be defined by Eq. 6 using the elastic analysis and inelastic analysis solution. The inelastic constitutive law describes the stress and strain relation expressed by an elastic perfectly plastic body. Ludwik equation was used to estimate the strain range, as shown in Eqs. 7 and 8. Figure 7 shows the conceptual schematics of the estimated strain range definition method.

$$q_p = 1 - \frac{E(\Delta\varepsilon - S_p/E)}{\Delta\sigma - S_p} \quad (6)$$

$$\Delta\varepsilon = \Delta\sigma/E + (\Delta\sigma - 2\sigma_p/10^{A_0})^{1/A_1} (\Delta\sigma/2 > \sigma_p) \quad (7)$$

$$\Delta\varepsilon = \Delta\sigma/E (\Delta\sigma/2 \leq \sigma_p) \quad (8)$$

$$A_0 = 0.9772687 + 0.6446708 \times 10^{-2} \times T - 0.4675557 \times 10^{-5} \times T^2 \\ - 0.3724201 \times 10^{-8} \times T^3$$

$$A_1 = 3.69012 - 0.1847969 \times 10^{-1} \times T - 0.3544927 \times 10^{-4} \times T^2 \\ - 0.2297822 \times 10^{-7} \times T^3$$

$$E = 2.10236 \times 10^4 + 9.71895 \times T$$

$$\sigma_p = 25.5655 - 5.58937 \times 10^{-2} \times T + 1.04384 \times 10^{-4} \times T^2 \\ - 7.42535 \times 10^{-8} \times T^3 - (44.3068 - 1.78933 \times 10^{-2} \times T) \\ \times (0.002)^{0.279395 + 7.749 \times 10^{-5} \times T}$$

The best-fit fatigue failure curve of 304SS estimates the allowable number of cycles N_f , is expressed by the following equations, as given in the fast reactor design code [2]:

$$N_f = 10^{\left\{A_0 + A_1 \cdot \log_{10} \Delta\varepsilon + A_2 \cdot (\log_{10} \Delta\varepsilon)^2 + A_3 \cdot (\log_{10} \Delta\varepsilon)^4\right\}^{-2}} \quad (9)$$

$$A_0 = 1.621827 - 0.4567850 \times 10^7 \times T^2 \times R$$

$$A_1 = 1.131346 + 0.8665061 \times 10^8 \times T^2$$

$$A_2 = 0.3439663$$

$$A_3 = -0.1374387 \times 10^{-1} + 0.4910723 \times 10^{-4} \times R$$

$$R = \log_{10} \dot{\epsilon} = -3$$

The coefficients A_0 , A_1 , A_2 , and A_3 are expressed as functions of temperature and the strain rate parameter R . The methods, for conservativeness, use the higher of the two temperatures at time steps t_1 and t_2 . In this research, cracks were considered to occur when the fatigue-life consumption exceeds 0.5, which corresponds with a crack initiation width of 1.0 mm in the experiment in [8].

4 Assessment of Thermal Fatigue

4.1 Numerical Validation of the SRL Behavior

Before performing the thermal fatigue assessment, the results of the numerical validation of the SRL behavior were obtained. First, thermal transient analyses were conducted. Next, elastic and inelastic analyses were conducted, and the results from the analyses were compared.

Figures 8, 9, and 10 show the results for the SRL behavior. These figures indicate that the SRL curves also approached a straight line under thermal stress loadings in a fully plastic situation for each temperature gradient. Figs. 11, 12, and 13 display the results for the apparent elastic follow-up factor obtained from elastic and inelastic analyses. These results indicate that the SRL curves approached a straight line because the apparent elastic follow-up factors converged to a constant value, and the apparent elastic follow-up factors become large as the stress exponent increased.

4.2 Thermal Transient and Elastic Stress Analyses

The thermal transient analysis results obtained with the open-source FEA software (Salome-Meca, Code Aster [5]) were compared. Figure 14 shows the temperature distributions at 3056 s during the 2nd hot shock. Figure 14 also indicates that the temperature difference widened in the analysis model. Figure 15 illustrates the

changes in stress components. The results of the analyses suggest that hoop and axial stresses were the dominant stress components. Figure 16 presents the stress ranges calculated using the obtained stress components. Method 1 and 2 provided in almost the same assessment results as that obtained by the ASME-based method. On the other hand, Method 3 consistently overestimated the stress range under non-proportional loadings. However, Method 2 may be evaluated during the non-conservative assessment, when the analysis model has structural discontinuities. Figure 17 shows the changes in the strain components. The results of the analyses suggest that hoop and axial stresses were the dominant stress components. Figure 18 display the strain ranges calculated using the obtained strain components. In the case of inelastic analysis, simplified Methods 1 and 2 resulted in almost the same assessment as that obtained by the ASME-based method. The simplified Method 3 led to a conservative assessment and the elastic analysis results. Figures 19 and 20 show the stress/strain paths of the dominant stress/strain components (hoop and axial) obtained using the FEA methods.

4.3 Calculation of Fatigue-Life Consumption

The fatigue-life consumption was calculated from the estimated strain range using an elastic FEA-route assessment. Figure 21 shows the results of fatigue-life consumption obtained by each method. Method 1 and 2 resulted in almost the same consumption rates as that obtained by the ASME-based method. As with the stress range evaluations, Method 3 led to conservative assessments. Among the methods, only Method 3 does not adopt a pair of time steps. Thus, the reference temperatures were set as the maximum temperature in a load cycle. Figure 22 shows the ranges at which the fatigue-life-consumption rate exceeds 0.5, along with a comparison with the crack observations reported by JAEA [3]. These figures confirm that the fatigue-life assessment agrees well with the test observations reported by JAEA [3].

5 Conclusion

In this paper, assessments of thermal fatigue-life consumption were conducted by referencing the thermal fatigue test performed by JAEA. This paper showed the effectiveness of the simplified methods except for Method 3. Method 3 can be employed for simple and conservative fatigue assessment results. However, Method 2 can lead to non-conservative assessment under non-proportional loadings in a complicated model with structural discontinuities.

In the case that the SRL method using an apparent elastic follow-up factor is applied to the strain range estimation method, the fatigue-life consumption can be evaluated more realistically than when using Neuber's rule. In addition, the same

value can be used for the apparent elastic follow-up factor when the analysis model has the same shape.

This work was supported by JSPS KAKENHI Grant Number JP18K02963.

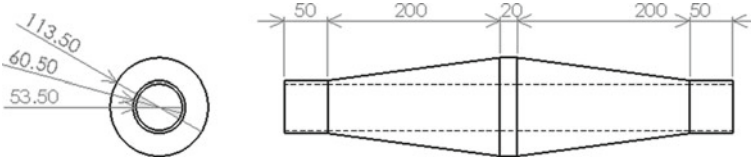


Fig. 1 Dimensions and configuration of the axisymmetric specimen [3]

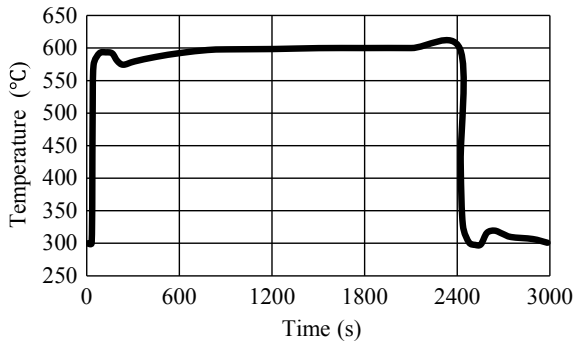


Fig. 2 Measured temperature history of sodium during one thermal cycle [3]



Fig. 3 Initiated thermal cracks on the inner surface of the specimen after the test [3]

Table 1 Material properties used for the numerical validation of the SRL behavior

| | |
|---|----------------------------------|
| Modulus of elasticity, E | 200 GPa |
| Poisson's ratio, ν | 0.3 |
| Thermal expansion coefficient, α | $2.0 \text{ E} - 05 \text{ 1/K}$ |
| Yield strength, σ_y | 200 MPa |
| Stress exponent for Ramberg–Osgood law, n | 3, 5, or 10 |
| Plastic-strain coefficient, κ | 0.002 |

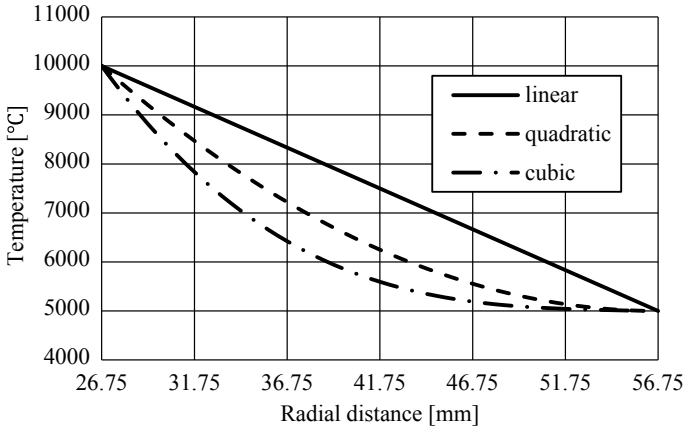


Fig. 4 Thermal loadings for the numerical confirmation of the SRL behavior

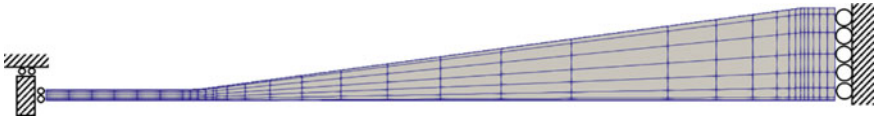


Fig. 5 Analysis model and mechanical boundary conditions

Table 2 Material properties of the 304SS and heat transfer coefficient of sodium used in heat transfer analysis [3]

| T [°C] | ρ [ton/mm ³] | λ (W/m · K) | C_p (J/kg · °C) | h (W/m ² · °C) |
|----------|-------------------------------|---------------------|-------------------|-----------------------------|
| 300 | 7.90E – 09 | 18.28 | 539.7 | 13.098 |
| 350 | 7.88E – 09 | 19.08 | 548.1 | 12.709 |
| 400 | 7.86E – 09 | 19.67 | 552.3 | 12.335 |
| 450 | 7.83E – 09 | 20.33 | 556.5 | 11.976 |
| 500 | 7.81E – 09 | 21.00 | 560.7 | 11.633 |
| 550 | 7.79E – 09 | 21.67 | 569.0 | 11.303 |
| 600 | 7.76E – 09 | 22.36 | 577.4 | 10.99 |

Table 3 Material properties of the 304SS used in elastic analysis [3]

| T [°C] | ν | α (1/°C) | E (MPa) | S_m (MPa) |
|----------|-------|-----------------|------------|-------------|
| 300 | 0.287 | 1.88E - 05 | 176,519.7 | 114.7 |
| 350 | 0.291 | 1.92E - 05 | 172,597.7 | 110.7 |
| 400 | 0.295 | 1.96E - 05 | 168,674.38 | 106.8 |
| 450 | 0.298 | 1.99E - 05 | 163,771.06 | 101.9 |
| 500 | 0.302 | 2.03E - 05 | 158,867.73 | 98.0 |
| 550 | 0.306 | 2.06E - 05 | 153,964.41 | 95.1 |
| 600 | 0.310 | 2.09 E - 05 | 149,061.08 | 92.1 |

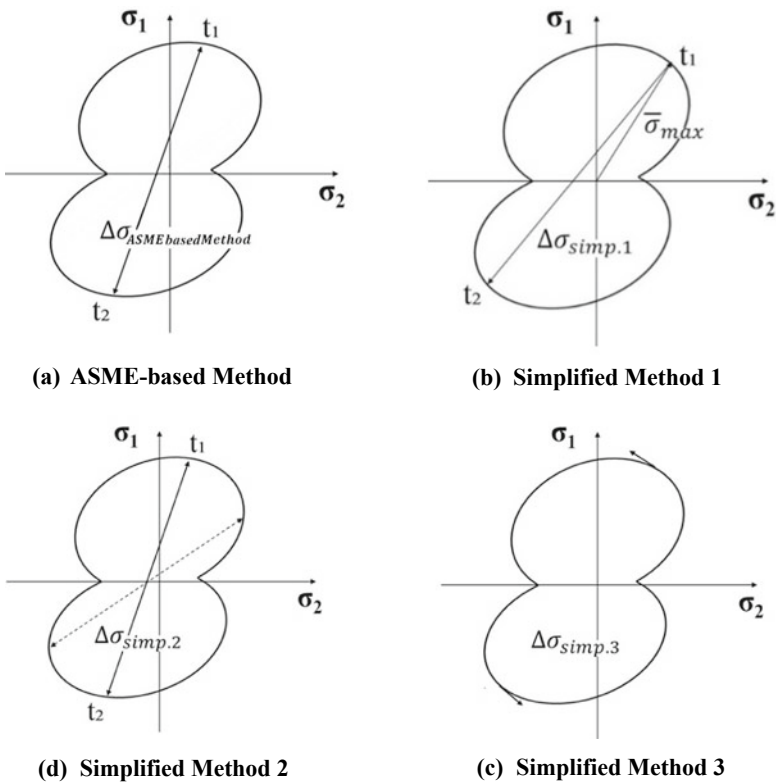


Fig. 6 Conceptual schematics of the ASME-based method and simplified methods

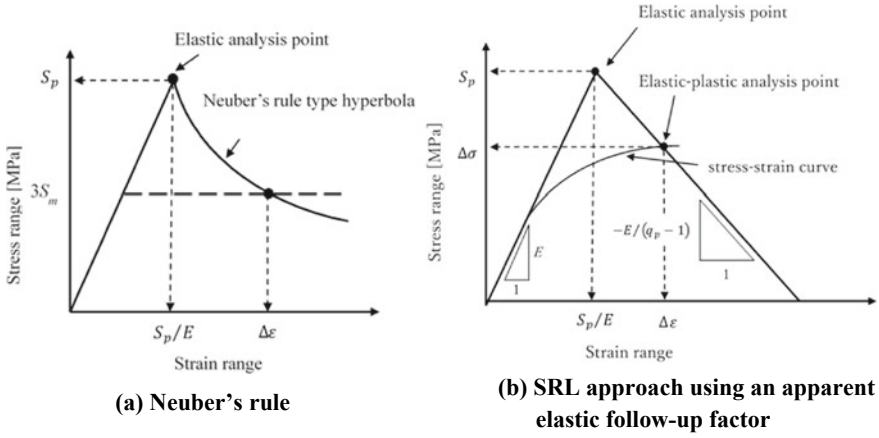


Fig. 7 Conceptual schematics of the estimated strain range of the defined methods

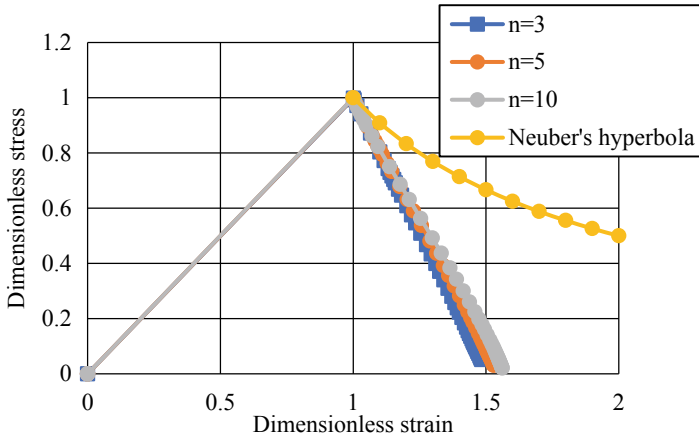


Fig. 8 Confirmation of the SRL behavior subjected to linear thermal-gradient loadings

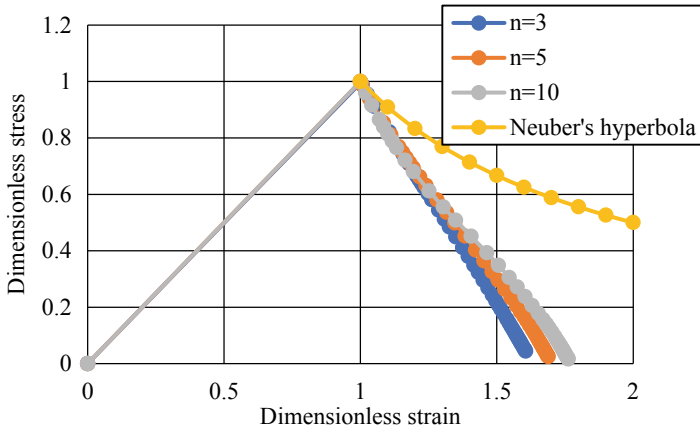


Fig. 9 Confirmation of the SRL behavior subjected to quadratic thermal-gradient loadings

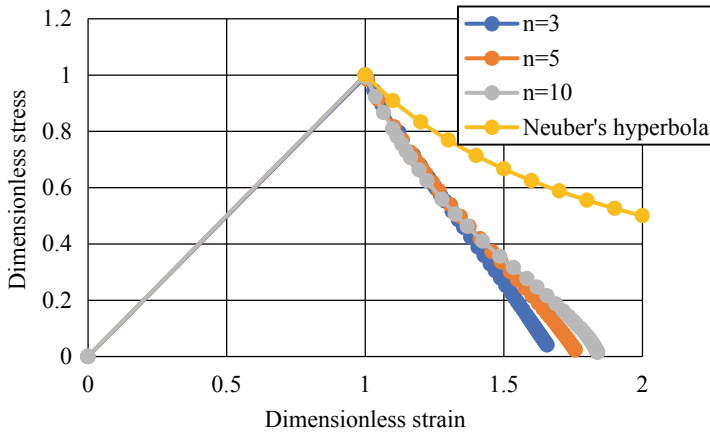


Fig. 10 Confirmation of the SRL behavior subjected to cubic thermal-gradient loadings

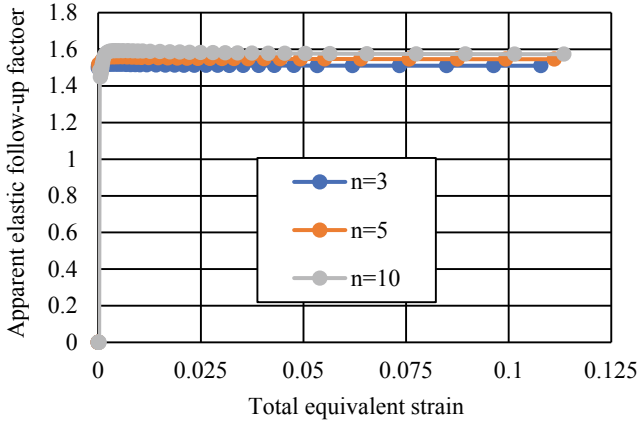


Fig. 11 Confirmation of the apparent elastic follow-up factor subjected to linear thermal-gradient loadings

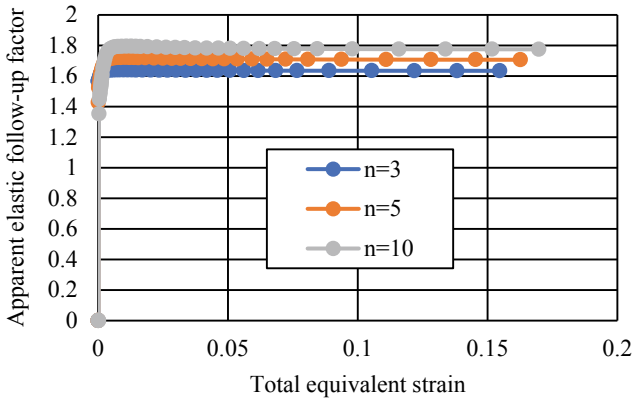


Fig. 12 Confirmation of the apparent elastic follow-up factor subjected to quadratic thermal-gradient loadings

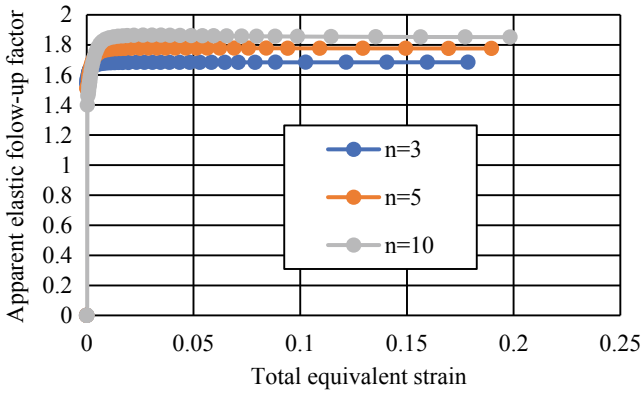


Fig. 13 Confirmation of the apparent elastic follow-up factor subjected to cubic thermal-gradient loadings

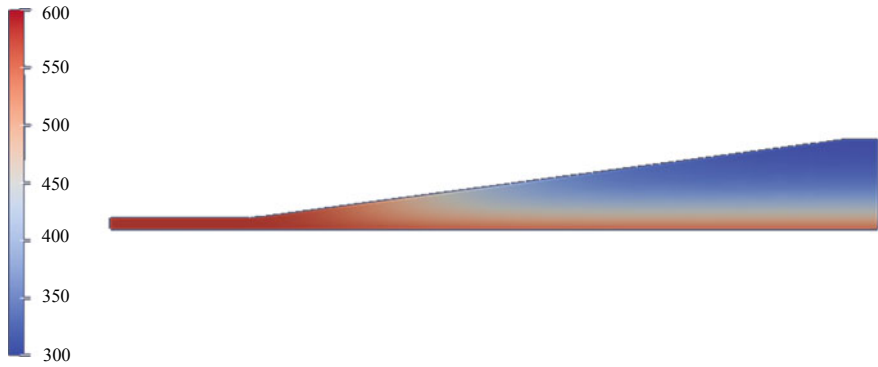


Fig. 14 Results of thermal transient analysis obtained at 3056 s (during the 2nd hot shock)

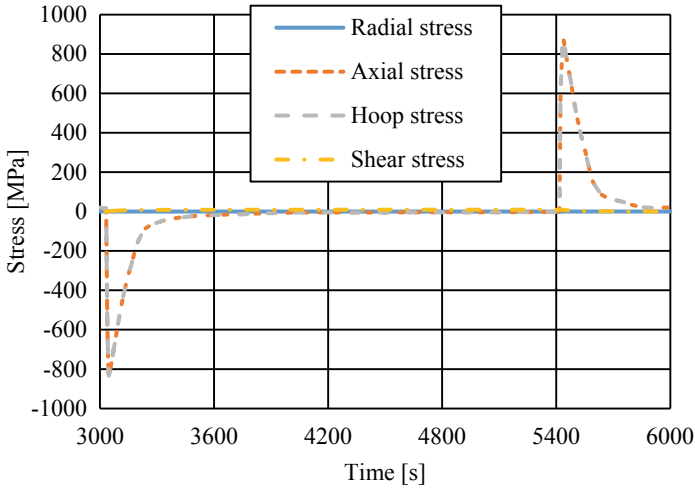


Fig. 15 Comparison of elastic stress analysis results obtained using Salome-Meca

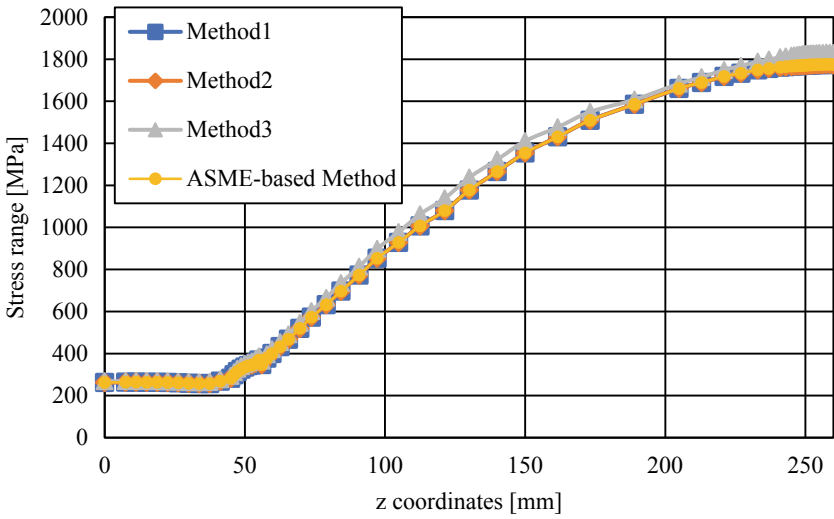


Fig. 16 Comparison of the stress range obtained using different methods

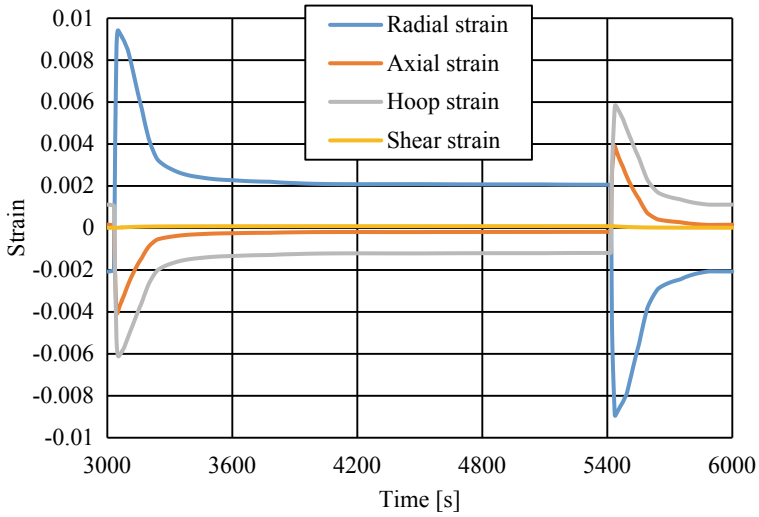


Fig. 17 Comparison of elastic stress analyses obtained using Salome-Meca

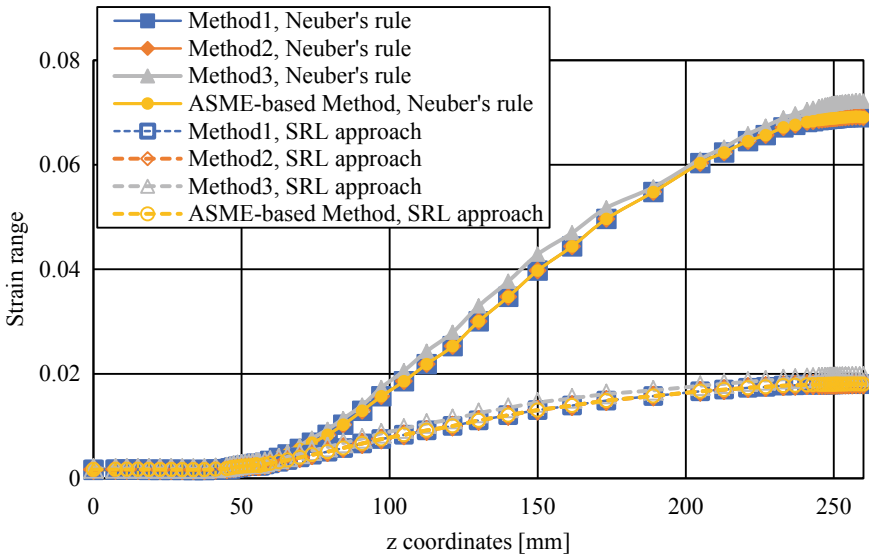


Fig. 18 Comparison of the strain range between Neuber's rule and the SRL approach

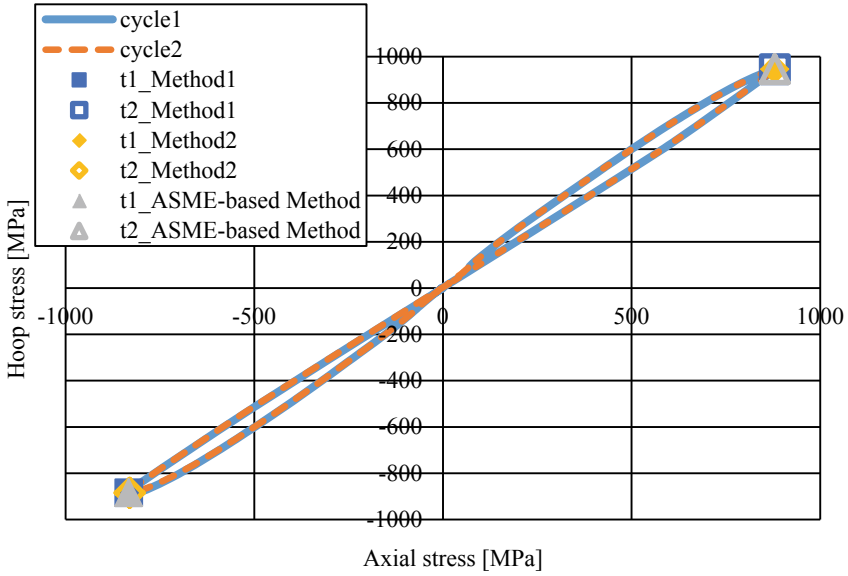


Fig. 19 Confirmation of the pair of time steps obtained by each method in the elastic analyses

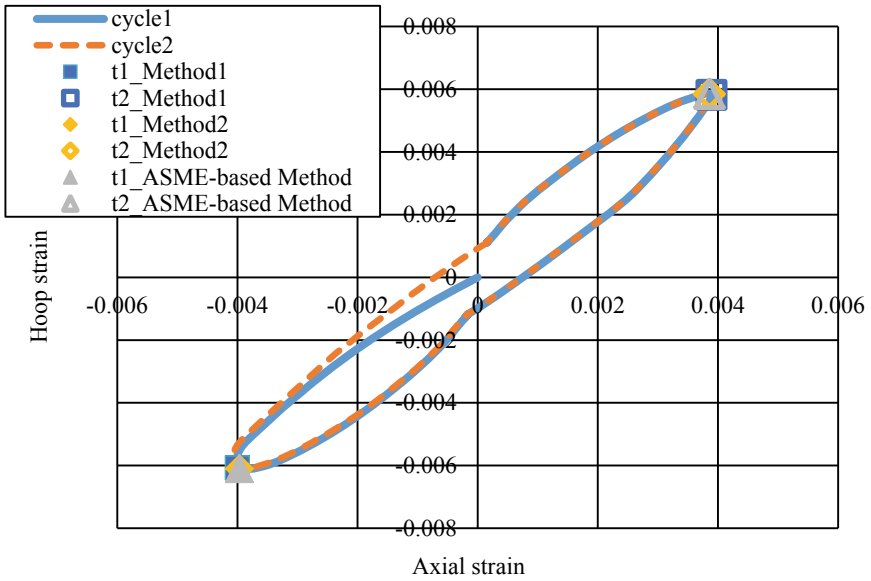


Fig. 20 Confirmation of the pair of time steps obtained by each method in the inelastic analyses

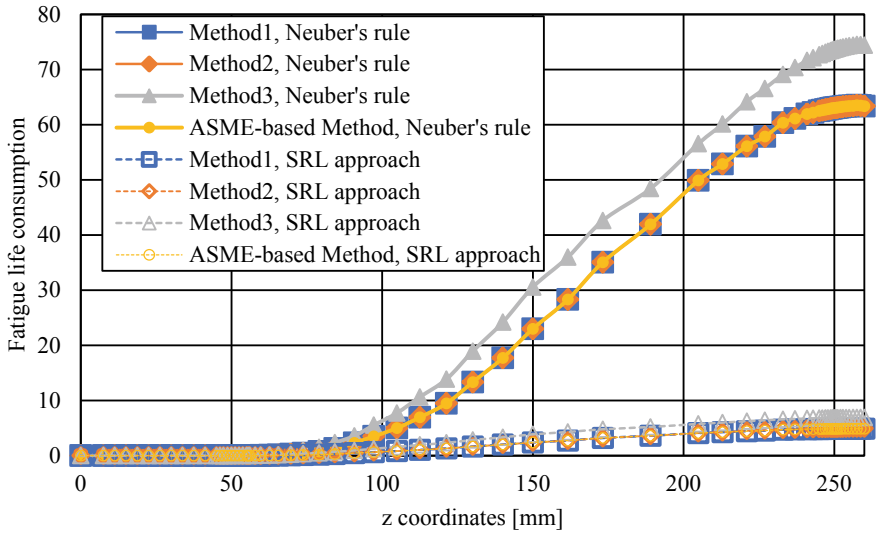


Fig. 21 Comparison of fatigue-life consumptions between Neuber's rule and the SRL approach

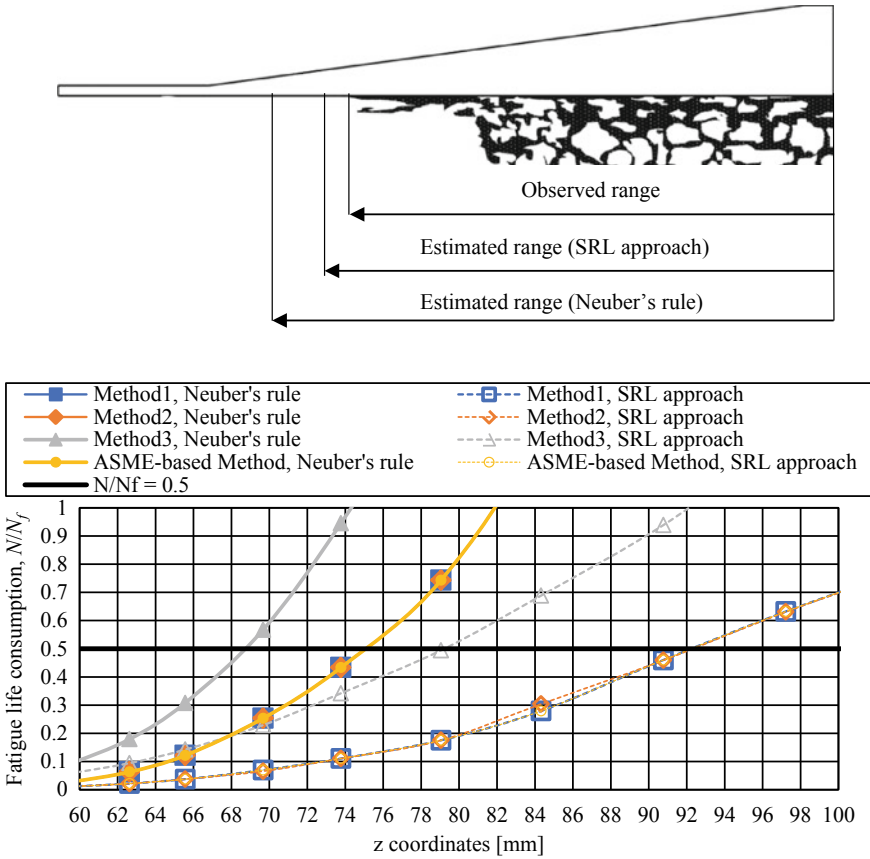


Fig. 22 Comparison of the observed and estimated crack ranges

References

1. ASME (2019) Boiler and pressure vessel code, Section III, Division5
2. JAEA (1985) Structural Design guide for class 1 components of prototype fast breeder reactor for elevated temperature; standard for strength of material, PNC TN9421 85-08, Japan Atomic Energy Agency, Japan, pp 253 (in Japanese)
3. Ishizaki K, Watashi K, Takahashi N, Iwata K (1989) Thermal Fatigue of SUS304, PNC TN 9410 84 101. Japan Atomic Energy Agency, pp 1-112 (in Japanese)
4. Fujioka T (2016) Analytical expression of elastic follow-up factor in fully-plastic situation for creep-fatigue damage assessment of high temperature components. In: Proceedings of the ASME 2016 Pressure Vessels and Piping Division Conference PVT2016-63031, pp 1-6
5. Electricity de France <https://www.code-aster.org/spip.php?rubrique2>, last accessed 2021/3/1
6. Sakon T, Wada H, Asada Y (1987) Procedure of creep-fatigue life consumption applied to inelastic conference on structural mechanics in reactor technology, SMiRT-9. Switzerland, pp 267-272

7. Sato M, Kikuchi H, Kasahara N (2011) Study on mechanism of stress-strain redistribution by elastic-plastic-creep deformation. In: Proceedings of the ASME 2011 pressure vessels and piping division conference. PVT2011-57552, pp 1-7
8. Fukuda Y, Sato Y (1995) Micro-crack propagation and fatigue life of large welded structures. J Soc Mat Sci Japan 44(496) 65-70 (in Japanese)

Simple Fatigue Crack Propagation Evaluation by Enhanced Reference Stress Method Using Open-Source CAE



Bohua Li and Terutaka Fujioka

Abstract Although J-integral type fracture mechanics parameters are effective for estimating crack propagation behaviors under elastic–plastic situations such as low-cycle fatigue, calculation of J-integral type non-linear fracture mechanics is still time-consuming and laboring. Instead of costly inelastic FEA of cracked components, the enhanced reference stress method can be used in estimating elastic–plastic J-integral from stress intensity factors and limit load solutions. The solution of limit loads and limit load correction factors (database) required to use this method is limited to some simple representative component geometries. This study aims to improve the usability of the reference stress method by creating database using open-source CAE (Salome-Meca, code_aster, ver. 2018) to obtain solutions of stress intensity factors and other necessary solutions such as limit load correction factors. The solutions obtained were compared with commercial CAE (Marc, Mentat, ver. 2019) and the fully plastic solutions by Ueda and Yagawa. Finally, fatigue crack propagation was calculated using the elastic–plastic J-integral obtained using the simplified methods of a pure elastic method, the fully plastic solution approach, the original reference stress method, and the enhanced reference stress method. In addition, the results of the simplified methods were compared with the results of the fatigue crack growth experiment under fatigue load previously conducted by Fukuda and Satou, and then the effectiveness of the correction coefficients obtained in this study has been verified. In addition, automatic modeling of cracked geometry was employed with a Python script that saves labor to construct FEA models for the fracture mechanics parameter database effectively.

Keywords Crack propagation · Fatigue · Open Source · Inelastic J-integral

B. Li (✉)

Course of Advanced Mechatronics Systems Graduate School of Science and Engineering, Toyo University, 2100 Kujirai Kawagoe, Saitama 350-8585, Japan

T. Fujioka

Department of Mechanical Engineering Faculty of Science and Engineering, Toyo University, 2100 Kujirai Kawagoe, Saitama 350-8585, Japan

1 Introduction

Fatigue crack propagation under low-cycle fatigue loading is thought to be estimated by Paris' law and fatigue J-integral range. Calculating the fatigue J-integral range for a three-dimensional surface crack in realistic components from inelastic FEA of a cracked geometry is still difficult to perform because of the treatment of crack closure. Some simplified methods to convert monotonic fracture mechanics parameters to cyclic fatigue conditions may be feasible for the straightforwardness of the assessment. The reference stress approach, which can estimate the elastic–plastic J-integral from the limit load and linear elastic J-integral, may be one of the options for low-cycle fatigue crack propagation prediction without performing a costly inelastic FEA of cracked geometry. However, the reference stress approach's accuracy can be deteriorated when applied to some complex geometries.

The enhanced reference stress approach proposed by Kim [1] can improve the accuracy of the original reference stress approach by introducing limit load correction factors. To put this modified method into practical use, a database of correction factors is needed. This paper describes the development of a database of correction factors using open-source FEA software (Salome-Meca and code_aster) [2] and an in-house Python script that automatically produces FEA mesh of cracked geometry to generate fracture mechanics solutions effectively.

2 Theoretical Backgrounds

2.1 Small Scale Yielding Condition

To evaluate automatically produced mesh models, the elastic solutions by Code-Aster were compared with stress intensity factors, K , by Raju–Newman solution [3] in Eq. 1 for a semi-elliptical crack, and F is a correction factor for K . The material properties of the cracked plate model are shown in Table 1. The load applied to the plate model are S_t (tensile) and S_b (bending). The correction factor for bending load is H_s . Q is the correction factor for the crack depth of a , and c is the half of crack width. The half of width and thickness of the plate are b and t , respectively, and Φ is the angle along the crack-tip on the inscribed circle.

$$K = (S_t + H_s S_b) \sqrt{\pi \frac{a}{Q}} F\left(\frac{a}{c}, \frac{a}{t}, \frac{c}{b}, \Phi\right) \quad (1)$$

Table 1 Material properties of plate mode (elastic condition)

| | |
|--------------------------------|------------|
| Elastic modulus, E | 200 GPa |
| Poisson's ratio, ν | 0.3 |
| Modified Young's modulus, E' | 219.78 GPa |

The pure elastic J-integral, J_e , caused by a purely elastic reaction moment, M^e , is calculated using Eq. 2 as follows. Simplified elastic–plastic J-integral estimated by this equation is likely to become reasonably conservative in components subjected to secondary stresses in medium-scale yielding. The modified Young’s modulus E' equals E when E is in plane stress conditions and $E/(1-\nu^2)$ in plane strain conditions.

$$J_e(M^e) = \frac{K(M^e)^2}{E'} \quad (2)$$

2.2 Large Scale Yielding Condition

2.2.1 Stress–Strain Relation

The analysis target of this study is a pre-notched plate specimen made of SUS304 which was loaded by the strain range, $\Delta\varepsilon = 0.004$, at a temperature of 550 °C. This analysis condition was determined by referring to Fukuda’s experiment [4]. The stress–strain relation of SUS304 is expressed by Ludwik equation [5, 6] as follows. The plastic strain range is determined by the stress range, $\Delta\sigma$, proportional limit stress, σ_p , and material constants, A_0 , A_1 .

$$\Delta\varepsilon = \frac{\Delta\sigma}{E} + \left(\frac{\Delta\sigma - 2\sigma_p}{10^{A_0}} \right)^{\frac{1}{A_1}} \quad (3)$$

It is also useful to express the stress–strain relation by the following Ramberg–Osgood Law as shown in Eq. (4). The equation of the relation is as follows, and the stress exponent, n , was equated to 3, 5, or 10 in the elastic–plastic FEAs to evaluate analysis results. α is the plastic strain coefficient. Figure 1 shows the stress–strain curves. The stress–strain relation of SUS304 is also expressed by Ramberg–Osgood Law because the correction factor of the enhanced reference stress method should be calculated using a power-law. The two stress–strain curves are compared in Fig. 2. The material properties are shown in Table 2.

$$\varepsilon = \left(\frac{\sigma}{E} \right) + \alpha \left(\frac{\sigma}{\sigma_Y} \right)^n \quad (4)$$

2.2.2 Fully Plastic Solution Approach

The fully plastic solution approach may be expressed in Eq. 5, where M is the applied moment, and M_L is the limit moment. The factors of f were obtained and tabulated in reference [7]. This method was also compared with the present analyses and used

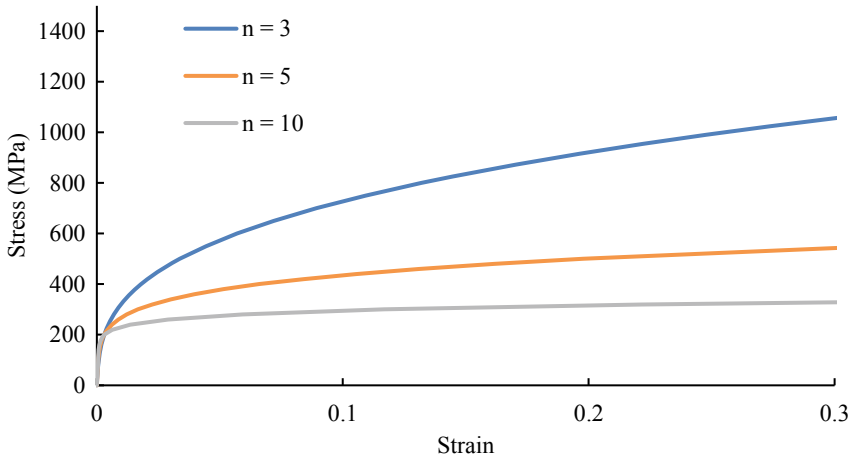


Fig. 1 Comparison of Ramberg–Osgood Law with different stress exponents

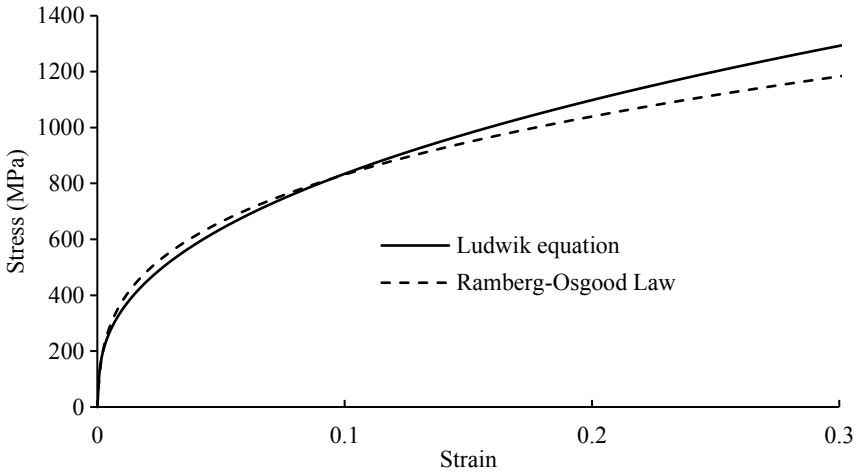


Fig. 2 Comparison of Ramberg–Osgood Law with Ludwik equation

Table 2 Material properties of plate mode (SUS304)

| | |
|--------------------------------------|------------|
| Elastic modulus, E | 153.65 GPa |
| Yield stress, σ_Y | 125 MPa |
| Stress exponent, n | 3.2 |
| Plastic strain coefficient, α | 0.00022 |

to evaluate the results of crack propagation.

$$J = f\alpha\sigma_Y t \left(\frac{M}{M_L} \right)^{n+1} \tag{5}$$

2.2.3 Reference Stress Method (Original)

According to the original reference stress method [8], elastic–plastic J-integral, J_{ref} , can be obtained by multiplying the ratio of the reference strain, ε_{ref} , to the reference elastic strain, σ_{ref}/E , as shown in Eq. 6. The reference stress is simply estimated by Eq. 7. The limit moment [9] in the surface crack model was calculated using the simplified Eqs. 8 and 9. These equations were derived from a simplified model with a square-shaped crack shown in Fig. 3.

$$J_{ref} = \frac{\varepsilon_{ref}}{\sigma_{ref}/E} \times J_e(M) \tag{6}$$

$$\sigma_{ref} = \left(\frac{M}{M_L} \right) \sigma_Y \tag{7}$$

$$M_L = \frac{\sigma_Y [b^2 t^2 - 2abct + a^2 c(2b - c)] a(2b - c)}{2b b} \leq t \tag{8}$$

$$M_L = \frac{\sigma_Y [b(b - 2c)t^2 - 2abct + a^2 c(2b - c)] a(2b - c)}{2(b - c) b} > t \tag{9}$$

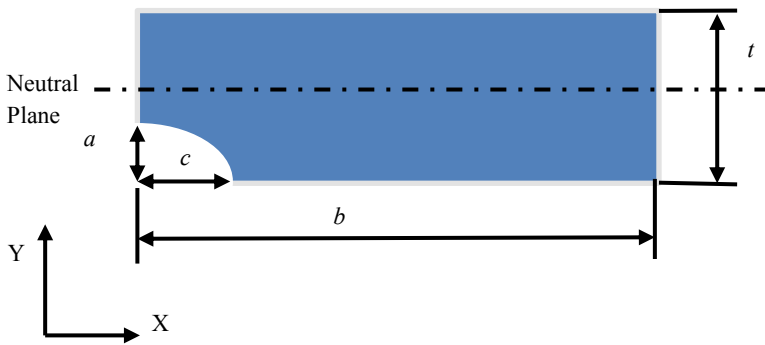


Fig. 3 Neutral plane of the analysis model

2.2.4 Enhanced Reference Stress Method

The enhanced reference stress method was modified in Ref. [10] and expressed by Eq. 10 for Ramberg–Osgood type of power-law plasticity. Two correction factors were introduced as follows. One of the factors, C_L (net section stress correction factor), is to compensate for the inaccuracy of the limit load solution in Eqs. 8 and 9, and the other, γ , is to correct J-integral depending on the stress exponent by Eq. 12.

$$J_{ref} = \frac{\varepsilon_{ref}}{\sigma_{ref} \times C_L \times \gamma} \times J_e \quad (10)$$

$$C_L \rightarrow \frac{M_L(FEA)}{M_L} \quad (11)$$

$$\gamma \rightarrow (J_{ref}/J_{FEM})^{1/(n-1)} \quad (12)$$

3 Numerical Analysis

3.1 Analysis Model

The analysis model used was a three-dimensional plate with an elliptical crack under bending load. The plate was symmetrical on all sides, so only the upper-right quarter shown in Fig. 4 was analyzed to save time. An example of the mesh is shown on the right-hand side of Fig. 4. Four analysis cases in Table 3 were performed using different crack depths and crack aspect ratios.

The boundary conditions were displacement-controlled bending, as shown in Fig. 5. To stabilize the correction factors of the enhanced reference stress method, a linear function of displacement with a neutral axis as the origin was applied to the top surface of the analysis model from the cracked surface to the inner surface, instead of the boundary conditions of the experiment. Only the upper-right quarter of the plate was analyzed, so the left side was fixed in the X-axis direction, and the bottom side can be moved up and down freely.

3.2 Analysis Procedures

The analysis was performed using the open-source software Salome-Meca and code_aster [11]. To validate the elastic analyses, the J-integral (energy release rate method) was outputted by Code-Aster directly and the estimates were compared with stress intensity factors by the Raju–Newman solution. The net section stress correction factors were calculated by comparing the limit moment of FEA with a

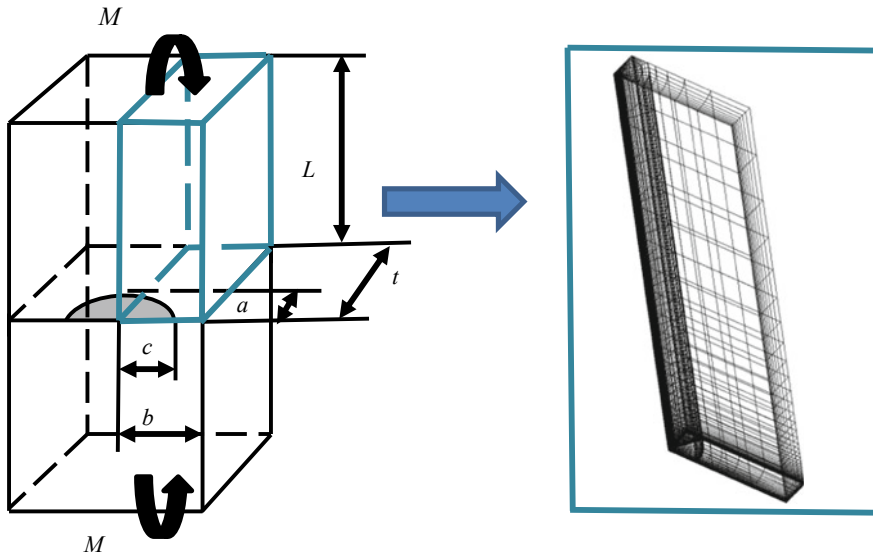


Fig. 4 Analysis model

Table 3 Cases of elastic–plastic analysis of the plate in bending with a semi-elliptical surface crack

| Case.No | Common (mm) | Loading | Dimensionless crack length a/t | Dimensionless crack length a/c |
|---------|------------------------------------|---------|----------------------------------|----------------------------------|
| 1 | $t = 50$ $b = 250$ $L = 800$ | Bending | 0.2 | 1 |
| 2 | | | | 0.2 |
| 3 | | | 0.6 | 1 |
| 4 | | | | 0.2 |

perfectly elastic–plastic body with the estimates made by the simplified equations of Eqs. 8 and 9. The limit load optimization correction factors were obtained from the comparison made by Eq. 10 with the estimated J-integral by Code-Aster. The results of elastic–plastic J-integral estimates were also compared with the fully plastic approach using Yagawa’s solution (Fig. 6).

3.2.1 Evaluating Analysis Result

In Figs. 6 and 7, the elastic FEAs by Code-Aster are compared with elastic J-integral that converted from the stress intensity factor by Raju–Newman solution. It can be confirmed that J-integral at the surface point approaches that converted from the stress intensity factor assuming plane strain conditions, and that J-integral in the

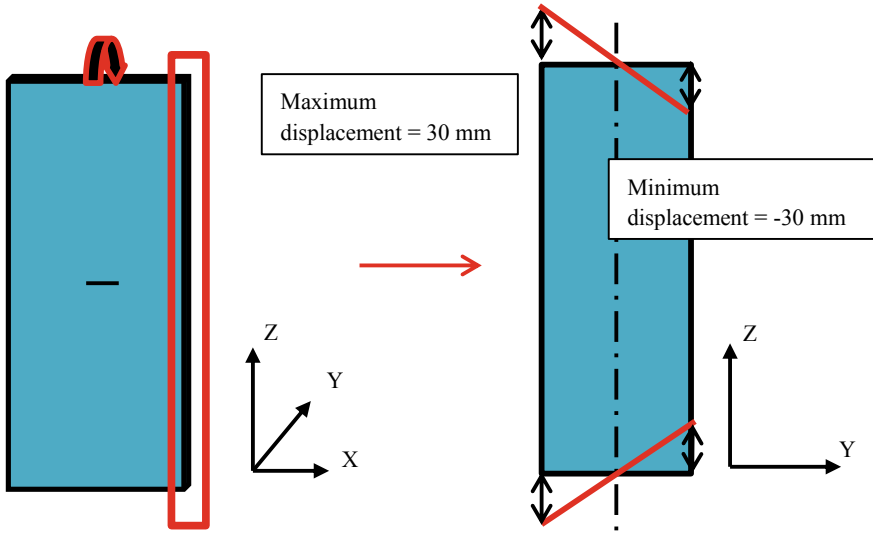


Fig. 5 Boundary conditions of the plate with a semi-elliptical surface crack

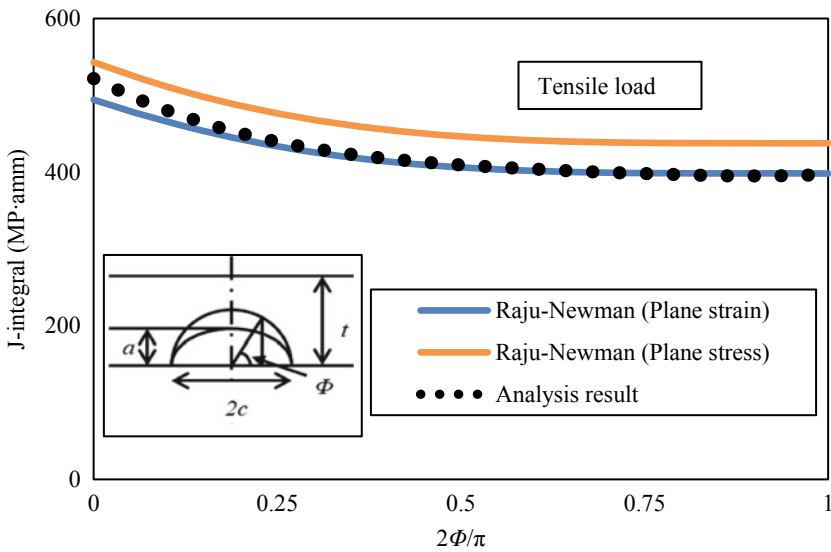


Fig. 6 Comparison of J-integral with Raju–Newman’s solution (Elastic analysis by tensile load)

inner points should be converted from the stress intensity factor with the assumption of plane stress.

Figure 8 shows the comparison of J-integrals along the crack-tip in the elastic–plastic analyses. The horizontal axes in Figs. 6, 7, and 8 are the ratios of the angle

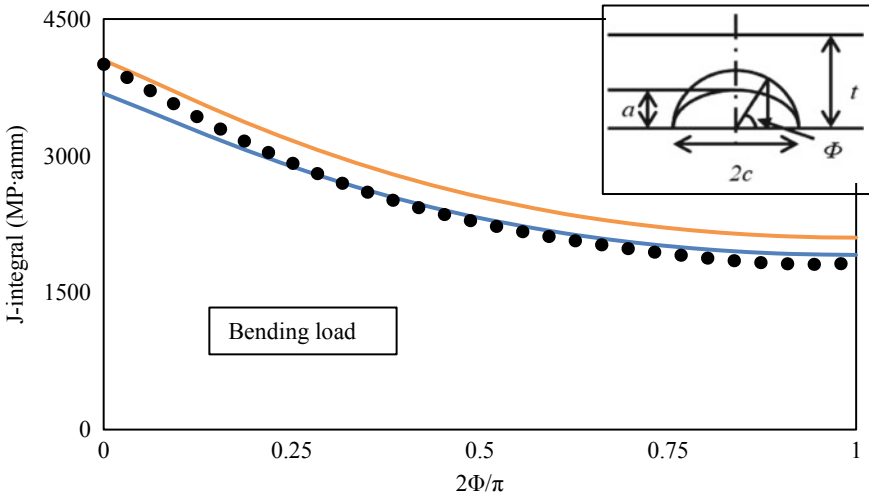


Fig. 7 Comparison of J-integral with Raju–Newman’s solution (Elastic analysis by bending load)

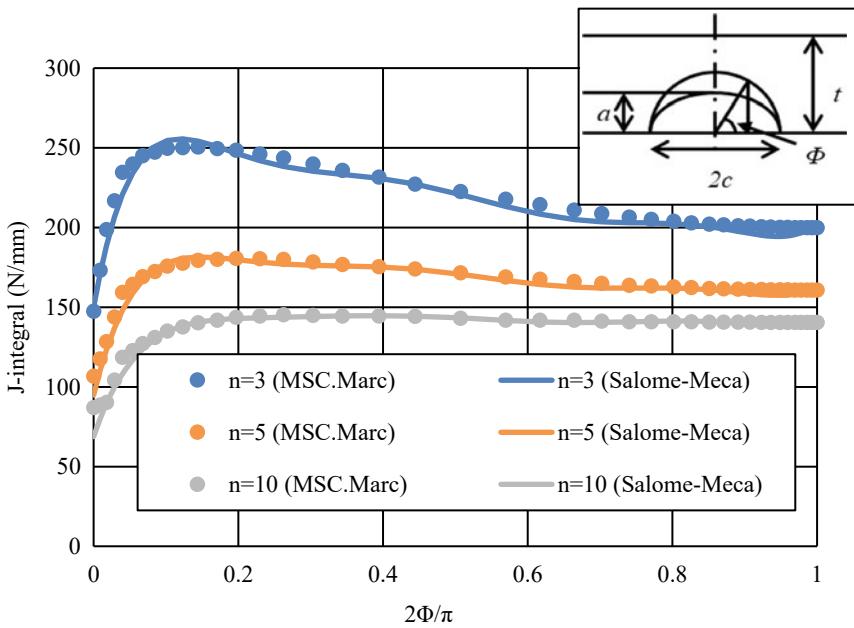


Fig. 8 Comparison of J-integral by MSC. Marc and Code-Aster (elastic–plastic FEA)

along the crack-tip on the inscribed circle and $\pi/2$. Comparing the elastic–plastic analysis results by Code-Aster with those made by MCS.Marc [12] in Fig. 8, solutions by Code-Aster seem rather consistent with those by MSC.Marc. The analysis results of elastic–plastic J-integral estimating on surface points and inner points of the crack with four cases were also compared with the fully plastic approach using Yagawa’s solution, and the error between them is kept within 5%.

4 Fatigue Crack Propagation

The stress–strain curve of SUS304 approximated by Ludwik equation is used for the elastic–plastic analysis results to obtain the bending moment in the same boundary conditions as in the experiment without a crack, then the bending moment was used to estimate the crack propagation. The elastic–plastic analysis results using the stress–strain curve of SUS304 approximated by Ramberg–Osgood Law were used to calculate the correction factors of the enhanced reference stress method in the four cases, and the correction factors are summarized in Table 4. Based on the above, to obtain the correction factors for all crack shapes, the coefficients A_1, A_2, A_3 , and A_4 were calculated, as shown in the following equation, and the results of the coefficients are summarized in Table 5.

$$\gamma(C_L) = A_1\xi + A_2\eta + A_3\xi\eta + A_4 \tag{13}$$

$$\xi = a/t, \eta = a/c$$

Table 4 The correction factors of the enhanced reference stress method

| Case.No | Common (mm) | Loading | Dimensionless crack length a/t | Dimensionless crack length a/c |
|---------|------------------------------------|---------|----------------------------------|----------------------------------|
| 1 | $t = 50$ $b = 250$ $L = 800$ | Bending | 0.2 | 1 |
| 2 | | | | 0.2 |
| 3 | | | 0.6 | 1 |
| 4 | | | | 0.2 |

Table 5 The coefficients of Eq. 13

| | A_1 | A_2 | A_3 | A_4 |
|--------------------------|-------|-------|---------|-------|
| γ (Surface point) | 0.038 | 0.143 | – 0.288 | 1.077 |
| γ (Inner point) | 0.969 | 0.361 | – 1.359 | 0.712 |
| C_L | 1.783 | 0.162 | – 1.166 | 0.728 |

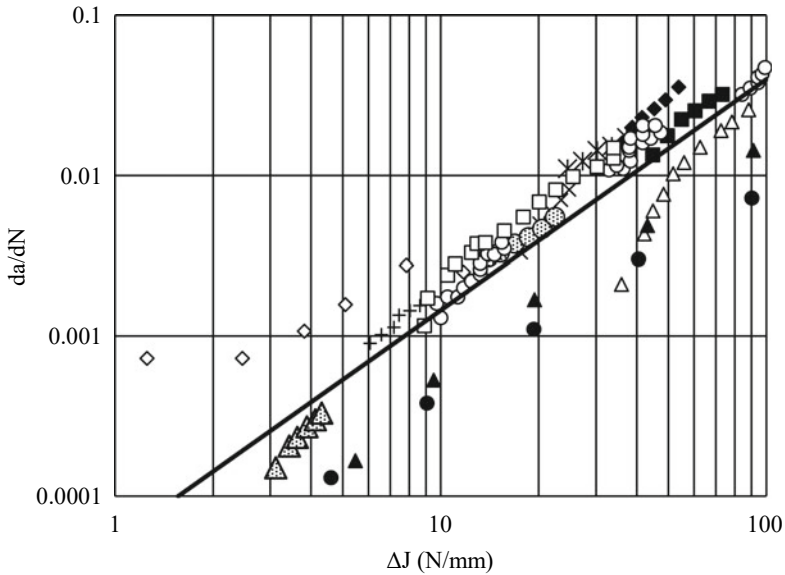


Fig. 9 Crack propagation test data and crack propagation law

Fatigue crack propagation rate, $\frac{da}{dN}$, under low-cycle fatigue loading can be evaluated using Paris' Law as follows. In this equation, ΔJ is fatigue J-integral range and was calculated as $2J$ in this study, both $C = 5.25 \times 10^{-5}$ and $m = 1.44$ are the material constants obtained from the experimental data of PNC [12, 13], as shown in Fig. 9.

$$\frac{da}{dN} = C \Delta J^m \tag{14}$$

Walker's equation [14] for considering the effect of the compressive load is shown in Eq. 15. K_{max} and K_{min} are, respectively, the maximum stress intensity factor and the minimum stress intensity factor. R is the ratio of stress (in this study $R = 1$).

$$\Delta K_{eff} = \frac{K_{max} - K_{min}}{\sqrt{1 - R}} \tag{15}$$

Finally, the pure elastic solution approach, fully plastic solution approach, reference stress method, and enhanced reference stress method were used to obtain the J-integral to evaluate the crack propagation; then these four approaches were compared with the experimental results, as shown in Fig. 10. The procedures of the pure elastic solution method are simple, but the method was too conservative. The results of the enhanced reference stress method became more accurate than that of the original reference stress method by introducing the correction factors (Table 6).

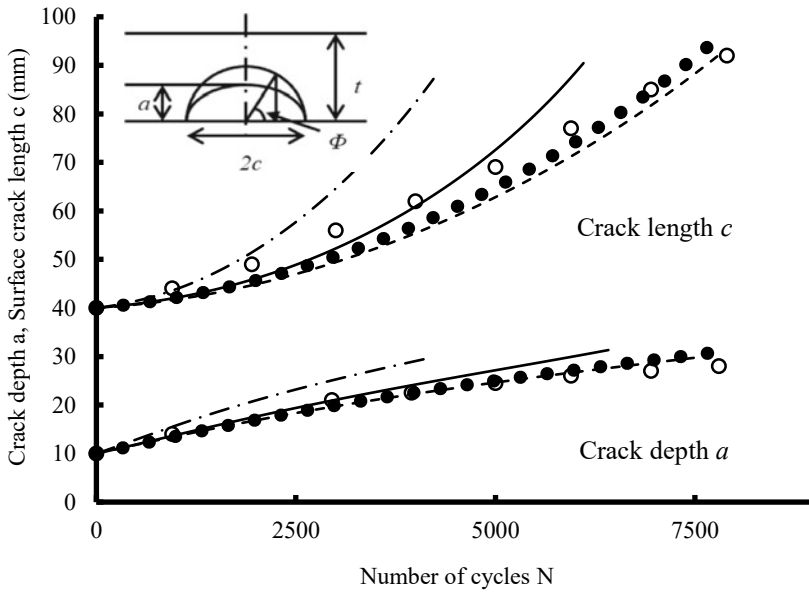


Fig. 10 Comparison between experimental results and crack propagation behavior with J-integral estimated by the simplified method using Paris’s law with PNC data

Table 6 The legend of Fig. 10

| | |
|----------------------------------|-------|
| Base metal | ○ |
| Pure elastic solution approach | - . - |
| Reference stress method | — |
| Enhanced reference stress method | ● |
| Fully plastic solution approach | - - - |

5 Summary

The enhanced reference stress approach to estimate the elastic–plastic J-integral from a limit load modified by correction factors and stress intensity factor was applied to the J-integral estimate for a surface crack in a plate subjected to displacement-controlled

bending. Compared with the original reference stress approach, the accuracy of the simplified estimate of J-integral has been improved.

References

1. Kim YJ, Huh NS (2001) Enhanced reference stressbased J and crack opening displacement estimation method for leak-before-break analysis and comparison with GE/EPRI method. *Fatigue Fract Eng Mater Struct* 24:243–254
2. Electricite de France, <https://www.code-aster.org/spip.php?rubrique2> (Accessed 2020–12–20)
3. Newman JC, Raju IS (1984) Stress-intensity factor equations for crack in three-dimensional finite bodies subjected to tension and bending load. NASA Technical Memorandum 85793 N 84- 23925
4. Fukuda Y, Satoh Y, Kashima K (1991) Surface crack propagation in SUS304 stainless steel wide plates under creep-fatigue bending load. *SMiRT 11 Trans Vol. L* 187–192
5. PNC (currently JAEA) (1985) Structural design guide for class 1 components of prototype fast breeder reactor for elevated temperature; Standards for strength of materials. PNC-TN241 85–08 (in Japanese)
6. Wada Y, Iwata K, Aoto K, Kawakami Y. (1986) Analytical representation for the cyclic stress-strain hysteresis loops of Type 304 austenitic stainless steel. *Int Conf Comput Mech* 86 IV-25–IV-30.
7. Ueda H, Ygawa G (1988) Fully plastic solutions for surface-cracked plates subjected to bending loads. *Trans JSME Series A Vol. 54, No. 499, No.87–0662 B*, 552–556 (in Japanese)
8. Ainsworth RA, Ruggles MB, Takahashi Y (1992) Flaw assessment procedure for high-temperature reactor components. *Transactions of the ASME* 114:166–170
9. Ruggles MB, Takahashi Y, Ainsworth RA (1991) High-temperature flaw assessment procedure. ORNL-6677 DE92 000387, p.54
10. Fujioka T (2013) Simplified estimate of elastic-plastic J-integral of cracked components subjected to secondary stresses by the enhanced reference stress method and elastic follow-up factors. *Int J Press Vessels Pip* 108–109:1–12
11. MSC Software <https://www.mscsoftware.com/ja> (Accessed 2020–12–20)
12. Takahashi Y, Ogata T, Fukuda Y, Sato Y (1989) Interim report of study on high-temperature flaw assessment procedure CRIEPI Report T89010
13. Asada Y (1987) Creep-fatigue crack propagation behavior of structural materials for LMFBR (General report). PNC SJ 2534 87–002 (2) JWES-AE-8706
14. Walker K (1970) The effect of stress ratio during crack propagation and fatigue for 2024–T3 and 7075–T6 aluminum. American society for testing and materials, STP 462:1–14

Fatigue Life Prediction Under Interspersed Overload in Constant Amplitude Loading Spectrum via Crack Closure and Plastic Zone Interaction Models—A Comparative Study



Chandra Kant and G. A. Harmain

Abstract In this article, comparative study of analytical fatigue crack propagation models has been presented under the effect of interspersed overload in constant amplitude loading. Effect of interspersed overload induced retardation is simulated via crack closure model (Modified virtual crack annealing model), plasticity zone interaction models (Wheeler model). Overload induced plastic zone is the measure of fatigue crack propagation decelerating zone which comes in picture due to mechanisms involved such as compressive residual stress, propagating crack plastic wake, etc. Retardation zone is determined using the Irwin's model. Analytical models chosen for this study encompasses almost all anticipated mechanisms and elucidation of overload induced retardation (plasticity induced crack closure and plastic zone interactions). Investigation is conducted for the steel and aluminum alloys for variable load ratio and overload ratios. Effect of varying inception of overload on the retardation zone is also analyzed. The performance of the models have been quantitatively compared via error analysis conducted taking experimental data as reference. A brief discussion on the used analytical models is also presented. Life estimation has been done via linear elastic fracture mechanics based Paris model. Critical qualitative analysis has been presented for the parameters involved in the discussed analytical models.

Keywords Fatigue crack propagation · Crack closure · Overload · Retardation · Error analysis

C. Kant · G. A. Harmain (✉)
NIT Srinagar, Srinagar, Jammu and Kashmir, India
e-mail: gharmain@nitsri.net; gharmain@nitsri.ac.in

C. Kant
e-mail: chandra07phd17@nitsri.net

© The Author(s), under exclusive license to Springer Nature Singapore Pte Ltd. 2022
M. Abdel Wahab (ed.), *Proceedings of the 9th International Conference on Fracture, Fatigue and Wear*, Lecture Notes in Mechanical Engineering,
https://doi.org/10.1007/978-981-16-8810-2_18

253

1 Introduction

The integrity of the most structures are designed via damage tolerant approach, which has been essential from few decades. After elucidation of fracture mechanics, damage tolerant approach has been very useful and most used approach. It provides residual life of flawed or damaged structures considering the shape and size of flaw. Also, it tells about the damage accumulation in the structure or emanating crack propagation rate.

Damage accumulation rate depend on material internal resistance which varies with material microstructure generally. Flawed structure provide resistance to propagation of crack, which is distinctly related to crack size, load, and orientation of crack. Stress intensity factor is a parameter which gives stress field near crack tip and encompasses the effect of load and flaw size. One of the earliest and simple fatigue crack propagation model was given by Paris [1]. But, the model was valid under specific circumstances of loading generally in constant amplitude load (CAL) spectra. In practical situation, structures have complex loading (variable load, programmed load, interspersed overloads and under loads, loading sequence, and specific loading patterns). In complex loading, damage accumulation determination is multivariate resulting in the increased number of decision parameters, which makes the fatigue life forecast tedious and intricate.

In case of interspersed overloads in CAL, overload increases the residual life of structure which is beneficial. This observation makes the study of over load effect important. Downshift of disseminating crack rate is explained via following mechanisms (a) over load (OL) induced large plastic zone (b) plasticity induced crack closure (c) crack branching (d) crack tip blunting.

OL induce plastic deformation produce a compressive residual stress inside the zone. Compressive residual stress facilitates the crack growth decrement. Crack passes through the compressive zone, material flow out towards crack flank. The deposited material on crack flank produce extra resistance in crack opening and closing fully, this phenomena is named crack closure. Crack blunting dispersedly distribute the applied load near crack tip, so effective local (crack tip) stress decreases. Effect of retardation is directly proportional to over load ratio (OLR). Quantitative measure of retardation is increased life cycle, and deceleration zone. Crack propagation retardation zone is generally equal to [(monotonic plastic zone)—(constant amplitude plastic zone)]. In [2–4], reported that with overload ratio, the delayed zone can vary.

OL induced retardation increase with increasing OL location. OL induced effect under constant amplitude loading typically shows sequence acceleration, and then acceleration up to CAL fatigue crack propagation but, in case of high OLR (≥ 2.5) initial crack acceleration has not been observed [2, 5].

Stress ratio effect influences the crack propagation rate in CAL as well as in over load spectra. In [5, 6], observed that OL induced fatigue crack propagation rate (FCPR) retardation increases with increasing stress ratio. In [7], reported the effect

of stress ratio on delayed zone/overload induced plastic zone decreasing under plane stress condition (PSS).

Over load assisted crack branching cannot be seen before and after under and overload monotonic plastic zone [4, 8].

In the presented study, over load induced effects are simulated. Effect of OLR on crack propagation and on delayed zone are reported. The study uses 2 models (1) Wheeler, and (2) crack annealing model. For the study, 304L-SS and 2024 Aluminum alloy are used.

2 Fatigue Crack Propagation Models

Fatigue life prediction models are inevitable for structural design. Fatigue life experiment is a costly and time consuming affair. Most of the designers rely on fatigue life prediction models. In case of interspersed single over load in constant amplitude loading, over load effect simulating models are broadly categorized in two categories- yield zone models, and crack closure models. Detailed discussion of various life prediction models was reported in [9].

3 Material and Methodology

In this study, effect of single overload on fatigue crack propagation rate is studied on 2024 aluminum alloy and 304L SS and simulated using virtual crack annealing model [10] and wheeler model [11]. The study is conducted on SEN and DCT geometry. Simulation are validated by using experimental data of [12, 13]. Model used for simulation are chosen from two category of over load induce retardation explanations, crack closure phenomena & yield zone model. Involved parameters are determined via standard procedures. Wheeler model is highly sensitive to wheeler exponent which is determined via optimization.

Crack closure based crack annealing model parameter γ is determined using experimental data.

4 Results and Discussion

In this comparative study, two different mechanical property materials steel and aluminum are used to see the horizon of the used models. In Table 1, comparative prediction matrix are presented. In terms of delay cycle prediction, wheeler and crack annealing prediction show good agreement with experimental data. In case of aluminum, prediction of crack annealing model shows better prediction in terms of cycle consumed but the fatigue crack propagation rate versus stress intensity factor

Table 1 Life prediction in case of single over load with OLR = 2.5 and 2

| Actual value (Number of Cycle) | Predicted value (number of cycle) | Percentage error (number of cycle) (%) | Model used and material |
|--------------------------------|-----------------------------------|--|--------------------------|
| 173,400 | 159,000 | 8.3 | Wheeler, AI-2024 |
| 591,941 | 590,800 | 0.19 | Wheeler, 304L-SS |
| 173,400 | 161,400 | 6.92 | Crack Annealing, AI-2024 |
| 591,941 | 589,020 | 0.49 | Crack Annealing, 304L-SS |

with experimental data shows less coherence. For 304L-SS fatigue life prediction via wheeler and crack annealing model is found in good coherence with experimental data.

Figures 1, 3, 5 and 7, shows the sudden fatigue crack propagation rate reduction and gradual recovery wheeler model prediction in such case is within limits. The sudden retardation is due to compressive residual stress.

Table 1 indicates the quantitative analysis of model in terms of total consumed or residual life. Wheeler and crack annealing model show discrepancy in fatigue crack propagation rate with experimental data.

Result based on yield zone model-wheeler has good agreement with both aluminum and austenitic stainless steel 304lss.

Figure 2 shows wheeler model prediction for alluminium-2024 which is in very good agreement with delayed number of cycle.

It is observed that at higher OLR crack propagation approximately arrests from 80,000 to 100,000 cycles and then crack propagation rate increases linearly from 100,000 to 220,000. The crack arrest might be due to crack blunting and again crack sharpen during 80,000 to 10,000 and then crack propagation starts again.

Figures 4, 6, and 8 shows a comparison of cyclically loaded geometries in case

Fig. 1 Fatigue crack propagation under SOL via Wheeler model

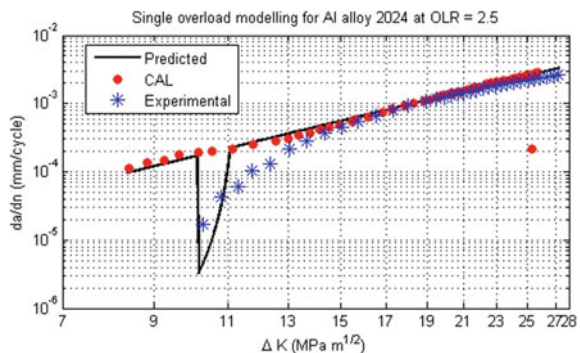


Fig. 2 Consumed life and crack length under various loading

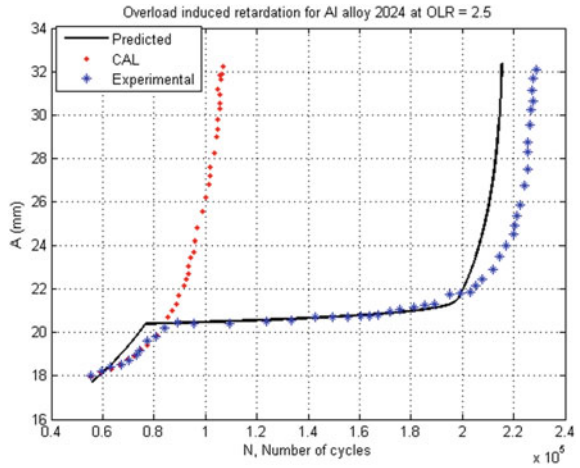


Fig. 3 Fatigue crack propagation rate variation due to SOL using Wheeler model

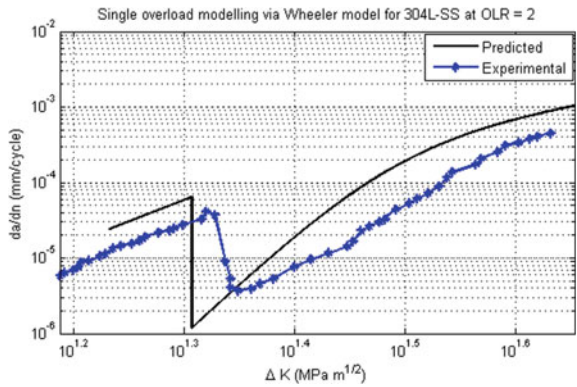
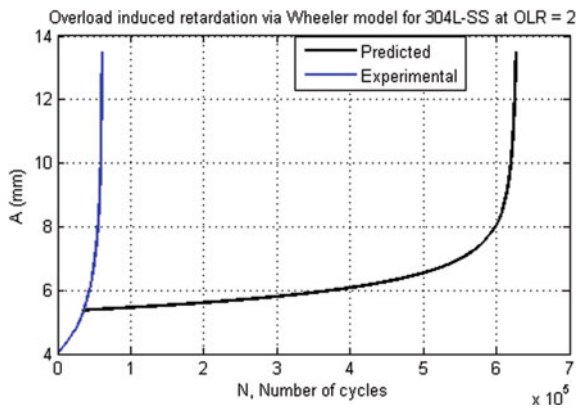


Fig. 4 Fatigue life enhancement due to SOL



of CAL and interspersed single overload.

Figures 4 shows significant life increment in case of single overload than CAL.

Both wheeler and crack annealing model are not capturing the single over load induced, fatigue crack propagation retardation trend exactly. Figures 1, 3, 5, 7 shows forecast is not capturing minimum fatigue crack propagation rate in overload retardation zone while in case of recovering (increasing fatigue crack propagation rate) wheeler and crack both in coherence with experimental data.

Fig. 5 Fatigue crack propagation rate prediction via crack annealing model

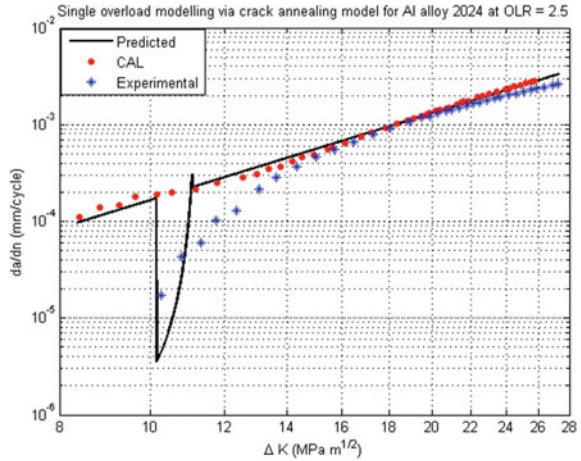


Fig. 6 Representation of SOL induce retardation via crack annealing model

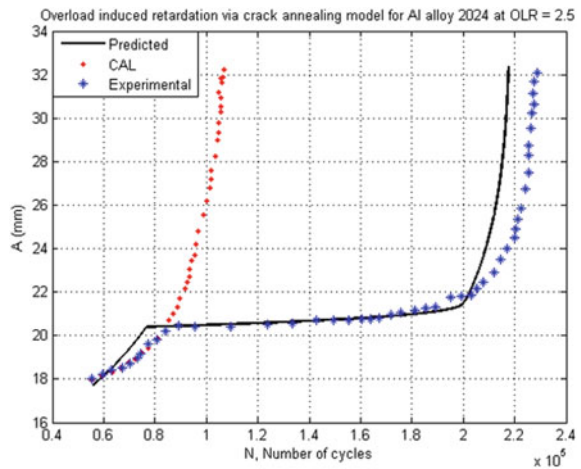


Fig. 7 Fatigue crack propagation rate versus stress intensity factor

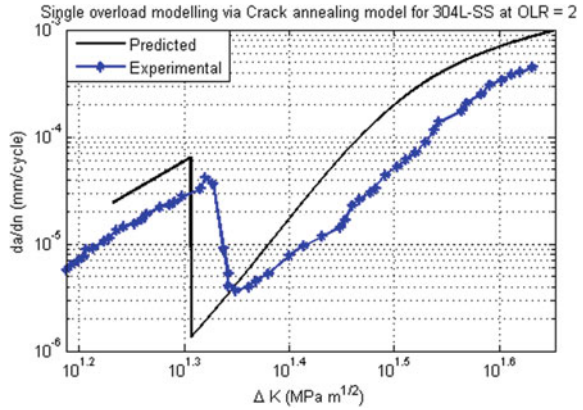
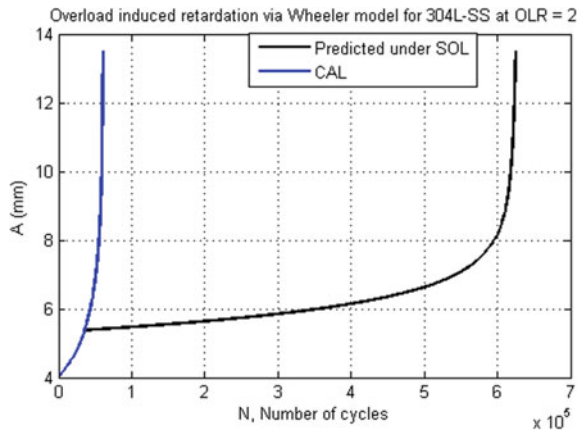


Fig. 8 Crack length versus Number of cycles



5 Conclusion

The analytical study shows that emanating fatigue crack under overload induced plastic zone is related to before overload crack growth rate. Interaction of before overload plastic zone and OL induce plastic zone are one of the major cause of OL induced fatigue crack propagation. OL induced retardation observed up to OL induced plastic zone. Prediction of wheeler and crack annealing model is in good conformity with experimental data for aluminum alloy 2024 and 304L-SS. The accuracy of both Wheeler and crack annealing model is found to be dependent on parameter optimization.

References

1. Paris P, Erdogan F (1963) A critical analysis of crack propagation laws. *J. Fluids Eng. Trans. ASME*. 85:528–533. <https://doi.org/10.1115/1.3656900>
2. Ward-Close CM, Blom AF, Ritchie RO (1989) Mechanisms associated with transient fatigue crack growth under variable-amplitude loading: An experimental and numerical study. *Eng Fract Mech* 32:613–638. [https://doi.org/10.1016/0013-7944\(89\)90195-1](https://doi.org/10.1016/0013-7944(89)90195-1)
3. Shin CS, Hsu SH (1993) On the mechanisms and behaviour of overload retardation in AISI 304 stainless steel. *Int J Fatigue* 15:181–192. [https://doi.org/10.1016/0142-1123\(93\)90175-P](https://doi.org/10.1016/0142-1123(93)90175-P)
4. Shuter DM, Geary W (1996) SOME ASPECTS OF FATIGUE CRACK GROWTH RETARDATION BEHAVIOUR FOLLOWING TENSILE OVERLOADS IN A STRUCTURAL STEEL. *Fatigue Fract Eng Mater Struct* 19:185–199. <https://doi.org/10.1111/j.1460-2695.1996.tb00958.x>
5. Damri D, Knott JF (1991) TRANSIENT RETARDATIONS IN FATIGUE CRACK GROWTH FOLLOWING A SINGLE PEAK OVERLOAD. *Fatigue Fract Eng Mater Struct* 14:709–719. <https://doi.org/10.1111/j.1460-2695.1991.tb00700.x>
6. Tsukuda H, Ogiyama H, Shiraiishi T (1996) TRANSIENT FATIGUE CRACK GROWTH BEHAVIOUR FOLLOWING SINGLE OVERLOADS AT HIGH STRESS RATIOS. *Fatigue Fract Eng Mater Struct* 19:879–891. <https://doi.org/10.1111/j.1460-2695.1996.tb01023.x>
7. Pereira MVS, Darwish FAI, Camarão AF, Motta SH (2007) On the prediction of fatigue crack retardation using Wheeler and Willenborg models. *Mater Res* 10:101–107. <https://doi.org/10.1590/S1516-14392007000200002>
8. Basic Questions in Fatigue: Volume I. ASTM International (1988). <https://doi.org/10.1520/stp924-eb>.
9. Kant, C., Harmain, G.A.: A Model Based Study of Fatigue Life Prediction for Multifarious Loadings. In: *Advances in Material Science*. pp. 296–327. Trans Tech Publications Ltd (2021). <https://doi.org/10.4028/www.scientific.net/KEM.882.296>.
10. Jiang, S., Zhang, W., Li, X., Sun, F.: An Analytical Model for Fatigue Crack Propagation Prediction with Overload Effect. *Math. Probl. Eng.* 2014, (2014). <https://doi.org/10.1155/2014/713678>.
11. Wheeler OE (1972) Spectrum loading and crack growth. *J. Fluids Eng. Trans. ASME*. 94:181–186. <https://doi.org/10.1115/1.3425362>
12. Mohanty, J.: Fatigue Life Prediction Under Constant Amplitude and Interspersed Mode-I and Mixed-Mode (I and II) Overload using An Exponential Model, <http://ethesis.nitrkl.ac.in/2802/>, (2009).
13. Kalnaus S, Fan F, Jiang Y, Vasudevan AK (2009) An experimental investigation of fatigue crack growth of stainless steel 304L. *Int J Fatigue* 31:840–849. <https://doi.org/10.1016/j.ijfatigue.2008.11.004>

Wear

Numerical Fretting© Wear Simulation of Deep Groove Ball Bearing Under Radial Variable Load



David Cubillas, Mireia Olave, Iñigo Llavori, Ibai Ulacia, Jon Larrañagsa, Aitor Zurutuza, and Arkaitz Lopez

Abstract Bearing has become one of the most widely used mechanical components over the world. Even this component has been extensively studied, there exist especial applications or untypical operating conditions that still must be studied. This work accomplished a numerical wear simulation based on a finite element model of a deep groove ball bearing under radial variable load. This analysis considers a reduced symmetry model and the implementation of the friction energy model as wear damage indicator. This allows to simulate the effect of different bearing parameters, such as, ball-raceway conformity factor and friction coefficient. Results allow to understand the effect of different bearing parameters and concludes how to reduce this fretting wear damage.

Keywords Fretting wear · Wear simulation · Bearing failure · Frictional energy

1 Introduction

Since Sven Wingquist invented the bearing in 1906, they have become in one of the most widely used mechanical components in machine design and manufacturing. Deep groove ball bearings support radial and axial loads in both directions, are easy to fit, require less maintenance than other bearing types, have a low friction, low noise and low vibration which enables high rotational speeds. These advantages have made this bearing type being the most widely used bearing type. Despite of the design is focused on rotational applications; this bearing can remain motionless

D. Cubillas (✉) · M. Olave

Ikerlan Technology Research Centre, Basque Research and Technology Alliance (BRTA), J.M. Arizmendiarrieta, 2, 20500 Arrasate/Mondragón, Spain
e-mail: dcubillas@ikerlan.es

I. Llavori · I. Ulacia · J. Larrañagsa

Dpto. de Mecánica Y Producción Industrial, Escuela Politécnica Superior de Mondragon Unibertsitatea, Mondragon, Spain

A. Zurutuza · A. Lopez

Laulagun Bearings, Harizti Industrialdea, 201-20212 Olaberria, Spain

© The Author(s), under exclusive license to Springer Nature Singapore Pte Ltd. 2022
M. Abdel Wahab (ed.), *Proceedings of the 9th International Conference on Fracture, Fatigue and Wear*, Lecture Notes in Mechanical Engineering,
https://doi.org/10.1007/978-981-16-8810-2_19

for large periods of time. An example of this operation condition is the transport of the machines, such as cars, where bearings are supporting the dynamic loads of the car weight. This condition can develop fretting damage at the contact between the ball and the bearing raceway. First mention of this phenomenon is attributed to Almen [1] in 1930 when cars, trucks or motorcycles bearings present vibration and noisy problems after being transport. The bearings were disassembled, and present equidistant marks in the raceway that coincided with the position of each ball of the bearing. These marks were commonly attributed to the well-known “brinelling” failure mode. This consists in the indentation of the balls on the track due to an overload in the bearing (plastic deformation). However, there was no evidence that any overload occurred during transport.

After Almen first contribution, multiple authors have studied the effect of this fretting damage; Godfrey [2] and Errichello [3] focused their efforts establishing the main differences between false brinelling, brinelling and fretting corrosion. Markus Grebe [4] studied standstill marks and established three different damage zones that were produced by different tribological agents. C. Barthou [5] and Grebe [6] test small oscillating movements in bearings under different operating parameters and lubricants. Varied parameters like amplitude oscillation angle, frequency, temperature, lubricant and applied load have been studied and its damaged effects correlated. Tongyan Yue, Wang and Magd Abdel Wahab [7] have studied the effect of loads on fretting wear and reviewed recent numerical methods on fretting wear simulation [8]. Fabian [9], Khosro [10, 11] have made an approach to damage problems with the finite element method (FEM) model wear using Archard or frictional energy as wear damage indicators. Stammer et al. [12] have considered the influence of tribolayers formation on oscillating applications and confirmed the influence of oscillating sequence on raceway wear damage.

Although small oscillations have been studied, the effect of the normal loading, such as, radial fretting remains unclear. Through this paper a numerical analysis of the radial fretting wear is performed as part of the continuation of the work accomplished on Ref. [13]. In addition, in this paper the effect of different parameters on the fretting wear such as coefficient of friction and conformity aspect ratio are studied.

This paper is organised in three sections. Firstly, a numerical model is presented for the contact analysis of a ball bearing and the raceway. Secondly the results are exposed for different conformity aspect ratio and friction coefficients, and finally, the main conclusions are summarized.

2 Methodology

Deep groove bearings are especially indicated for applications where the main loading are the radial forces. Xiaoli [14] studied how loads are transmitted and concluded an analytical expression that theoretically allow to calculate the load of any ball. Figure 1a shows ball bearing distribution under a radial load. As it can be observed load are expected to be distributed heterogeneously through all balls.

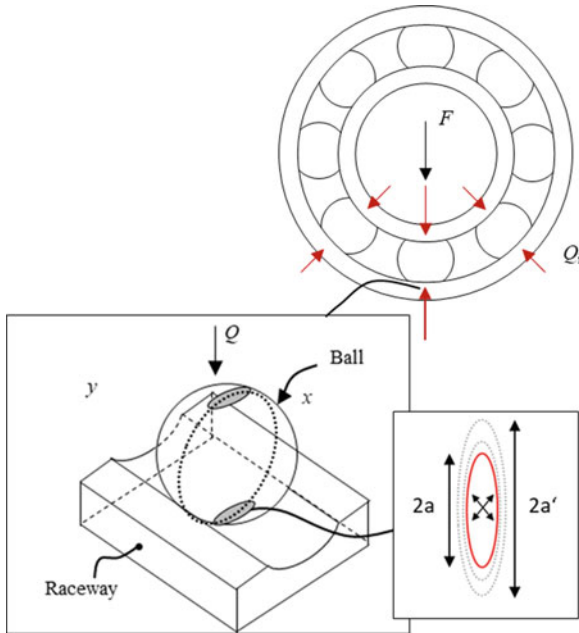


Fig. 1 Bearing ball load distribution and contact effects

This analysis is focused on the contact, for this reason only one ball is considered. The model simulates a 1/4 ball being pressed against a static ring, so no rolling is considered. Similar models can be found in [15] for roller bearings and wear prediction having a good correlation with laboratory tests. In this case, simplifications from the complete geometry were taken and it was assumed 3 symmetry planes, see Fig. 2. Special attention was paid to the contact with a symmetric behavior and augmented Lagrange formulation, second order hexahedron elements were placed in the entire model (628,501 nodes) and finer mesh was placed at contact with a maximum size of 0.05 mm. The contact detection is on nodal point—normal from contact surface (projection-based method) and an isotropic friction model based on Coulomb coefficient of friction.

The simulation was divided in 200 increments for 5 complete loading cycles, as per Fig. 3.

In addition, the effect of the coefficient of friction and the conformity ($c = r_p/d_b$, where r_p is the raceway radius; d_b is the ball bearing diameter) will be studied along this analysis. For this purpose, multiple combination of typical values of these parameters are simulated following Table 1.

There are two main approaches to modelling contact wear, the Reye hypothesis with the more recent Fouvry theory [17], and the Archard wear model [18]. In Reye's hypothesis, the volume of material removed is proportional to the work done by the friction forces. More recently, Fouvry has proposed a wear model based on this hypothesis (1).

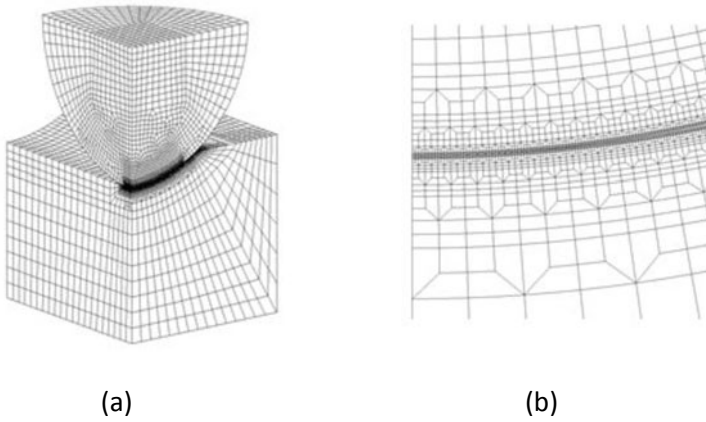
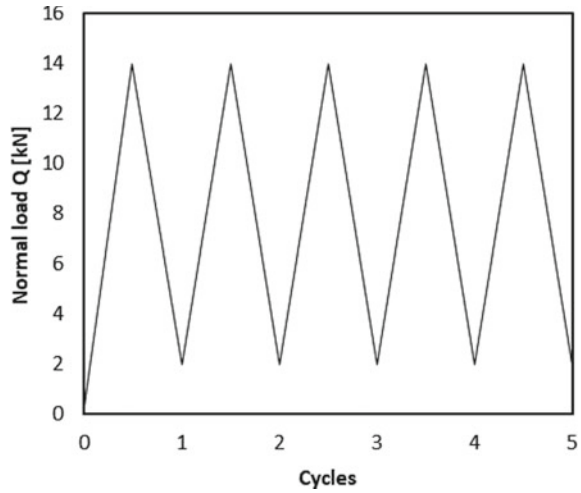


Fig. 2 Finite Element Model for contact analysis

Fig. 3 Simulation loading cycles input



$$E_f = \iint \vec{S}(x, y) \cdot \vec{T}(x, y) \cdot dx \cdot dy \tag{1}$$

where, S is the relative displacements on the contact; and T is the tangential stresses.

A similar expression can be reached for the density of friction energy:

$$\rho_f(x, y) = \vec{S}(x, y) \cdot \vec{T}(x, y) \tag{2}$$

where, T is the tangential stress at the point and S is the relative displacement at that point.

Table 1 Simulation parameters

| id | CoF | Conformity |
|----|------|------------|
| 1 | 0.02 | 0.54 |
| 2 | 0.04 | 0.54 |
| 3 | 0.06 | 0.54 |
| 4 | 0.08 | 0.54 |
| 5 | 0.1 | 0.54 |
| 6 | 0.12 | 0.54 |
| 7 | 0.08 | 0.52 |
| 8 | 0.08 | 0.53 |
| 9 | 0.08 | 0.54 |
| 10 | 0.08 | 0.55 |
| 11 | 0.08 | 0.56 |

Table 2 100Cr6 bearing mechanical properties

| Mechanical properties | | |
|-----------------------|-----------------|-------------|
| E | Elastic modulus | 210.0 [GPa] |
| G | Shear modulus | 80.0 [GPa] |
| V | Poisson's ratio | 0.3 |
| H | Hardness | 62.0 [HRC] |

Table 3 Bearing geometrical characterises

| Bearing dimensions | | |
|--------------------|--------------------|-------------|
| R_{pw} | Main raceway radio | 130.00 [mm] |
| R_b | Ball radio | 10.00 [mm] |

For analysis purpose deep groove bearing has been taken as case of study. The main bearing properties and parameters can be found in Tables 2 and 3.

3 Results and Discussion

Results shows a clear difference between first cycle wear rate and the following 4 cycles, see Fig. 1. First cycle presents a higher rate of wear with, an also, higher maximum density of friction energy value. After first cycle, wear become linear with the cycles. This result may indicate a transient effect on the tangential stresses that is conclude after one cycle. At this point is important to mention that the effect of the wear on the own wear is not considered and a linearity of wear and cycles can be expected. After the first cycle, the density of friction energy is concentrated in two different regions of the contact with an elliptical shape, however, following cycles will produce a wear damage at the same region but with a clear different shape, a

horseshoe shape. This effect seems to be related with the amplitude and range of the own cycle, and a further investigation is necessary to clarify this effect.

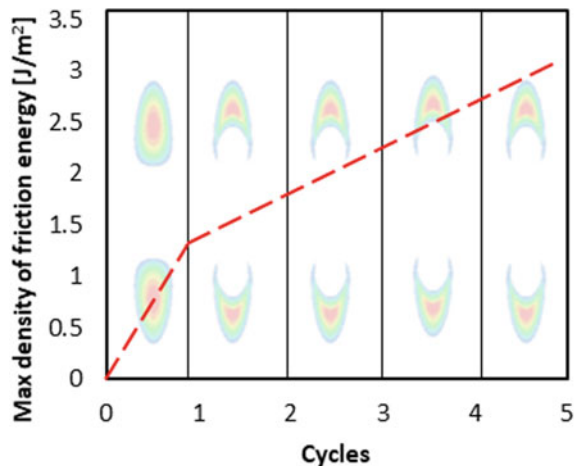
Figures 5 and 6 shows the effect of the friction coefficient on the wear damage for a 0.54 ball-bearing raceway conformity ratio. Figure 2a, shows the area of the damage for different coefficient of friction, and as can be observed the lowest coefficient of friction of the contact leads to the highest damage area. In terms of intensity, Fig. 5, shows that a maximum value of the wear damage is achieved for a friction coefficient close to 0.06 and indicate that a higher value of the coefficient of friction can help to reduces the damage.

Figure 6 shows the total friction energy dissipated along the completed damage area for different friction coefficient. As can be observed, friction energy dissipated grows with the friction coefficient until a maximum value is reached for coefficient of friction close to 0.04, from this point the friction energy dissipated decrease. Again, a higher value of the friction coefficient seems to aid to reduce the wear damage.

Figures 7 and 8, shows the effect of the conformity on the wear damage. Figure 4a, shows the total damage area for different bearing conformities and indicate a higher area is developed with lower values of conformity ratio. Same effect is observed in the maximum value of the density of friction energy, the lower friction coefficient leads to the highest intensity of the density of friction, that indicates the higher deep damage.

In Fig. 8, it can be observed the effect of the conformity on the total accumulated friction energy for a typical value of coefficient of friction 0.08. Results shows a clear dependency and a considerable impact that indicate that a lower bearing conformity led to a higher total dissipated friction energy. In consequence a higher total damage can be expected in bearings with high conformal contacts.

Fig. 4 Effect of cycles on the friction energy



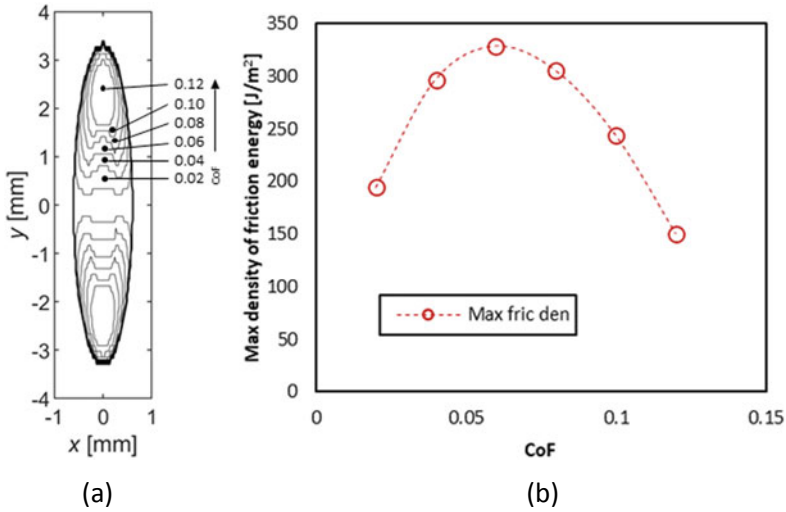
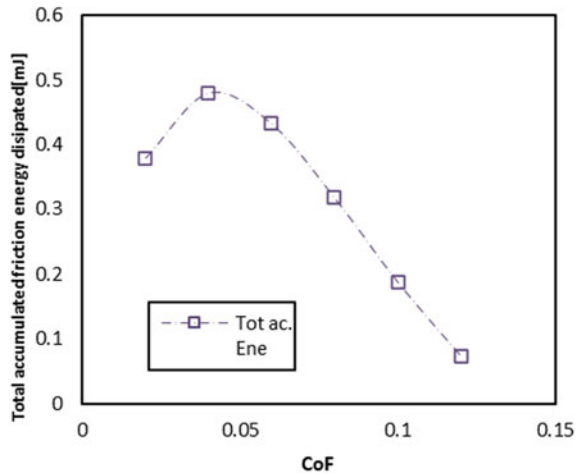


Fig. 5 Effect of friction coefficient on the friction energy

Fig. 6 Effect of coefficient of friction on the total accumulated friction energy



4 Conclusions and Future Work

The aim of this work was to study the effects on the wear of ball to raceway contact under pure normal loading cycles. To this end, a parametric finite element model was developed to carry out a numerical analysis and the following conclusions were drawn:

- Wear damages present a transient effect on the tangential stresses that is conclude after one cycle that become linear after first cycle.

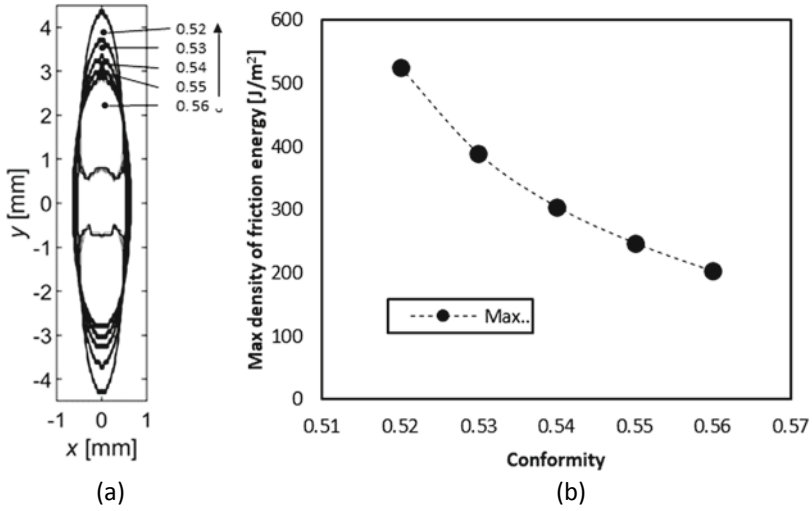
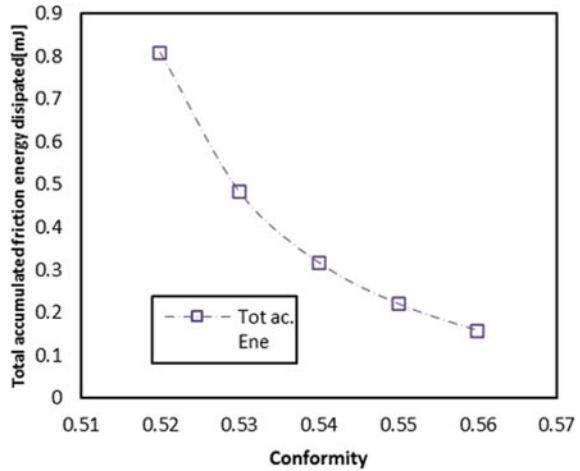


Fig. 7 Effect of the conformity ratio on the density of friction energy

Fig. 8 Effect of the conformity ratio on the total accumulated friction energy



- The lowest coefficient of friction of the contact leads to the highest damage area
- A maximum value of the wear damage is achieved for a friction coefficient close to 0.06 and indicate that a higher value of the coefficient of friction can help to reduces the damage.
- A maximum value is reached for coefficient of friction close to 0.04, and again, a higher value of the friction coefficient seems to aid to reduce the wear damage
- The total damage area developed is higher for lower values of conformity ratio.
- The lower friction coefficient leads to the highest intensity of the density of friction.

References

1. Almen JO (1937) Lubricants and false brinelling of band roller bearings. *Mech Eng* 59(6) 415–422
2. Godfrey D (1999) Iron oxides and rust (hydrated iron oxides) in tribology. *Tribol Lubric Technol* 55(2) 33
3. Errichello R (2004) Another perspective: False brinelling and fretting corrosion. *Lubric Eng* 60 34–36. Retrieved 2017-06-27
4. Grebe M, Feinle P, Hunsicker W (2008) Influence of various factors on the occurrence of service life marks (false-brinelling effect). *Tribol und Schmierungstechnik* 55(1):16–20
5. Barthou C, Vannes B, Girodin D, Pierantoni M, Sauger E (1998) Methodology of characterisation of the raceway/lubricant/ball contacts submitted to vibrations and degraded by false brinelling. *Tribol. Ser.* 34(2) 389–398. [https://doi.org/10.1016/S0167-8922\(98\)80095-3](https://doi.org/10.1016/S0167-8922(98)80095-3)
6. S. U. of T. Grebe, Markus (Institute of Production Technologies, Faculty of Materials Science and Technology) (2013) New investigations and approaches to explain standstill marks on roller bearings (false brinelling). Markus GREBE 1 1–10
7. Yue T, Abdel Wahab M (2017) Finite element analysis of fretting wear under variable coefficient of friction and different contact regimes. *Tribol Int* 107(November 2016) 274–282. <https://doi.org/10.1016/j.triboint.2016.11.044>
8. Yue T, Wahab MA (2019) A review on fretting wear mechanisms, models and numerical analyses. *Comput Mater Contin* 59(2):405–432. <https://doi.org/10.32604/cmc.2019.04253>
9. Schwack F, Bader N, Leckner J, Demaille C, Poll G (2020) A study of grease lubricants under wind turbine pitch bearing conditions. *Wear* 454–4s55: 203335. <https://doi.org/10.1016/j.wear.2020.203335>. ISSN 0043-1648
10. Fallahnezhad K, Oskouei RH, Badnava H, Taylor M (2017) An adaptive finite element simulation of fretting wear damage at the head-neck taper junction of total hip replacement: The role of taper angle mismatch. *J Mech Behav Biomed Mater* 75:58–67. <https://doi.org/10.1016/j.jmbbm.2017.07.003>
11. Fallahnezhad K, Oskouei RH, Taylor M (2018) Development of a fretting corrosion model for metallic interfaces using adaptive finite element analysis. *Finite Elem Anal Des* 148(April):38–47. <https://doi.org/10.1016/j.finel.2018.05.004>
12. Stammer M, Poll G, Reuter A, The influence of oscillation sequences on rolling bearing wear, pp 19–25
13. Cubillas D, Olave M, Llaviori I, Ulacia I, Larrañaga J, Numerical analysis of the wind turbine pitch bearing raceway tribo-contact due to cyclic loading under constant pitch angle, pp 1–14
14. Xiaoli R, Jia Z, Ge R (2017) Calculation of radial load distribution on ball and roller bearings with positive, negative and zero clearance. *Int J Mech Sci* 131–132:1–7. <https://doi.org/10.1016/j.jmeosci.2017.06.042>
15. Fallahnezhad K, Brinji O, Desai A, Meehan PA (2019) The influence of different types of loading on false brinelling. *Wear* 440–441(October) 203097. <https://doi.org/10.1016/j.wear.2019.203097>
16. Harris T, Rumbarger JH, Butterfield CP, Wind turbine design guideline DG03 : yaw and pitch rolling bearing life. Nrel (December) 63
17. Fouvry S, Liskiewicz T, Kapsa P, Hannel S, Sauger E (2003) An energy description of wear mechanisms and its applications to oscillating sliding contacts. *Wear* 255(1–6):287–298. [https://doi.org/10.1016/S0043-1648\(03\)00117-0](https://doi.org/10.1016/S0043-1648(03)00117-0)
18. Archard JF (1953) Contact and rubbing of flat surfaces. *J Appl Phys* 24(8):981–988. <https://doi.org/10.1063/1.1721448>

Contribution Self-lubrication Mechanism of New Antifriction Copper-Based Composites in the Vehicles' Heavy-Loaded Friction Units



Krzysztof Jamroziak  and Tetiana Roik 

Abstract The article studies the self-lubrication mechanism of new antifriction copper-based composites alloyed with Ni, Al, Si and Ti, with CaF₂ solid lubricant for operation in the vehicles' heavy loaded friction units. The developed manufacturing technology provided CaF₂ uniform distribution throughout the material's entire volume. The composite's structure ensured the functional properties high level. During friction process, CaF₂ solid lubricant is smeared on both contact surfaces and forms a protective antifriction film together with the chemical elements of the friction pair. It has been shown the CaF₂ solid lubricant plays a key role in the anti-scoring films formation. The composite's self-lubrication mechanism consists in the continual formation of a protective antifriction film. This is achieved by dispersing the CaF₂ solid lubricant particles and spreading it over the entire contact surfaces. The anti-seize film with calcium fluoride protects the friction unit from adhesion, minimizes wear and stabilizes its operation.

Keywords Antifriction composite · Solid lubricant · Friction film · Self-lubrication mechanism

1 Introduction

The development of new high-tech machines and mechanisms is impossible without the use of new high-quality materials that ensure high reliability and durability. This fully applies to antifriction materials operating in severe operating conditions while simultaneously exposed to high loads, speeds, aggressive environment, etc. Such

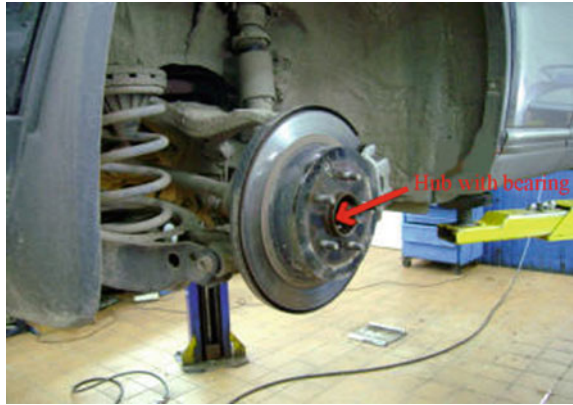
K. Jamroziak (✉)

Department of Mechanics, Materials and Biomedical Engineering, Wrocław University of Science and Technology, Smoluchowskiego 25, 50-370 Wrocław, Poland
e-mail: krzysztof.jamroziak@pwr.edu.pl

T. Roik

National Technical University of Ukraine Igor Sikorsky Kyiv Polytechnic Institute, 37 Peremogy ave, Kyiv 03057, Ukraine

Fig. 1 Place of a brass bearing installation in a heavily loaded friction unit of a vehicle chassis (shown by an arrow)



operating conditions are typical for friction units of metallurgical, thermal, power equipment, vehicles.

In particular, heavy loaded friction units of trucks and other vehicles are constantly exposed to dynamic loads of more than 3.0 MPa, vibrations and high speeds up to 10 m/s in working conditions with liquid lubrication. This causes the destruction of the liquid lubricant, leads to heating of the contact surfaces, in some cases above 450 °C, warping, destruction of parts and functional properties loss.

Traditionally, cast brass sliding bearings are used in such friction units (see Fig. 1). These are cast brass types CuZn36 and CuZn37 (BS EN 1652 – 98).

Unfortunately, the use of brass bearings is ineffective for friction units in vehicles under severe operating conditions. This is due to the fact that the liquid lubricant begins to burn under such loading conditions, burn spots are formed on the contact surfaces of the bearing bushing and the vehicle shaft.

Cases of an increase in the friction coefficient of a vehicle's brass bushing to 0.97 are described, depending on the loading conditions, when the material becomes frictional rather than antifrictional [1, 2]. A high friction coefficient and intense wear are the result of such processes on the friction pair's surfaces [2–4], which leads to the complete destruction of the friction unit. Therefore, the frictional behavior of friction unit parts depends to a large extent on the materials of the contact pair. In this regard, the use of composite self-lubricating bearings is very promising for heavily loaded vehicle units and has no alternative.

Many authors have obtained a number of positive results in the development of antifriction composites based on copper. These composites contain alloying elements Fe, Cr, Ti, Al, etc., which allowed to obtain materials with sufficient antifriction properties for high speeds and low loads [5, 6]. Copper composites often work in a presence of liquid oil [5]. Other composites contain solid lubricant graphite (or its allotropic modifications), Pb, Sn, Bi, or MoS₂ [5–7]. The solid lubricant in such composites allows operating in self-lubrication mode at high speeds, but at low loads. Increasing the solid lubricant content causes a sharp decrease of mechanical properties and structural strength loss.

High loads lead to the surfaces significant heating; the result is the instantaneous oxidation of solid lubricant, which penetrates into the depth of material, resulting in the composites destruction. The reason of such phenomena is not only the imperfection of production technologies, but also in the lack of targeted technological influence on the functional properties of materials, on which depends the starting stage of running, behavior at sudden stops and subsequent stable operation. Today these problems still remain unexplored.

In many cases existing production technologies are multi-stage for compaction of composites and its internal oxidation prevention [1, 8], often with the involvement of complex equipment. These technologies are difficult and, as a result, expensive. Other known copper composites are made in the form of two-layer materials for their strengthening, which gives satisfactory results at friction, but only under small loads [8–10]. However, the technology of their manufacture involves at least 6 main technological stages, from melting to consolidation and hardening, which is not economical and expensive. Now there are no studies of changes in the materials' tribological properties during manufacture, operation and capabilities of their forecasting. Unfortunately there are no research of the relationship between antifriction behavior and the mechanism of self-lubricating films formation, which are carriers of tribological properties at friction process without liquid oil.

The self-lubricating bearing bushings based on alloyed copper developed by the authors [4, 11–14] have shown positive results. This stabilized the operation of the friction unit in the vehicle chassis, increased its durability when operating without additional liquid lubrication, and simplified maintenance. The authors of [4, 11–14] investigated the effect of manufacturing technology on the physic mechanical and tribological properties of new composites based on alloyed copper containing solid lubricant calcium fluoride CaF_2 . It has been shown the antifriction films are formed on contact surfaces under operating conditions without liquid lubrication [4, 14]. These antifriction films contain chemical elements from both parts of the contact pair and are effective protection against intense wear.

However, such factors as the behavior of the CaF_2 solid lubricant under action of loads, its distribution in the material's copper metal matrix have not yet been studied. Also it remains unexplored the effect of CaF_2 on the self-lubrication mechanism of the copper-based composite under heavy loaded operating conditions in the vehicle chassis' friction unit. This was the motivation to carry out the comprehensive in-depth research on this issue.

The objective of this article is to research the self-lubrication mechanism of new antifriction copper-based composites in the vehicles' heavy loaded friction units, to study the distribution of CaF_2 solid lubricant in the material's metal matrix, to determine the features of CaF_2 behavior in friction process and its role in the friction unit stable operation.

2 Experimental Procedure

The study was focused on the new antifriction composite materials based on copper alloyed with Ni, Al, Si and Ti. Liquid lubricant is ineffective under extreme conditions (high speeds and loads) at the friction units of vehicle chassis. The reason is the ejection of liquid lubricant from the friction zone by centrifugal forces. As a result, the contact surfaces remain unprotected, which leads to high wear and subsequent seizure of surfaces in the friction units of the heavy vehicles chassis. Therefore, a solid lubricant calcium fluoride was added into the initial composition of the material. Numerous studies show the use of calcium fluoride CaF_2 (which is a thermally and chemically stable substance) stabilizes friction, especially under severe conditions [12, 13, 15–19].

Chemical composition of composites has been presented in Table 1 [11].

The choice of alloying elements (see Table 1) was based on the nature of their interaction with copper and with each other. Nickel and silicon strengthen the metal base of the material, forming an alloyed α -solid solution based on copper. This has a positive effect on the performance of the composite under high loads and speeds. The presence of silicon in the material reduces its inclination to seizing and transfer to the mating surface [11–13].

Nickel also enhances corrosion resistance and heat resistance due to the formation of Ni_3Al intermetallics. This is especially important when the composite works in the air.

The presence of aluminum in the material causes the formation of γ_2 -phase ($\text{Cu}_{32}\text{Al}_{19}$). The formed intermetallic γ_2 -phase has a high hardness, which provides the increased wear resistance of the material [11–13].

Titanium contributes to strengthen the composite's metal matrix by entering to the crystal lattice of an alloyed α -solid solution based on copper. In addition, Ti forms the intermetallics Ni_3Ti and NiTi_2 , which increases the composite material's resistance to abrasion and seizing during friction process [11–13].

Structure and distribution of CaF_2 solid lubricant in the metal matrix were determined using scanning electron microscopy (SEM). Tribotechnical tests were carried out using a VMT-1 friction test machine under the following conditions: $V = 8.0$ m/s; $P = 3.0 - 9.0$ MPa; steel 20Cr4 counterface [20] containing $C = 0.2\%$, $\text{Cr} = 4.0\%$ with hardness $\text{HRC} = 48-50$, and surface roughness parameter $R_a = 0.92 - 1.28$ μm after mechanical polishing with boron nitride abrasive wheels; GOI-54 liquid lubricant used for CuZn_{37} cast-brass samples, because an extremely gross wear and frictional seizure occurred, when dry friction tests. Such parameters of tribological tests (sliding speed and load) correspond to the operation of the bearing bushings under real conditions. The counterface of 20Cr4 steel corresponded to the material of

Table 1 Chemical composition of the composites based on copper (DN5A8CTKF7), wt.%

| Ni | Al | Si | Ti | CaF_2 | Cu |
|---------|----------|---------|---------|----------------|-------|
| 4.0–6.0 | 7.0–10.0 | 0.5–0.8 | 1.0–1.5 | 5.0–8.0 | Basis |

the real shafts in the high-loaded friction units of vehicles chassis. The counterface was heat-treated; this steel is usually used in commercial production of vehicle shafts making a thrust bushing—shaft friction pair in the vehicle’s chassis. The composites were manufactured using the technology developed by the authors [3, 4, 11–14]. It included powder mixing, cold pressing and hot pressing.

The powders mixing technology included three consecutive stages to avoid the segregation of powders: The 1st stage was mixing of powders Cu, Ni, Al, Si and Ti for 2.0 h; the 2nd stage was adding CaF_2 to powder mixture and “dry” mixing of all powders for 2.0 h; and the 3d stage was “wet” mixing of the mixture with the addition of glycerin for 1 h. This made it possible to obtain a homogeneous mixture [11, 12, 14].

The next step was compacting of mixture by two-stage pressing technology. It included the technology of cold pressing at room temperature at a specific pressure of 400–450 MPa and subsequent hot pressing at a specific pressure of 500 MPa at a temperature of 850–870 °C in a protective gas (H_2) to avoid oxidation. The relative density of the samples was 0.96–0.97 after hot pressing. The composite is almost completely compact. The homogeneous structure of the composite was formed after fabrication. The structure is a metallic copper matrix (α -solid solution) alloyed with Ni, Al, Cu and Ti, in which the solid lubricant particles of calcium fluoride are evenly distributed (see Fig. 2).

This distribution of calcium fluoride in the material is a consequence of the correct mixing technology (see Fig. 2) and has a very positive effect on the performance of the composite during friction and wear, especially under severe operating conditions. The formed structure of the composite provided the tribological properties high level. Tribological properties of the examined materials and cast brass have been presented in Table 2. As it can be seen from the Table 2, the developed composite demonstrates higher tribological properties compared to cast brass CuZn37 in the wide range of loads. Tribological tests have shown the antifriction properties of cast brass CuZn37 are extremely unsatisfactory at loads above 2.5 MPa.

Fig. 2 Microstructure of composite DN5A8CTKF7

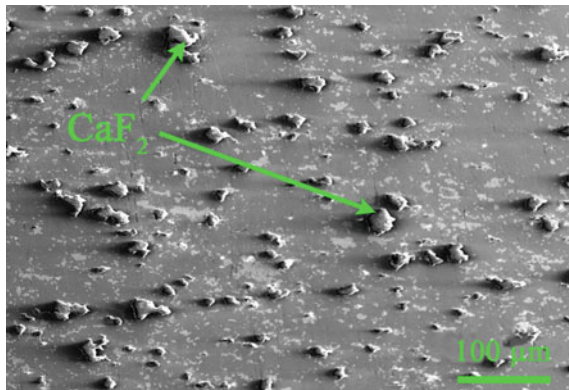


Table 2 Tribological properties of copper-based composite and cast brass

| Chemical Composition, wt. % | Friction coefficient (f) and wear rate (I), $\mu\text{m}/\text{km}$, at load, MPa | | | | | | Maximum allowable, P , MPa |
|-----------------------------|--|-----------|-----------|---|-----------|--------|------------------------------|
| | 3.0–4.0 | | 5.0–7.0 | | 7.0–9.0 | | |
| | f | I | f | I | f | I | |
| DN5A8CTKF7* [11] | 0.16–0.17 | 54–56 | 0.19–0.21 | 64–72 | 0.21–0.26 | 72–124 | 9.0–9.5 |
| CuZn37 brass (cast)** [21] | 0.42–0.57 | 1240–1430 | 0.92–0.94 | Extremely gross wear, liquid lubricant smokes and burns, frictional seizure | | | 2.0–2.5 |

Note $V = 8.0$ m/s: *No liquid lubricant friction, **Liquid lubricant friction

This is due to the fact that the liquid grease becomes inoperative during friction because of its ejection from the friction zone by centrifugal forces under high speed. Also liquid grease is squeezed out from contact area under action of load. In this case, the contact surface heats up, and the oil starts to burn. The consequence of this is a catastrophic increase in wear, which leads to the seizure and destruction of the friction pair.

At the same time, the new copper-based composite demonstrates high tribological characteristics and is capable of operating under high loads at the same time at high speeds. Such behavior of the copper-based composite is associated with the constant presence of CaF_2 solid lubricant on the contact surfaces during friction. The phenomenon of CaF_2 mass transfer takes place. Calcium fluoride is smeared on both contact surfaces and creates a protective antifriction film together with the friction pair's chemical elements.

The scheme of the mechanism of the CaF_2 lubricating action under severe operation conditions has been shown in Fig. 3. As we can see on Fig. 3 the solid lubricant particles is smeared on the friction surface under action of loads and speed. This ensures the formation of homogeneous antiscoring friction films. The friction surfaces have a smoothed microtopography, without zones of mechanical damage.

The formed antifriction film with calcium fluoride is a constantly working lubricant, as the third participant in the friction process [22]. This film completely covers the contact surfaces (see Fig. 4).

Such a lubricating film with calcium fluoride is constantly in dynamics during the operation of the friction pair (see Fig. 4). At the places of individual sections wear in the anti-seize film, new ones immediately appear. This demonstrates the equilibrium between wear and the formation of new film sections under the specified operating conditions ($V = 8$ m/s, P up to 9.5 MPa). This balance breaks when increasing loads over 9.5 MPa, and the lubricating film's new areas don't have time to form at the places of its wear. Film's sections wear out faster than a new one is formed. This can lead to adhesion of surfaces that are not protected. The CaF_2 solid lubricant plays a key role in the antiscoring films formation. Calcium fluoride has a number of positive properties that allow it to be used under severe friction conditions. Among others it is thermally and chemically stable lubricant [15–19]. It does not chemically react with

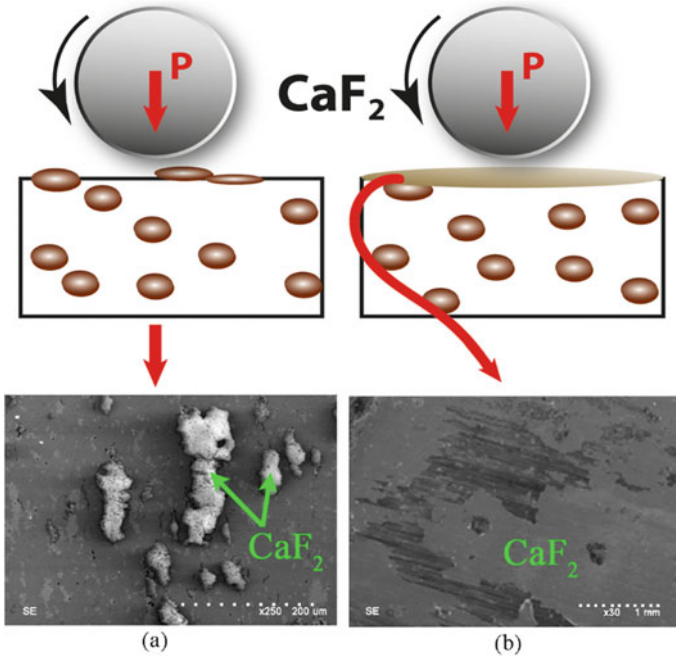


Fig. 3 The scheme of the mechanism of the CaF_2 lubricating action under severe operation conditions. **a** initial state of CaF_2 particles in the composite structure, **b** CaF_2 is smeared on the friction surface

Fig. 4 Antifriction film on the working surface

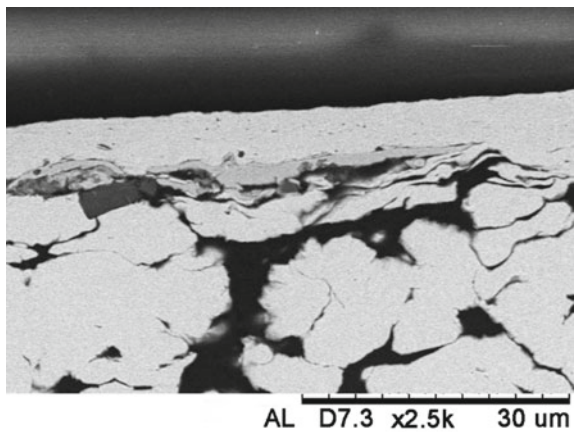
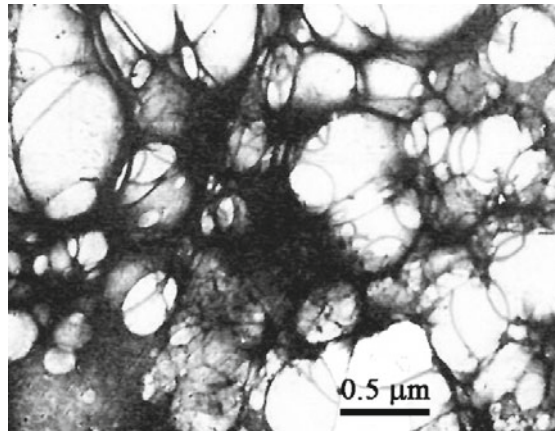


Fig. 5 Solid lubricant CaF_2 particles inside friction film



any of the composite elements and remains unchanged under high loading conditions. Under the influence of high specific loads a plastic deformation is localized only in such films (see Fig. 4) without penetrating into the volume of the material. In a case of cast bronze the deformation penetrates into the middle of the metal, which does not have a protective film. This leads to deformation of the cast bearing as a whole and functional properties loss (see Table 2).

One of our tasks was to study the behavior of CaF_2 inside film under high friction loads while studying the mechanism of the calcium fluoride lubricating action. For this, precision studies were performed using an electron microscope. The behavior of calcium fluoride was peculiar and special at the micro- and nanoscale precisely under severe friction conditions. The CaF_2 particles had an average diameter of 21.9 μm in the initial state before friction loading. The situation changed when the load began to act on the friction pair. White rounded CaF_2 inclusions were found in the structure of the friction film (see Fig. 5).

They have range in size from tenths to hundredths of a micrometer. The CaF_2 particles inside film are easily deformed and flattened to an oval shape without destruction under the action of shear stresses during friction process (see Fig. 5). This indicates the superplasticity of this layer. The high particles' strength with enough plasticity is a consequence of their ultradispersity.

It is known, starting from a particle size of less than 100 μm , and their further decrease leads to an increase in strength while maintaining plasticity [23–26]. Such extremely small sizes of CaF_2 particles determine their defectlessness and contribute to an increase in the cohesion and adhesion forces in the layer and between the layers inside the friction film. These data indicate the layer's fine structure and the maximum localization of surface deformation inside it during friction process. Balanced wear of areas in the anti-seize film with calcium fluoride and its new areas formation contributes to the friction stabilization and wear minimization. Thus a self-lubrication mode is realized at the indicated friction conditions.

Summarizing the studies of the self-lubrication mechanism of new antifriction copper composites, it can be argued the solid lubricant calcium fluoride plays an important role in stabilizing friction and minimizing wear under severe operating conditions. The tribological properties analysis made it possible to determine the rational operation modes for new copper-based composites: loads 3.0–9.0 MPa, sliding speed 8.0 m/s, in air. Bearing bushings made of investigated composites can be recommended for work in the friction units of the heavy loaded vehicles chassis as an alternative to cast brass bearings.

3 Conclusion

We have researched the self-lubrication mechanism and tribological properties of a new copper-based composite for operation at severe operation conditions which are typical for heavy loaded friction units in vehicles chassis. The study showed the Cu–Ni–Al–Si–Ti–CaF₂ composite has higher antifriction properties compared to cast brass CuZn37 in the wide range of loads. Such behavior of the composite is associated with the constant presence of CaF₂ solid lubricant on the contact surfaces during friction. The self-lubrication mechanism of the composite consists in the continuous formation of a protective antifriction film. This is achieved by dispersing the CaF₂ solid lubricant particles and spreading it over the entire contact surfaces. The phenomenon of CaF₂ mass transfer takes place.

Due to this, plastic deformation is localized in the surface film, keeping the material from deformation under the action of an external load. In addition, the anti-seize film with calcium fluoride protects the friction unit from adhesion, minimizes wear and stabilizes its operation. Undoubtedly, the formed anti-seize film contains all the chemical elements of the contact friction pair and atmospheric oxygen in addition to calcium fluoride. Our next research will focus on studying their effect on the anti-scoring film composition, the antifriction behavior of the composite, and its functional properties.

References

1. Prasan K, Samal P, Newkirk J (2015) Powder metallurgy. Volume 7 of the ASM handbook. ASM International, New York
2. Savitsky VY, Khvatov GA, Semenov AA, Dolyagin AV, Demeshova TS (2011) Investigation of the boundaries of the area of possible application of bushings made of polymer composite materials in heavily loaded friction units. In: Proceedings of the international symposium reliability and quality. Penza State University, Peneza, pp 1–13
3. Roik TA, Gavrysh OA, Vitsiuk II, Khmiliarchuk OI (2018) New copper-based composites for heavy-loaded friction units. Powder Metall Met Ceram 56:516–522. <https://doi.org/10.1007/s11106-018-9924-x>

4. Roik T, Gavrysh O, Vitsiuk I, Khmiliarchuk O (2018) Boundary conditions analysis of the possible use bushings made from copper composite materials for towing vehicle's chassis. *Scientific Journal of the Military University of Land Forces* 187(1):140–149
5. Guangrong H, Xinchuang T (2016) Copper-based alloy sliding-bearing material and preparation method thereof. Patent CN103602849A, China
6. Liu Q, Castillo-Rodríguez M, Galisteo AJ, Guzmán de Villoria R, Torralba JM (2019) Wear behavior of copper-graphite composites processed by field-assisted hot pressing. *J Compo Sci* 3(1):29. <https://doi.org/10.3390/jcs3010029>
7. Hhussein M, Jameel WW, Fadhil N (2018) Fabrication of copper-graphite MMCs using powder metallurgy technique. *J Eng* 24(10):49–59. <https://doi.org/10.31026/j.eng.2018.10.04>
8. Dyachkova LN, Fel'dshtein EE, Letsko AI, Kelek P, Kelek T (2017) Tribotechnical properties of sintered bronze strengthened by aluminate of Ti–46Al–8Cr. *J Friction Wear* 38(2):98–103. <https://doi.org/10.3103/S1068366617020088>
9. Lariionova T (2015) Copper-based Composite Materials Reinforced with Carbon Nanostructures. *Mater Sci* 21(3):364–368. <https://doi.org/10.5755/j01.ms.21.3.7348>
10. Dyachkova LN, Volchek, AY, Voronetskaya LY (2009) Investigation of the process of obtaining two-layer antifriction materials for heavily loaded friction units of axial piston pumps. In: *Powder metallurgy. Republic of Interdepartmental. Collection of scientific. Works, Belaruskaya Navuka, Minsk*, pp 128–132
11. Roik TA, Gavrysh OA, Vitsiuk II (2019) Patent UA135076 IPC, Antifriction composite material based on copper
12. Roik T, Jamroziak K, Lesiuk G, Gavrish O, Vitsiuk J (2020) Copper based anti-friction composite material. Patent PL237229, Poland
13. Roik T, Gavrysh O, Vitsiuk I, Khmiliarchuk O (2018) New copper-based composites for heavy-loaded friction. *Powder Metall Met Ceram* 56:516–522. <https://doi.org/10.1007/s11106-018-9924-x>
14. Jamroziak K, Roik T, Gavrish O, Vitsiuk I, Lesiuk G, Correia JAF, De Jesus AMP (2018) Improved manufacturing performance of a new antifriction composite parts based on copper. *Eng Fail Anal* 91:225–233. <https://doi.org/10.1016/j.engfailanal.2018.04.034>
15. Kurzawa A, Roik T, Gavrish O, Vitsiuk I, Bocian M, Pyka D, Zajac P, Jamroziak K (2020) Friction mechanism features of the nickel-based composite antifriction materials at high temperatures. *Coatings* 10(5):454. <https://doi.org/10.3390/coatings10050454>
16. Jamroziak K, Roik T (2019) Structure and properties of the new antifriction composite materials for high-temperature friction units. In: Abdel WM (eds) *Proceedings of the 7th international conference on fracture fatigue and wear*. Springer, Singapore, pp 628–637. https://doi.org/10.1007/978-981-13-0411-8_57
17. Shevchuk YF, Roik TA, Varchenko VT (2007) Antifriction composite materials for friction joints of centrifugal equipment. *Powder Metall Met Ceram* 46:404–407. <https://doi.org/10.1007/s11106-007-0063-z>
18. Jamroziak K, Roik T (2019) New antifriction composite materials based on tool steel grinding waste. *WIT Trans Eng Sci* 124:151–159
19. Jianxin D, Tongkun C (2007) Self-lubricating mechanisms via the in situ formed tribofilm of sintered ceramics with CaF₂ additions when sliding against hardened steel. *Int J Refract Metal Hard Mater* 25:189–197
20. ISO 683–17 (2014) Heat-treated steels, alloy steels and free-cutting steels—Part 17: ball and roller bearing steels. International Organization for Standardization ISO, Geneva
21. EN 1652 (1997) Copper and copper alloys. Plate, sheet, strip and circles for general purposes. European Committee for Standardization, Brussels
22. Roik TA, Gavrish AP, Kirichok PA, Vitsiuk II (2015) Effect of secondary structures on the functional properties of high-speed sintered bearings for printing machines. *Powder Metall Met Ceram* 54:119–127. <https://doi.org/10.1007/s11106-015-9688-5>
23. Ditenberg IA, Smirnov IV, Grinyayev KV, Tyumentsev AN (2020) Influence of oxygen concentration on the formation features and thermal stability of the V–Cr–W–Zr alloy microstructure under combined treatment conditions. *Mater Charact* 168 110517. <https://doi.org/10.1016/j.matchar.2020.110517>

24. Zhou Y, Wang F, Jin X, Yang J, Du K, Feng T, Lei J (2020) Rapid preparation of ultra-fine and well-dispersed SnO₂ nanoparticles via a double hydrolysis reaction for lithium storage. *Nanoscale* 12:15697–15705. <https://doi.org/10.1039/d0nr02219e>
25. Chammingkwan P, Bando Y, Terano M, Taniike T (2018) Nano-dispersed ziegler-natta catalysts for 1 μm-sized ultra-high molecular weight polyethylene particles. *Front Chem* 6:524. <https://doi.org/10.3389/fchem.2018.00524>
26. Mukhamatdinov I, Khaidarova AR, Zaripova RD, Mukhamatdinova RE, Sitnov SA, Vakhin AV (2020) The composition and structure of ultra-dispersed mixed oxide (II, III) particles and their influence on in-situ conversion of heavy oil. *Catal* 10(1):114. <https://doi.org/10.3390/catal10010114>

Wear Behavior of Bovine and Porcine Bone Versus Biocompatible Synthetic Materials, Case of Knee Prosthesis



M. Castillo Sánchez, D. Zarate Lara, M. Velázquez Vázquez,
G. Rodríguez Castro, and L. H. Hernández Gómez

Abstract The objective of this research work is to observe and analyze the wear behavior of the tribological pairs of bovine and porcine bone in contact with ultra-high molecular weight polyethylene and Teflon, biomaterials used in the manufacture of knee prostheses. The wear tests were carried out using a bolt-on-disc machine, which is a dry condition. They were performed for two load conditions, considering a healthy person and an overweight person. The friction coefficients were determined, optical and SEM microscopy was used to observe the footprint and type of wear present in the tested materials. The bovine bone against ultra-high molecular weight polyethylene wear couple presented the highest coefficient of friction, and the wear mechanisms observed were severe abrasion, detachment of particles, adhesion and fracture.

Keywords Friction coefficients · Wear behavior · Tribological pairs · Biomaterials

1 Introduction

1.1 Osteoarthritis of the Knee

Osteoarthritis or osteoarthritis of the knee consists of the wear and subsequent degeneration of the cartilage in the knee joint. This results in pain and inflammation, which prevents free movement in the joints. It is considered a very common pathology in traumatology and is one of the disorders that reduce the quality of life of people linked to greater longevity. The patient presents pain and mobility problems and thus loses quality of life. The replacement of the joint by a prosthesis is then necessary [1].

M. Castillo Sánchez (✉) · D. Zarate Lara · M. Velázquez Vázquez · G. Rodríguez Castro ·
L. H. Hernández Gómez

National Polytechnic Institute, ESIME-Zacatenco, Unidad Profesional “Adolfo López Mateos”,
Colonia Lindavista. Gustavo A. Madero, Edificio 1, 1er Piso, 07738 Cd. De México, México

1.2 Knee Joint Implant

It consists of a surgery that replaces the natural knee joint with an artificial joint, known as a prosthesis or knee prosthesis. It is generally recommended in people older than 60 years [2]. Total, knee replacement is one of the greatest engineering challenges in biomechanics, starting from a materials science point of view. The selection of materials for knee replacement has many points to discuss. The mechanical properties such as hardness, ductility and elasticity, it is worth mentioning that also tribological characteristics such as low friction, low wear, resistance to corrosion and biocompatibility. These are some of the aspects that must be taken into account [3]. There are many published works on the characterization of materials and tribological pairs with suggested materials for hip and knee prostheses, using ultra high molecular weight polyethylene (UHMWPE) against cobalt chromium alloy [4], using lubricants such as bovine serum [5], tests lasting millions of cycles [6], as well as, polyethylene against stainless steel in pin on disc tests [7]. The researches consulted refer that using a pin-on-disk (POD) configuration is viable, economical and efficient, since it determines the behavior of the prosthesis materials. However, in terms of their clinical relevance, they are limited in some respects.

1.3 Compatibility—Biomaterials

The term biomaterial refers to those materials that are capable of interacting with biological systems, and that their function is to increase, replace or treat some organ or tissue or some function in the body. These materials will work interfacially with biological tissue and it is intended that they benefit and are not harmful, that is, they are viable. Currently, more than fifty million people have a prosthesis, so it is necessary to ensure that in the short and long term they do not generate rejection processes [1, 8]. One of the great problems that occurs in the implantation of hip and knee prostheses is failure due to wear, fracture and loosening of the same and the health problems that they entail [9].

1.3.1 Ultra High Molecular Weight Polyethylene (UHMWPE)

A widely used material in joint prostheses is ultra-high molecular weight polyethylene (UHMWPE). For many years, it has been used as an interposition material in total hip and knee prostheses [10].

1.3.2 PTFE (Teflon)

PTFE was one of the first materials used in hip replacement, it has great thermal stability. It is very stable in chemical environments, and inert in contact with biological tissue of the human body. The disadvantage it presents is a high wear rate with a detachment of large particles that cause a very intense reaction of the body towards them [11, 12].

1.3.3 316L Stainless Steel

316L stainless steel is commonly used in surgical procedures, to replace biological tissue, and to stabilize biological structures. Such is the case with bone to help it in its healing process. This steel is very convenient in surgical practices because it is highly resistant to corrosion in direct contact with biological fluid [13, 14].

1.3.4 Hydroxyapatite

Hydroxyapatite is a compound that is naturally found in bone, comprises 70% of the weight and provides rigidity and hardness to it. It is synthetically obtained from the reaction between ammonium phosphate and calcium nitrate, maintaining the ability to chemically bind to bone tissue, preserving its osteoconductive properties [9].

1.3.5 Other Biocompatible Materials

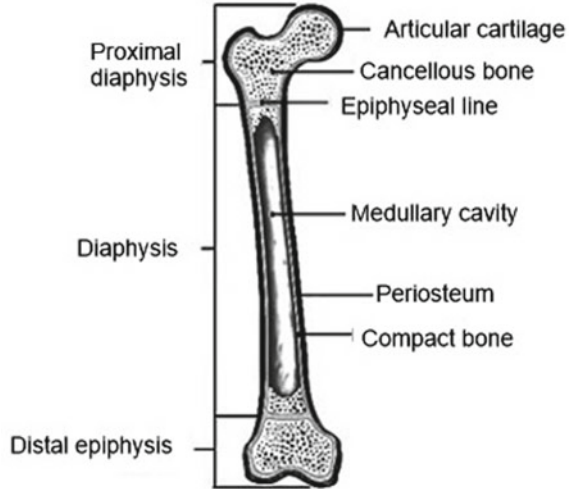
Other materials have been developed to replace bone, alloys based on Ti-Co-Ni and Fr-Cr, Co-Cr, which have proven to be biocompatible Ni-Ti alloys, for use in trauma and rehabilitation. Every day new knowledge is generated about materials that can be used in bioimplants; a first condition that must be fulfilled is the tolerance towards them of the human body, that they do not cause any adverse effect, such as allergy, toxicity or inflammation [8].

1.4 Generalities of Bones

1.4.1 Bone Structure

The skeleton is the total and organized set of bony pieces (bones) that provide its structure to the human body, support the body and protect some organs. The adult human body consists of approximately 206 bones, while newborns have approximately 300. There are two types of bone: trabecular and cortical. These are clearly represented

Fig. 1 Structure of the long bone [16]



in a bone such as the femur. The cortical bone forms the wall of the diaphysis and the trabecular bone is at both ends of the bone that becomes the epiphysis.

The latter is the epiphysis is an articular surface covered by cartilage, in turn covered with the synovial membrane and the rest of the bone is covered by the periosteum on the outside and on its inner surface by the endosteum. Inside is the medullary cavity. The cortical bone is compact and constitutes the diaphysis, which is the elongated part of the bones between the epiphyses; it is dense and has low microporosity. The trabecular bone is spongy and constitutes the epiphysis found at the ends of the long bone, it is less dense and it is constituted by a high microporosity. Bone is a material considered anisotropic and viscoelastic, see Fig. 1, [15].

1.4.2 Mechanical Behavior of Bones

Bones mechanically fulfill three functions:

- Give Support: these form the skeleton or also called the framework of the human body.
- Protection: they form boxes and walls to protect the viscera and organs that enable the body to function.
- Mechanical levers responsible for the movement of the bone system.

The bones are built to combine strength, low weight, and stiffness. They comply with three mechanical properties that are rigidity, toughness and resistance, they can also support compression and traction forces, sustain dynamic and static loads equivalent to forces twice their weight [17].

1.4.3 Similarities Between the Bone Structure of the Human, Porcine and Bovine Body

The bone structure of the human body, the bovine and the porcine have some points in common, from the anatomical point of view, they share a lot of similarity in the composition of their bones and others. They have been used to heal in some cases such as heart surgery (aortic valve) and liver production (anticoagulant). The porcine is a very good candidate for organ transplants. Both have the similarity in their bones thanks to hydroxyapatite and collagen. A way has been found to obtain from the bones of these animals the biohydroxyapatite that is expected to be compatible with the human body [18, 19].

1.5 Wear

Wear can be defined as the loss of surface material from two or more bodies, which are in repetitive motion under the action of a force. The contact between the surfaces happens through the surface structure of both materials and therefore the real contact area is much smaller than the apparent area [20]. Dry wear requires that a normal load be present, a relative sliding speed, mechanical properties and temperature influence.

1.5.1 Adhesive Wear

This type of wear occurs when two materials slide against each other under load in relative motion. It occurs when the surface of a body comes into contact with the rough edges of the opposite surface. These roughnesses are deformed by the action of interatomic forces, some of which come together. The base material tends to flow if the bonding conditions are strong enough, providing hardening. Wear occurs when the movement of the interfaces begins, presenting damage to one or both parts, with different wear rates. In some cases, there is no loss of material, but there is surface damage. This damage is commonly called “galling”, understood as severe galling [21].

In the sliding of the surfaces, either a plastic flow or a fracture in the materials can occur. The rate of wear generated by the process will depend on the specific properties of each of the components, and will depend on some characteristics such as shape, contact between bodies, temperature, chemical reactivity and environmental conditions, among other things [22–24].

1.5.2 Abrasive Wear

This type of wear is caused by the product of hard particles or protrusions, which hit or are forced to move along a solid surface causing damage and progressive loss

of material. It is also generated in hard areas that show relative movement in the worn area. Damage presents as chipping, scratching, cutting, or fatigue cracking. The properties of the material, the type of movement and the load have a marked influence during the removal of material. It is important to mention that this type of wear can occur in a dry state or in the presence of a fluid [25–27].

1.5.3 Three-Body Abrasive Wear

This type of wear occurs when very small abrasive particles are found between the sliding surfaces. It includes considerably the size of the particles, the resistance to fracture, the roughness of the surfaces, the hardness and the type of movement present. The case may present that the type of wear is of two bodies due to the encrustation of the hard particles in the soft materials. When the particles are not very hard, or are less hard than the sliding surfaces, they only temporarily embed themselves in the surfaces, however, when the sliding movement begins, they are released and the wear rate is relatively lower [28, 29].

The aim of this research work is to characterize the wear of mechanical pairs such as high molecular weight polyethylene, Teflon against porcine and bovine bone, simulating knee movement, to get an idea of their behavior as they are applied in knee replacement frequently.

2 Methods

2.1 Mechanical Properties of Porcine and Bovine Bone

The tests were carried out using a testing machine of the CSM Instrument NHT® brand (Nanoindentation Hardness Tester) standardized according to the ASTM E2546 standard, the microhardness of both bones was determined, as well as their modulus of elasticity.

2.2 Microscopy

The surface damage caused by the abrasion test was observed using a Versamet® metallographic light microscope, model Union 647.

2.3 Abrasion Test

The experimental Pin-on-Disk (POD) test. It is carried out to observe the wear behavior of a friction couple. To carry out the experiments, the procedure indicated in the ASTM G99-03, ASTM G99-04, ASTM G99-95 standards was followed.

The pin-on-disc machine used to carry out the experiments is a CSEM® Instrument, Pin-on-disc wear tester machine.

The tests carried out were carried out using pairs of high molecular weight polyethylene test specimen versus Porcine bone bolt, high molecular weight polyethylene vs. Bovine bone bolt, Teflon versus Porcine bone bolt and Teflon vs. Bovine bone bolt, 3 experiments were performed for each trial.

2.3.1 Preparation of Specimens

Ultra high molecular weight polyethylene (UHMWPE) and polytetrafluoroethylene discs, better known as Teflon, were manufactured according to the standard. These materials were considered, as they are one of the most used for prosthetics. Said specimens were manufactured in the shape of a disk with the following measurements, diameter 2.54 cm, thickness 0.60 cm.

The pins are made of animal, porcine and bovine bone; both were taken from the knee (femur). The porcine bones that were selected were of the Landrace breed that are slaughtered approximately between 6 and 7 months of age with a weight of approximately 100 kg, while the bones of the selected bovine were of the Angus breed that are approximately slaughtered between 2 and 3 years old weighing approximately 450 kg to 500 kg. All the pins of both types of animals were made in a spherical shape with a diameter of 0.50 cm.

2.3.2 Test Parameters

In this type of test, wear is determined as a function of load and sliding distance. The case of an average person in Mexico is considered, with a height of 1.65 m. The physical conditions considered are two, a person of normal weight equal to 65 kg and a person with an overweight of 100 kg, since in these examples their BMI is measured. A BMI (Body Mass Index) equal to or greater than 25 determines overweight and 30 is called obesity. Likewise, a constant speed is taken into account when walking in both cases. The test is carried out for 2,160 cycles, which would be a 100-m track since it is considered one of the sports where knee injuries occur most frequently.

This simulates wear and tear on the prosthesis with two types of people (overweight and healthy weight). Table 1, summarizes the parameters used for all wear

Table 1 Test conditions for overweight and healthy weight people

| | Healthy weight | Overweight |
|------------------|---------------------|---------------------|
| Test temperature | 23° C to 24° C | 23° C to 24° C |
| Test time | 17 min | 17 min |
| Cycles | 2160 | 2160 |
| Sliding speed | 0.10 m/s | 0.10 m/s |
| Load | 5 N | 10 N |
| Type of contact | Sphere versus plane | Sphere versus plane |
| Pin radius | 2.5 mm | 2.5 mm |
| Conditions | Dry | Dry |

tests [5, 30]. This work aims to qualitatively establish the wear rate under the established conditions. The conditions under which the wear tests were carried out are indicated in Table 1.

3 Results and Discussion

3.1 Hardness and Elastic Modulus

The values obtained from the experiments, microhardness and the modulus of elasticity obtained from various test pieces are shown (Table 2). As can be seen in Table 2, there is a great variation in the hardness values, which shows that it is not a homogeneous material, although we know in advance that bone is an anisotropic and viscoelastic material. Likewise, the values obtained for the modulus of elasticity also

Table 2 Hardness and elastic modulus Pork and Bovine bone

| No. Test | Hardness (MPa) | | Elastic Modulus (GPa) | |
|--------------------|----------------|--------|-----------------------|--------|
| | Pork | Bovine | Pork | Bovine |
| 1 | 496.62 | 246.90 | 11.14 | 5.79 |
| 2 | 496.67 | 214.63 | 11.24 | 5.50 |
| 3 | 532.52 | 215.90 | 11.41 | 6.01 |
| 4 | 445.19 | 379.24 | 10.44 | 9.90 |
| 5 | 566.04 | 329.43 | 12.02 | 8.91 |
| 6 | 803.78 | 344.53 | 14.46 | 8.30 |
| 7 | 451.37 | 360.11 | 10.71 | 8.84 |
| 8 | 469.45 | 189.18 | 11.15 | 6.36 |
| Media | 530.03 | 284.99 | 11.53 | 7.45 |
| Standard deviation | 109.53 | 75.97 | 1.18 | 1.71 |

show a great variation. We also know that these mechanical properties have a great influence on the behavior of bone subjected to wear conditions, which are aggravated when combined with a dry condition.

3.2 Microscopic Analysis

The wear mechanisms present in general for the four cases considered, that is, bovine and porcine bone, with a load of 5 (Figs. 2 and 3) and 10 N (Figs. 4 and 5) are abrasion, detachment of material, permanence of debris on the surfaces. The grooves produced by wear are similar in all cases, the debris presents with irregular morphology since

Fig. 2 Material detachment is observed on Teflon and polyethylene surface disc, load 5 N

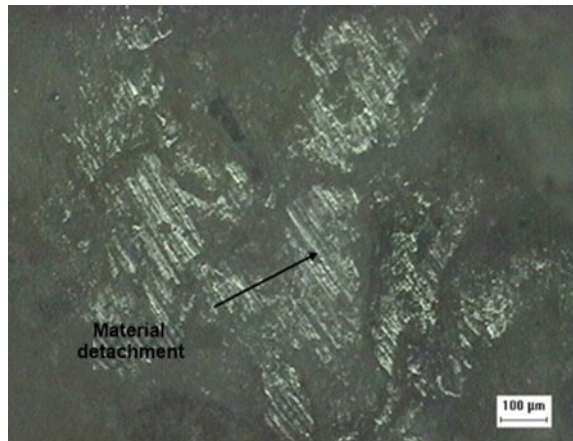


Fig. 3 The wear observed on bovine and porcine pin is abrasion, load 5 N

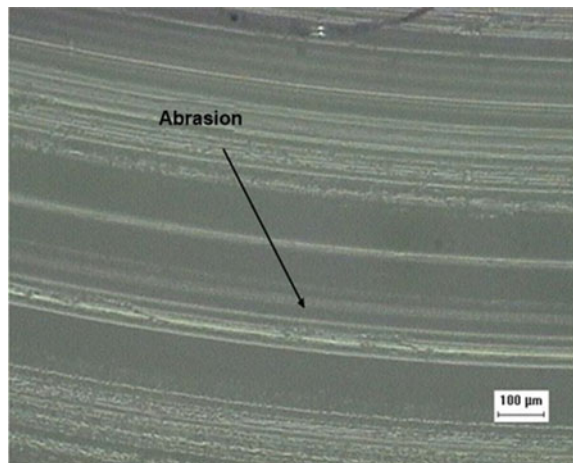


Fig. 4 Material detachment is observed on Teflon and polyethylene surface disc, load 10 N

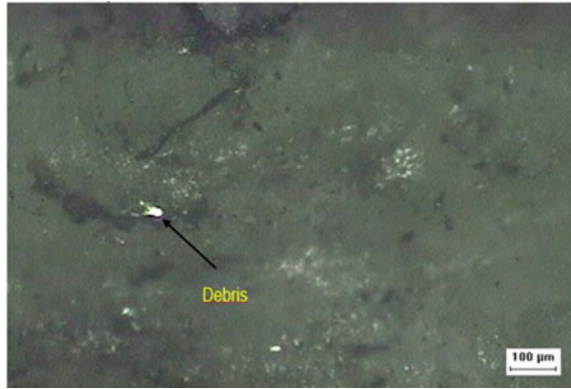
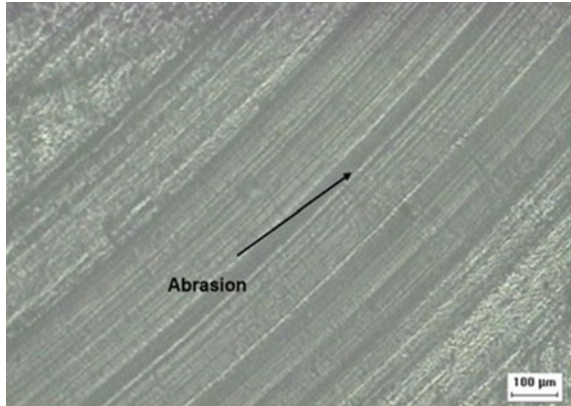


Fig. 5 The wear observed on bovine and porcine pin is abrasion, load 10 N



they are particles torn off and transferred to the surface of the disc in a process of adhesive wear. In some cases, the most severe damage is observed in Teflon surface, the least damage was presented in the bovine bone vs polyethylene pair.

3.3 Abrasion Test

Determination of the Friction Coefficients

The coefficient of friction was determined first for a load of 5 N in the tribological pairs UHMWPE and Teflon vs Bone, the coefficients obtained are shown in Figs. 6 and 7.

In the analysis of the friction coefficient with a load of 5 N, we find that for the polyethylene/porcine bone pair the value varies from 0.16 to 0.19, for the polyethylene/bovine bone pair the interval is between 0.16 and 0.21. The Teflon/bone pair

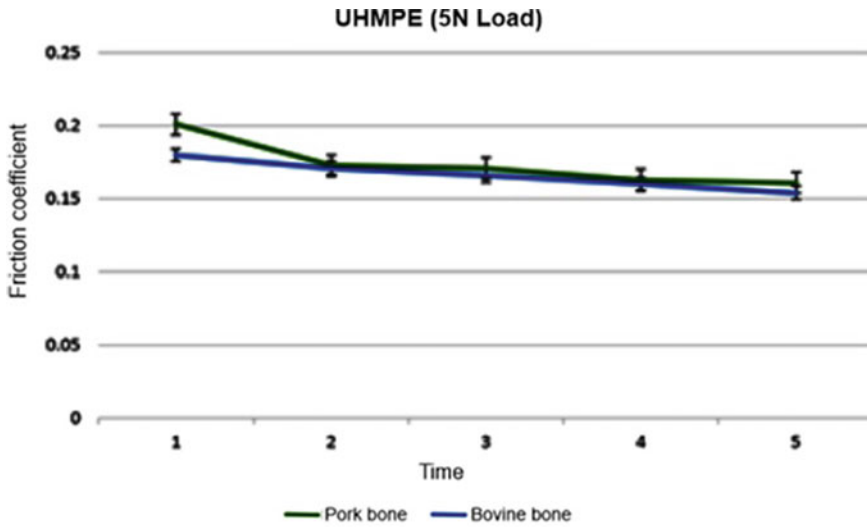


Fig. 6 Friction coefficient in dry condition for UHMWPE versus Porcine and bovine bone (5 N load)

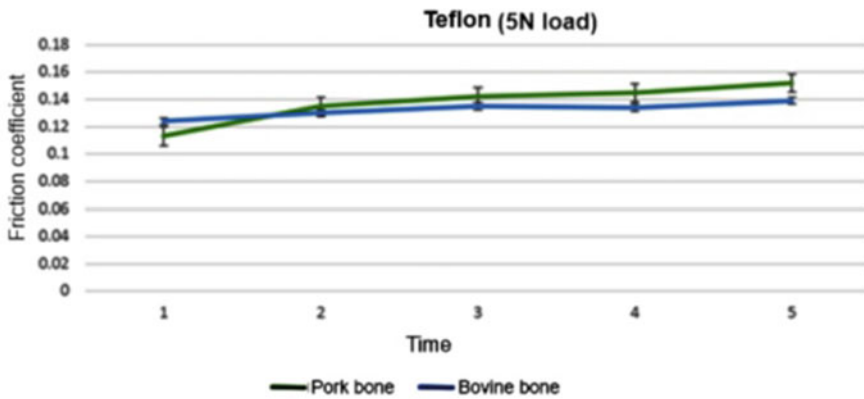


Fig. 7 Friction coefficient in dry condition for Teflon versus Porcine and bovine bone (5 N load)

Porcine is in the range of 0.11 to 0.12 and in the Teflon/bovine bone pair it is 0.4 to 0.5. This indicates that the pair with the lowest coefficient and therefore the lowest resistance to sliding is the pair bovine bone against Teflon.

The measurement obtained from the friction force with a load of 5 N in the polyethylene/porcine bone pair varies from 0.6 to 1.05, the polyethylene/bovine bone pair is in the range of 0.55 to 1.09. The Teflon/porcine bone pair ranges from a value from 0.3 to 0.8, and the Teflon/bovine bone pair is in the range of 0.6 to 0.8,

it is observed that the pair that shows a lower friction force is the one that forms the Teflon/porcine bone.

The coefficient of friction was determined second for a load of 10 N in the tribological pairs UHMWPE and Teflon vs Bone, the coefficients obtained are shown in Figs. 8 and 9. When the 10 N load was applied, the friction coefficient for the polyethylene/porcine bone pair, we have a value of between 0.12 to 0.13, the polyethylene/bovine bone pair is between 0.14 to 0.18 and the Teflon/porcine bone pair is 0.17 to 0.18, while the Teflon/bovine bone pair is 0.17 to 0.18. In this case, the lower friction coefficient is observed in the polyethylene/porcine bone pair, this

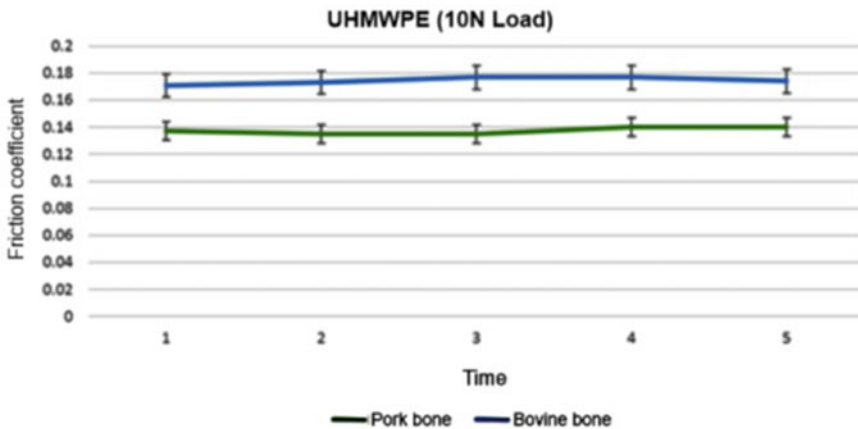


Fig. 8 Friction coefficient in dry condition for UHMWPE versus Porcine and bovine bone (10 N load)

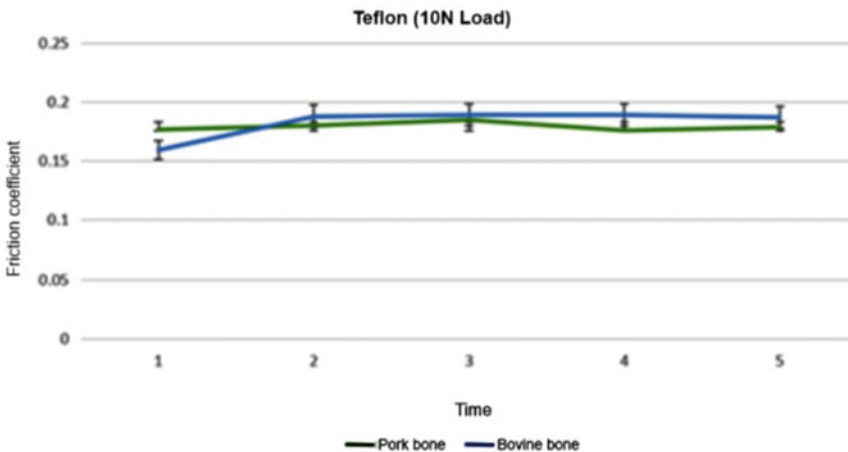


Fig. 9 Friction coefficient in dry condition for Teflon vs. Porcine and bovine bone (10 N load)

pair allows a sliding with less opposition. In the case of the measurement with a load of 10 N of the friction force, we have that the polyethylene/porcine bone pair ranges from 0.3 to 1.6 N. The polyethylene/bovine bone pair is in the range of 1.25 to 2.0 N, and the pair Teflon/porcine bone has a value that is between 1.55 to 1.88 N, while the Teflon/bovine bone pair ranges from 1.6 to 1.88 N, this shows that the lowest friction force occurs in the polyethylene/porcine bone pair.

Comparing both cases, it was observed that at a lower load there is less friction force, but the properties of the materials also intervene, at a low load Teflon allows the sliding of the bone with less deformation. At a higher load, the surface of the Teflon deforms more ratio per bolt, which slows down the movement generating a higher coefficient of friction. In the case of polyethylene, its surface resists more, deforming less, allowing the bolt to slide, generating a lower coefficient of friction.

3.4 Wear Rate

Wear rates were determined applying a load of 5 N and 10 N, for both cases UHMWPE and Teflon vs Bone, the graphs obtained are shown in Figs. 10 and 11.

Both materials exhibit a similar behavior, where increasing wear (Teflon vs. porcine bone) means that there was a greater removal of material from the surface because of a mechanical action.

The wear rate for the Teflon couple against porcine bone applying a load of 5 N was the highest, while with a load of 10 N it was presented in the Teflon couple against bovine bone. It should be noted that when applying the 10 N load, the wear process becomes more critical, with which the loss of material is intensified for both materials.

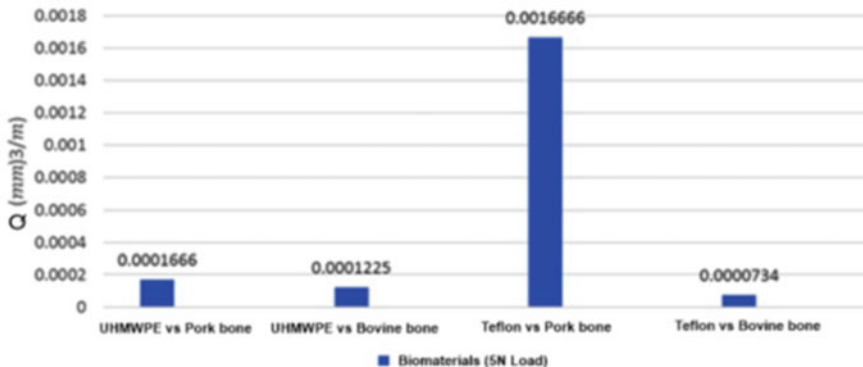


Fig. 10 Wear rate, Q, UHMWPE and Teflon versus Bone (5 N Load)

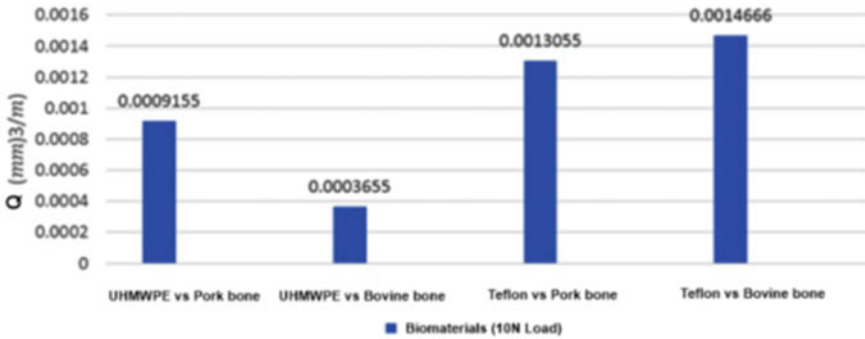


Fig. 11 Wear rate, Q , UHMWPE and Teflon versus Bone (10 N Load)

3.5 Wear Coefficient (K)

Wear coefficient were determined applying a load of 5 N and 10 N, for both cases UHMWPE and Teflon vs Bone, the graphs obtained are shown in Figs. 12 and 13.

The lowest wear coefficient applying a load of 5 N and 10 N was presented in the polyethylene vs. bovine bone pair. Teflon and porcine and bovine bone reached high values, which agrees with the data obtained on lost mass and wear rate. The higher value of the wear coefficient results in higher shear forces on the materials, which causes a higher material detachment in both pairs.

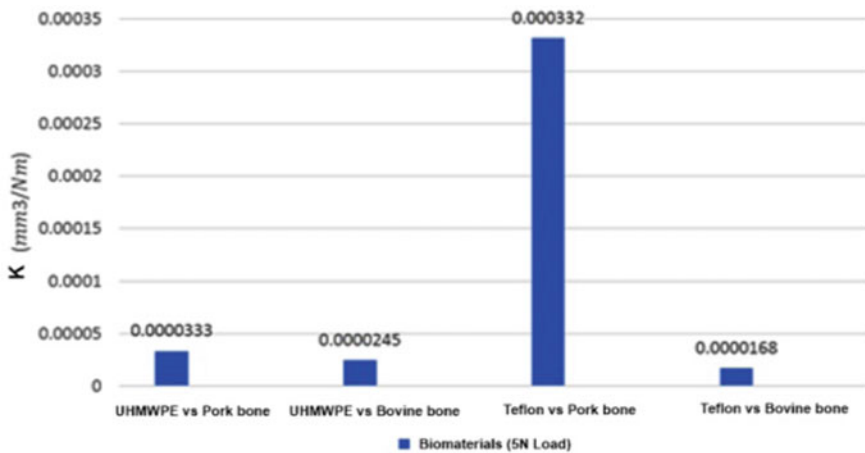


Fig. 12 Wear coefficient, K , UHMWPE and Teflon versus Bone (5 N load)

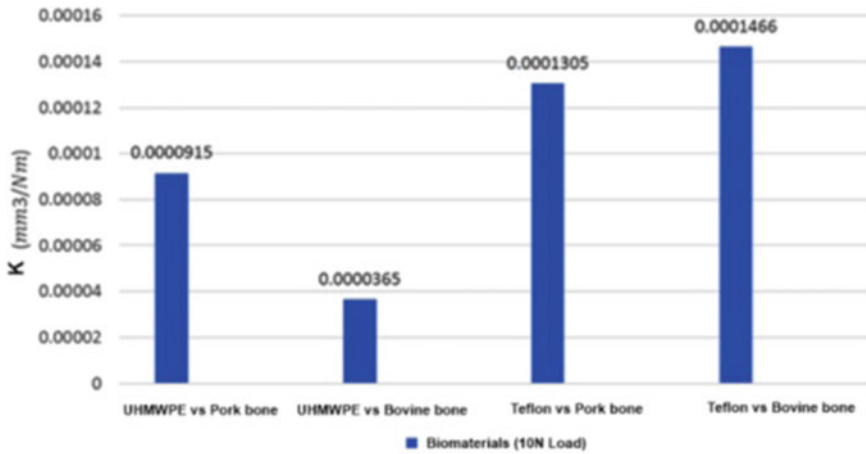


Fig. 13 Wear coefficient, K, UHMWPE and Teflon versus Bone (10 N load)

4 Conclusions

The wear tests on the pairs of materials proposed show the material that presents the greatest damage caused by wear is Teflon, although porcine and bovine bone in both cases of load application suffers quite notable damage. Likewise, Teflon is the material that allows less resistance to sliding, and ultra-high molecular weight polyethylene has a more efficient wear behavior.

When the 5 N (healthy weight) load test was performed, the wear on the high molecular weight polyethylene was lower and the porcine and bovine bones behaved very similarly, leaving a very similar wear mark on the material. In the wear test with a Teflon disc, only a very small trace of wear was observed, in the bones of the animals tested the damage was maintained, although with lower coefficients of force and friction.

In the test carried out with a load of 10 N (overweight), it is observed that the wear in the ultra-high molecular weight polyethylene was greater since a more pronounced mark is appreciated and in both bones, there is a more pronounced mark. This indicates that there was more wear. Bone debris was observed on the surface of the specimens, in the Teflon there was a wear mark on the surface of the material less than in the polyethylene.

According to the results obtained, the lower wear coefficient occurs in the pair of bovine bone against ultra-high molecular weight polyethylene, which indicates a better performance of polyethylene for prostheses.

To increase the quality of life in people who need a type of prosthesis, it is necessary to carry out studies on their materials, so that their behavior when inserted into the human body reaches a high level of quality and efficiency.

Acknowledgements The authors acknowledge the support given by the National Polytechnic Institute and the National Council of Science and Technology, Mexico.

Credit M. Castillo Sánchez: Conceptualization; Writing - review & editing. D. Zarate Lara: Investigation; Writing - original draft. M. Velázquez Vázquez: Supervision; Resources; Project administration. G. Rodríguez Castro: Validation; Formal analysis. L. H. Hernández Gómez: Methodology; Visualization; Data curation.

References

1. Rubber International. Latest surgical advances improve results in knee osteoarthritis. <http://www.ruberinternacional.es/ultimos-avances-quirurgicos-mejoran-resultados-artrosis-rodilla>. Last accessed 2018/10/30.
2. U.S. National Library of Medicine, Department of Health and Human Services, National Institutes of Health. Medical Encyclopedia. Knee joint replacement. <https://medlineplus.gov/spanish/ency/article/002974.htm>, last accessed 2018/10/01.
3. Gómez Barrena E. García F. (2010). Wear of polyethylene in hip and knee prostheses, <https://www.semanticscholar.org/paper/Desgaste-del-poli-etileno-en-pr%C3%B3tesis-de-cadera-y-Barrena-C3%81lvarez/84870cb3f84e3a40674616b93e32a8a978cfd3#citation-papers>, last accessed 2010/10/30.
4. Flannery M. McGloughlin T. Jones E. Birkinshaw C. Analysis of wear and friction of total knee replacements, Part I. Wear assessment on a three station wear simulator. *Wear* 265 999–1008 (2008).
5. Patten Eli W. Van Citters Douglas, Ries Michael D. Pruitt Lisa A. Wear of UHMWPE from sliding, rolling, and rotation in a multidirectional tribo – system. *Wear* 304, 60–66 (2013).
6. Schwenke T, Borgstede LL, Schneider E, Andriacchi TP, Wimmera MA (2005) The influence of slip velocity on wear of total knee arthroplasty. *Wear* 259:926–932
7. Urriolagoitia Calderon G. Urriolagoitia Sosa G. Hernández Gómez L. H. Wear analysis applying a pin – disc configuration to femoral head and acetabular cup. *Rev. Colomb. Vol. X. No. 1. 94 – 110* (2008).
8. Vallet Regí María. Biomaterials for tissue replacement and repair. Complutense University School of Pharmacy; Spain.
9. <http://www.aecientificos.es/empresas/aecientificos/documentos/Biomateriales.pdf>. Last accessed 2018/10/01.
10. Martínez, F. Dpto. Traumatology. Centro Ramón y Cajal de la S. S. de Madrid.
11. http://www.madrid.org/cs/Satellite?cid=1354509007730&language=es&pagename=HospitalRamonCajal%2FPage%2FHRYC_contenidoFinal, last accessed 2019/10/02.
12. Díaz J (2015) Biomaterials: Ultra high molecular weight polyethylene (UHMWPE) in joint prostheses. Universidad de Zaragoza, España
13. Sinha RK (2002) Hip Replacement: Current Trends and Controversies. Marcel Dekker, New York City, NY, USA
14. Maguire JK, Coscia MF, Lynch MH (1987) Foreign Body Reaction to Polymeric Debris Following Total Hip Arthroplasty. *Clin Orthop Relat Res* 216:213–223
15. Massimiliano M, Saverio A (2019) Materials for Hip Prostheses: A Review of Wear and Loading Considerations. *Materiales* 12(19):3226
16. Shrivastava S (2004) Materials for medical devices. Proceedings of the Conference on Materials and Processes for Medical Devices. ASM International, Anaheim, California
17. Medical Encyclopedia, Long Bones
18. https://medlineplus.gov/spanish/ency/esp_imagepages/9582.htm, last accessed 2021/03/23.
19. Rho J-Y, Kuhn-Spearing L, Zioupos P (1998) Mechanical properties and the hierarchical structure of bone. *Med Eng Phys* 20:92–102

20. Mendoza Juan Álvaro. Study of the mechanical properties of the bone system, Ed. National University of Colombia; Colombia. (1991).
21. Rommy HT, Roberto P (1998) Hydroxyapatite and its applications. Mexican Journal of Physics, Mexico 45(supplement 1):144–147
22. Rho JY, Spearing ST, Zioupos T (1998) Mechanical properties and the hierarchical structure of bone. Med Eng Phys 20(2)
23. Albarracín P (2006) Tribology and industrial and automotive lubrication; 3a ed, Ed. Tribos Eng. Mexico
24. Bharat B (1999) Principles and applications of tribology. Ed. Wiley-Interscience. New York
25. Maryory Astrid Gómez Botero. Characterization of the tribological properties of hard coatings. Barcelona. Doctoral thesis, University of Barcelona. Spain (2005).
26. Peña A (2002) Mechanical and tribological characterization of Al 6061-T651 and Al 6061-T651 with chromium phosphate coating. Doctoral thesis. IPN SEPI- ESIME Zacatenco. Mexico
27. Stachowiak GW, Batchelor AW (2001) Engineering tribology. United Kingdom, Butterworth Heinemann
28. Blau P (1992) ASM Handbook, Volume 18 Friction, Lubrication, and Wear Technology. United States of America: ASM International
29. Kovaříková I, Szewczykóvá B, Blaškoviš P, Hodúlová E, Lechovič E (2008) Study and characteristic of abrasive wear mechanisms. Faculty of Materials Science and Technology, Slovak University of Technology, Institute of Production Technologies
30. Stachowiak GW, Batchelor AW (1993) Engineering tribology, vol 24, Elsevier Ltd..All Rights reserved
31. Sobotta Anatomy text. Ed. Waschke, Koch, Kürten, Schulze-Tanzil & Spittau, Elsevier Connect. (2018).
32. Jeff Kerns. What's the Difference between Types of Wear? Machine Design. <https://www.machinedesign.com/print/materials/what-s-difference-between-type>, last accessed 2020/09/10.
33. Suh NP (1977) The delamination theory of wear. Elsevier, New York

Prediction of Surface Finish Model in Cutting AISI 4140 Steel with Different Approaches



Yusuf Şahin, Acar Can Kocabiçak, and Senai Yalçinkaya

Abstract This experimental study describes the development of surface roughness model with main parameters including tool radius using full-factorial design approach and artificial neural network (ANN). Cutting tests and analysis of variance were used in cutting AISI 4140 steels by coated cutting tools. Factorial design/multi quadratic regression (MQR) were compared to ANN model. The results indicated that surface finish decreased with decreasing feed rate and increasing nose radius. It is showed that both feed rate and tool nose radius were effective while other factors were insignificant effect. For testing stage of both methods, data was selected randomly from the existing experimental runs. Further, both randomly selected ANN and MQR indicated no significant differences for prediction the surface roughness because PE and RMSE were 2.73%, 2.21%, 0.063 and 0.046 for MQR and ANN, respectively. Both approaches can used effectively for prediction of any machinability studies in manufacturing engineering due to high accuracy of results. In the future work, other nonlinear models like support vector machine and principal component analysis would be conducted to improve performance accuracy.

Keywords Surface finish · Alloy steel · Coated carbide tools · Cutting · Full factorial design · ANN

Y. Şahin

Department of Mechanical Engineering Faculty of Engineering&Architecture, Nişantaşı University, 1453 Neotech Campus Maslak, Sarıyer, İstanbul, Turkey

A. C. Kocabiçak (✉)

Repkon Machine and Tool Industry and Trade Inc, Istanbul 34980, Turkey

S. Yalçinkaya

Department of Mechanical Engineering, Technology Faculty of Marmara University, Istanbul 34722, Turkey

1 Introduction

Turning is the most important production process in metal cutting processes because of its complexity and generating high cutting temperatures between tool inserts and workpiece. Productivity can be increased with this type of machining process. To increase productivity and reduce the manufacturing costs in turning process, an appropriate machining parameters can be selected, but cutting with high productive may be reduced the efficiency of machining process and output of quality characteristics. In the past few decade, there have been many developments of carbides or ceramics for machining various hard and hardened materials including cast irons. Coated tools indicate a better wear resistance, lower heat and lower forces during machining. This is, especially true for better performance under heavy machining parameters when compared to uncoated tools [1].

Surface roughness parameter is one of the basic concern of metal cutting processes for characterizing the surface features. Cutting parameters, workpiece material, tool types, tool shapes and vibrations affect the surface finish [2]. Quality of surface finish plays a key role for machining different applications because of its effecting on fatigue behaviour, while machining cost leads to higher. Among available method, center line average (CLA or Ra) is the most widely accepted measurement of surface finish. For any metal cutting processes, unless appropriate conditions are chosen, lower roughness and right dimensional size can not be achieved. Thus, number of studies have been conducted in past three decades for determining the optimal machining conditions [1, 3]. Their experimental results indicated that it reduced with enhanced speed and depth of cut, respectively. Davim [4] indicated that larger effect was obtained from speed, but feed rate and depth of cut had no effective on surface finish. Escalona and Cassier [5] exhibited that surface roughness improved with speed, nose radius by reducing feed rate when developed roughness model for some steels. An empirical model for surface finish was developed through factorial design depending upon hardness of workpiece, feed rate, tool's point angles, speed and cutting time [6]. Transformation of logarithmic scale data and nonlinear regression analysis were applied on the empirical developed model. The developed model indicated a satisfactory results for both generating model and confirmation tests due to producing lower errors when compared to existing research. Suresh et al. [7] studied the AISI 4340 steel and Wang and Zheng [8] searched the hardened AISI H13 steel using coated carbide and TiAlN coated carbide tool, respectively. Higher speed and lower feed rate were minimization of the surface finish. Power/tool wear increased linearly with increasing speed and feed rate. Further friction coefficient and chip shearing energy were larger for ductile materials. Moreover, different models for surface roughness were developed using factorial/Taguchi method in turning various steels using carbide/coated carbide cutting tools [9–13].

Further, there have been numbers of surface roughness optimization models for ceramic cutting tools on cold-work, hot work and bearing steels [14–20]. Junaid and Wani [14] studied the surface finish of cutting AISI D2 steel by boron nitride, ceramic

and coated tools conducting tests through RSM approach. Quadratic regression equation was generated to examine the relationship between inputs and responses. The results showed that the dominant factor was cutting time and cutting speed, respectively. Davim and Figueira [15] performed a machinability test for AISI D2 tool steels having hardness 60 HRC using statistical investigation. Cutting tests were carried out with wiper and traditional ceramic tools. Basic factors affecting the flank tool wear of ceramic tools were time and speed. A better performance was revealed with wiper ceramic tools than that of traditional tools. Aouici et al. [16] observed that feed rate was most effective in terms of depth of cut for hard turning AISI D3 hardened steel with ceramic base on turning force/power. The minimum force and better surface finish were achieved at around 0.12 mm/dev. feed rate associated with higher speed and lower depth of cut. Bensouilah et al. [17] observed the machining AISI D3 steel through coated and uncoated CC650 ceramic tools. The better surface quality was obtained with coated ceramic insert (1.6 times) than that of uncoated CC650 ceramic. Elbah et al. [18] studied these two types cutting tools for cutting AISI 4140 steel. Their results indicated that wiper ceramic tool's performance was 2.5 times better than that of uncoated ceramic tool. Further, RSM has been studied widely with some other researchers on surface finish models [21, 22].

Moreover, number of studies have been performed in terms of tool nose radius besides main parameters [23–38]. Effect of the tool's radius were studied during the machining results for tough materials [23, 24]. It was observed that surface finish was highly affected with nose radius. It is found that increasing tool's nose radius led to higher difference between surface tensile stress and sub-surface compressive stress. Chou and Song [25] investigated the turning process with changing tool's nose radius and feed rates. Higher nose radius indicated a finer surface roughness while feed rate strongly affected the surface quality. Ranganath and Vipin [26] studied the surface roughness in terms of design of experiments. The surface finish decreased by increasing speed and reducing by enhanced nose radius. Ranganath et al. [27] predicted the surface finish in cutting EN8 steel by uncoated carbide inserts with RSM. Second order model indicated a quite good result for predicted and measured surface finish. Nataraj and Nagarajan [28] studied the machining EN31 alloy steel under wet condition based on speed, feed rate and nose radius. It is formed theoretical model with RSM to reduce the surface roughness and increase volume of the material. Their results exhibited that surface finish decreased with increasing nose radius. These findings were not only true for different steels as mentioned above, but also for Al 6061 alloy, TiB2/7075 Al alloy composites and Inconel 718 alloy [29–32]. In the composites, cutting force increased with increasing nose radius and caused to lower surface residual stress and more deep residual stress for penetrated layer. Maximum residual stress position transferred to deep surface from machining top surface while tool wear increased. Cutting force, microstructural changes and residual stress distributions were analyzed. They concluded that enhancing tool nose radius resulted in increasing cutting force and increased depth of deformation layers and more higher surface tensile stresses occurred [33, 34]. Taha et al. [35] observed the effects of insert geometries on surface finish in cutting AISI D2 steel. Measured surface roughness and theoretical surface finishes of two different inserts like 'C'

and 'T' type were compared. Surface roughness was lower for 'C' type insert than that of 'T' type under 0.4 mm/rev feed rate. It is concluded that cutting parameters in addition to tool's nose radius were effective. Agrawal et al. [36] studied the AISI 4340 steel with 69 HRC using CBN cutting tools under dry conditions. Three regression models like multiple-, randomly forestry and quantity regression. Spindle speed was effective on the surface finish among parameters. Randomly oriented forestry model was found to be better than that of multiple regression model. Liu et al. [37] studied tool's effect on radius of nose and tool wear of JIS SUJ2 bearing steels with CBN tools in terms of residual stress distributions. X-Ray Diffraction method revealed the radius of tool nose affecting on residual stress distributions. Whereas, the residual squeezed stress increased largely under machined surface when wear of tool increased. Dhar et al. [38] searched the effect of tool wear on the surface quality of mild steel (AISI 1060) in cutting at various conditions. Trends in average Ra values increased with cutting time and tool wear. In addition, higher Ra values were observed with wet cutting than that of dry cutting.

Predicting surface finish models was made using response surface methodology (RSM), fuzzy logic (FL), multiple regression analysis (MRA) and artificial neural network (ANN). Akkuş and Asilturk [39] studied that surface roughness was carried out with various parameters and compared to hard turning with ANN, FL and MRA. It is indicated that FL method was better for optimum predictive model than that of ANN based on mean squared errors. Davim et al. [40] examined the surface finish model for prediction with ANN method. Process parameters for this model were basic cutting factors with three levels according to L27 orthogonal arrays. It was indicated that surface roughness reduced significantly with speed and feed rate while increased with depth of cut. Ozel and Karpuz [41] developed an ANN model to estimate the wear and surface finish. Experimental results were used with Levenberg–Marquardt training. The model applied was found to be better when compared to empirical model. The results indicated that better results could be obtained from ANN with single output in comparison to ANN with multiple output. Rajeev et al. [42] worked the surface finish in turning hardened low alloy steel (AISI4140) with 47 HRC by central composite design. Prediction model for surface finish was developed with MRA and ANN. The results showed that more accuracy was provided with ANN model compared to regression. Chavoshi and Tajdari [43] searched the machining of AISI 4140 steel in cutting by Cubic Boron Nitride tools. They conducted 18 experiments, but keeping the depth of cut and feed rate fixed. These models were used in specifying the optimum parameters. The results indicated that significant factor was hardness on the roughness. Dimla and Lister [44] developed the multilayer perception network for predicting wear using force and acceleration for AISI 4340 steel. Similar studies on carbon steels using different design were carried out with the previous researchers [45–49].

The purpose of the experimental study is, thus, to estimate the prediction of surface finish with factorial design. Coated carbide cutting tools were selected in machining of AISI 4140 steel at dry conditions, and developed a second-order quadratic model (MQR). In addition, MQR and ANN method were compared in terms of root mean squared error (RMSE) and percentage error (PE).

2 Materials

2.1 Theoretical Model

Second order model (quadratic) for surface finish can be generated from the formula following;

$$\hat{y} = y - \varepsilon = b_0 \cdot x_0 + b_1 \cdot x_1 + b_2 \cdot x_2 + b_3 \cdot x_3 + b_4 \cdot x_4 + b_{11} \cdot x_1^2 + b_{22} \cdot x_2^2 + b_{33} \cdot x_3^2 + b_{44} \cdot x_4^2 + b_{12} \cdot x_1 \cdot x_2 + b_{13} \cdot x_1 \cdot x_3 + b_{23} \cdot x_2 \cdot x_3 + b_{24} \cdot x_2 \cdot x_4 + b_{34} \cdot x_3 \cdot x_4 \tag{1}$$

where; b values are estimates of β parameters, ε is experimentally random error, parameters of Eq. (1) were estimated through a Minitab computer software system.

2.2 Workpiece Material and Design of Experiments

The used material of the study was an AISI 4140 steel. Table 1 indicates the chemical compositions of elements in AISI4140 steel (wt.%) used for machining tests under various cutting conditions. Cylindrical shape of specimens, which is 120 mm diameter, 280 mm length were studied in these tests. Cylindrical bars were cut at dry condition. Before actual machining tests, the bars were cleaned by removing about 1–2 mm from outside the specimen surface.

In order to improve a second order model, a method was made with factorial approach, which is consisted of 54 experiments. Two levels for each variable were denoted by -1, 0, + 1 that was used for augments points. Full factorial design was chosen so that all interacted variables would be found out. Four factors like speed, feed rate, depth of cut and nose radius were considered. Cutting conditions and levels of each factors for turning to be used for this study are presented in Table 2.

Table 1 Chemical compositions of elements in AISI4140 steel (wt.%)

| Elements of weight percentages (wt.%) | | | | | | | |
|---------------------------------------|-------|-------|-------|------|-------|------|----|
| C | Si | Mn | Cr | Mo | Ni | Cu | Fe |
| 0.40–0.50 | 0.236 | 0.816 | 0.989 | 0.16 | 0.144 | 0.18 | 97 |

Table 2 Cutting conditions and their levels in turning application

| Factors | Units | Levels | | |
|------------------------------|----------------------|--------|------|--------|
| | | - 1 | 0 | + 1 |
| Cutting speed (X_1) | m.min ⁻¹ | 300 | 375 | 450 |
| Feed rate (X_2) | mm.rev ⁻¹ | 0.1875 | 0.25 | 0.3125 |
| Depth of cut (X_3) | mm | 0.5 | 1 | 1.5 |
| Tool's nose radius (X_4) | mm | 0.8 | - | 1.2 |

2.3 Cutting Tools/Measurement

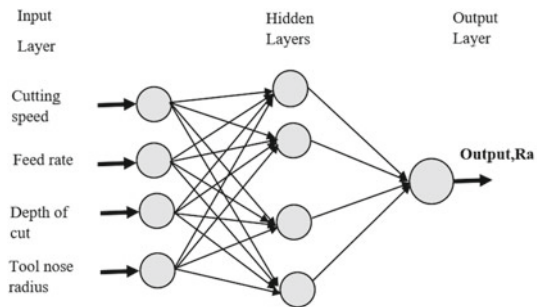
Industrial type of CNC lathe machine (Johnford TC35) was used for turning tests. Spindle speeds varied from 50 to 3500 rpm. The tools selected for the experiments were coated carbide cutting tools, which are manufactured on substrate cemented carbide tool with chemical vapor deposition (CVD) technique, called as TP100. Carbide tool has a multiphase coatings including Ti (C,N) + Al₂O₃ + TiN here. Insert types were TNMG 160,412-MF2 and TNMG 160,408-MF2, respectively. These were provided from Seco Inc. for cutting tests.

A MAHR Perthometer-M1 type of portable was used to measure the surface finish of mild steel. Ra is defined as an arithmetic mean deviation of roughness profile. Three measurements are taken along the axis of specimen to collect the surface finish of cylindrical shaft.

2.4 Artificial Neural Network (ANN)

ANN works through a learning algorithm by adjusting weights and biases that reduce the error through activation function [50]. To develop model, four parameters were taken as input criterions such as speed, feed rate, depth of cut and nose radius while output was surface roughness. Each network composes of three layers like input, output and hidden layer, as shown in Fig. 1. ANN was implemented using the

Fig. 1 ANN architecture



developed feed-forward backpropagation (BP) network (4–5–1). Many activation functions were used to train algorithms of ANN.

The data [9] was normalized between 0 and 1 according to Eq. (2). Data were split into training (80%) and testing (20%) stage. Input and output data were used between 0 and 1 according to Eq. (2),

$$N = \frac{\beta_1 - \beta_{min}}{\beta_{max} - \beta_{min}} \tag{2}$$

where N is normalized data; β_i is measured data while β_{min} , β_{max} show minimum and maximum values, respectively. Normalisation gives an equal result for whole factors.

Model’s performance were evaluated in terms of RMSE and PE through Eqs. (3), (4), respectively.

$$RMSE = \sqrt{\sum_{i=1}^N \frac{(Q_o - Q_p)^2}{N}} \tag{3}$$

$$PE = \frac{Q_o - Q_p}{Q_p} \times 100 \tag{4}$$

which Q_o , Q_p and Q_m are the obtained result, estimated and mean results, respectively. When R^2 approaches to 1 and RMSE gets closer 0, it means that higher efficiency and high performance can be achieved for model formed.

The experimental data for surface finish of alloy sample was collected from total 54 measurements performed in the past study [9].

3 Results and Discussion

3.1 Surface Roughness

Minitab software analysed the data. Second order regression (MQR) equation can be found in the following equation, but $\times 1$ and $\times 3$ are not effective. Therefore, they are neglected.

The second order model equation is given by;

$$Ra, \mu m = 0.154 + 1.240X_2 + 0.4203X_4 + 0.1519X_2 * X_2 - 0.6242X_2 * X_4 \tag{5}$$

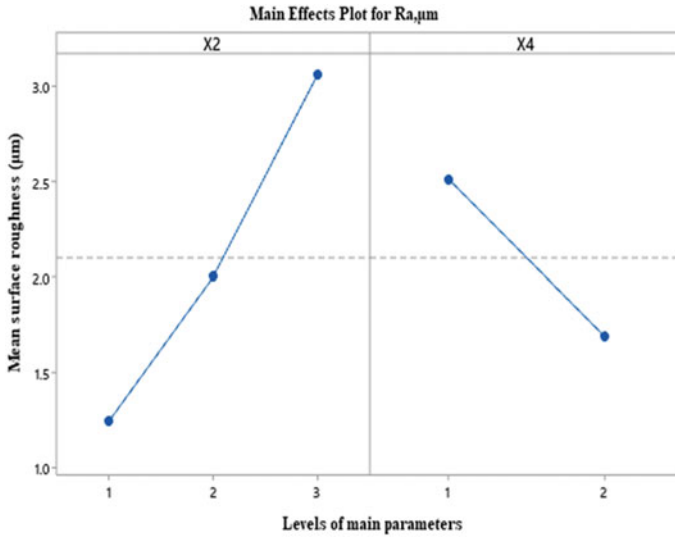


Fig. 2 Main effects plot for Ra values

Equation (5) showed that feed rate ($\times 2$) and tool nose radius ($\times 4$) had positive effects on surface finish when used TiN-coated tools. The model had an adjusted R^2 value of 98%.

Figure 2 indicates the main effects plot for Ra values of tested samples. It can be shown in this figure, feed rate was more effective than that of tool nose radius because it improved by reducing surface roughness while it reduced with enhanced the nose radius. In other words, a better surface finish was achieved using lower feed rate or bigger tool's nose radius. Similar findings were reported within previous studies [23–26, 28, 29]. The variations of these parameters on Ra values were changed more or less linearly.

Pareto chart is one of the basic quality tools for analysing data among factors. Figure 3 indicates the Pareto chart for standardised influence of factors on the surface finish of tested steels. In this chart, the length of bars visually revealed the degree of effect of each parameter for observed results. As was shown in this figure, the Pareto chart indicated that increase of B, D (X2, X4) main parameters, BB quadratic and BD interaction factors had a positive, statistically important effect on the surface finish of tested specimens. This model's adequacy could be examined by the observation of residuals.

The surface finish for steel specimens with normal probability plot residuals are indicated in Fig. 4. This graph shows a cumulative distribution of standardised residuals that determine from theoretical and measured results. The error distributions seemed to be normal since these were appropriated for both positive and negative side of trials. Whereas, plots have had intervals, especially for forward points that had not dropped exactly along the straight line passing through the center while the

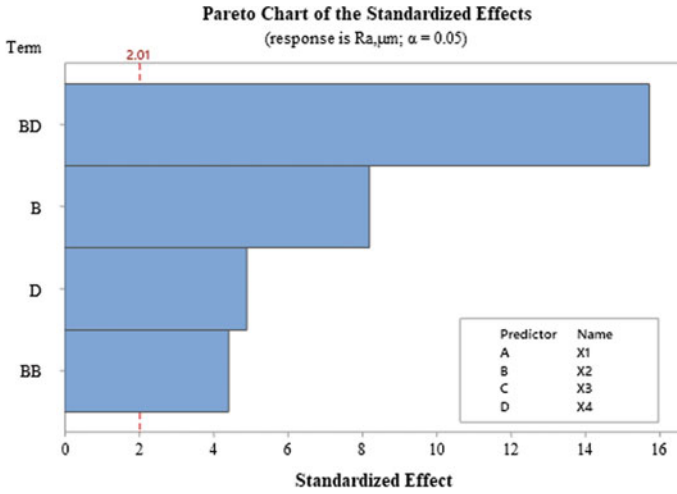


Fig. 3 Pareto chart for control factors of B,D and their interactions of BD

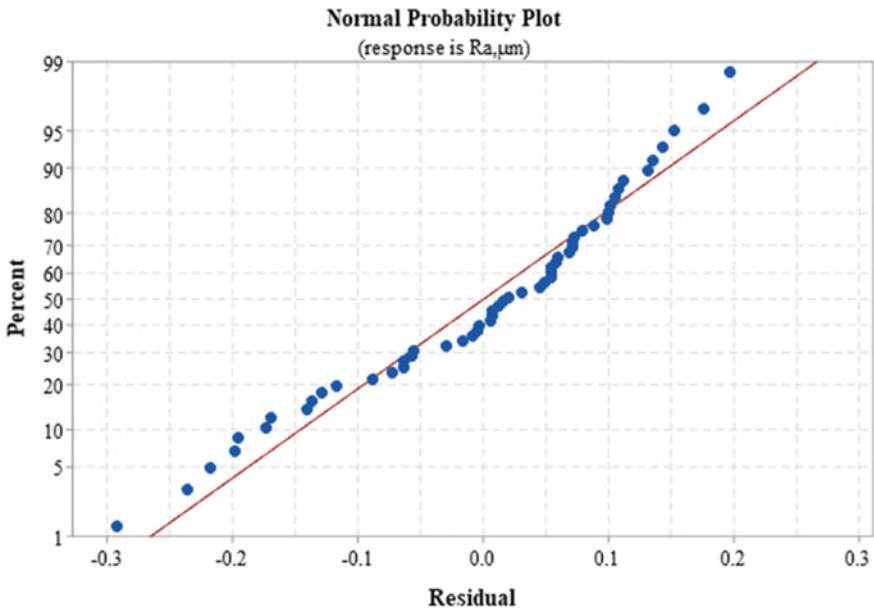


Fig. 4 Normal probability plot of residuals for surface roughness data in turning steels

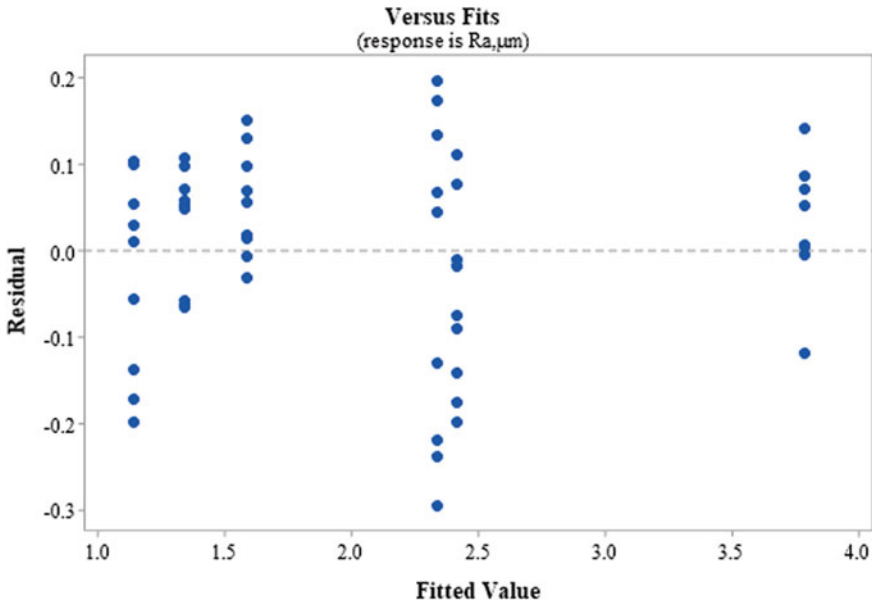


Fig. 5 Residuals plot versus Fitted Values of surface roughnesses

deviations from the normality had not seemed to be large. These results indicated that the model was adequate because of the residual points on probability. Standardised residual was about ± 2.5 .

Figure 5 indicates the residuals plot versus fitted values of the surface roughness. These residuals vs. fitted values data should not indicate any obvious patterns and they had no usual structure, which indicated an adequate model. The residual seemed to be scattered randomly around zero line [21, 23].

3.2 Analysis of Variance (ANOVA)

ANOVA was selected to observe that control factors affecting on steel surface finish quality. ANOVA results for the surface finishes of Ra in machining steels under different parameters are demonstrated in Table 3.

The probability values (p-values) of the model were about 0.0 and 0.0 for X2 and X4 factors, respectively. In this table, smaller result of p-values signified that the related regression coefficient was very important. It meant that both nose radius and feed rate were effective to surface finishes. It is concluded from this work that surface roughness was highly affected by feed rate, followed by nose radius of tools [3, 7, 32]. However, there were no absolute agreements among the researchers. Davim [4], Ranganath and Vipin [26], Agrawal et al. [30] concluded that cutting speed was effective factor on the surface finish, whereas, other studies indicated that cutting

Table 3 Variance for Ra values analysis for second order model

| Source | DF | Adj SS | Adj MS | F-Value | P-Value |
|------------|----|---------|---------|---------|---------|
| Regression | 4 | 42.9547 | 10.7387 | 755.10 | 0.000 |
| X2 | 1 | 0.9546 | 0.9546 | 67.12 | 0.000 |
| X4 | 1 | 0.3407 | 0.3407 | 23.96 | 0.000 |
| X2*X2 | 1 | 0.2770 | 0.2770 | 19.48 | 0.000 |
| X2*X4 | 1 | 3.5066 | 3.5066 | 246.57 | 0.000 |
| Error | 49 | 0.6969 | 0.0142 | | |
| Total | 53 | 43.6516 | | | |

time was the effective factor, followed by cutting speed when turned AISI D2 steel using various cutting tools [14, 15].

3.3 Comparison of Factorial and ANN

The surface roughness results of two models such as MQR and ANN models are compared and presented for all testing stages in Tables 4 and 5 based on R2, PE and RMSE criteria. Figures 6 and 7 exhibit the comparison of the experimental and predicted results for surface finishes against randomly selected experimental run for testing of MQR and ANN outputs, respectively.

Table 4 Comparison of the experimental and predicted results of surface roughness values through randomly selected tests data for testing of MQR model

| Trial number | Randomly tests | Exper., Ra (μm) | Theor., Ra (μm) | Percentage Error (PE), % |
|--------------|----------------|------------------------------|------------------------------|--------------------------|
| 1 | 5 | 1.396 | 1.342347 | 3.996954588 |
| 2 | 9 | 2.3255 | 2.414083 | 3.669426445 |
| 3 | 11 | 2.3405 | 2.414083 | 3.048072498 |
| 4 | 13 | 3.6725 | 3.789681 | 3.092107225 |
| 5 | 19 | 1.414 | 1.342347 | 5.337889532 |
| 6 | 28 | 1.556 | 1.586028 | 1.893283095 |
| 7 | 29 | 2.405 | 2.414083 | 0.376250527 |
| 8 | 33 | 3.862 | 3.789681 | 1.908313655 |
| 9 | 43 | 2.273 | 2.414083 | 5.844165259 |
| 10 | 49 | 3.8435 | 3.789681 | 1.420145917 |
| 11 | 51 | 3.797 | 3.789681 | 0.193129712 |
| 11 | 54 | 2.3825 | 2.337431 | 1.928142478 |
| | | Average error, % | | 2.73 |

Table 5 Comparison of the experimental and predicted results of surface roughness values through randomly selected tests data for testing of ANN model

| Trial number | Randomly tests | Exper.Ra (µm) | Theor.Ra (µm) | Error, % |
|--------------|----------------|------------------|---------------|-------------|
| 1 | 5 | 1.396 | 1.380933408 | 1.091044084 |
| 2 | 9 | 2.3255 | 2.273858264 | 2.271106211 |
| 3 | 11 | 2.3405 | 2.316227352 | 1.047938931 |
| 4 | 13 | 3.6725 | 3.573510782 | 2.770083102 |
| 5 | 19 | 1.414 | 1.586872236 | 10.89389755 |
| 6 | 28 | 1.556 | 1.501875556 | 3.603790186 |
| 7 | 29 | 2.405 | 2.42486775 | 0.819333333 |
| 8 | 33 | 3.862 | 3.87660827 | 0.376831205 |
| 9 | 43 | 2.273 | 2.242473557 | 1.361284404 |
| 10 | 49 | 3.8435 | 3.882511519 | 1.004801112 |
| 11 | 51 | 3.797 | 3.786990151 | 0.264322034 |
| 12 | 54 | 2.3825 | 2.356811338 | 1.089975309 |
| | | Average error, % | | 2.21 |

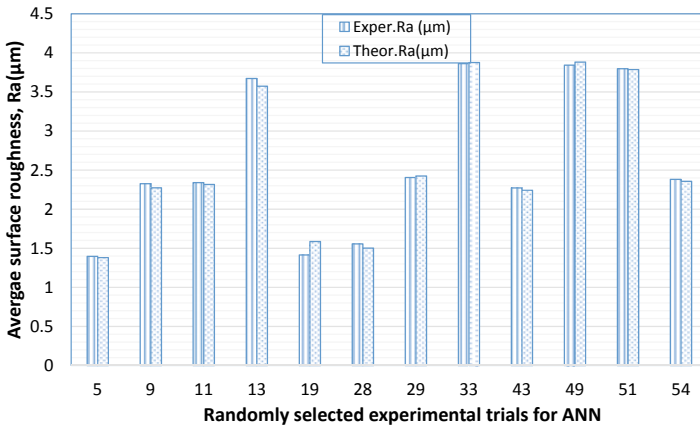


Fig. 6 Comparison of surface roughness between the experimental and predicted factorial results against selected experimental run for testing

The data were randomly selected such as 5, 9, 11, 13, 19, 23, 28, 29, 33, 43, 49, 51 and 54 for testing runs, as shown in Tables 4 and 5 for both designs. This figure demonstrated that there were some differences between the experimental and theoretical prediction values for testing algorithm. Error percentages in results of the surface roughness of steel for MQR and ANN were estimated. Percentage error (PE) was calculated using the data from experimental run - theoretical ones, divided by theoretical run $\times 100$.

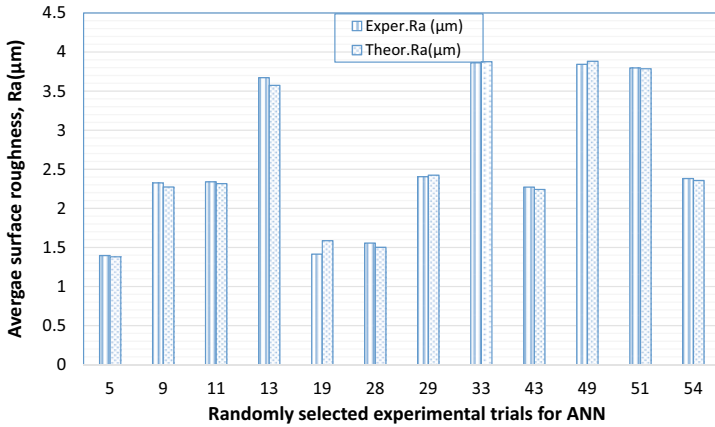


Fig. 7 Comparison of surface roughness between the experimental and predicted ANN results against selected experimental run for testing

The average error reached to 2.73% for MQR approach. This might be because more fluctuations appeared among the measured surface roughness values that was ranged from 0.1931 to 8.431 μm , but most of the data was around 1.9–3.6 μm except a few data like 5, 10 and 11. Figure 7 also indicates the comparison between the experimental surface finish and corresponding ANN outputs. Although same data points were used again, there was small differences between the experimental and theoretical one, which are ranged from 0.095 to 4.16 μm , but most of the data was around 0.81–2.27 μm except a few data like 6, 5 and 7. The average error was about 2.21% for ANN method due to nonlinear behaviour. Therefore, randomly selected ANN data provided a little more precise results than that of randomly selected MQR. These models indicated a strong correlation between the input and output because the PE was 2.73% for MQR while it was % 2.21 for ANN, respectively. In terms of R2 criteria, there was no significant variations provided between ANN and MQR for selected run data. RMSE were about 0.063 and 0.046 for MQR and ANN, respectively. The previous study indicated that the fuzzy logic model was found to be better prediction model than that of ANN in terms of only MSE criteria [39]. In contrast, applications of ANN were shown better estimations for other studies [41, 42]. As a summary, a comparison made between two different methods, as shown in Tables 4 and 5 and Figs. 6 and 7, ANN methodology gave a slightly better prediction results for Ra values.

It was obvious that Ra values predicted by MQR were found to be very close to experimental values of ANN results due to carrying out 54 experiments.

4 Conclusions

This study describes the improved of surface roughness models when cutting alloy steels (AISI 4140) using coated cutting tools at various dry conditions. Second-order method prediction equation was developed through full-factorial design of experiment and compared with ANN approach for RMSE, R^2 and PE. The experimental conclusions exhibited that surface quality enhanced with decreasing feed rate, but decreased with increasing nose radius. Variance analysis indicated that both feed rate and tool nose radius were effective on the surface finishes while other factors were in-significant. Moreover, in testing stage, randomly selected ANN exhibited a slightly better prediction ability than that of MQR because the average errors were 2.21 and 2.73% for ANN and MQR, respectively. Further, RMSE values were about 0.063 and 0.046 for MQR and ANN, respectively. Both methods can be used effectively for prediction tools in any types of machining applications in industry because of the high accuracy of the results. In the future work, other nonlinear models like support vector machine and principal component analysis would be performed for improving the accuracy of performance.

References

1. Sahin Y, Motorcu AR (2004) Prediction of surface roughness in machining of carbon steel by CVD coated cutting tools. In: Proceedings of 8th international conference on numerical methods in industrial forming processes, uniform 2004, Ohio State University, Mechanical Engineering Department, USA, 712, pp 1414–1419
2. Şahin Y (2001) Metal cutting principles, Vol 2. Seçkin Yayın & Dağıtım, Ankara, Turkey
3. Sahin YM (2005) Surface roughness model for machining of mild steel by coated cutting tools. *J Mater Des* 26:321–326
4. Davim, JP (2001) A note on the determination of optimal cutting conditions for surface finish obtained in turning using design of experiments. *J Mater Process Technol* 116: 305–308
5. Escalona PM, Cassier Z (1998) Influence of critical cutting speed on the surface finish of turned steel. *Wear* 218:103–109
6. Feng (Jack) CX, Wang X (2002) Development of empirical models for surface roughness prediction in finish turning. *Int J Adv Manuf Technol* 20: 348–356
7. Suresh R, Basavarajappa S, Gaitonde VN, Samuel GL (2012) Machinability investigations on hardened AISI 4340 steel using coated carbide insert. *Int J Refract Metals Hard Mater* 33:75–86
8. Wang JJ, Zheng M (2003) On the machining characteristics of H13 tool steel in different hardness states in ball end milling. *Int J Adv Manuf Technol* 22:855–863
9. Sahin Y, Motorcu AR (2004b) A model for surface roughness in turning AISI 4140 steel using coated carbide cutting tools. in: Proceedings of 11 th international conference on Mach Des Prod. Antalya/Turkey, pp 11–15. <https://www.researchgate.net/publication/281865348>.
10. Asiltürk, I., Akkuş, H. (2011)“Determining the effect of cutting parameters on surface roughness in hard turning using the Taguchi method”. *Measurement* 44(9):1697–1704.
11. Feng, C-X. (2001)“An experimental study of the impact of turning parameters on surface roughness”. Proceedings of the 2001 Ind Eng Res Conf.No.2036.
12. Yang WH, Tarn YS (1998) Design optimization of cutting parametres for turning operations based on the Taguchi method. *J Mater Process Technol* 84:122–129

13. Kopac J, Bahor M, Sokovic M (2002) Optimal machining parameters for achieving the desired surface roughness in fine turning cold pre-formed steel work processing. *Int Mach Tools Manuf.* 42:707–716
14. Junaid Mir, M., Wani, MF. (2018) “Modelling and analysis of tool wear and surface roughness in hard turning of AISI D2 steel using response surface methodology”. *Int J Ind Eng Comp.* 9:63–74.
15. Davim, JP., Figueira, L.(2007) “Comparative evaluation of conventional and wiper ceramic tools on cutting forces, surface roughness, and tool wear in hard turning AISI D2 steel”. *Proceedings of the Inst of Mech Eng. Part B: J Eng Manuf.* 221(4): 625–633.
16. Aouici H, Bouchelaghem H, Yaltese MA, Elbah M, Fnides B (2014) Machinability investigation in hard turning of AISI D3 cold work steel with ceramic tool using response surface methodology. *The Int J of Adv Manuf Technol.* 73(9–12):1775–1788
17. Bensouilah, H., Aouici, H., Meddour, I., Yaltese, MA., Mabrouki, T., Girardin, F. (2016) “Performance of coated and uncoated mixed ceramic tools in hard turning process”. *Measurement* 82:1–18.
18. Elbah M, Yaltese MA, Aouici H, Mabrouki T, Rigal JF (2013) Comparative assessment of wiper and conventional ceramic tools on surface roughness in hard turning AISI 4140 steel. *Measurement* 46(9):3041–3056
19. Fnides B, Yaltese MA, Mabrouki T, Rigal JF (2009) Surface roughness model in turning hardened hot work steel using mixed ceramic tool. *Mechanika* 77:68–73
20. Şahin, Y., Yalcinkaya, S. (2017) “Study of the surface finish when turning hardened steels with coated ceramic cutting tools”. *Mater Met Technol.* 11:307–316.
21. Noordin, MY., Venkatesh, VC., Sharif, S., Elting, S., Abdullah, A. (2004) “Application of response surface methodology in describing the performance of coated carbide tools when turning AISI 1045 steel”. *J Mater Process Technol.* 145: 46–58.
22. Makadia AJ, Nanavati JI (2013) Optimization of machining factors for turning processes based on the response surface methodology. *Measurement* 46(4):1521–1529
23. Madariaga A, Esnaola JA, Fernandez E, Arrazola PJ, Garay A, Morel F (2014) Analysis of residual stress and work-hardened profiles on Inconel 718 when face turning with large-nose radius tools. *Int J Adv Manuf Technol* 71(9–12):1587–1598. <https://doi.org/10.1007/s00170-013-5585-6>
24. Liu M, Takagi J, Tsukuda A (2004) Effect of tool nose radius and tool wear on residual stress distribution in hard turning of bearing steel. *J Mater Process Technol* 150(3):234–241. <https://doi.org/10.1016/j.jmatprotec.2004.02.038>
25. Chou, YK., Song, H (2004) “Tool nose radius effects on finish hard turning”. *J Mater Process Technol.* 148(2):259–268. <https://doi.org/10.1016/j.jmatprotec.2003.10.029>.
26. Ranganath, MS, Vipin, H. (2014) “Effect of rake angle on surface roughness in CNC turning”. *Int J Adv Res Innov* 2:522–530.
27. Ranganath, MS., Vipin, H. (2015) “Surface roughness prediction model for CNC turning of EN-8 using Response Surface Methodology”. *Int J Emer Technol Adv Eng.* 5 (6):135–143.
28. Natara, j M., Nagarajan, N. (2019) Tepki yüzeyi metodolojisini kullanarak kesici takım burun radyüsünün yüzey pürüzlülüğüne etkisi. *Balkan Triboloji Derneği Dergisi* 25(1):224–235
29. Singh D, Chadha V, Singari RM (2016) Effect of nose radius on surface roughness during CNC turning using response surface methodology. *Int J Rec Adv in Mech Eng (IJMECH)* 5(2):31–45. <https://doi.org/10.14810/ijmech.2016.520331>
30. Ranganath, MS, Vipin, H. (2014) “Experimental investigation and parametric analysis of surface roughness in CNC turning using design of experiments”. *Int J Mod Eng Res.* 4(9):15–25.
31. Neseli S, Yıldız S, Türkeş E (2011) Optimising parameters of cutting tool geometry for turning operation based on RSM. *Ölçüm* 44(3):580–587. <https://doi.org/10.1016/j.measurement.2010.11.018>
32. Lin K, Wang W, Jiang R, Xiong Y (2019) The effects of tool nose radius and tool wear on residual stress distributions TiB₂/7075 Al alloy composites produced with in situ method for turning. *The Int J Adv Manuf Technol.* 100:143–151

33. Sharman ARC, Hughes JI, Ridgway K (2015) The effect of tool nose radius on surface integrity and residual stresses when turning Inconel 718™. *J Mater Process Technol* 216:123–132. <https://doi.org/10.1016/j.jmatprotec.2014.09.002>
34. Gürgen S (2019) An investigation on surface roughness and tool wear in turning operation of Inconel 718. *J Aer Technol Man.* 11:3–10. <https://doi.org/10.5028/jatm.v11.1030>
35. Taha, Z., Lelana, HK., Aoyama, H.(2010)"Effect of insert geometry on surface roughness in the turning process of AISI D2 steel". 11th Asia pacific industrial engineering and management system, Melaka 7–10. <https://www.researchgate.net/publication/321765930>.
36. Agrawal A, Goel S, Rashid WB, Price M (2015) Prediction of surface roughness during hard turning of AISI 4340 steel (69 HRC). *Applied Soft Comp* 30:279–286
37. Liu, M., Takagi, JI, Tsukuda, A. (2004)"Effect of tool nose radius and tool wear on residual stress distribution in hard turning of bearing steel". *J Mater Process Technol.* 150 (3): 234–24120.
38. Dhar, NR., Ahmed, MT., Khoda, AKMB. (2007) "Analysis of influence of machining time and tool wear on surface roughness in turning AISI-1060 steel". Proceed of the Int Confer on Mech Eng 2007 (ICME2007), Dhaka, Bangladesh ICME07-AM-37, 29- 31 December 2007. <https://www.researchgate.net/publication/342446958>.
39. Akkus, H., Asilturk, I. (2013)"Predicting surface roughness of AISI 4140 steel in hard turning process through Artificial neural network fuzzy logic and regression models". *Sci Res Ess* 6:2729–2736.
40. Davim JP, Gaitonde VN, Karnik SR (2008) Investigations into the effect of cutting conditions on surface roughness in turning of free machining steel by ANN models. *J Mater Process Technol* 205:16–23
41. Ozel T, Karpat Y (2005) Predictive modeling of surface roughness and tool wear in hard turning using regression and neural networks. *Int J Mach Tools Manuf* 45:467–479
42. Rajeev, D., Dinakaran, D., Muthuraman, S.(2016) "Prediction of roughness in hard turning of AISI 4140 steel through artificial neural network and regression models". *Int J Mech Eng Technol (IJMET)*7(5): 200–208. Article ID: IJMET-07–05–022.
43. Chavoshi SZ, Tajdari M (2010) Surface roughness modelling in hard turning operation of AISI 4140 using CBN cutting tool. *Int J Mater Forming.* 3(4):233–239
44. Dimla DE, Lister PM (2000) On-line metal cutting tool condition monitoring II: tool-state classification using multi-layer perceptron neural networks. *Int J Mach Tools Manuf* 40:769–778
45. Gupta AK (2010) Predictive modeling of turning operations using response surface methodology artificial neural networks and support vector regression. *Int J Manuf Technol* 48:763–778
46. Abburi, NR, Dixit, US. (2006)"A knowledge-based system for the prediction of surface roughness in turning process". *Robot and Comp-Integ Manuf.* 22:363–369.
47. Neseli, S., Tasdemir, S., Yaldız, S.(2009)" With artificial neural network approach to predict surface roughness in turning". *J Eng Arch Faculty Esk. Osmangazi University* 2(3):65–75.
48. Karayel D (2009) Prediction and control of surface roughness in CNC lathe using artificial neural network. *J Mater Process Technol* 3125–313:2009
49. Rosales A, Vizán A, Diez E, Alanís A (2019) Prediction of surface roughness by registering cutting forces in the face milling process. *Euor. J. Sci. Res.* 41(2):228–237
50. Şahin Y, Şahin F (2021) Effects of process factors on tribological behaviour of epoxy composites including Al₂O₃ nanoparticles: a comparative study on multi-regression analysis and artificial neural network". *Adv. in Mater Process Technol.* 2021;TMPT #1878712:1–15. <https://doi.org/10.1080/2374068X.2021.1878712>.